Investigating Corrosion Behaviour of Nickel-Plated Steel for Circulation Coinage

By

Rebecca Kate Waldram

A Thesis

Submitted to Swansea University

in fulfilment of the

requirements for the Degree of

Engineering Doctorate (EngD)

in

Materials Engineering

College of Engineering, Swansea University, 2019

Investigating Corrosion Behaviour of Nickel-Plated Steel for Circulation Coinage

Abstract

Nickel plating has been used as a barrier coating to protect more reactive metals against corrosion, to improve their wear resistance or as a decorative feature since the early 1800's. Since then there have been many changes to the bath composition to develop different deposit characteristics. The most widely used bath for nickel electrodeposition was developed by Professor O.P. Watts in 1916, which, with a few minor alterations is still commonly used today.

Circulation coinage is made from a diverse range of metals and alloys, which varies widely across the world. Until recently, these tokens were produced solely from solid metal sections; however rising metal prices for those commonly used such as nickel, copper and zinc meant alternative, cheaper production methods required investigation. Nickel plating was selected to reduce raw metal costs, by only using a thin layer of this more expensive metal over a cheaper substrate, such as steel. Nickel has excellent corrosion resistance in a wide variety of environments, good wear resistance and an attractive lustre.

Part of this thesis examines the use of nickel-plated coin sections in conjunction with other metallic sections to discover their compatibility for circulation, in terms of the risk of a galvanic corrosion cell forming. Comparisons between such sections were made using in-situ SVET and SKP analysis to obtain current density distribution maps to show the locations of anodic and cathodic activity, as well as classic electrochemical techniques including open circuit potential to form a galvanic series and zero resistance ammetry to measure the current generated when sections were immersed in the same electrolyte. The results from these experiments indicated that where bi-metallic construction is used there is a risk of galvanic corrosion to varying extents under both immersion and atmospheric conditions. Different countries use coins of varying compositions, and results from four bimetallic coins showed some compositions are more prone to galvanic corrosion than others.

Nickel-plated coatings have previously been found to suffer from porosity, and therefore can be susceptible to pitting corrosion when immersed in aggressive chloride-based environments. To monitor this in atmospheric conditions, defects were made in the nickel-plated deposits and electrolyte droplets containing chlorides were introduced. A variety of hole sizes and chloride concentrations were used, and the spreading of these droplets was monitored using time-lapse photography and a Scanning Kelvin Probe. Overall, increased chloride concentration up to 2 M led to an increase in the observed spreading, although above this a decrease was seen. Defect size was shown to have little effect on the spreading distance.

As a possible alternative to standard electrolytic nickel plating, electroless nickel plating solutions were investigated. This technology plates via a chemical process and requires no applied current, which could potentially reduce manufacturing costs. Three commercially available plating solutions were compared to a basic in-house bath, where it was found changing the bath pH and temperature could significantly alter the properties of the final deposit. Increasing plating temperature led to an increase in the phosphorous content, plating rate, corrosion resistance and Vickers hardness of the deposit, whilst increasing bath pH led to a decrease in the phosphorous content and corrosion resistance, and an increase in the plating rate and Vickers hardness of the deposit.

Additions of organic compounds taurine and thiamine hydrochloride were made to the in-house bath in varying quantities to effect changes in the deposits and improve the properties. These compounds were selected as they are both amino acids, similar in structure to some additives previously used in electroless nickel baths, are non-toxic, low cost and contain sulphur, previously shown to have a brightening effect on nickel deposits. Taurine additions led to similar phosphorous contents and plating rates and lowered the corrosion resistance of the deposits. Thiamine hydrochloride lowered the phosphorous content of the alloy, increased the plating rate and lowered the corrosion resistance of the samples produced.

Author Declaration

This work has not previously been accepted in substance for any degree and is not being concurrently submitted in candidature for any degree.

Signed: ______________________________________

Date: ______________________________________

STATEMENT 1

This thesis is the result of my own investigations, except where otherwise stated. Other sources are acknowledged by footnotes giving explicit references.

Signed: ______________________________________

Date: ______________________________________

STATEMENT 2

I hereby give consent for my thesis, if accepted, to be available for photocopying and for inter-library loan, and for the title and summary to be made available to outside organisations.

Signed: ______________________________________

Date: ______________________________________

Table of Contents

Acknowledgements

There are a great number of people I would like to thank for their help in making this project happen. Firstly, I'd like to thank all the staff within the M2A scheme for all their help throughout the project and running of the COATED scheme. None of this would have happened without your help and encouragement. This work would not have been possible without the supervision of Professor Geraint Williams, thank you for all the support you have provided over the last four years. I am very grateful to The Royal Mint for sponsoring this project, and especially to Matthew James and Ciaran Martin for their assistance and involvement throughout the project. This work would not have been possible without support from numerous funding bodies, including the EPSRC and WEFO.

I could not have done this without the support of my family and friends, there are too many of you to name everyone individually, but your support has been greatly appreciated and I will remember this experience forever. A special mention to the Tom's and Phil for all the laughs and weighty life conversations.

I can't express my gratitude enough to my Tom, for always being there, putting up with me and his support on the bad days, and sharing this experience with me on the good. You mean more to me than I can ever say.

Also massive thanks to my Dad, for being there for me every step of the way and believing in me. I hope to become slightly saner once this work is submitted!

It has been a tough four years for many different reasons, but I wouldn't have it any other way.

List of Figures

List of Tables

Glossary

ACD	Allergic contact dermatitis
AFS	Artificial sweat
DI	Deionised
E_{corr}	Free corrosion potential
EDS	Energy Dispersive X-Ray Spectroscopy
EN	Electroless nickel plating
EP	Electroplated nickel
$g \cdot L^{-1}$	Grams per litre
I_{corr}	Corrosion current
LPR	Linear Polarisation Resistance
MPa	Megapascals
NaCl	Sodium Chloride
Ni-P	Nickel-Phosphorous
°C	Degrees Celsius
OCP	Open Circuit Potential
PDP	Potentiodynamic Polarisation
ppm	Parts per million
RH	Relative Humidity
SCE	Saturated Calomel Electrode
SEM	Scanning Electron Microscope
SKP	Scanning Kelvin Probe
SVET	Scanning Vibrating Electrode Technique
TRM	The Royal Mint
$\mu g \cdot cm^{-2} \cdot week^{-1}$	Micrograms per centimetre^2 per week
$\mu m \cdot hr^{-1}$	Microns per hour
wt.%	Weight percent
XRD	X-Ray Diffraction
ZRA	Zero Resistance Ammetry

Chapter 1. Introduction and Literature review

1.1 Introduction

Coins have been used around the world as trading currency for thousands of years. Original coins were created from precious metal tokens and traded for their intrinsic value. However, fluctuations in metal prices led to the creation of fiat money, a system that uses inexpensive metal tokens assigned a value by the governing body of each region. The first record of minted coinage is thought to date back to around 800 BC in Lydia, and the first nickel-alloy coins are understood to have been issued in around 130 BC in ancient Bactria, now Afghanistan [1]. Today, around 60% of the world's circulating coinage is made from nickel or a nickel containing alloy [2].

Selecting the metal or alloy for creation of a coin requires great consideration. Within a currency, each denomination must be unique, for easy identification. This is possible using different metals and alloys to alter colour, along with changes in shape and size. The material chosen must not tarnish in circulation and should maintain a minted image for the expected lifetime of around 30 years. Ease of counterfeiting should be considered; each denomination must have an individual electronic signature, as automated machines use this to check for counterfeits. The electronic signature of each coin is dictated mainly by composition. The material must be soft and ductile for minting but must be wear resistant to maintain the embossed image.

Nickel has become popular in the manufacture of the world's coinage due to price, weight, wear resistance, ease of minting and low release values in artificial sweat solution [3], [4]. With the increased incidence of plated coinage, alternative cheaper and faster methods of plating nickel are under investigation, and how this affects performance under circulation conditions.

Chapter 1 provides a review of current literature around nickel and its uses, corrosion mechanisms affecting samples examined in this thesis, as well as some history and developments of electroless nickel plating. Chapter 2 details the methods and techniques used to create and experiment on the samples. Chapters 3 to 6 show results and discuss findings, whilst Chapter 7 concludes all the work carried out within this thesis.

In this thesis, three main issues facing circulation coinage will be discussed:

The suitability of current metallic pairings used for bi-metallic coins will be investigated, to gauge whether or not galvanic corrosion is a large risk for current bimetallic coin pairings. Bi-metallic coins have been used in modern coinage since 1982, initially in Italy, where counterfeiting of the 500 lire was a problem. This construction has been widely adopted, most notably for the €1 and €2 coins introduced in 1999 and more recently in the new UK £1 in 2017. These coins are more difficult to manufacture but provide a significant challenge for counterfeiters to replicate. However, it is unknown how these materials react together in circulation, despite their significant use in coinage throughout the world [5]. Chapter 3 will investigate the potential for galvanic corrosion to happen between the sections of different circulation coins.

Nickel-plated substrates used for coins can suffer from porosity [6], so it is important to understand how such defects can effect corrosion of circulation coinage. Previous research showed nickel-plated coins can display red rust formation after immersion in artificial sweat for 1 week [7]; Chapter 4 investigates the affect of various chloride containing electrolytes on defects in nickel-plated steel. Experiments were conducted under atmospheric corrosion conditions using a chloride containing droplet deposited over an area comprising a defect.

Electroless nickel plating forms a barrier coating, used to protect electrochemically active materials from corrosive environments. They are chosen for their high hardness, wear and corrosion resistance, and are used in a wide range of industries including the petroleum, aerospace, automotive and nuclear sectors [8]–[12]. Electroless nickel (EN) plating is a chemical, or auto-catalytic way to deposit a nickel alloy onto a suitable substrate. Regardless of substrate material or geometry, EN plating forms an even and consistent deposit.

The deposition proceeds through oxidation of a reducing agent which catalyses nickel ion reduction onto a substrate. After deposition of an initial layer, the process becomes auto catalytic. Electroless nickel deposition results in an alloy, based on the reducing agent used. Depending on the desired properties, alloys contain between 2 – 14 wt.% phosphorous or 2.5 – 8 wt.% boron which can be produced using different reducing agents. Chapter 5 investigates the potential for nickel-phosphorous alloys to replace standard electrolytic nickel plating, whilst Chapter 6 investigates the addition of novel ingredients to the plating bath.

1.2 Effects of nickel on health

The main objective is to reduce the nickel ions released from circulation coinage. Despite the advantageous qualities of nickel, studies show it can have detrimental effects on human health. Previous studies showed nickel has a strong sensitising potential and can cause significant health problems, depending on its state of matter [13]. Airborne nickel, such as fumes, aerosols or dust can increase the risk of lung and respiratory cancers [13]. All nickel compounds are classified as carcinogenic, except metallic nickel [14], [15].

Nickel allergic contact dermatitis (ACD) is a delayed type hypersensitivity which manifests itself as an inflammatory reaction, and is the most common adverse response from regular nickel contact, affecting millions of people worldwide [13], [15]–[17]. The symptoms include dry skin, inflammation, eczema and blisters. Whilst nickel metal itself does not cause ACD, salts formed when nickel reacts with sweat on the skin has been shown to cause an adverse reaction [18], [19].

Previous research claimed coin handling is responsible for some cases of ACD [20], however interactions with coins tends to be transient making them less likely to elicit a response [3], [21]. Results from investigations into the effect of coins on nickel sensitive patients concluded hand eczema is likely to be caused by other sources like soap or food, rather than coin handling [22]. It has also been shown that ingestion of nickel in small amounts may be a more important factor in hand eczema than skin contact with metals [23]. An additional paper emphasised normal coin use should not involve long periods of skin contact and could only cause problems for already sensitised individuals or those exposed for prolonged periods. It has been suggested in such cases protective equipment should routinely be used [1].

The release of nickel is regulated in the EU, under BS EN 1811, which states the rate of nickel release from objects in direct and prolonged contact with the skin should be less than $0.5\ \mu g \cdot cm^{-2} \cdot week$ measured via an immersion release trial [24].

The release of nickel by objects is generally caused by a corrosion reaction. When a nickel object is in contact with an aggressive electrolyte such as sweat or another chloride containing solution, degradation of the metal can occur, leading to the release of ions from the surface. The following section reviews the pertinent literature related to the field of corrosion, with a focus on nickel surfaces.

1.3 Corrosion theory

Corrosion is an electrochemical mechanism, characterised by the reaction of a metal in an aqueous environment, leading to damaging attacks on the surface. Some metals are significantly more susceptible to corrosion, highlighting the need for considered material selection. Corrosion is inevitable for all metals and can lead to the weakening and failure of metal or alloy parts in service. This leads to costs for repairing and replacing parts, additional to the development of new corrosion resistant solutions. A 2016 NACE report estimated the global cost of corrosion at US$2.5 trillion, equivalent to 3.4% of the 2013 global Gross Domestic Product (GDP) [25]. Controlling and minimising corrosion could lead to potential savings of US$375 to $875 billion.

1.3.1 Basics of corrosion

Corrosion affects metals in service as they sit in a higher energy state than their corrosion products. Metals are often found as ores and must be extracted and refined to be useful. This process adds energy, resulting in the metal becoming thermodynamically unstable. Metals in this higher energy state undergo oxidation and corrosion resulting in a negative Gibbs free energy change (ΔG). The Gibbs Free energy diagram in Figure 1.1 illustrates this effect. The activation energy barrier (ΔG*) is the energy required for corrosion to take place. Metals with a larger ΔG* corrode more slowly, as more energy is required for corrosion to initiate, whilst those with a small ΔG* corrode faster, as less energy is needed for this process to start. In aqueous conditions, the ΔG* value reduces, increasing the probability of corrosion.

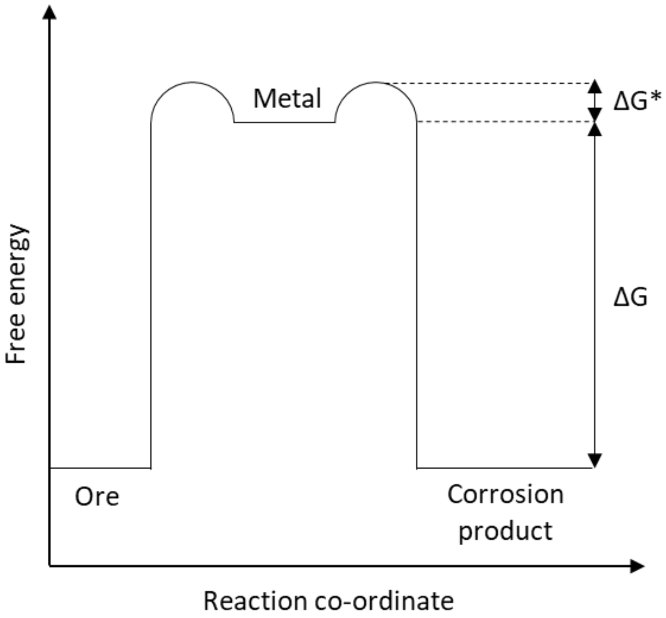

Figure 1.1. Gibbs Free energy diagram for the states of metals [26]

Corrosion can occur in wet and dry environments, although is most common in aqueous conditions. Dry corrosion involves the oxidation of metal in air and is typically very slow. Wet corrosion requires an electrolyte, anodic and cathodic sites and electron flow between them. A corrosion cell is incomplete if these conditions are not met.

Anodic and cathodic activity happens on the same surface, an example is shown in Figure 1.2. Electrons flow through a metal between the sites of activity, whilst ions travel through the electrolyte to balance the charges at each.

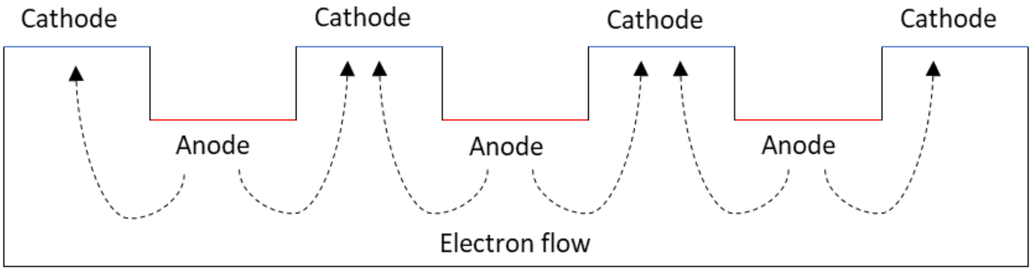

Figure 1.2. Schematic of the basics of corrosion

1.3.2 Generalised corrosion

Under general or uniform corrosion conditions, anodic and cathodic reactions are co-located. Individual cells of activity develop over the entirety of an exposed surface, resulting in uniform metal loss. If there is significant spacing between the sites of anodic and cathodic activity, localised corrosion cells form. At the anode, metal (M) is oxidised leading to the dissolution of ions from the surface and release of a number (n) of electrons (e), as shown in equation 1.1. The metal ions either disperse in the electrolyte or react to form insoluble precipitates. These can act to passivate a metal by reducing electrolyte contact at the surface. Simultaneously, a cathodic reaction occurs with the electrons generated from the anodic process. There are two possible cathodic reactions, depending on electrolyte conditions. At neutral or basic pH values, the oxygen reduction reaction is more common, shown in equation 1.2, whilst at acidic pH values the hydrogen evolution reaction becomes more favourable, shown in equation 1.3.

$$M \leftrightarrow M^{n+} + ne^{-} \tag{1.1}$$

$$2H_2O + O_2 + 4^{e-} \leftrightarrow 4OH^{-} \tag{1.2}$$

$$2H^{+} + 2e^{-} \leftrightarrow H_2 \tag{1.3}$$

1.3.3 Pitting corrosion

Pitting corrosion is initiated by defects on the surface of a metal, caused by mechanical faults or microstructural defects such as dislocations or inconsistences like precipitates. These are locations where the protective oxide film on the surface of a metal has is either weakened or been broken down, leading to the initiation of a pit. Once a suitable defect begins to corrode, oxygen is consumed at the base of the pit and is not replenished due to the greater diffusion distance. The oxygen reduction reaction occurs on the surface of the uncorroded metal adjacent to the pit, where oxygen can easily be replenished. Positive charges build up inside the pit, causing negative ions from the bulk solution flow to the pit to maintain electroneutrality. These are often aggressive chloride ions. As the reactions within the pit progress, metal cations are hydrolysed generating protons (H^+), which leads to the lowering the pH within the pit, further increasing the damage to the metal.

As the reaction progresses, corrosion product deposits at the edges of the pit and can form a protective cover, slowing oxygen diffusion to the area. This creates a differential aeration cell, resulting in stable pitting; this is the most damaging pit type. Metastable pits are those which have been initiated but have not formed a completed oxide cover to enable the damaging environment to thrive. If an oxide film is ruptured, the detrimental pit environment is lost. Examples of pitting behaviour are shown in Figure 1.3. Most initiation points form unstable pits, where corrosion product cover is too slow to develop a differential aeration cell.

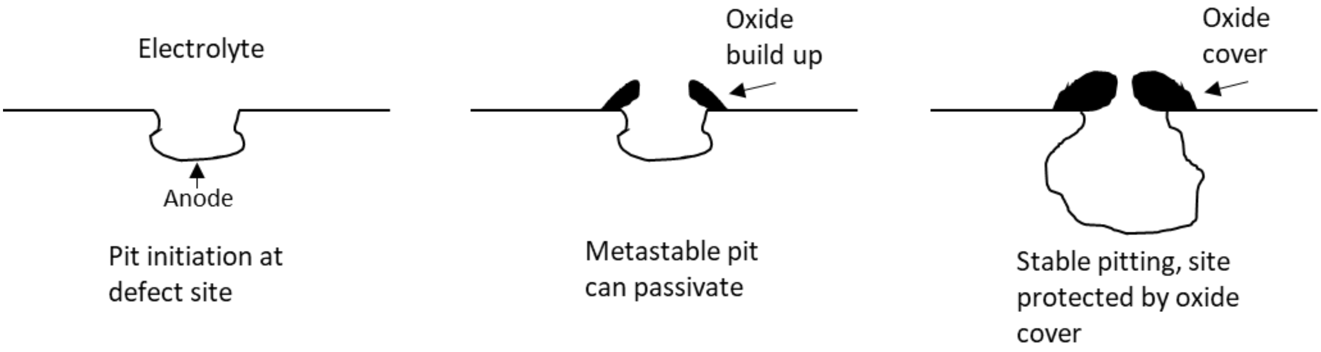

Figure 1.3. Pit initiation, metastable pitting and stable pitting

1.3.4 Galvanic corrosion

Galvanic corrosion, known as bimetallic or dissimilar metal corrosion, happens when different metals or alloys are electrically connected in an electrolyte [27]–[29]. Different metals and alloys have varying electrode potentials resulting in a current being generated between them, leading to the development of a galvanic cell.

Free corrosion potentials are measured under standard conditions when a metallic element is in contact with a 1M concentration of an aqueous solution of its own ions and expressed as reduction potentials. However, these are very unlikely conditions and do not indicate how a metal may behave in other, more realistic environments. This can be predicted using a galvanic series, where the open circuit potential of metals and alloys can be measured in a relevant environment, such as one containing chloride ions at a temperature close to that expected in service. The example shown in Figure 1.4 is a galvanic series with experiments conducted in seawater at ambient temperature. The black boxes represent the rest potentials under passive conditions, whilst the white boxes display the potentials under active conditions. Metals with higher potentials are more noble, and those with lower potentials are more electrochemically active. When two metals are placed in electrical contact in electrolyte, the one with a lower potential forms the anode and undergoes metal dissolution, whilst the more noble metal experiences cathodic reduction [28]. A larger difference in free corrosion potential increases the corrosion current developed between the two metals. When two metals are connected and in electrolyte, both are polarised away from their standard free corrosion potential, resulting in changes in corrosion rate. The free corrosion potential of the couple is where the rate of oxidation equals the rate of reduction [29], [30].

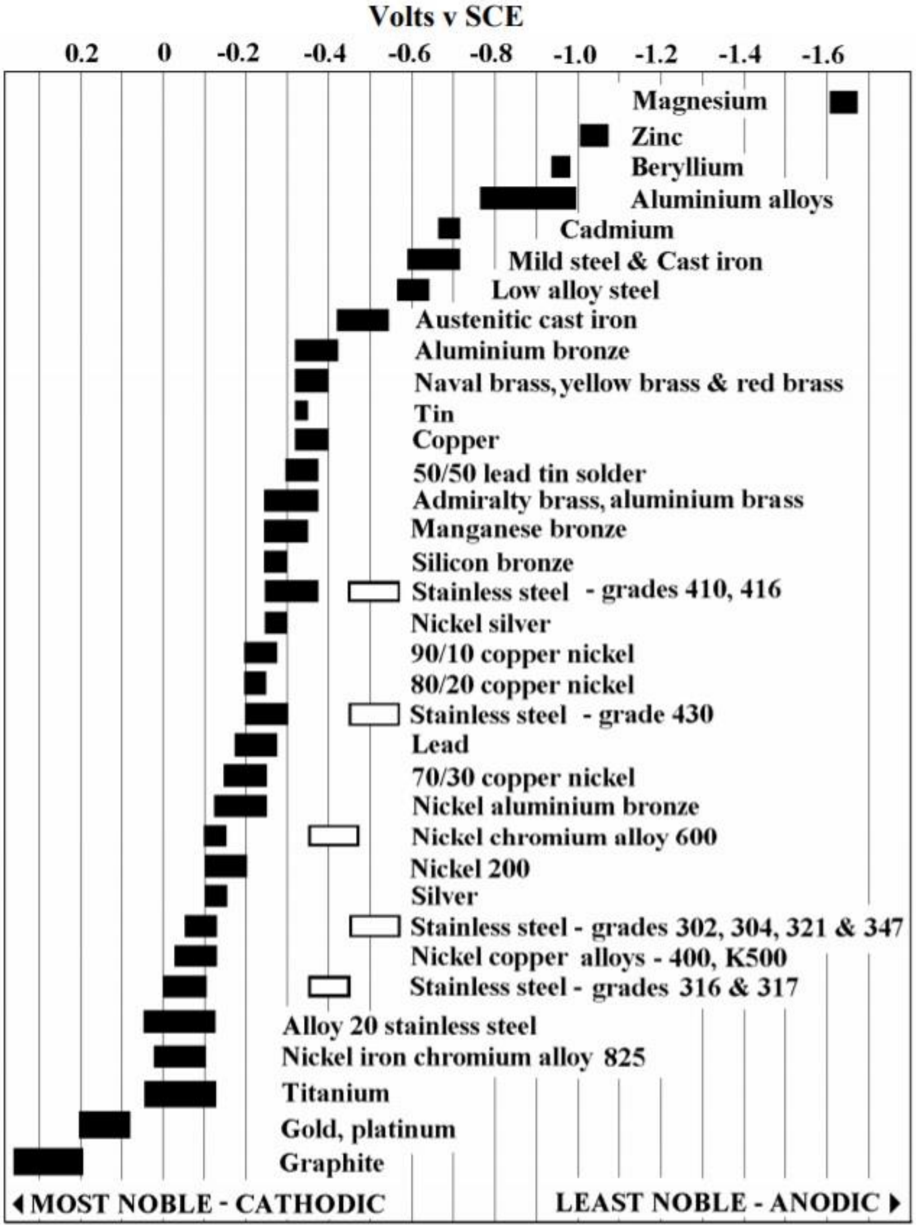

Figure 1.4. Galvanic series in seawater [31]

1.3.4.1 Galvanic corrosion of coins

An example of how galvanic corrosion could affect coinage is in nickel-plated steel coins. Nickel, has a free corrosion potential of around -0.2 V vs. saturated calomel electrode (SCE) whilst steel is measured around -0.6 V vs. SCE. Nickel is a more noble metal, therefore if the steel substrate, with the more active potential, was exposed corrosion and metal dissolution would happen causing discolouration and significant damage to the coin. It is unlikely that the nickel-plated layer would encounter significant damage in circulation, however it is important to consider the implication of this. This thesis will examine how such damage may affect circulation coinage, and if galvanic corrosion cells could initiate on bimetallic coins under immersion and atmospheric conditions.

Differences in free corrosion potential of a few millivolts are unlikely to generate a galvanic cell. When this becomes a few tens to hundreds of millivolts, bimetallic corrosion is more likely; differences over 200 mV are considered a concern [27], [31]. Monitoring potential difference alone cannot predict the intensity of corrosion or kinetics of the reactions. The severity of corrosion is not directly related to potential difference and is affected by exposed surface area, temperature and electrolyte composition [27], [29], as well as reaction kinetics and formation of corrosion products and oxide layers [28]. Uncoupled metals undergo different corrosion processes to those joined together.

The formation of galvanic corrosion cells is highly dependent on the surface areas of the metals involved. If the cathode is large and the anode is small, a large galvanic current can be generated at the anode leading to a fast corrosion rate [30]. This is due to the faster rate of oxygen diffusion at the cathode [27]. However, if the cathode is small compared to the anode, a lower current density develops, spread out over the anode area. This weakens the corrosive effect of the couple, and can cease the corrosion reaction altogether [32]. The galvanic current produced by a bimetallic couple is independent of anode size, but directly proportional to cathode size [28]. The size of anode and cathode are determined by the area in direct contact with the electrolyte, not total surface area of the component. It is important when studying bimetallic coins to consider the whole surface area, as well as likely contact area with skin under normal conditions.

There has been some previous study on the interaction between sections of bimetallic coins. Nestle et al. [5] conducted an initial study in 2002 after the release of the bimetallic one- and two-Euro coins in 1999, on high nickel release from such coins. The team found these coins released more nickel than pure nickel, and there was a significant difference in the nickel release values for ring (outer) and pill (inner) sections of the one-Euro coin. It was also discovered that there was a difference in the electrode potentials of the sections, leading to the conclusion that a galvanic corrosion cell could be initiated in bimetallic coins. Work in this thesis will build on this finding, using the SVET as a spatially resolved technique to show where different parts of the corrosion reaction are happening on the surface of a bimetallic coin, in an attempt to verify where metal is most likely to be released from such coins.

1.3.5 Corrosion of nickel

The corrosion of nickel, as an element and in alloys has been widely studied. Nickel has good corrosion resistance in many environmental conditions, more so in neutral and slightly basic solutions due to its nobility and ability to form passive oxides. In acidic solutions oxide layers dissolve more readily, however their solubility is lower in neutral solutions [33]. Common compositions of nickel oxides include NiO, $Ni(OH)_2$ and NiO(OH) [34], [35].

In this thesis, neutral and slightly acidic electrolytes have been used. The corrosion mechanism in acidic chloride conditions suggest nickel oxidises to form Ni^{2+} and evolves H_2 from the reduction reaction [36]. The performance of nickel in acidic environments is better than expected, as protective oxide films form readily. Increasing the concentration of hydrochloric acid increases anodic dissolution of nickel, as does raising the temperature. Increased oxygen decreased corrosion rates, due to greater surface passivation [36]. The presence of oxygen in solution often reduced corrosion rates, due to its role is the formation of protective oxide films. In aerated environments above pH 4, it is most likely the reduction of oxygen will be the predominant reaction at the cathode.

The potential-pH, or Pourbaix diagram for nickel can predict how it will behave under different potential and pH conditions. Figure 1.5 shows the oxides and hydroxides which may form under such conditions when immersed in water at 25°C. It is important to remember potential-pH diagrams are condition specific. These diagrams provide approximations of behaviour; many factors including impurities can affect corrosion processes [37].

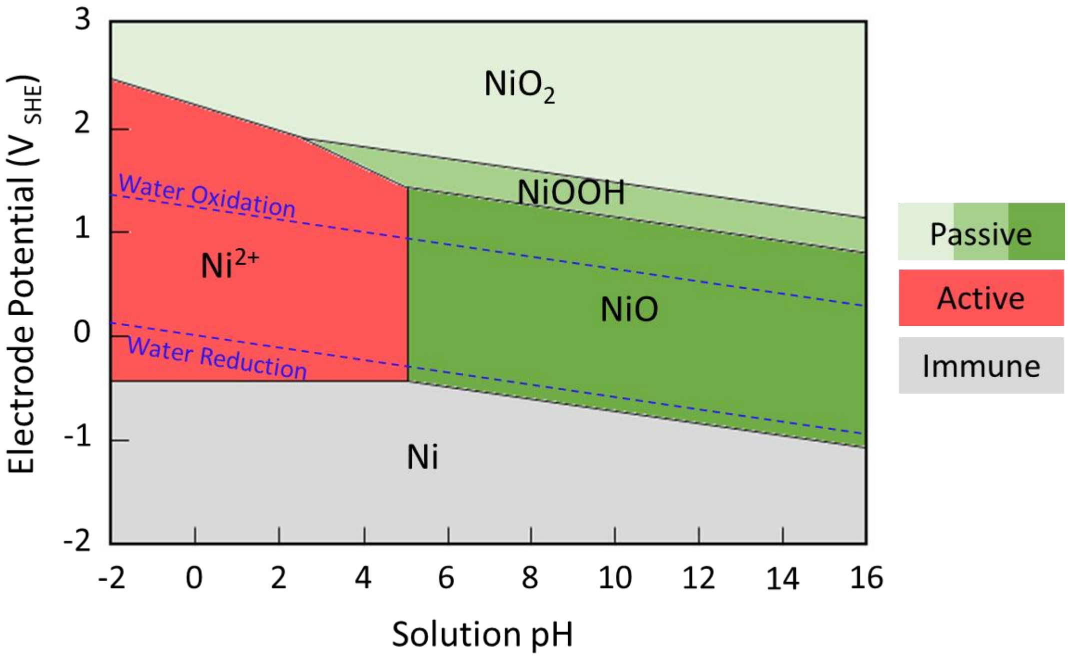

Figure 1.5. Potential-pH diagram for nickel, recreated from [38]

It has previously been found that the process of anodic dissolution of nickel in acidic media is catalysed and rate controlled by OH^- ions, as described by the following sequence of reactions [39], [40]:

$Ni + OH^- = NiOH_{ads} + e^-$

$NiOH_{ads} = NiOH^+ + e^-$

$NiOH^+ = Ni^{2+} + OH^-$

The corrosion of nickel can also depend on how the metal has been produced – processes such as annealing can lead to increased corrosion rates [41].

Pitting corrosion is a common form of localised corrosion, often observed on nickel surfaces. This reaction is initiated when the passive oxide film on the surface is damaged, for nickel this is normally under acidic conditions and in the presence of chloride ions, which act to inhibit passive film formation [42], [43]. Such conditions lead to small breaks in the passive oxide layer, where pitting corrosion and anodic activity commence. On nickel, the most common locations for pits to initiate have been found to be grain boundaries or inclusions [44], [45].

Minimal research has been completed concerning nickel surfaces in atmospheric conditions, due to their good corrosion resistance [35]. Studies on nickel in external humid conditions found the films formed were NiO (bunsenite) and $Ni(OH)_2$ (theophrastite) [34], [35], [46] after a few hours and $NiSO_4 \cdot 6H_2O$ after 1 year [34]. Nickel corrodes more readily in external environments [47] due to changes in humidity and temperature [35].

Most corrosion products formed on nickel in atmospheric conditions are caused by sulphur dioxide. A previous UN/ECE study [35] found sulphur dioxide concentration was directly linked to the corrosion rate of nickel in external environments. These corrosion products form white and insulating layers, consisting of nickel, oxygen and sulphur. Above 70% relative humidity (RH), several monolayers of water adsorb on the surface, acting like a bulk phase for corrosion, leading to nickel ion mobilisation. The oxidation reaction is shown in equation 1.4 and is balanced in acidic solutions by equation 1.5. These are multistep reactions which are not yet fully understood.

$$Ni(s) \rightarrow Ni^{2+} + 2e^- \quad [35] \qquad 1.4$$

$$O_2 + 4H_3O^+ + 4e^- \rightarrow 6H_2O \quad [35] \qquad 1.5$$

Chloride ions are found in small amounts within the atmosphere and can rapidly increase the corrosion rate of nickel [35]. Chloride ions on a nickel surface in acidic conditions will lead to pitting corrosion [43] as these ions damage the passive oxide film. The unprotected metal surface in contact with chloride ions is the site for anodic activity, whilst cathodic activity is sited on the intact surface allowing a corrosion cell to develop. Previous experimentation on nickel has shown defects form at surface features such as grain boundaries or inclusions [44], [45].

High relative humidity and the presence of chloride ions present the ideal corrosion conditions for nickel; circulation coins are likely to experience both through contact with human skin and sweat. Nickel 200, a 99.6% commercially pure wrought product has excellent corrosion resistance, however in artificial sweat (0.5% NaCl, 0.1% urea, 0.1% lactic acid, pH 6.5) it succumbs to pitting corrosion. It was suggested nickel 200 should not be used in products which contact oxygenated sweat, due to high nickel ion release and the potential impact on nickel ACD suffers [48]. It is essential any nickel alloy used in circulation coinage is rigorously investigated in suitable and relevant environments.

1.3.6 Atmospheric corrosion and the differential aeration cell

Atmospheric corrosion affects all metals and alloys exposed to the environment. The formation of oxide layers increases the longevity in some circumstances but can affect the lustre of the metal. Coinage metals and alloys require the original optical properties to be maintained. Coins are subjected to many environments, from acidic and basic household cleaning products to acidic sweat; the materials used must resist a wide range of aggressive environments. As such, it is important to understand how different environments affect coinage materials.

Some early studies on atmospheric corrosion were published by U.R. Evans in 1926 [49], whose model of a water droplet on iron explains differential aeration. Various areas under the droplet have different oxygen diffusion distances, causing separation in anodic and cathodic activity. An example of this droplet has been re-created in Figure 1.6 below.

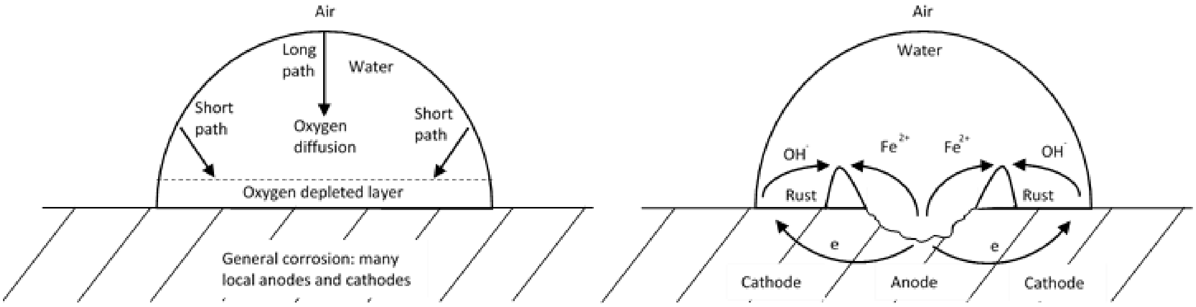

Figure 1.6. Evans water drop experiment explaining the development of a differential aeration cell, recreated from [49]

Initially, the concentration of oxygen is equal throughout the droplet, so anodic and cathodic reactions take place over the entire surface. Equation 1.2 shows the cathodic reaction for this case, resulting in fast oxygen consumption. It is significantly easier for oxygen to diffuse in at the edge of the droplet, where the distance to the metal surface is smallest. As a result, less oxygen is present at the centre of the droplet, so little cathodic activity happens here. As this process progresses, the anodic dissolution reaction shown in equation 1.6 occurs within the centre of the droplet whilst the cathodic reaction continues in the oxygen rich area at the edges. Once this separation of processes is established, metal ions released from the anodic reaction migrate outwards, whilst hydroxide ions from the cathodic reaction diffuse inwards to maintain electroneutrality. Where these ions meet, a ring of corrosion product forms, as shown in equation 1.7.

$$Fe = Fe^{2+} + 2e^{-} \qquad 1.6$$

$$2H_2O + O_2 + 4e^{-} = 4OH^{-} \qquad 1.2$$

$$Fe^{2+} + 2OH^{-} = Fe(OH)_2 \qquad 1.7$$

This work has been significantly expanded over time in order to understand the exact processes happening on this and other metals. Jiang et al. [50] investigated the electrochemical properties of a similar droplet containing 100ppm NaCl. The open circuit potential (OCP) was -300 mV vs. SCE at the outer edge, and -450 mV vs. SCE at the centre, with this difference increasing over time. The potential difference developed very quickly between the centre and outer edge of the droplet, caused by the difference in OH^- concentration. The anodic current density was larger at the centre, whilst the cathodic current density was larger at the outer edge. Due to the metal dissolution reaction at the centre, a concentration of Fe^{2+} ions were created which diffuse outwards. The OH^- and Fe^{2+} ions met and deposited as a corrosion product ring. This is caused by the same mechanism as described for the Evans droplet above.

Due to the differing reactions, pH concentrations can also be setup within a droplet. Evans [49] performed experiments with droplets containing phenolphthalein and ferricyanide indicators, to observe pH changes and the presence of Fe^{2+} ions. The outer edge of the droplet where cathodic activity happened turned red due to the presence of OH^- ions indicating a basic pH, and the anodic area at centre of the droplet turned blue indicating the presence of Fe^{2+} ions. A further paper investigating NaCl droplets on zinc used indicator paper which estimated a pH of 13 at the edge of the droplet [51].

Past experimentation using sodium chloride droplets discovered a spreading effect progressing passed the confines of its original geometry. Tsuru et al. [52] placed 0.5 M NaCl droplets on a carbon steel in 90% relative humidity, and discovered micro-droplets form around the initial droplet, increasing in number and volume over time whilst the original droplet remained the same. Potentials measured for a droplet containing NaCl indicated anodic activity was limited to the original droplet area, whilst the cathode expanded with the formation of micro-droplets over time. When this was repeated using 0.25 M $MgCl_2$ droplets, the cathode did not extend beyond the original droplet, and no spreading was observed [52].

Similar work has also previously carried out on other metals, such as zinc, by Neufeld et al. [51], where the formation and spread of sodium chloride droplets on zinc metal was monitored using a

Scanning Kelvin Probe. This work showed how the potential at the centre of the droplet was at a minimum at -550 mV vs. SHE, which rose to around -350 mV vs. SHE in the area of secondary spreading, and increased to a maximum of -150 mV vs. SHE at the intact zinc metal surface, as shown in Figure 1.7. A similar approach will be investigated here to discover how defects in a nickel-plated layer through to mild steel affect the locations of anodic and cathodic activity under a chloride containing droplet.

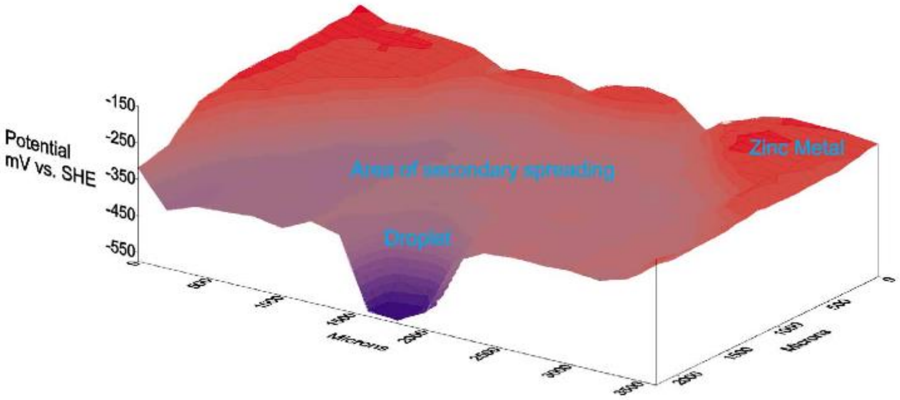

Figure 1.7. Kelvin probe potential map of droplet and secondary spreading area after 7 h in humid air [51]

Micro-droplets were found to contain mainly sodium ions, and very few chloride ions [51], [52]. This suggests sodium cations migrated from the primary droplet to areas of cathodic activity which have high hydroxide concentration, like the micro-droplets, to balance the ionic charges. The increased prevalence of OH^- leads to an increase in the pH of the solution surrounding the original droplet. It is suggested the droplet area expands as water is absorbed from the humid environment to dilute and decrease the alkalinity. Precipitation of hydroxide species has also been found to reduce the pH and not lead to droplet expansion [52].

Work in this thesis aims to observe secondary spreading when NaCl droplets are placed on a defect at the surface of a nickel-plated sample. This work also tries to quantify if secondary spreading increases the size of the cathode and whether this increases the rate of corrosion at the centre of the droplet.

1.3.7 Corrosion of brass

Brass has been used in circulation coinage for many years including in the UK £1 and £2, so it is important to consider this alloy when assessing the corrosion properties of coins. The main mechanism of typical brass corrosion is dezincification, either through the dissolution of both copper and zinc followed by the redeposition of copper, or purely through the release of the more active zinc. In both cases, this results in the removal of zinc leaving copper rich areas on the surface. These methods of dezincification have previously been studied in great detail and are widely accepted

[53]–[56]. It is worth noting these results were obtained for brasses with a range of different copper and zinc contents, but none containing nickel, which is often found in brasses used in coin manufacture. Further research suggests nickel additions to brass do not affect the corrosion mechanism [57].

1.4 Electroless nickel plating

There are many coins in circulation composed of nickel-plated steel, including the UK 5 and 10 pence coins. The use of nickel in circulation coinage has previously formed the basis of an MRes thesis [7], where the possibility for standard electrochemical measurements to be used as a faster and cheaper alternative to standard nickel immersion testing for monitoring nickel ion release was investigated. This work comprised a comprehensive review of the use of nickel for coinage, and to avoid repetition will not be reviewed here. The subject of electroless nickel plating is considered here, as the principle of this work is to evaluate its credibility as an alternative, more economically viable production method when compared to standard nickel electroplating techniques.

1.4.1 History of Ni-P alloys

As with many discoveries, electroless nickel plating was initially discovered by accident. In 1844, Wurtz [58] found nickel cations were reduced by hypophosphite anions but could not create more than a black nickel powder. It was not until 1911 that a bright metallic deposit was obtained from the reduction of nickel using this method by Breteau [59], and in 1916 Roux [60] became the first to patent this technology. There were many issues with these early baths, due to the spontaneous decomposition and deposition of nickel onto any surface the solution touched [61]. Many of these problems were due to inadequate equipment as well as misuse and misunderstanding of the process [62].

The first well documented successful deposition of electroless nickel-phosphorous alloys was Brenner and Riddell’s investigation in the 1940’s into additives for standard nickel electroplating baths. They examined a variety of antioxidants in their regime, including the reducing agent sodium hypophosphite. During one trial, the cathodic efficiency of the electroplating bath was greater than 100%. This phenomenon was investigated, and it was discovered nickel was plating without an applied current. This new process was originally named electrodeless plating, although confusion with electroplating caused a rename to autocatalytic plating. Today this process is most commonly known as electroless plating [63]–[66]. In 1950, Brenner and Riddell patented the process they had accidently discovered [67]. Since then, the technology has developed and is now used in many industries, with different bath compositions tailored to satisfy specific requirements. With the correct surface preparation, this process also allows nickel to be plated on non-conductive surfaces, such as plastics and ceramics [37], [68]. The literature reviewed here will focus solely on the deposition and properties of electroless nickel alloys plated onto metallic substrates.

1.4.2 Surface Preparation

For electroless Ni-P deposition the surface of the substrate must be prepared and activated, which can be completed in a number of different ways. The majority of papers suggest first grinding and polishing the substrate, before cleaning, degreasing and activating the surface [63], [64], [68], [69]. A wide range of cleaning and degreasing solutions have been used, including anodic cleaning in an alkaline solution [63], electro cleaning in 10% NaOH [68] and degreasing in carbon tetrachloride and sodium gluconate [70]. In nearly all papers, the final step before plating was activation and etching in hydrochloric or sulphuric acid solutions [62]–[64], [68], [70], [71]. This preparation is required as surface finish of the substrate strongly impacts the quality of the deposit. Contamination on the surface prior to plating can lead to a reduction in bond strength between deposit and substrate, which could lead to flaking or blistering post heat treatment [72]. Many of the issues with this process can be linked to insufficient cleaning or lack of pre-treatments.

1.4.3 Bath composition and set-up

There are many different bath compositions depending on the required deposit composition, desired plating thickness, deposition rate and final properties. An electroless nickel (EN) plating bath requires a source of nickel ions (sulphate or chloride), a reducing agent (sodium hypophosphate for phosphorous alloy or sodium borohydride for boron alloy) and a complexing agent (citric, acetic succinic, propionic or glycolic acid) and if required, a stabilising compound (heavy metal salts, thiourea, fluoride compounds) [61], [70]. Aside from the bath components, temperature and pH can affect the deposit properties, and bath lifetime.

Whilst stabilisers in an EN plating bath can help control the deposition process and increase the bath lifetime, it is not an essential component. Two current theories exist describing how an EN plating bath can be stabilised. The first is a substitution mechanism, where heavy metal ions are added in small quantities to reduce activity at the substrate, and the second is via adsorption using anion stabilisers to reduce the auto-catalytic behaviour of EN plating by adsorbing to active sites on the substrate [61], [73], [74]. Many of the stabilisers used are not environmentally friendly, so finding ones with less damaging properties is necessary.

Some organic chemicals such as thiourea and isothiuronium propyl sulfonate (UPS) have previously been successfully trialled as stabilisers [75], [76], but are both potentially harmful to humans and the environment. A promising group of chemicals is amino acids, and compounds derived from these.

Previously sulphur containing amino acids cysteine and methionine were added to EN plating baths. In one case cysteine accelerated the deposition rate and evolution of hydrogen gas by increasing the anodic oxidation of hypophosphite [77], whilst another found both cysteine and methionine inhibited the anodic hypophosphite reaction by adsorption onto active substrate sites [78]. The properties of the deposits are reliant on other bath constituents and the operating parameters.

There are two main different types of bath, acid and alkaline. These baths create deposits with different properties and are used for specific applications. Acid baths are generally run between pH 4-6 and operated at temperatures between 70-90°C [79]. This type of bath is used for plating metallic substrates. Alkaline baths are normally run between pH 8-11 and operated over a much wider range of temperatures between 40-80°C depending on bath composition [79]. This type of bath plates low phosphorous deposits containing 3-4 wt.% P. Deposits from this bath can also plate polymeric substrates due to the lower operating temperature, and can also be used where good solderability is required [62]. Alkaline baths can produce toxic fumes, whilst acid baths are less volatile, even at higher operating temperatures. Acid baths are easier to control than alkaline baths, and are able to plate a larger range of phosphorous contents at a much faster rate than alkaline baths [74]. This work will focus on plating from acid baths, as their properties are more promising for coinage applications.

From examining the literature, unique values for the temperature and pH must be selected depending on the concentration of bath ingredients, required deposition rate and phosphorous content, as well as desired mechanical properties. These parameters will be investigated in this work.

1.4.4 Chemical processes

Electroless plating is an auto-catalytic process and can be characterised by a series of chemical processes, resulting in the deposition of nickel and phosphorous onto a substrate. Several different mechanisms for the deposition of nickel-phosphorous from hypophosphite-based solutions have been suggested. Due to the potentials developed during the chemical reactions, positive and negative ions are attracted to the substrate, where the following overall charge transfer process happens:

$$R^{n+} \rightarrow R^{(n+z)+} + ze^- \tag{1.8}$$

$$M^{z+} + ze^- \rightarrow M \tag{1.9}$$

Where R is the reducing agent and M is the metal ion deposited [71]. The most widely accepted mechanisms are shown equations 1.10 to 1.17, originally published by Gutzeit in 1959 and 1960 [80] and republished by Agarwala and Agarwala in 2003 [81]. These mechanisms are supported in work by Molla et al. [71] and Cheong et al. [76].

The first suggested mechanism is electrochemical, where the catalytic oxidation of hypophosphite yields electrons at the surface, leading to the reduction of nickel and hydrogen ions. This is shown by the series of reactions below:

$$H_2PO_2^- + H_2O \rightarrow H_2PO_3^- + 2H^+ + 2e^- \tag{1.10}$$

$$Ni^{++} + 2e^- \rightarrow Ni \tag{1.11}$$

$$2H^+ + 2e^- \rightarrow H_2 \tag{1.12}$$

$$H_2PO_2^- + 2H^+ + e^- \rightarrow P + 2H_2O \tag{1.13}$$

The second mechanism is based on the release of atomic hydrogen due to catalytic dehydrogenation of the hypophosphite molecules adsorbed at the surface. This is shown by the following series of reactions:

$$H_2PO_2^- + H_2O \rightarrow HPO_3^{--} + H^+2H_{ads} \tag{1.14}$$

$$2H_{ads} + Ni^{++} \rightarrow Ni + 2H^+ \tag{1.15}$$

$$H_2PO_2 + H_{ads} \rightarrow H_2O + OH^- + P \tag{1.16}$$

The adsorbed active hydrogen then reduces nickel at the surface of the catalyst.

$$(H_2PO_2)^{2-} + H_2O \rightarrow (HPO_3)^{2-} + H_2 \tag{1.17}$$

Simultaneously, a small quantity of absorbed hydrogen reduces a fraction of the hypophosphite at the catalytic surface to form water, hydroxyl ions and phosphorous (equation 1.16). During the deposition of nickel-phosphorous the majority of the hypophosphite behaves in a catalytic way and oxidises to form orthophosphite and hydrogen gas (equation 1.17) making the process inefficient [81].

The overall reaction for the reduction of nickel by hypophosphite is widely accepted as follows:

$$2H_2PO_2^- + 2H_2O + Ni^{2+} \rightarrow 2H_2PO_3^- + H_2 + 2H^+ + Ni \quad \text{[71], [76], [81]} \tag{1.18}$$

Hydrogen is released as a by-product of nickel reduction. Some of this is released as hydrogen gas, whilst the rest is absorbed into the solution, increasing the concentration of hydrogen ions leading to a decrease in bath pH, as pH = $-\log_{10}[H^+]$. Further hydrogen can be released through the volatilization of ammonia where present [61], [64], [67], [81]. Variations in pH during plating cause inconsistencies in the composition and structure of the deposit, altering the physical properties including corrosion resistance. A decrease in bath pH leads to a coating with an increased phosphorous content [64]. Additives are often included in the bath to negate the effects of hydrogen ion production and maintain a stable plating pH. Any buffers used are generally salts of organic acids [74]. Additives have also been used to prevent the precipitation of nickel salts and reduce the free nickel ion concentration [66].

Due to consumption of bath constituents during the chemical processes described above, the bath will deplete some components over time. Most notable is the decrease in the sodium hypophosphite reducing agent, resulting in less nickel deposition as plating time increases. Sodium hypophosphite additions can be made, although eventually the bath will reach saturation of reduced phosphite species. It is possible to remove excess phosphite, although it is more economical to discard the solution and create a brand-new bath. If sodium hypophosphite additions are made at suitable intervals, bath lifetime can be increased. Over time the bath will consume the nickel salt, but this is much easier to replenish with any suitably soluble nickel salt [67], [74].

Investigations into treatment of bath waste to reduce disposal costs and extend bath life have been carried out. Problems occur when high levels of impurities, mainly phosphite species collect in the bath. Normally, waste solution from EN plating baths is treated by precipitation and sent to landfill. As the prevalence of electroless plating increases, this will become unsustainable. It was estimated in Japan in 2004, nickel waste solutions totalled over 100 tonnes. Ookubo et al. [82] investigated synergistic extraction of nickel from waste, the most promising experiments used D2EHPA and nicotinic acid ester. If the system was optimised, extraction of over 95% yield could be achieved [82]. However, further work is required in this area, especially as concerns regarding negative environmental effects increases.

1.4.5 Nickel-Phosphorous alloys – microstructure and properties

The microstructure of Ni-P alloys is very unusual for a metal, as it can contain both crystalline and amorphous phases. The proportion of each in an as-plated sample is dictated by the phosphorous content, which significantly effects the properties of the coating [83]. An example micrograph showing the difference between the typical surface of an electroplated nickel surface compared to an electroless plated surface is shown in Figure 1.8. There is a very clear difference in the appearance of surface features; where electroplated nickel forms a fine grain structure, the surface of electroless nickel samples formed in nodes across the surface as plating progresses.

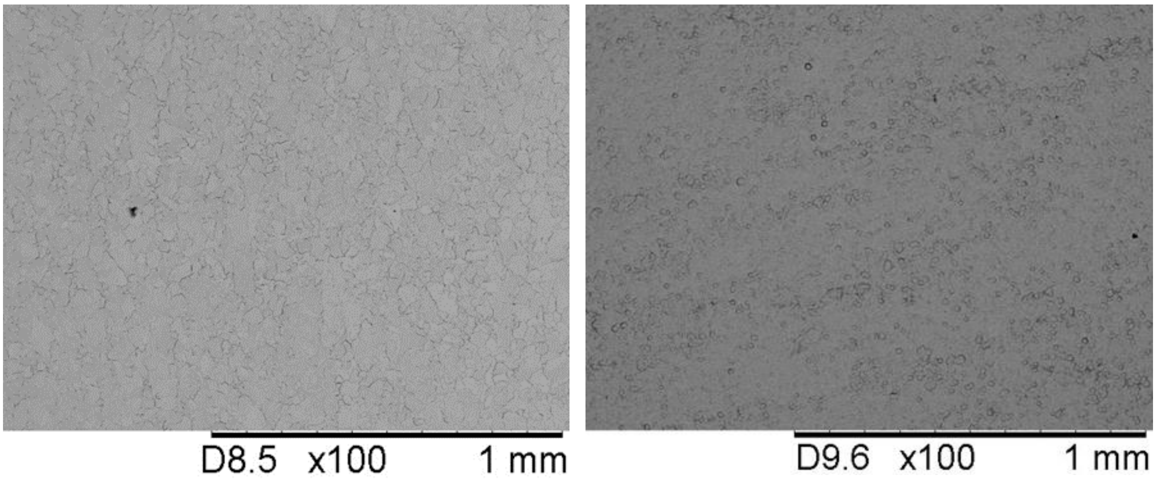

a) Etched electroplated nickel surface (100x) *c) Electroless nickel surface, 10 wt.% P (100 x)*

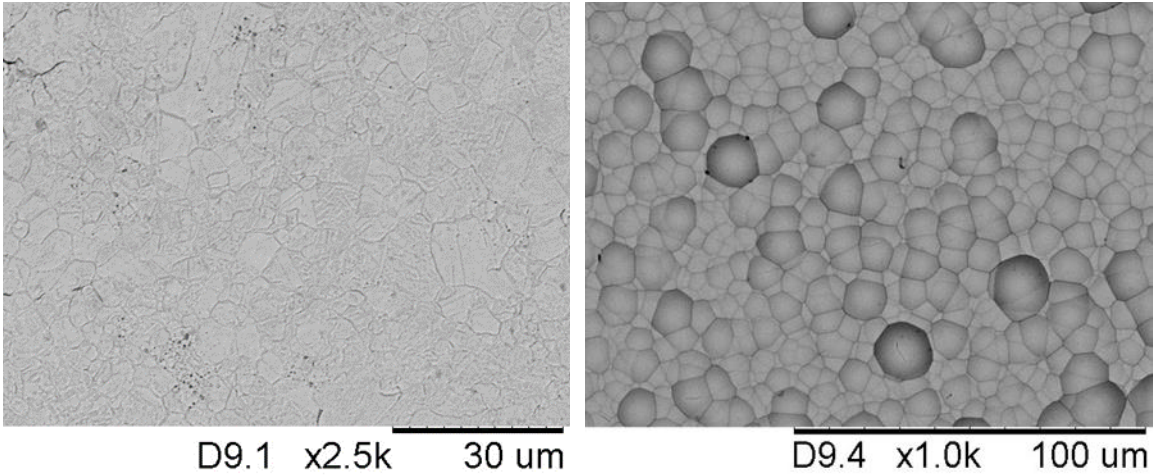

b) Etched electroplated nickel surface (2500x) *d) Electroless nickel surface, 10 wt.% P (1000x)*

Figure 1.8. Comparison between the surfaces of electroplated and electroless nickel

The amount of phosphorous in the coating has great effect on the final microstructure. This structure varies significantly from the entirely crystalline phases deposited by standard nickel electroplating baths. Electroless nickel-plated deposits generally display an amorphous matrix with a dispersion of fine crystallites. Electroless nickel-phosphorous alloys become increasingly amorphous with increasing phosphorous content [84], and are considered as completely amorphous above 10.5 wt.% P. These alloys have excellent corrosion resistance as the possibility of inter-granular corrosion is minimised [85]. It has been reported alloys with 1.9 to 3.7 at. % P (1-2 wt. % P) are completely crystalline, whilst above 17.4 at. % P (10.6 wt. % P) a purely amorphous phase is formed. Between these compositions, an amorphous matrix containing micro crystallites is prevalent [69]. Previous investigations into coatings containing over 8.5 wt. % P were analysed using electron diffraction, and no crystalline structure was seen at magnifications up to x 150,000 [86]. High phosphorous alloys are amorphous as the larger phosphorous atoms distort the nickel lattice, changing the microstructure. At lower phosphorous contents there are not enough phosphorous atoms to create this distortion so the structure remains crystalline [81], [84].

EN baths are strongly affected by the plating pH and temperature. Previous studies showed that at a constant pH, when bath temperature is increased from 40°C to 100°C, the deposition rate and phosphorous content increased. When temperature was constant and pH was increased from 4 to 10, the deposition rate increased and the phosphorous content decreased [64]. A further paper showed increasing bath pH from 4.8 to 5.5 resulted in faster deposition and a decrease in phosphorous content. At constant temperature, decreasing the concentration of sodium hypophosphite led to a slower plating rate and lower phosphorous content [69]. An additional paper stressed the importance of bath temperature, suggesting below 90°C deposition will be slow and more likely to contain impurities, which may adversely affect the corrosion properties [67].

Both plating temperature and pH affect the final microstructure of the deposit. Figure 1.9 and Figure 1.10 below present the results from work previously completed in this area, where deposits were made onto a mild steel substrate.

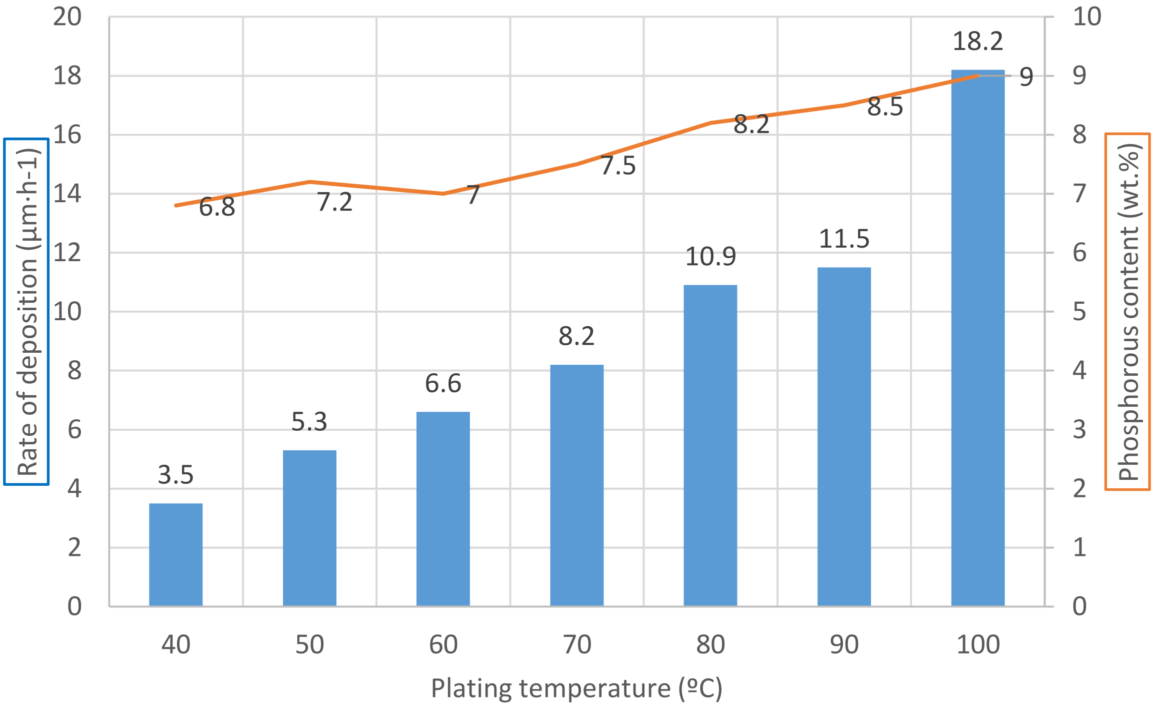

Figure 1.9. Effect of bath temperature on the rate of deposition and phosphorous content at pH 5 [64]

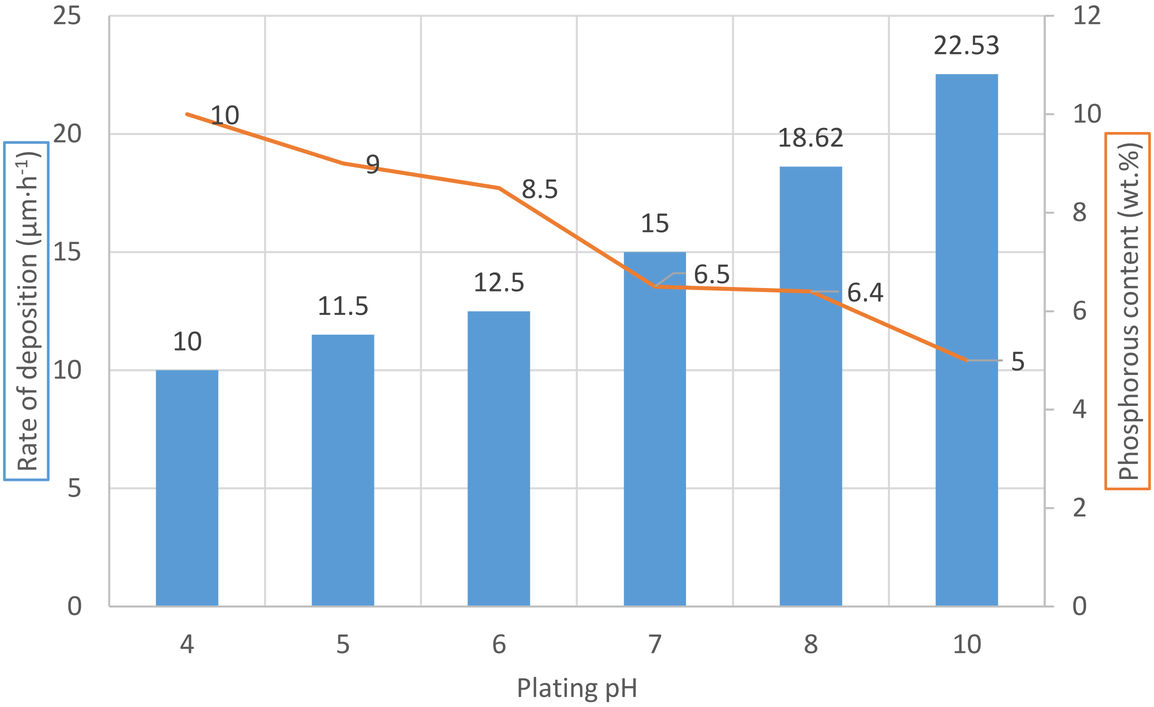

Figure 1.10. Effect of pH on rate of deposition and phosphorous content at a bath temperature of 90°C [64]

These results show that increasing plating temperature increases the rate of deposition and phosphorous content. The tables above also show as bath pH increases, deposition rate increases but is accompanied by a drop in phosphorous content. It is well established that as plating proceeds, the pH will drop due to the production of hydrogen, so maintaining a constant pH is essential for a consistent deposit [64].

Heat treatment can be used to alter the properties of nickel-phosphorous alloys post plating by allowing the atomic structure to order resulting in increased crystallinity. The Ni-P phase diagram suggests if more than 11% phosphorous is present, heat treatment will lead to nickel phosphide formation before the pure nickel phase. The nickel phosphide phase grows within the amorphous matrix until the phosphorous content falls below 11%. At this point, nickel crystallises, whilst phosphorous is incorporated into the amorphous matrix due to its low solubility in the crystalline phase [68]. When heat treatment is carried out on medium and high phosphorous alloys, shrinking on re-crystallisation can cause cracking in the coating, leading to very poor corrosion resistance [85].

Previous experimentation showed the first structural changes happen on heating to between 220-260°C, forming nickel phosphite (Ni_3P) particles in the matrix. As the temperature increases, these particles agglomerate and form a secondary phase. Alloys containing more than 8% phosphorous will form an Ni-P matrix; below this the matrix is pure nickel. At this stage, the hardness and wear resistance have been shown to increase substantially, but the corrosion resistance and ductility will have decreased. If long term heat treatments at high temperatures are performed on nickel-phosphorous deposits which have been plated onto mild steel (4 hours at temperatures over 650°C), a nickel-iron intermetallic forms. This has been found to increase the corrosion resistance in some environments [86].

The physical and mechanical properties of this alloy are difficult to specify, due to varying phosphorous contents, heat treatments, etc; however, some general properties are described below.

The effect of phosphorous content on physical and mechanical properties has previously been studied. Phosphorous significantly effects the melting point compared to pure nickel. Pure nickel melts at around 1455°C, whereas a Ni-P coating with 8 wt. % phosphorous has a melting point of just 880°C [62], [85], [86]. In terms of electrical properties electroless nickel coatings can have a resistivity ten times greater than pure nickel (7.8 x 10^{-6} ohm·cm^{-1}) due to lattice distortions caused by phosphorous atoms. The ferromagnetic properties of pure nickel decrease with increasing phosphorous content, and alloys over 11 wt.% phosphorous are non-magnetic. For thermal properties, the coefficient of thermal expansion of high purity nickel is 14-17 µm·m^{-1}·°C, whilst electroless plate varies from 11.1 µm·m^{-1}·°C with 11 wt.% phosphorous to 22.3 µm·m^{-1}·°C with 3 wt.% phosphorous [85]. Average density values are listed in Table 1.1 below:

Table 1.1. Density of nickel and nickel phosphorous deposits [62], [85]

Material	**Density (g·cm^{-3})**
Pure nickel	8.9
Ni-3 wt. % P	8.52
Ni-7.5 wt. % P	7.92
Ni-11 wt. % P	7.75

With respect to mechanical properties no values have been quoted, but comparisons between materials have been made. The hardness of electroless Ni-P deposits is greater than electroplated nickel and can be increased further by heat treating. Wear resistance of Ni-P coatings has been described as good and can be increased using heat treatment. The ductility is described as low, making deposits brittle due to the amorphous microstructure [72], [85].

Previous research found the mechanical properties of nickel-phosphorous deposits are similar to those of glass, due to the amorphous microstructure. Ni-P alloys have high strength, limited ductility and a high modulus of elasticity. The ultimate tensile strength exceeds 700 MPa, equal to many grades of hardened steel. It was suggested electroless Ni-P coatings should not be used where the material undergoes further mechanical deformation, as the deposit is brittle and may crack, reducing the corrosion and abrasion resistance [86].

1.4.6 Nickel-phosphorous alloys – corrosion

Nickel-phosphorous is generally selected due to its excellent corrosion resistance. It provides a barrier coating, which surrounds the substrate and prevents corrosive electrolyte contact, unlike sacrificial coatings which corrode in preference to the substrate [62], [85].

The corrosion properties of Ni-P alloys have been thoroughly examined in a range of electrolytes, although there is little information regarding their performance in artificial sweat solutions. One paper investigated EN plated on magnesium in artificial sweat solution and found that urea acts as a corrosion inhibitor, but the presence of NaCl and lactic acid reduced its effectiveness. The material was found to be active in these conditions and dissolved readily [87]. Much experimentation has been completed in chloride conditions, the main constituent of sweat, and when combined with behavioural data of performance in acidic media will act as a good guide about how a deposit may perform in artificial sweat.

Nickel-phosphorous coatings have good corrosion resistance in a wide range of environments. Several papers found that by varying the phosphorous content, the corrosion resistance can be optimised for the environment the coating may encounter. If the environment is neutral, acidic or low temperature, Ni-P coatings containing more phosphorous perform better, whereas in alkaline media and at high temperatures, a lower phosphorous content is more resistant to corrosion [62], [85], [88].

Other research showed electroless Ni-P coatings are almost completely resistant to alkalis, salt solutions, chemical and petroleum environments, as well as hydrocarbons and solvents, and have good resistance in solutions containing ammonia, organic and reducing acids. The corrosion resistance was poor in strongly oxidising solutions, such as concentrated nitric acid [62]. Laboratory trials on deposits in seawater heated up to 95°C showed a maximum mass loss of $1\mu m \cdot yr^{-1}$. Investigations in fresh water predicted a mass loss of 0.3-0.8 $\mu m \cdot yr^{-1}$ at ambient temperatures. This paper [82] also covered the effects of pH on corrosion rate, using 0.1% hydrochloric acid neutralised with sodium hydroxide to obtain pH values from 1.4 to 12. Above pH 3, the corrosion rate was uniformly less than $2\mu m \cdot yr^{-1}$. Below pH 3, the rate increased to a maximum of $20\mu m \cdot yr^{-1}$.

Additionally, electroless plating gives better corrosion resistance due to low porosity and a more uniform coating thickness, resulting in fewer sites for pitting and crevice corrosion to occur [66], [85]. At higher phosphorous contents, the microstructure is amorphous, increasing the corrosion resistance as there are fewer grain boundaries and less corrosion initiation sites, and a glassy passive film develops to protect the surface [62].

Heat treatments impact the corrosion resistance of Ni-P alloys. Some research suggests annealing improves the corrosion resistance [89], however other papers claim the opposite is true. How the microstructure alters depends on time and temperature. Research was conducted on microstructural changes during the annealing process. When the temperature reaches 260°C, nickel phosphide (Ni_3P) particles form, and as the temperature approaches 340°C the coating loses its amorphous structure and becomes crystalline. At higher temperatures nickel phosphide particles conglomerate, forming a matrix. Simultaneously, the phosphorous content elsewhere decreases, reducing the passivity and corrosion resistance of the coating. The phosphite particles act as initiation sites for localised corrosion. Heat treatments also cause cracking, as the matrix and particles cool at different rates resulting in stresses within the coating [62], [66]. Further experimentation suggests the as-plated corrosion resistance is excellent, and parts should not be heat treated if corrosion resistance is a key property [72].

Overall the research agrees electroless plated coatings are more corrosion resistant than their conventionally electroplated counterparts. This has been confirmed by salt spray analysis, seaside exposure and through contact with nitric acid [62], [90]. It was noted that electroplated coatings performed better in aerated lactic acid [65], an active ingredient in sweat, so this must be considered.

1.4.7 Advantages and disadvantages of EN plating

As with all developing technologies, there are advantages and disadvantages, both in terms of the process and the deposits produced.

In terms of advantages, the process of electroless plating is simpler than standard electroplating, and requires no specialist equipment [69], [91]. As was discovered in the literature, Ni-P alloys offer better mechanical properties than conventional nickel plating, as well as increased corrosion and chemical resistance due to lower porosity, lower internal stress values and an amorphous microstructure with better wear resistance and hardness. The wear resistance of the plated layer can be increased by post plating heat treatments [63], [65], [66], [68], [69], [72], [81], [84], [89], [92]–[95]. Electroless Ni-P plated layers have a bright, shiny appearance with a high reflectivity value, ideal for the production of coinage [81], [92], [96].

A further advantage of electroless plating is excellent throwing power. This results in a highly uniform plating thickness with no height variations, unlike electroplating variations in potential can cause uneven deposition. The throwing power of standard nickel electroplating is significantly lower, as it is difficult to maintain a constant current throughout deposition. As no current is required for electroless plating, deposit thickness is constant even with a complex geometry. Sharp edges and pipe internals can also be plated providing the surface has been activated. It is possible to coat non-metallic surfaces including plastics, glass and ceramics using electroless technology [65], [66], [68], [69], [72], [81], [88], [92], [96], [97].

There is less documentation regarding the disadvantages of this process. Longevity of the solution has been brought into question as the bath becomes saturated in waste product over time, resulting in costly solution disposal and replacement of the ingredients [68], [88], [91], [97]. A higher operating temperature is required for electroless plating, so energy costs may increase. The deposition rate of EN is generally slower than electroplating, but can depend on bath composition and desired deposit properties [96], [97]. Mechanical investigations of deposits found Ni-P coatings have a higher tendency to crack under cyclic loading conditions, and are less ductile than electroplated nickel samples [93], [98].

1.5 Project aims

- To evaluate the potential for galvanic corrosion to occur between the sections of bimetallic coins

This work will use a variety of techniques, including in-situ SVET and SKP combined with potentiostat techniques to determine if some combinations of metals used for coinage are more susceptible to galvanic corrosion than others. Experimentation will be carried out in both artificial sweat and saline solutions, as well as under immersion and atmospheric conditions.

- To assess the atmospheric corrosion on nickel plated layers with induced defects, mimicking porosity

Droplets of different chloride compositions and concentrations will be used to assess how nickel-plated steel corrodes when a defect is present. This will be measured be observing the spreading distance of the droplets, and SEM/EDS evaluation of the area surrounding the defect post-experiment.

- To deposit electroless nickel-phosphorous alloys with a range of phosphorous contents and assess their properties

Electroless nickel deposits will be made from commercially available proprietary solutions and a bath designed in the laboratory. Samples from each will be evaluated for their surface, corrosion and mechanical properties.

- To evaluate the potential for electroless nickel plating to be used for coinage applications.

The properties of the samples obtained will be compared to both each other and the properties displayed by the current electroplated layers used for nickel coinage. The advantages and disadvantages of these will be discussed and a conclusion as to which is most suitable will be ventured.

- To investigate novel additions to electroless plating baths and assess the properties obtained.

Novel additions will be made to the electroless nickel plating bath mixed in the laboratory, to try and improve the properties of the deposits. Two organic compounds, taurine and thiamine hydrochloride will be added to the plating bath to observe if these affect plating rate, phosphorous content or mechanical properties of the deposits.

Chapter 2. Experimental Methods

2.1 Chemicals and proprietary solutions

Table 2.1 lists the chemicals, their supplier and purity used throughout this thesis.

Table 2.1. Chemicals and proprietary solution

Chemical	Supplier	Grade
De-ionised water	De-ionised in-house	Up to 18 MΩ·cm^{-1}
Sodium chloride	Sigma-Aldrich	≥ 99%
Urea	Sigma-Aldrich	99 – 100.5%
Lactic acid	Sigma-Aldrich	37% (ACS reagent)
Hydrochloric acid	Sigma-Aldrich	37% (ACS reagent)
Sodium hydroxide	Sigma-Aldrich	98 – 100.5%
Lacomit Varnish	Agar Scientific	-
Magnesium chloride hexahydrate	Sigma-Aldrich	99%
Acetone	Fisher Scientific	99.5% +
Niklad ELV 835	MacDermid Enthone	-
Niklad ELV 849	MacDermid Enthone	-
VandAloy 4100N	MacDermid Enthone	-
Sodium hypophosphite monohydrate	Sigma-Aldrich	≥ 99%
Sodium acetate	Sigma-Aldrich	USP test specification
Nickel (II) sulfate hexahydrate	Fisher Scientific	> 95% (Laboratory reagent grade)
Sulphuric acid	Sigma-Aldrich	95 – 98%
Ammonium hydroxide	Sigma-Aldrich	1 M in H_2O
Taurine	Sigma-Aldrich	≥ 99%
Thiamine hydrochloride	Sigma-Aldrich	≥ 99%
L-Cysteine	Sigma-Aldrich	97%

2.2 Bimetallic sample manufacture

A range of bimetallic coins were supplied by the Royal Mint for this work. These coins are designed to be harder to counterfeit and are more complicated to produce than single metal coins.

The Royal Mint make most of their metals and alloys in-house, with the exception of the steel, which is supplied by Tata Steel. These metals and alloys are cast into slabs, which are hot rolled to reduce the thickness, then coiled until needed. The coils are unwound, cleaned and processed to reach the desired coin thickness. These strips are then fed into a blanking machine, where the ring and pill sections are pressed out. The pill sections undergo an additional manufacturing step, where a groove is milled around the outer edge, shown in Figure 2.1c. If required, steel blanks are plated at this stage.

a. UK £2 ring *b. UK £2 pill* *c. UK £2 pill groove*

d. UK £2 ring and pill pre-minting *e. UK £2 minted coin*

Figure 2.1.a-e. Components of a bi-metallic coin, UK £2

The ring and pill sections are fed into the minting press at the same time, and a force of 60 tonnes is used to mint and join the parts together. Under this pressure, the inside edge of the ring is pushed into the groove of the pill, effectively locking them in place. These sections are impossible to separate by hand.

2.3 Electrolyte preparation – artificial sweat solution

Artificial sweat was prepared in accordance with the BSI Standards Publication EN 1811:2001, entitled “Reference test method for release of nickel from all post assemblies which are inserted into pierced parts of the human body and articles intended to come into direct and prolonged contact with the skin” [24].

To make 1 litre of the artificial sweat solution, 1 g (±0.01) of urea, 5 g (±0.05) of sodium chloride and 1 g (±0.01) of lactic acid were added to 900 ml (±10) of deionised water in a conical flask. This was stirred for 10 minutes or until all the constituents had dissolved. A pH meter was calibrated, and 1 M and 0.1 M solutions of sodium hydroxide were prepared. After stirring, 1 M sodium hydroxide was added dropwise until a pH of 5.5 (±0.01) was reached. A 0.1 M solution of sodium hydroxide was then added dropwise until a pH of 6.5 (±0.01) was reached. The volume of solution increased to 1000 ml (±10) and left for 10 minutes to stabilise. The pH was then re-checked. If the pH needed increasing, drops of 0.1 M sodium hydroxide were added. If the pH was too high, a 0.1 M hydrochloric acid solution was prepared and added dropwise until a pH of 6.5 (±0.01) was reached. The solution was prepared daily and refrigerated to prevent decomposition if not in use for extended periods.

2.4 Electroless nickel plating

2.4.1 Electroless nickel plating from commercially available solutions

The first set of electroless nickel-plated samples were produced from three proprietary solutions. These were supplied by MacDermid Enthone and named Niklad ELV 835, Niklad ELV 849 and Vand-Aloy 4100N. The predicted deposit properties from each is shown in Table 2.2, below. To change the thickness of the deposits, substrates were plated for 30, 60 and 120 minutes.

Table 2.2. Predicted properties of the proprietary electroless plating solutions [99]–[101]

Property/Plating solution	Niklad ELV 835	Niklad ELV 849	Vand-Aloy 4100N
Wt.% P	4-7	7-9	10-12
Deposition rate ($\mu m \cdot hr^{-1}$) {optimum}	20-25	15-22 {18}	8-15 {10-13}
Temperature (°C) {optimum}	82-93 {88}	85-91 {88}	85-91 {88}
pH {optimum}	5-5.7 {5.2}	4.8-5.2 {5}	4.8-5.2 {5}
Density ($g \cdot cm^{-3}$)	8.4	8.0-8.3	7.8
Hardness (as plated, HK_{100})	650-750	500-550	475-550
Wear resistance (as plated, TWI*)	12-18	22-26	18-24
Corrosion resistance	Good	Not stated	Excellent

*TWI – Taber Wear Index, weight loss in mg per 1000 cycles

The substrates for these trials were steel blanks normally used for UK five pence coins. Prior to plating, substrates were cleaned with acetone to remove manufacturing debris and machine lubricants, then etched. Plating was undertaken in a borosilicate beaker on a hot plate, filled with 300 ml of plating solution. The temperature was constantly monitored using a mercury-in-glass thermometer and the hot plate adjusted to maintain a solution temperature of 88°C, as specified in the guidance notes [99]–[101] for all the solutions. Substrates were suspended in the bath using a crocodile clip and wire, hung in the centre of the beaker to plate both sides evenly. Two samples were plated in each solution for each plating time, a photograph and a schematic diagram of the setup are shown below in Figure 2.2.

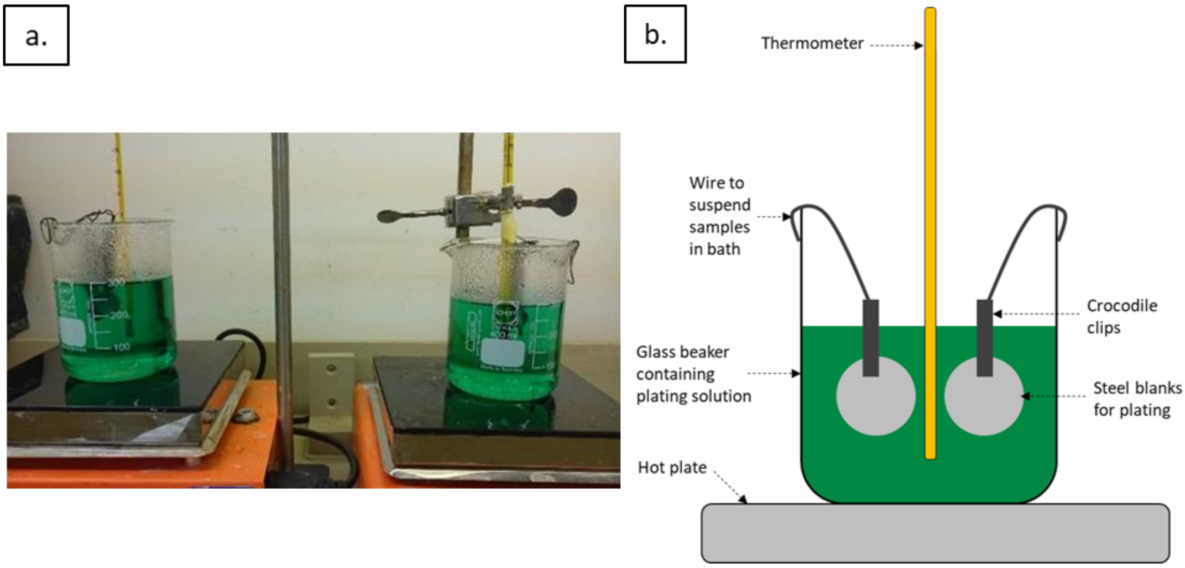

Figure 2.2a. Photograph of equipment for electroless plating from commercial solutions and b. a schematic of this set up

Once the desired plating time had elapsed, samples were removed from solution, rinsed with DI water and dried with a hot air blower. Each sample was individually bagged and labelled for future analysis.

2.4.2 Electroless nickel plating from an in-house bath

The second set of electroless nickel-plated samples were deposited from a bath made in-house. The plating solution was made in 1 L batches. To produce 1 L, 750 mL of high purity 18.2 MΩ de-ionised water was used with ingredients added separately, allowing time for the previous chemical to dissolve before adding the next. The pH buffer was added first, followed by the reducing agent and finally, the source of nickel ions. The solution was then adjusted to the required pH using sulfuric acid. Deionised water was added until a volume of 1 L was reached, then stirred for 10 minutes before re-checking the pH. The chemicals used are listed in Table 2.3, along with the relevant quantities.

Table 2.3. In-house plating bath composition

	Chemical	**Quantity ($g \cdot L^{-1}$)**
pH buffer	Sodium acetate	10
Reducing agent	Sodium hypophosphite	20
Source of nickel	Nickel sulfate	30

Substrates were 99.5% purity iron purchased from Goodfellow and cut into 15 x 15 mm squares. No grinding or polishing was performed to ensure all samples started with the same surface features.

The substrates were prepared for plating by degreasing, cleaning and activation using the following procedure:

- Degrease with acetone – shaken for 5 minutes
- DI water rinse
- Alkaline clean/soak – 10% NaOH, swirled for 5 minutes
- DI water rinse
- Activation – 10% HCl for 2 minutes
- DI water rinse
- Ready for plating

The solutions were created in batches of 1 L. Each litre was adjusted to the target pH, before splitting into five 200 mL beakers. The substrates were suspended in solution from a crocodile clip, attached to a plastic watch glass above the beaker. The pH of each solution was re-measured just before heating and adjusted as necessary. In the majority of cases, no adjustment was required.

The solutions were heated to 3 different temperatures, 70, 75 and 80°C using a hot plate. The temperature of the bath was constantly monitored using a digital thermocouple and maintained to within 0.5°C of the target. 3 different bath pH's, 4, 5, and 6, were used at each of these temperatures. The pH was measured at room temperature before plating and no adjustments were made during deposition. A plating time of 60 minutes was used for all solutions.

Two substrates were plated in each bath, to facilitate a range of destructive and non-destructive investigations to be performed post plating. Once the plating time had elapsed, samples were removed from the bath and thoroughly rinsed with DI water. These were dried with a hot-air blower and bagged for later analysis.

After one plating cycle each solution was discarded, to reduce the risk of bath failure by instability and to ensure samples produced from each bath were comparable.

2.5 Electroplated nickel samples

The standard nickel electroplated samples used for comparison were nickel plated UK five pence blanks, obtained from a commercial nickel sulphamate bath [$Ni(SO_3NH_2)_2$] at between 0.2 – 0.4 amps per square decimetre, at a temperature of 60°C, to obtain an average plating thickness of 25 µm. Post plating, these were annealed at 800°C for 35 minutes to reduce internal stresses, then finished using a High Energy Finisher with a load of 170 kg for 600 seconds.

2.6 Scanning Vibrating Electrode Technique

The Scanning Vibrating Electrode Technique (SVET) is a spatially resolved mapping technique used to observe the potential component of corrosion current density just above the surface of an immersed sample. This allows visualisation of anodic and cathodic activity on the surface and can help determine corrosion mechanisms and monitor the effect of inhibitor additions. Most experimentation is carried out in aggressive chloride-based solutions, so results can be obtained faster than under standard conditions or using other longer-term test methods. This technique has previously been used to monitor cut edge corrosion [102]–[105], galvanic corrosion [106], [107] as well as screening and evaluating the efficiency of inhibitor additions [108], [109] and the general corrosion of many different metals and alloys [110].

A typical SVET arrangement is shown in Figure 2.3, with details of the scanning head shown schematically in Figure 2.4. The microtip is made from platinum wire of 125 µm diameter encased in a borosilicate glass capillary tube. The glass is sealed around the wire to prevent electrolyte ingress and expose just the micro-disc at the extremity of the tip. The microtip vibrates through the oscillation of an electromagnetic driver at a constant amplitude, frequency and height above the surface of an immersed sample. The electromagnetic driver is normally a small speaker situated within a mu-metal (Ni-Fe alloy) enclosure. This has a very high magnetic permeability and shields the micro-electrode from electromagnetic leakage particularly as an AC drive voltage is used.

2.6.1 SVET equipment and theory

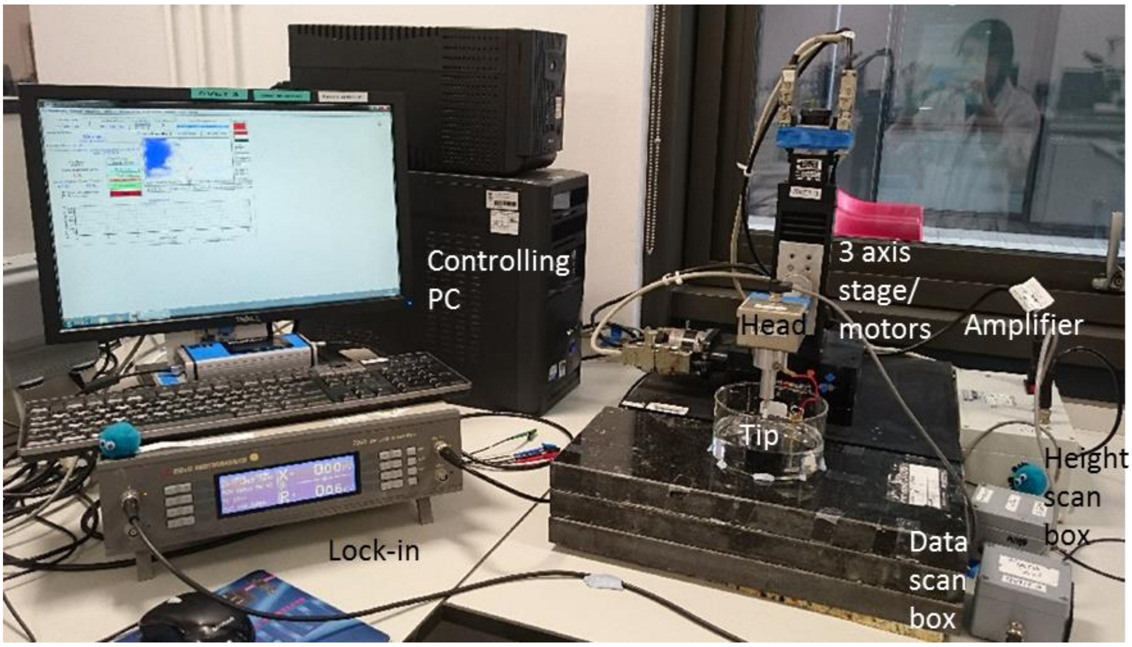

Figure 2.3. SVET equipment in the laboratory showing the typical hardware required for experimentation

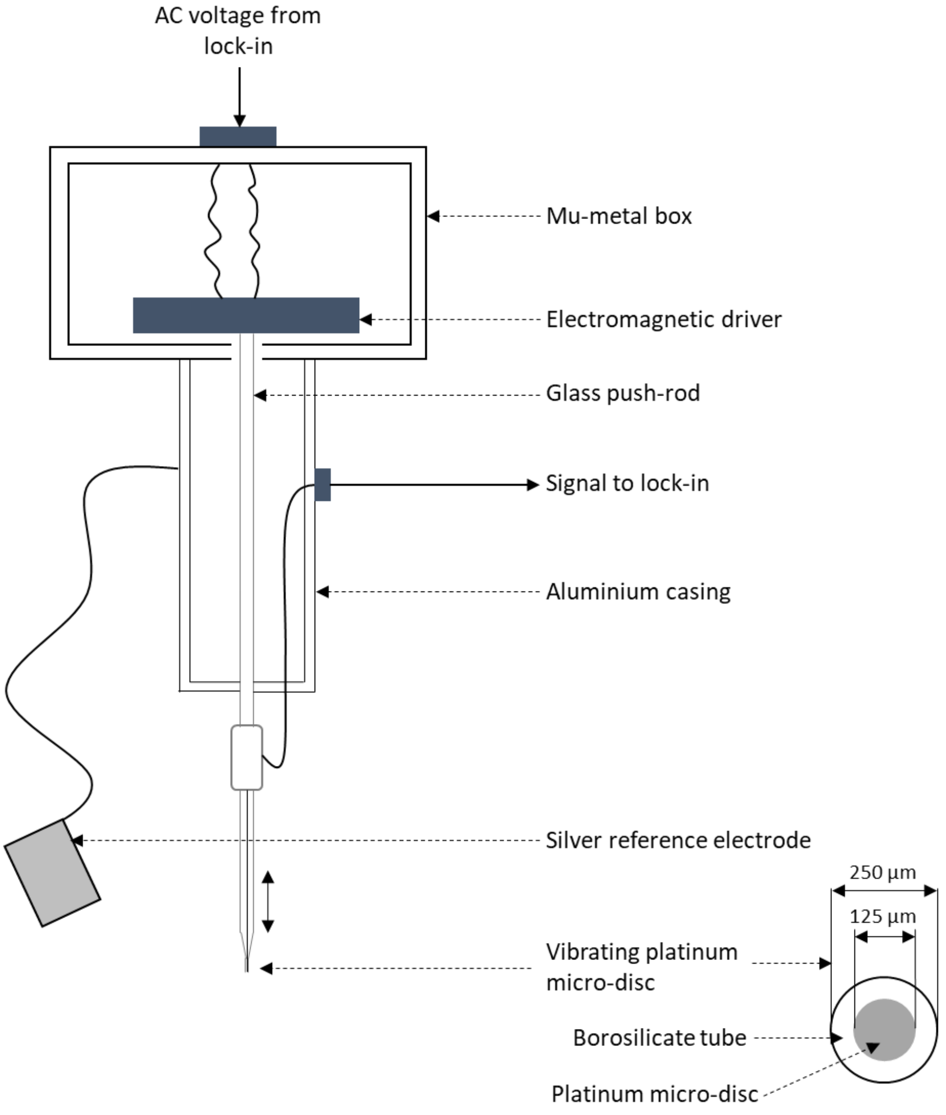

Figure 2.4. Schematic diagram of the SVET probe-vibrator assembly

The SVET registers alternating potential at the frequency of vibration, or the vertical component of potential gradients in solution, caused by ionic current flux passing through the electrolyte. This is directly proportional to the component of ionic current in the direction of probe vibration and provides a vector component for current density at a known height above the surface. A lock-in amplifier (EG&G Model 7265) sets the frequency of vibration, routed through an external amplifier to vibrate the probe at 140 Hz, resulting in a vibration amplitude of around 25 µm. The microtip scans 100 µm above the surface using a tri-axial manipulator stage, in conjunction with a controlling PC. The lock-in amplifier also monitors the AC voltage developed between the silver reference electrode and the platinum micro-disc. The recorded potentials can be converted to current densities using a calibration factor. This data can then be plotted as a spatially resolved map to identify regions of anodic and cathodic behaviour, and the intensity of activity occurring at each location.

It is understood potential fields in solution are produced by ionic current flux, emanating from locations of anodic activity on a corroding metal. The SVET microtip registers alternating potentials at the frequency of vibration, known to be proportional to the electrical field strength, F, or the vertical component of potential gradients in solution at a set distance above the surface. Any changes in F with respect to distance from a central point current source can be calculated using the following equation:

$$F = \frac{dE}{dz} = \frac{iz}{2\pi\kappa(x^2 + y^2 + z^2)^{1.5}} \qquad 2.1$$

Where:
i = current source
κ = electrical conductivity
x, y, z = distance from origin
The maximum field strength, F_{max}, at set height z will occur at the origin of the point current source when x = 0 and y = 0 and can be found using:

$$F_{max} = -\frac{i}{2\pi\kappa z^2} \qquad 2.2$$

The relationship between z^2, the square of the probe height and F_{max}, means maintaining a constant probe height during a scan is critical. Consequently, samples used for SVET must be either completely flat and featureless or subjected to a full height scan prior to the experiment. The height scanning process is detailed in Section 2.6.5 and was used extensively during this thesis to allow the examination of minted coin samples.

2.6.2 SVET limitations

It is important to consider the limitations of this technique, especially in terms of resolution. This is defined by the microtips ability to distinguish two separate localised corrosion events occurring in close proximity. The theoretical spatial resolution of SVET at any given scan height is shown by the signal peak width at half maximum (whm) where whm = 1.553·z. Therefore, at a scan height of 100 µm, resolution of individual corrosion events will be possible if separated by more than 155 µm, as considered previously [111]. However, in practice this is more likely to be around 250 µm, due to the dimensions of the microtip incorporating the borosilicate shield.

This resolution means SVET can only observe certain types of corrosion. When a corrosion event propagates on a surface, anodes and cathodes develop leading to a flow of ionic current from anodic areas towards cathodic areas. If activity on the surface is localised, the anodic and cathodic processes are separated by a distance greater than the scan height, meaning the microtip can intersect the iso-potentials generated, demonstrated in Figure 2.5. However, when corrosion is more generalised, the separation of anodic and cathodic events is smaller than the height of scan, so the microtip cannot intersect the iso-potentials generated, shown in Figure 2.6. The SVET is very useful when observing surfaces where localised corrosion such as pitting takes place, but less so for surfaces where only generalised corrosion occurs.

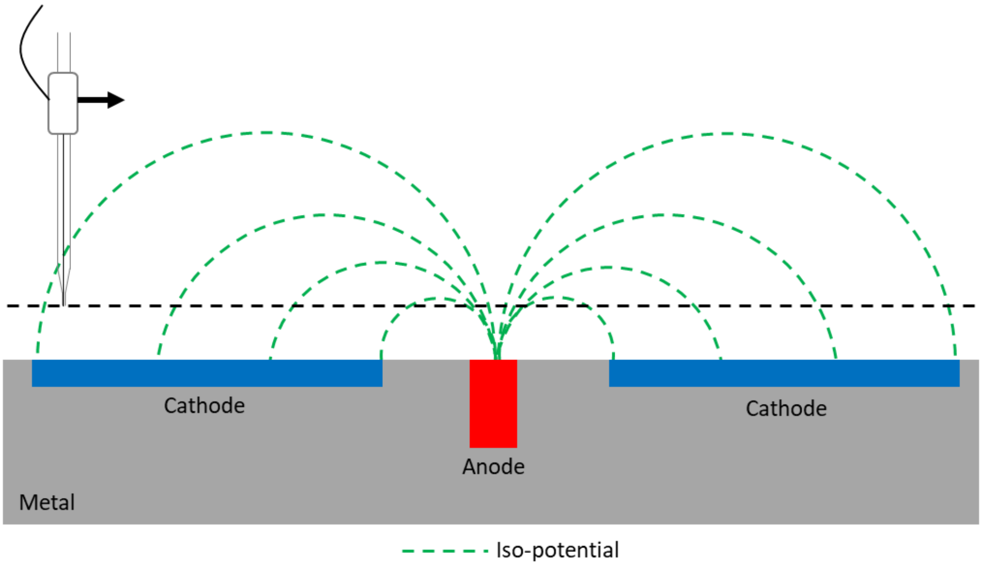

Figure 2.5. SVET microtip intersecting iso-potential lines when scanning localised corrosion events

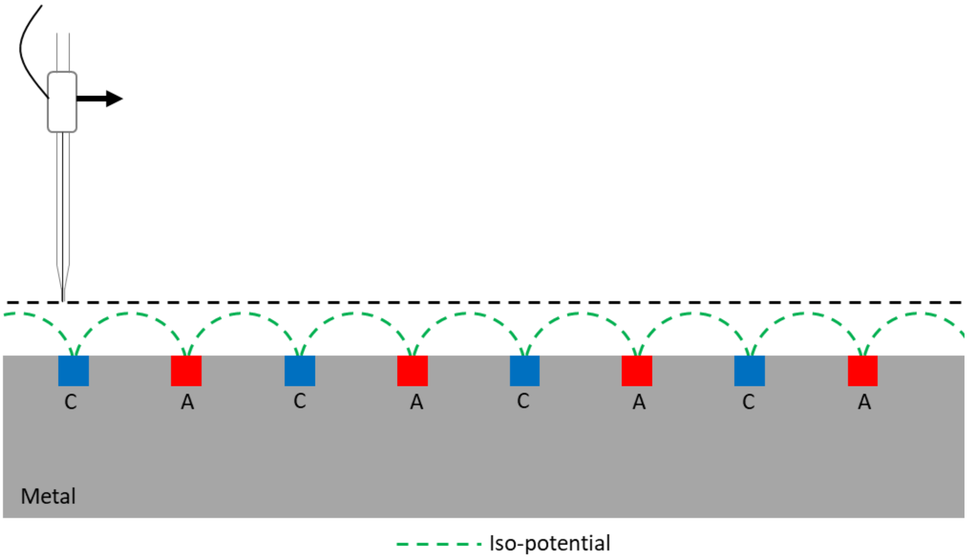

Figure 2.6. SVET microtip missing iso-potential lines when scanning generalised corrosion events

2.6.3 SVET calibration

Prior to each experiment, the SVET was calibrated to accurately convert the potentials recorded during the experiment by the lock-in amplifier, to corrosion current densities required for analysis. The SVET can be calibrated in three ways; through calculation, use of a point current source or use of a tube cell. A tube cell was used for all calibrations in this thesis, so is the only method that will be described here. The basic principle involves the passing of a range of ionic currents through the experiment electrolyte through a tube of known cross-sectional area, and recording the corresponding SVET voltage values displayed on the lock-in amplifier. The microtip is positioned a small distance inside the centre of the tube where the current emerges. A schematic of a typical calibration cell is shown in Figure 2.7. The SVET data scan settings used for calibration and experimentation in this thesis are shown in Table 2.4 below. Prior to calibration the tip was cleaned by immersion in 2 M hydrochloric acid for 10 minutes, then rinsed with deionised water.

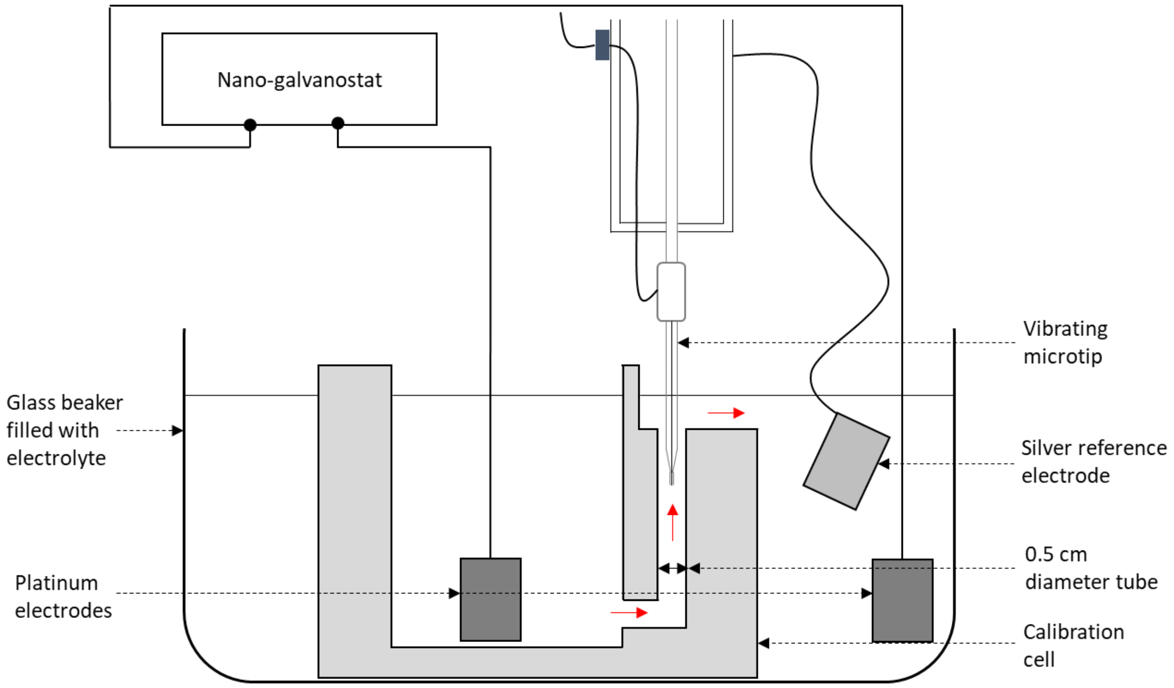

Figure 2.7. Schematic diagram of a typical SVET calibration cell

Table 2.4. Settings for SVET data scan

Setting	**Value**
Oscillator amplitude	0.015 V
Oscillator frequency	140 Hz
Lock-in sensitivity	100 µV
AC gain	40 dB
Time constant	50 ms

The calibration cell sits in a glass beaker, and comprises two compartments, as shown schematically in Figure 2.7. The pot is filled with the experiment electrolyte, above the level of the first tube opening but below that of the rim of the cell, to allow passage of ionic current. A nano-galvanostat applies a known current between the two platinum reference electrodes, positioned as shown in Figure 2.7, with the vibrating SVET microtip positioned in the centre of a tube with known cross-sectional area. It is assumed the current flux density is constant across the diameter of the tube, equal to the cell current divided by the cross-sectional tube area, and that the current flux direction is parallel to probe vibration. The tip registers this as a potential measured by the lock-in amplifier. This potential is noted in a spreadsheet, where slopes of applied current are plotted against measured voltage at a range of positive and negative currents. The gradient of this line is used as a calibration factor to convert results obtained as potential gradients in solution to normal current densities in the plane of scan. An example of a calibration plot for a 3.5% NaCl electrolyte is shown in Figure 2.8.

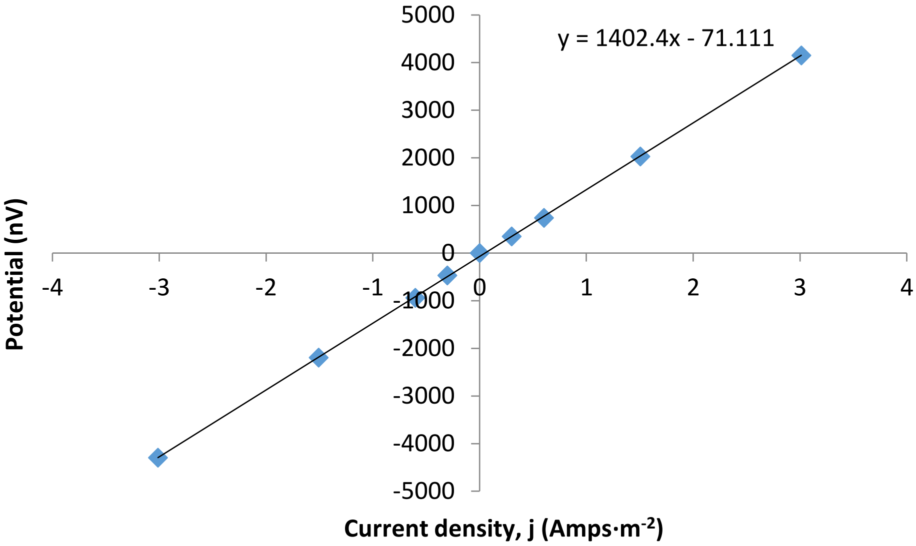

Figure 2.8. Example of a typical SVET calibration plot for a 3.5% NaCl electrolyte

2.6.4 SVET sample preparation

Samples used for SVET analysis were hot mounted in a non-conductive Bakelite resin. Lacomit stop-off varnish was used to isolate the scan area on each sample. The mounted samples were fixed to the base of a glass dish using double sided tape and Teflon tape, to prevent movement during scanning.

2.6.5 SVET height profiling

For samples with uneven surfaces, topographical profiles were needed to ensure the SVET microtip scanned at a constant height. This procedure was carried out after calibration and before electrolyte was added. To operate the SVET in height profiling mode, the settings in Table 2.5 below were applied.

Table 2.5. Settings for SVET height scan

Setting	Value
Oscillator amplitude	0.03 V
Oscillator frequency	900 Hz
Lock-in sensitivity	10 mV
AC gain	40 dB
Time constant	50 ms

Prior to height scanning, the sample dimensions were noted in the software, as well as the required resolution for height and data scans, i.e. the number of data points per mm to be recorded. The scan begins at the top left, with the microtip set 300 µm above the surface. During height scanning the loudspeaker is used as part of an inductance bridge circuit, which is initially balanced. As the probe touches the surface, the glass push rod moves the coil of the loudspeaker and it unbalances the bridge. The signal derived by the lock-in amplifier is used as an indicator that the surface has been reached and then the probe is retracted to its starting height and then this is repeated to build up a series of z-axis measurements at each xy coordinate which gives a constant probe-sample height. The probe rasters in the x direction, returns to its starting point, moves an increment in the y direction then resumes in the x direction. This pattern continues until the entire surface topography has been recorded, then returns the microtip to its start position, illustrated in Figure 2.9. Although this process is time consuming, it ensures the microtip maintains a constant height above the sample during data scanning. As height scanning is performed prior to the addition of corrosive electrolyte, it is not a time sensitive process. On commencement of a data scan, the software reads the file containing probe location information and replays it whilst collecting corrosion data. An example of the surface topography data collected during a height scan is shown in Figure 2.10.

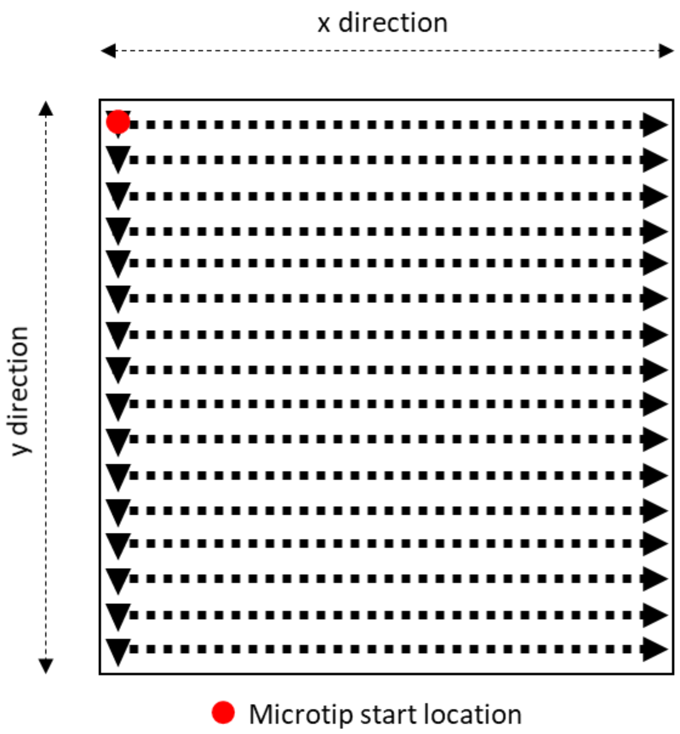

SVET height scanning

1. The SVET microtip starts in the top left corner

2. The tip scans in the x direction, pausing every 0.2 mm step to lower the probe to the surface. When the probe reaches the surface the x, y and z coordinates are saved

3. When the tip reaches the end of the first row, it lifts up and returns to the start of the row

4. The tip moves one step (0.2 mm) in the y direction

5. Repeat steps 2 – 4 until entire sample has been scanned

Figure 2.9. Pattern of SVET microtip rastering

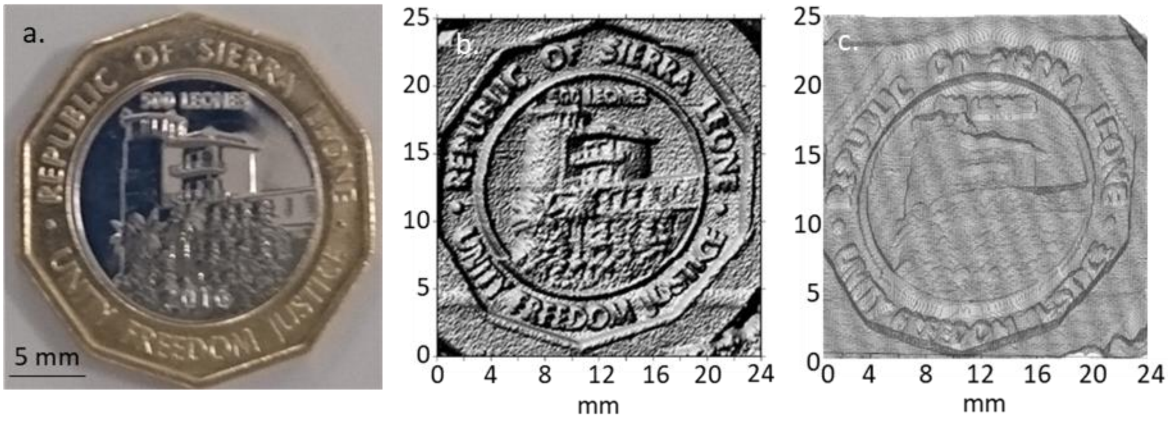

Figure 2.10a. Coin surface compared to b. an example SVET height scan in profile and c. in wireframe (max-min 115 μm)

2.6.6 SVET data mode

After height scanning, the lock-in must be setup to data scan as described in Table 2.4 above. The electrolyte was added to a level above the sample, and below the white sheath of the SVET tip. The experiment was then started. Throughout this thesis, experiments were set to scan once an hour for a total of 24 hours.

2.6.7 SVET data processing

The raw SVET data is stored in nano-volts which is converted to current densities in order to obtain meaningful results. This is completed using in-house software; the raw data is loaded and divided by the calibration factor obtained for the corresponding experiment, then stored in a new data file. This calibrated data was loaded into cartography software (Surfer, Golden Software) to produce spatially resolved maps of normal current density. These maps show areas of anodic and cathodic activity by applying false colour. Areas of negative current density are considered cathodic and coloured increasingly dark blue as intensity increases; areas of positive current density are anodic activity and coloured increasingly dark red as the intensity of this activity increases. Zero values are coloured white.

It is also possible to obtain values for total anodic current density. By summing the positive current densities from each scan, the total amount of anodic activity can be compared between scans taken at each hour, as well as between experiments on different samples to compare corrosion rates.

2.7 Scanning Kelvin Probe

The Scanning Kelvin Probe (SKP) is an advanced electrochemical scanning technique which is used to determine metallic work functions of samples under atmospheric conditions. No immersible reference electrode is required, so localised corrosion measurements can be made under very thin and resistive electrolyte films. This technique is potentiometric and so very non-perturbing; it does not interact or interfere with corrosion events happening on the surface. However, this technique only measures electrode potentials as opposed to currents, so cannot be used to calculate corrosion rates. The SKP is most commonly used to monitor the atmospheric corrosion of metals under thin electrolyte films [112]–[114] and the delamination of coatings from metal substrates [115]–[120]; in this thesis, observations of the potentials of bimetallic pairings and activity occurring under small droplets during secondary spreading phenomena are made.

2.7.1 SKP theory

During SKP operation, the reference probe is vibrated over a metallic sample; these form the two plates of a parallel plate capacitor. The medium between these two plates, normally either air or nitrogen, makes up what is considered as the capacitor dielectric. The capacitance of the parallel plate capacitor is given by:

$$C = \frac{\varepsilon\varepsilon_0 A}{d} \tag{2.3}$$

Where d is the plate separation, A is the plate area, ε_0 is the permittivity of vacuum and ε is the dielectric constant of the capacitor dielectric.

The Kelvin reference probe undergoes sinusoidal vibration above the surface at a known frequency, ω, such that the plate separation varies with time, t, according to:

$$d = \bar{d} + \Delta d \sin(\omega t) \qquad 2.4$$

Where $\bar{d}$ is the mean plate separation and d is the amplitude of vibration. This means the vibration produces a periodic fluctuation in capacitance, shown by:

$$C = \varepsilon\varepsilon_0 \frac{A}{\bar{d} + \Delta \mathrm{d} \sin(\omega t)} \qquad 2.5$$

If a Volta potential difference exists between the parallel plate capacitors, $\left(\Delta\psi_{Sample}^{Ref}\right)$, an alternating current (i_{ac}) will be made in the circuit connecting the two capacitors such that:

$$i_{AC} = \Delta\psi_{Sample}^{Ref} \frac{dC}{dt} \qquad 2.6$$

$$= \Delta\psi_{Sample}^{Ref} (\varepsilon \cdot \varepsilon_0 \cdot A \cdot \Delta d \cdot \omega) \frac{\cos(\omega t)}{(\bar{d} + \Delta d \ \sin(\omega t))^2} \qquad 2.7$$

$$\approx \Delta\psi_{Sample}^{Ref} (\varepsilon \cdot \varepsilon_0 \cdot A \cdot \Delta d \cdot \omega) \frac{\cos(\omega t)}{(\bar{d})^2} \text{ for } \bar{d} \gg \Delta d \qquad 2.8$$

The Kelvin probe signal current (i_{ac}) does not provide a direct value of the open circuit of $\Delta\psi \frac{Ref}{Sample}$, instead this is found through an externally applied DC bias voltage (U). This value, U, is changed so that i_{ac} becomes zero, meaning no current flows. Under such null current circumstances, the potential difference across the dielectric must be zero, so that:

$$-U_{null} = \Delta\psi_{Sample}^{Ref} \qquad 2.9$$

This means that $-U_{null}$ is the value measured in practice, rather than the quantity $\Delta\psi_{Sample}^{Ref}$.

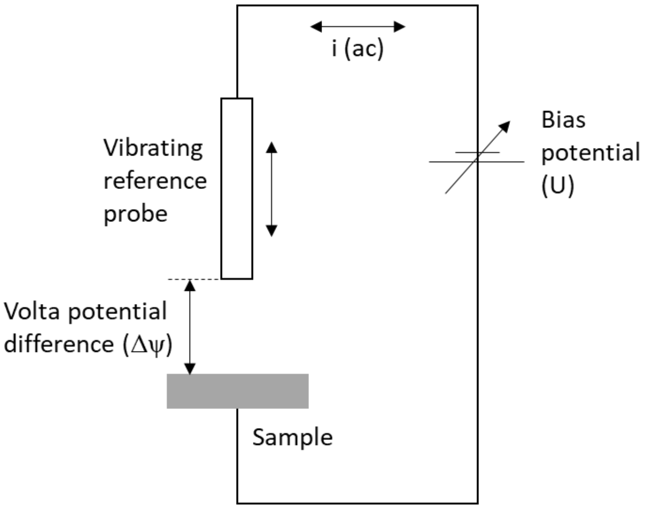

Figure 2.11. Principles of SKP operation

2.7.2 SKP setup

The SKP uses a range of different components, shown in Figure 2.12 and Figure 2.13. An environment chamber made from stainless steel maintains a controlled humidity environment and excludes electrostatic, electromagnetic and mechanical noise. The Kelvin probe is a 100 µm gold wire, vibrated at 280 Hz via an electromechanical driver at an amplitude of around 40 µm. A lock-in amplifier sets the probe vibration and detects the off null signal of the Kelvin probe. The sample is electrically connected to a current to voltage convertor inside the environment chamber, where the current is converted to an AC voltage, with a gain of 10^9 meaning 1 picoamp is converted to 1 mV. The integrator automatically adjusts the Kelvin probe bias to null the AC signal and is logged as -Δψ, the Volta potential difference or contact potential difference. A controlling PC manipulates the tri-axial motors and records the Δψ measurements according to their location on the sample.

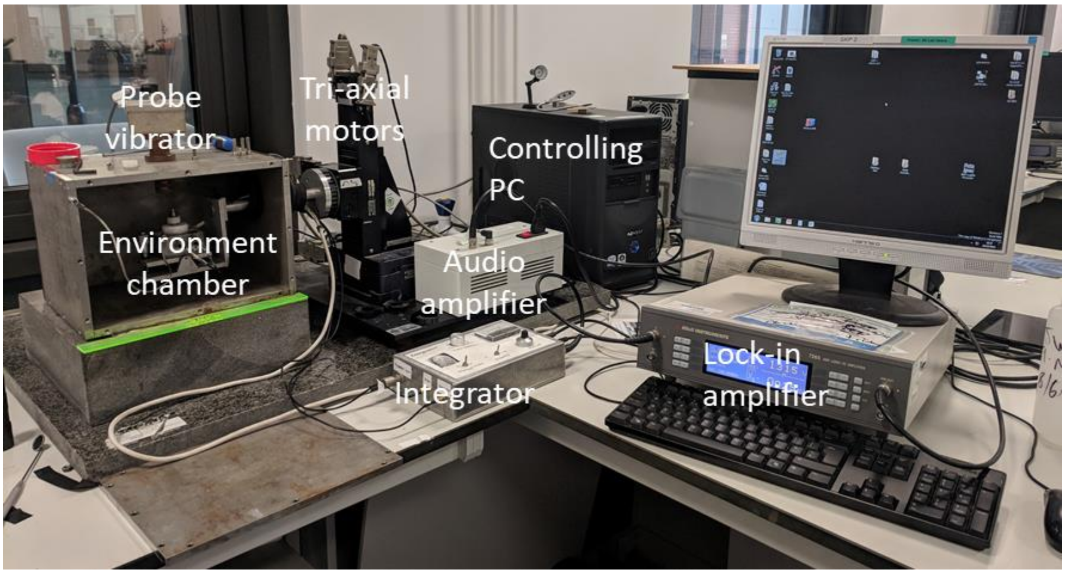

Figure 2.12. SKP setup and equipment

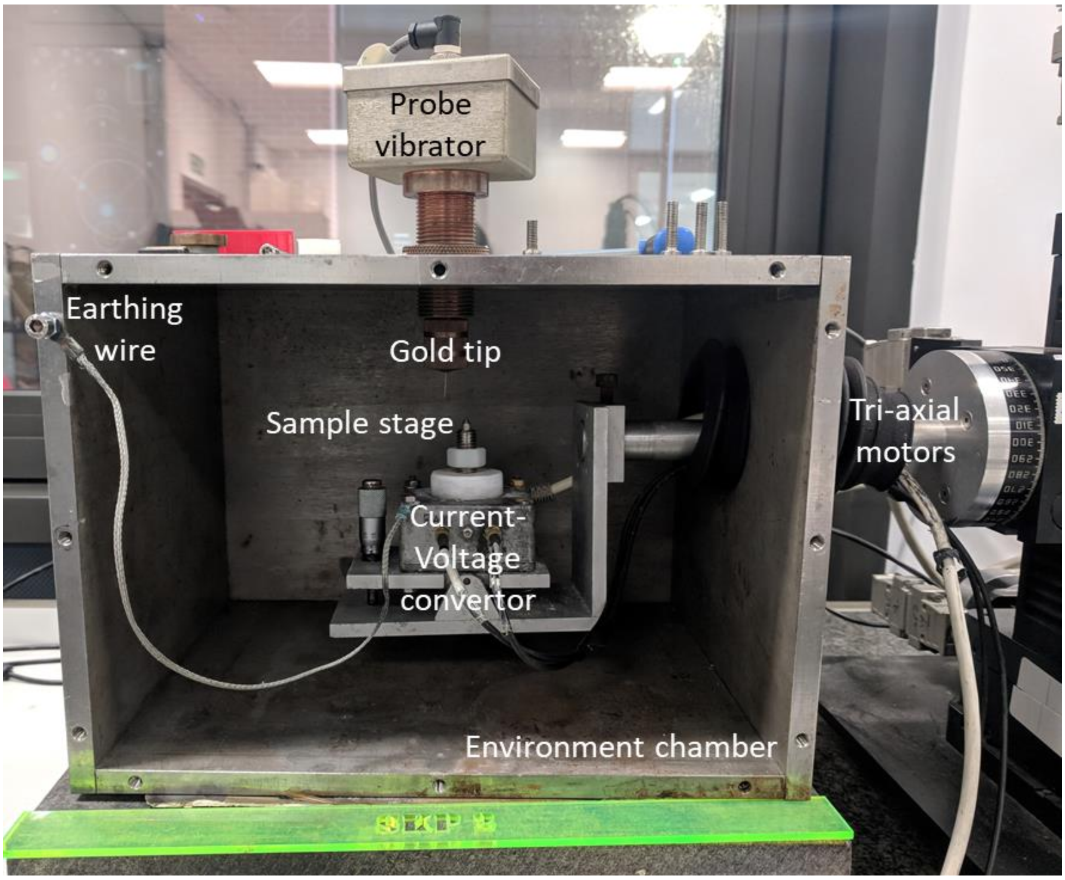

Figure 2.13. SKP humidity chamber

2.7.3 SKP calibration

Before starting an experiment, the tip was cleaned for 10 minutes in 2 M hydrochloric acid, followed by 10 minutes in DI water. Calibration was completed using a metal/aqueous metal ion couple, in this case a copper well filled with a 0.5 M copper sulphate solution. Δψ values were obtained with the Kelvin probe vibrating 100 µm above the centre of the electrolyte well. A schematic diagram of this process is shown in Figure 2.14. This value is expected to be around 314 mV vs. SHE as this is the potential of the half-cell reaction between copper and copper sulphate, as measured using a potentiostat and reference electrode.

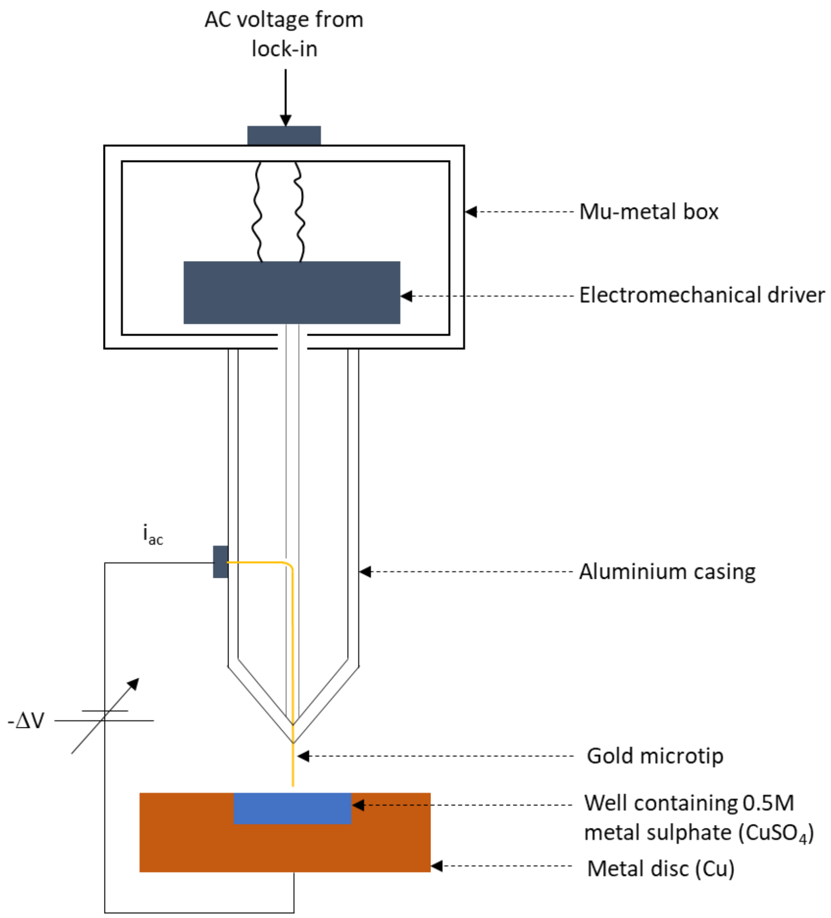

Figure 2.14. Schematic of SKP calibration

2.7.4 SKP sample preparation

Samples were held in the SKP chamber by a threaded bolt in the centre. This bolt holds a retractable pin, which makes an electrical connection to the back of the sample. M10 nuts were set on the back of each sample using Loctite Double-Bubble glue, for attachment in the SKP chamber. The Kelvin probe tip was positioned at the start point of the scan, in the top left corner, 100 µm above the surface and sample dimensions added to the software. If a height profile was required, this process was carried out prior to Volta potential mapping. The environment chamber was then brought to the required humidity, and the Volta scan commenced.

2.7.5 SKP height mode

For the samples used throughout this thesis, it was necessary to perform height scans prior to Volta scans due to the non-planer nature of the samples. To operate the SKP for height scanning, the lock-in amplifier was set to dual-harmonic mode. Height scanning using an SKP probe is based on the principle of harmonic distortion, as described previously by Chenan et al. [121] where the ratio of the Kelvin currents in both the primary (X1) and secondary (X2) harmonic frequencies was used to evaluate the distance between the Kelvin probe tip and the sample. The relationship between this ratio and the distance from the surface is shown in Figure 2.15. This method of height profiling is accurate to ±2.5 µm, so provides ample accuracy when scanning at a height of 100 µm above the surface.

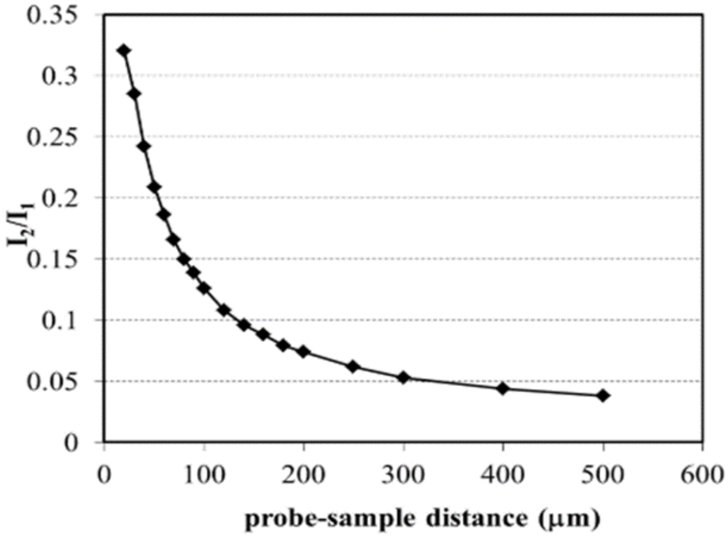

Figure 2.15. Demonstration of the relationship between the two harmonic phases and Kelvin probe distance from the sample surface [106]

When height scanning, the lock-in was setup as per Table 2.6. To obtain the ratio of X1 and X2, the following equation was set in the lock-in amplifier:

$$\frac{(X2-0)\times C1}{X1} \tag{2.10}$$

Where C1 = 1000.

The ratio increases as the tip approaches the surface, shown in Figure 2.15. A target ratio is set in the software when the tip is 100 µm above the surface. The sample moves under the probe in the same pattern as SVET scanning (Figure 2.9), and the tip height is adjusted until the ratio meets the target. An example of the profile obtained from SKP height scanning is shown in Figure 2.16.

Table 2.6. Settings for SKP height scan

Setting	**X1**	**X2**
Oscillator amplitude	0.05 V	0.05 V
Oscillator frequency	280 Hz	280 Hz
Lock-in sensitivity	100 mV	10 mV
AC gain	10 dB	10 dB
Time constant	100 ms	100 ms

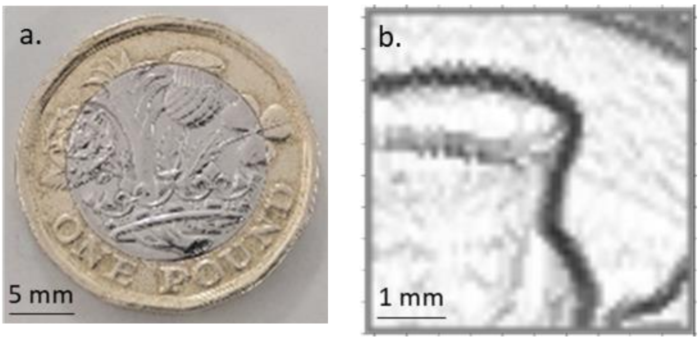

Figure 2.16a. Coin surface compared to b. an example SKP height scan in profile

2.7.6 SKP data mode

Before Volta scanning, the lock-in amplifier must be returned to Volta scan settings by adjusting the values to those shown in Table 2.7. A scan can then be started.

Table 2.7. Settings for SKP Volta scan

Setting	Value
Oscillator amplitude	0.05 V
Oscillator frequency	280 Hz
Lock-in sensitivity	10 mV
AC gain	0 dB
Time constant	20 ms

2.7.7 SKP data processing

For experiments where a bare metal under humid conditions is examined, the following equation was used to find E_{corr}, the corrosion potential:

$$E_{corr} = A + \Delta\psi_{El}^{Ref} \qquad 2.11$$

Where $\Delta\psi$ is the contact potential measured during calibration and A is a constant; the Volta potential measured for the Cu\Cu^{2+} calibration cell value determined previously. For additional detail, Williams and McMurray have fully described Kelvin probe theory and calibration [122].

2.8 Potentiostat techniques

Potentiostat characterisation was carried out using a Solartron SI 1280 connected to a PC and controlled by Scribner Associates CorrWare software. All experimentation was carried out at an ambient temperature of 21°C. Thin flat samples were mounted in an in-house manufactured sample holder, shown in Figure 2.17. Thicker, textured samples were masked with a Lacomit stop-off varnish to isolate a small area for investigation.

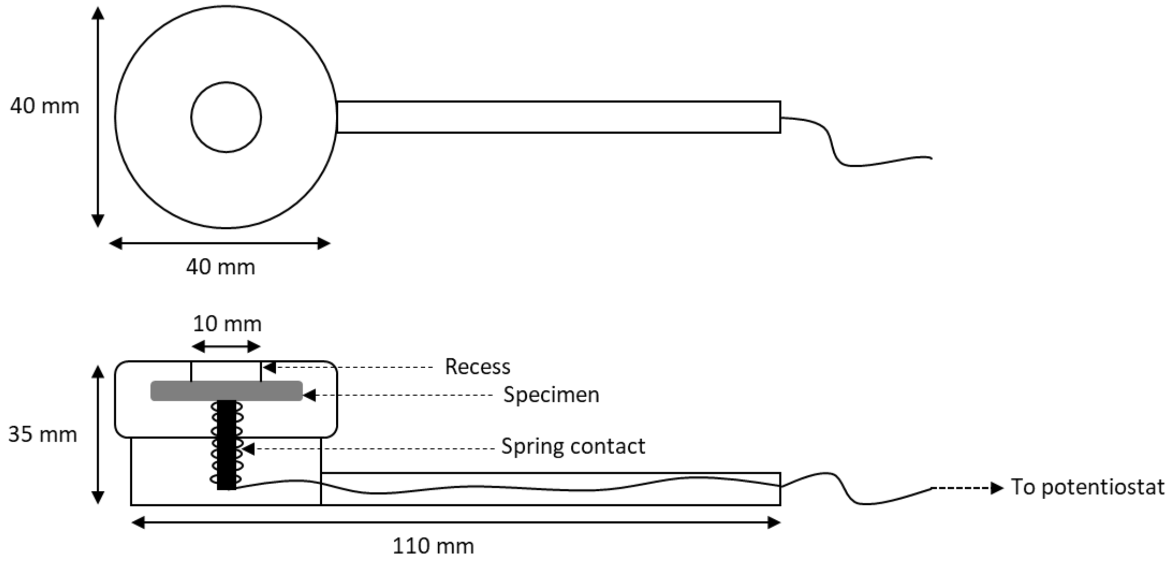

Figure 2.17. Sample holder for potentiostat experimentation

2.8.1 Open Circuit Potential

Open circuit potential was used to determine the rest potential, or free corrosion potential of metals and alloys in a corrosive electrolyte. A two-electrode cell, comprising a reference electrode and a working electrode was used for these experiments. A saturated calomel electrode (SCE) was chosen as the reference electrode, as it is very robust, and commonly used for experimentation in aqueous solutions. The exposed metal of interest functioned as the working electrode.

This simple measurement monitors the potential over time, with the potentiostat acting as a high resistance voltmeter. Each experiment was carried out for 60 minutes to establish a stable reading in the experiment electrolyte. These values were used to rank materials in terms of corrosion performance and to determine the voltage sweep ranges for potentiodynamic polarisation experiments.

2.8.2 Potentiodynamic polarisations

Potentiodynamic polarisations can be used to observe changes in corrosion current whilst an imposed potential swept through a series of values, from cathodic below the OCP to anodic above the OCP. A three-electrode cell consisting of a reference electrode, a working electrode and a counter electrode was used. A saturated calomel electrode (SCE) was the reference electrode, the material of interest was the working electrode, and a platinum foil was used as the counter electrode.

During a potentiodynamic characterisation, an external potential is applied between the working and reference electrodes. Simultaneously, changes in the current are measured between the working and counter electrodes. The potential is increased or decreased over a set range at a constant rate whilst the resulting current is monitored. From these results, applied potential versus measured current can be plotted. A sweep rate of 1 $mV \cdot s^{-1}$ was used, and the sweep range for each experiment is defined within the relevant chapter.

Graphs obtained from potentiodynamic polarisations can be used to obtain values for mass loss and provide the necessary co-efficient values for the Stern-Geary equation; this is used to calculate mass loss from linear polarisation experiments. This information is obtained using Tafel extrapolation on the linear regions of the cathodic and anodic sections of the graph, an example is shown in Figure 2.18. The gradients from the Tafel extrapolations, βa and βc, are used within the Stern Geary equation for mass loss, described in Section 2.8.3. To find mass loss from potentiodynamic polarisations (PDP), the Tafel lines are extrapolated until they intersect. At the intersection, the value of I_{corr} can be obtained and then equated to current density. The mass loss can then be calculated using the following equation:

$$Mass\ Loss = \left(\frac{[j_{corr} \times t \times A_r]}{nF}\right) \times 10^6 \qquad 2.12$$

Where:

J_{corr} = Current density in amps$\cdot$cm^{-2}

t = Seconds in a week – 604,800

A_r = Relative atomic mass, 58.7 for nickel, multiplied by 10^6

n = Number of electrons involved in the reaction, Ni = 2

F = Faraday's constant, 96,485 C$\cdot$mol^{-1}

This equation gives an answer in μg$\cdot$cm$^{-2}\cdot$week^{-1}.

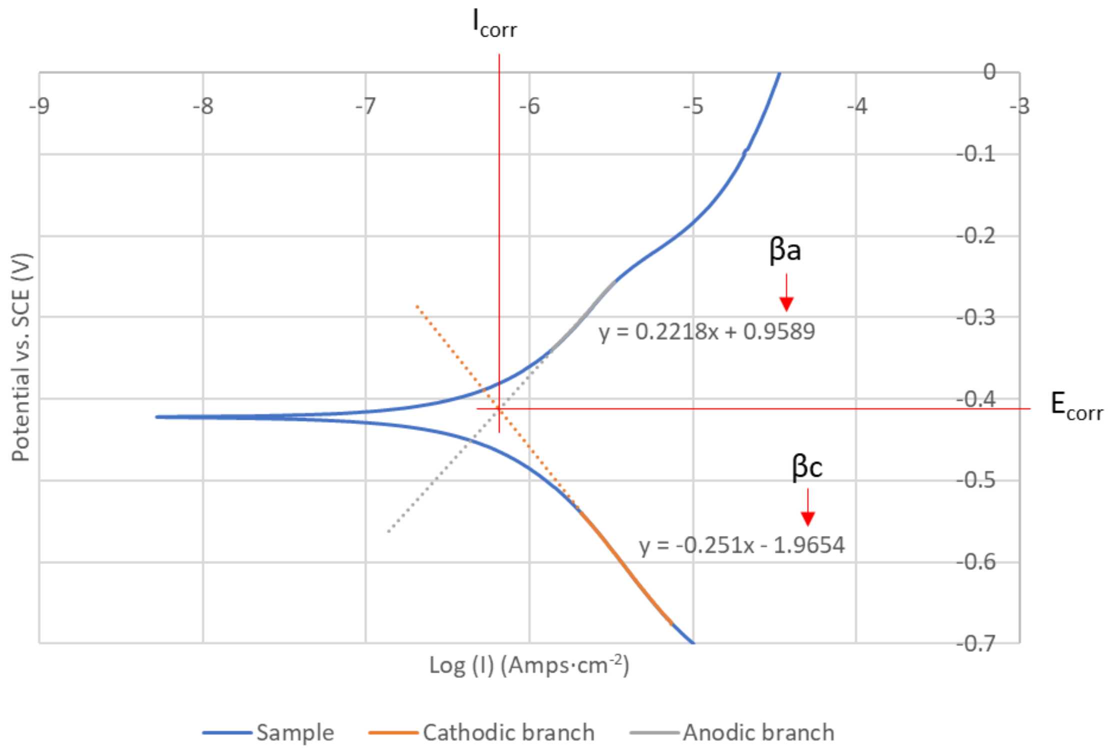

Figure 2.18. Example of analysis performed on potentiodynamic polarisation curves. Graph shown is an electroless nickel plated sample plated at 75ºC and pH 5, the experiment was performed in a 3.5% NaCl electrolyte at pH 7.

2.8.3 Linear Polarisation Resistance

Linear polarisation resistance is similar to potentiodynamic polarisation, as it involves the polarisation of a sample away from OCP, however in this case the degree of polarisation is small. This technique is less destructive and can assess changes in corrosion characteristics over time by repeating measurements. To obtain the most accurate results, potentiodynamic polarisations were necessary to obtain Tafel constants. LPR experiments polarised the samples ±10 mV either side of the OCP, at a scan rate of 0.25 $mV{\cdot}s^{-1}$, collecting 10 data points per second. This experiment produces a straight-line graph of current versus potential (vs. SCE), with the gradient equal to the polarisation resistance, R_p.

Mass loss data can be obtained by calculating i_{corr}, the corrosion current, using the following equation:

$$i_{corr} = \frac{B}{R_p} \qquad 2.13$$

Where B, the Stern-Geary constant was calculated from:

$$B = \frac{\beta a\ \beta c}{2.3\ \beta a + \ \beta c} \qquad 2.14$$

R_p, the polarisation resistance is the gradient of the LPR plot.

From i_{corr}, the mass loss can then be calculated from equation 2.12 in Section 2.8.2.

2.8.4 Zero Resistance Ammetry

The potentiostat can be used as a zero resistance ammeter (ZRA) to determine whether a galvanic couple is formed between two metals immersed in electrolyte. One metal is the working electrode, whilst the other is the counter/reference electrode and a potential difference of 0 V is applied between these two electrodes. Because one is more noble than the other, the net current flow between them can be measured over time. This technique is often used to assess the potential for a galvanic corrosion cell to occur, by monitoring the resultant current density of the cell. In this case, the size of the predicted cathodic material was varied to observe the effect on the magnitude of the current density observed.

The metal predicted as the anode had a set surface area, whilst the area of the cathode metal was varied to be one half, the same, and one and a half times the size of the anode. The samples were painted with Lacomit stop-off varnish allowing only specific area exposure to the electrolyte. The experiment used a two-electrode setup. The working electrode and 2nd reference cables were attached to the working electrode, whilst counter electrode and 1st reference cables were attached to the counter electrode. Of the metallic pair used in each experiment the metal most likely to be the site of anodic activity was treated as the working electrode whilst the other was the counter electrode. The electrodes were immersed in the electrolyte of interest, and the potentiostatic hold of 0 V was carried out for 1 hour, with net current density versus time behaviour monitored.

2.9 Hardness

Hardness testing measures a material's resistance to permanent deformation. This is important for coinage alloys, as minting involves deforming the coin to incorporate the desired image. Vickers hardness testing was performed using an Innovatest Nexus 4302 machine, with Impressions XT software on the controlling PC. This experiment applied the load with a square based diamond pyramid indenter with a point angle of 136°, leaving an indent with sides at 22°. Two measurements were taken from opposite corners of the indent and averaged to give d. $\frac{F}{A}$ can be used to calculate hardness, where F is the applied force and A is the surface area of the indent in square millimetres. To calculate A, the following equation is used:

$$A = \frac{d^2}{2\sin\left(136^\circ \div 2\right)} \qquad 2.15$$

can be evaluated to give;

$$A \approx \frac{d^2}{1.8544} \qquad 2.16$$

Using this in the F ÷ A, the equation now becomes:

$$HV = \frac{F}{A} \approx \frac{1.8544F}{d^2} \quad 2.17$$

To find an answer in kilograms-force per square meter (kgf·m^{-2}) and

$$HV = \frac{F}{A} \approx \frac{0.01819F}{d^2} \quad 2.18$$

To obtain an answer in SI units – gigapascals (GPa).

Unless otherwise specified, a force of 1 kg was applied, for a dwell time of 10 seconds.

2.10 Scanning electron microscopy with energy-dispersive x-ray spectroscopy

Scanning electron microscopy is a characterisation technique used to obtain high resolution images. A focused beam of electrons rasters over the surface of a sample and the resulting signal received by the detector creates an image. The SEM used in this project was a Hitachi TM3000 table top microscope, set at an accelerating voltage of 15 kV. Energy-dispersive x-ray spectroscopy (EDS) was used to identify the elemental composition of alloys and corrosion products. The EDS instrumentation was Bruker Quantax70, integrated with the SEM and analysed using the associated software.

2.11 X-ray Diffraction (XRD)

This technique uses diffraction patterns to determine the atomic structure and phases of materials present.

XRD experimentation used a Bruker D8 Discover, running Da Vinci software. The source of radiation was Cu Kα with a wavelength of 1.5418 Å. For all scans, an applied voltage of 40 kV and a current of 40 mA was used. All scans were carried out with a 2θ between 30 and 100°. Step size was set to 0.035° and time per step was set to 1 second, leading to an average scan time of 34 minutes.

A Göbel mirror, or parallel beam set-up was used for all experiments. The incident arm held the Cu source, a Göbel mirror, a 0.6 mm fixed slit, an axial soller of 2.5° and a rotary absorber, set to automatic. The secondary, or detector arm, held an adjustable slit, an axial soller of 2.5° and a 192-channel lynxeye 1D detector.

2.12 Analysis of atmospheric corrosion

Time lapse photography was used to monitor the atmospheric corrosion of samples in Chapter 4. This involved a Canon 600D DSLR camera and associated computer-controlled software, programmed to automatically record images of a sample at regular intervals.

The setup of this experiment used a sample, with or without an induced defect, and a droplet of known concentration and volume of sodium or magnesium chloride solution placed in the centre.

The sample was mounted in a petri dish, above a well of corrosive salt solution. A lid was placed on top to prevent evaporation of the droplet or the well during the experiment. A schematic of this setup is shown in Figure 2.19. Images were taken at 2-minute intervals for a total of 48 hours. The petri dish and camera were placed in a dark cupboard, illuminated with an LED strip to maintain constant lighting conditions. The camera was held on a tripod at an angle to prevent reflection into the lens.

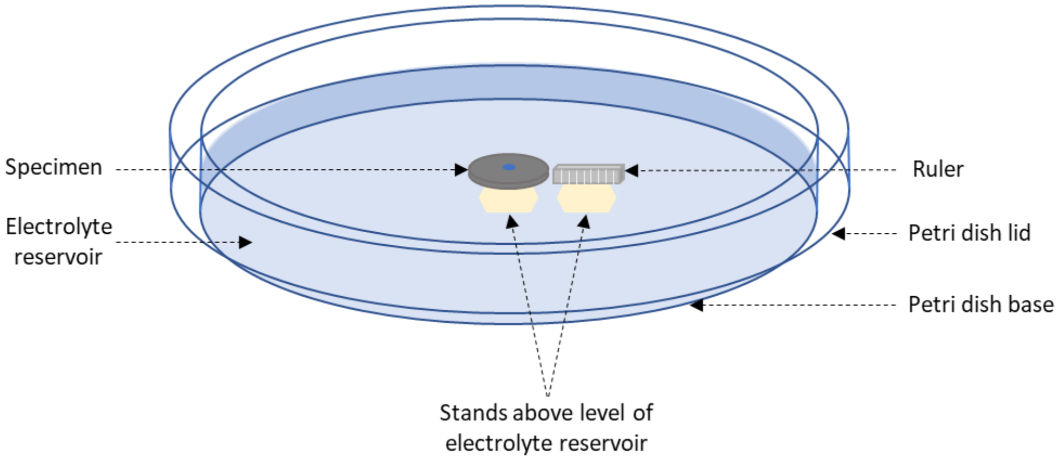

Figure 2.19. Schematic of time lapse photography setup

The main interest from these images were the changes in diameter of droplets on different metal surfaces with varying defect size over 48 hours. Image analysis was completed using Photoshop CS6 software, where 25 images taken 2 hours apart were examined. Each image contained a ruler, so the software could equate number of pixels to a known length. Photoshop was used to measure the diameter of the droplet and any spreading that had occurred both vertically and horizontally, shown in Figure 2.20. These measurements were imported to Microsoft Excel, and an average value for the distance between the centre of the drop and its perimeter was found for each image. These distances were then plotted versus time for each experiment.

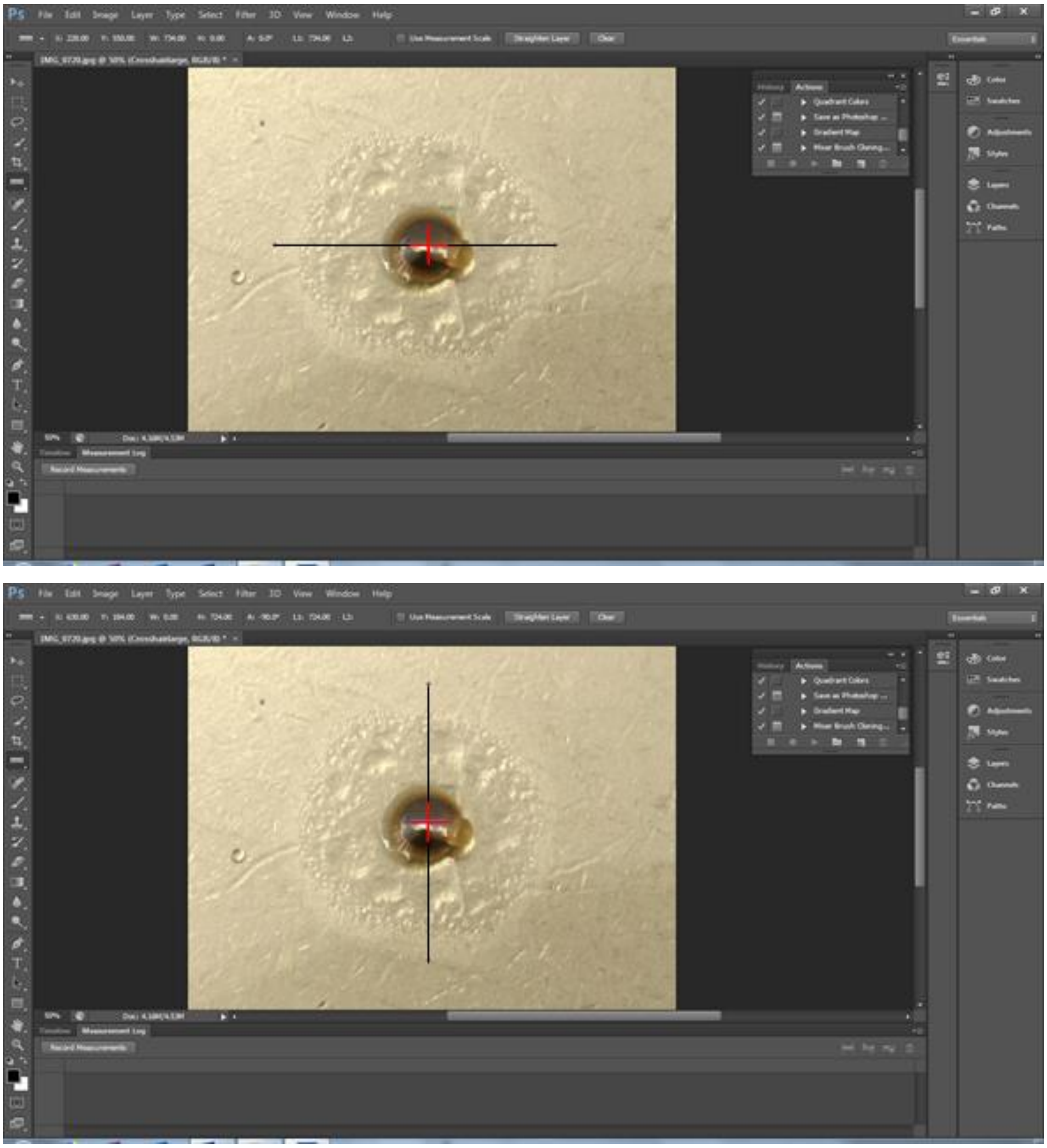

Figure 2.20. Example positioning of horizontal and vertical measurements when processing atmospheric corrosion data

Chapter 3. Investigating the interactions between the sections of bimetallic circulation coinage

3.1 Introduction

This chapter considers the potential for bimetallic, or two-metal coins to undergo galvanic corrosion in circulation and immersion conditions. Bimetallic coins have been used since the 17th century for special edition and token coinage and were only introduced into circulation in 1982 for the Italian 500 lire. The first UK bimetallic coin was the £2, issued in 1997. Today, many countries use at least one bimetallic coin in their currency. In most circulation applications, bimetallic construction is used for higher value coins, as they are harder for counterfeiters to reproduce accurately.

The manufacturing process for these coins is longer and more expensive than standard single metal coins. The two sections, known as the ring and pill (or inner and outer) are produced separately, and are only combined at the minting stage. The ring and pill sections can be manufactured from a homogeneous metal or alloy, or be formed from a plated substrate. Plated sections are increasing in popularity as they are cheaper to produce. Before minting, the pill fits loosely inside the ring. Around the circumference of the pill, a groove is milled. At the minting stage, these sections are fed into the press together, and struck with 60 tonnes of force. As well as minting the coin and turning it into legal tender, this process locks the two sections together. The inside of the ring deforms to fill the groove around the edge of the pill, like a tongue and groove joint, making them impossible to break apart.

Bimetallic corrosion happens when two electrically dissimilar materials in electrical contact are in a corrosive electrolyte. In such instances, one metal becomes the location of cathodic activity, where reduction occurs, whilst the other becomes the location of anodic activity, where oxidation occurs. For any given pairing of metals or alloys, predictions on which forms the anode and cathode can be made by comparing their corrosion potentials. Another influencing factor on corrosion is the relative size of the different sections. This effect is investigated on the coins examined in this chapter.

Since the popularity of bimetallic coins has soared in recent years, there has been some concern if metal ions, especially nickel, could be released. Amongst the first to raise these concerns were Nestle et al. [5] and Gee et al. [123] after the release of the Euro coins, specifically concerning the nickel based sections. Patch testing was completed, which involved the taping of potential sensitisers to the skin of patients and the development of any allergic reaction was monitored over time. Such experimentation has previously been completed using bimetallic coins on nickel sensitive patients and proved nickel is released especially from the 1 Euro coin [124]. Searle et al. [106]

completed scanning and electrochemical investigations on a range of bimetallic coins from various countries with different compositions and found potential interactions between the sections.

In this work a range of corrosion experiments were performed on several uncirculated minted and blank samples provided by The Royal Mint. To compare different combinations of metals and alloys, both homogenous and plated sections were used. The pairings were ranked, depending on their suitability in terms of the risk of galvanic corrosion occurring between them. The effect on corrosion of different cathode to anode ratios has been observed and compared to the ratio of sections used in circulation.

3.2 Experimental details

3.2.1 Samples

A range of uncirculated minted and blank sections of bimetallic coins were provided by The Royal Mint for examination in this thesis, listed in Table 3.1 below. All samples were taken from general production lines.

Denomination and Country	Ring (outer) composition	Pill (inner) composition	Image
500L (Sierra Leone)	Nickel-brass (76% Cu, 4% Ni, 20% Zn)	Electroplated 25 µm layer of nickel on steel substrate	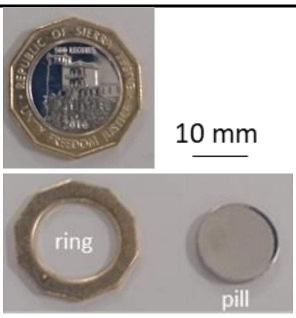
E£1 (Egypt)	Electroplated 25 µm layer of nickel on steel substrate	Duplex brass plated steel (around 25 µm layer) (Cu deposition followed by Zn deposition and interdiffusion)	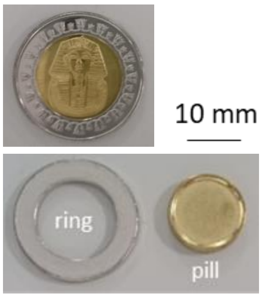
£2 (United Kingdom)	Homogeneous nickel-brass (76% Cu, 4% Ni, 20% Zn)	Homogeneous cupro-nickel (75% Cu, 25% Ni)	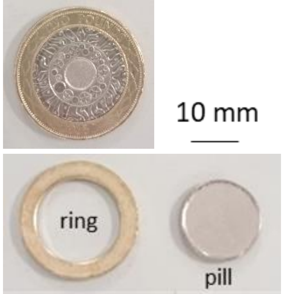

New £1 (United Kingdom)	Homogeneous nickel-brass (76% Cu, 4% Ni, 20% Zn)	Electroplated 25 µm layer of nickel	

Table 3.1. Bimetallic coin compositions

3.2.2 Sample preparation

All samples were cleaned with anionic surfactants to remove dirt and oil left from the manufacturing process. Immediately prior to experimentation, surface oxides were removed using a 5 µm alumina paste, to ensure consistency. Typical metallographic polishing was not possible due to the features on the minted coins, and the thickness of the plated layers.

Samples for SVET were prepared by exposing a small area of both metals, and the remaining surface covered using Lacomit stop-off varnish. This varnish is used in plating shops to prevent material adhesion, and in this case provides a barrier to the corrosive electrolyte. Masking was necessary to ensure only the area of interest corroded and activity was limited to the scan area.

Most potentiostat experiments were conducted on the blank samples, as the separated sections were easier to isolate and measure. Sections were masked using the Lacomit varnish previously mentioned, so different surface areas could be exposed. Minted sections of the new UK £1 were used as no blanks were available.

3.2.3 Experimental methods

Electrochemical investigations including open circuit potential (OCP), linear polarisation resistance (LPR), potentiodynamic polarisations (PDP) and zero resistance ammetry (ZRA) were completed using a potentiostat. Experiments were carried out in a 3.5% NaCl electrolyte, neutralised to pH 7 using 1 M and 0.1 M NaOH solutions. OCP measurements were also completed in an artificial sweat solution prepared as described in section 2.3. The samples were held at OCP for 1 hour to develop a stable surface oxide. ZRA evaluations were performed in 3.5% NaCl with varying cathode areas to monitor the effects on corrosion performance. Further descriptions of the potentiostat based techniques can be found in section 2.8.

Experimentation using the Scanning Vibrating Electrode Technique (SVET) required immersion in an aqueous electrolyte; in this case an artificial sweat solution was used. This was prepared as described in the BS EN 1811:2011 standard “Reference test method for release of nickel from all post assemblies which are inserted into pierced parts of the human body and articles intended to come into direct and prolonged contact with the skin” [24] and as described in section 2.3.

The SVET was prepared and calibrated as described in section 2.6. Due to the uneven surfaces of minted coins and the need for SVET to scan at a constant height above the surface, full height scans were completed on each sample. Each SVET experiment was run for a total of 24 hours, with a scan performed every 30 minutes.

Further investigations were completed using the Scanning Kelvin Probe (SKP), in a measured humidity of 89%. The SKP was set-up and calibrated as described in section 2.7. Due to the topography of the minted coins, height profiles were taken to ensure the probe scanned at a constant height above the surface. Volta scans were taken immediately after sample introduction to the chamber, after 1 hour and after 18 hours held at 89% RH.

3.3 Results and Discussion

3.3.1 Determination of corrosion potentials of bimetallic coin sections using potentiostat techniques

3.3.1.1 Open circuit potential

The E_{corr} of metals used for bimetallic coins has been studied in two different corrosive electrolytes, 3.5% NaCl and artificial sweat solution. Potentiostat based techniques were initially selected to predict what activity would occur on each section. This was achieved by performing open circuit potential experiments, linear polarisation resistance, potentiodynamic polarisations and zero resistance ammetry. From these, a galvanic series of the different metallic sections in 3.5% NaCl was produced, to ascertain which pairing had the lowest potential for galvanic cell formation. A 3.5 % NaCl electrolyte was used as high conductivity was required for consistent results from this technique. OCP was also completed in an artificial sweat solution (AFS) for comparison. Results from this were used to make predictions on which section of the pairing was more thermodynamically likely to form the anode and which the cathode.

OCP results are shown in Table 3.2. All the nickel-brass sections (UK £2 ring, E£1 pill, 500L ring and UK £1 ring) displayed a lower potential than their nickel and cupronickel counterparts. The cupronickel pill section of the UK £2 had the highest potential, followed by the nickel-plated UK £1 pill, E£1 ring and 500L pill sections. The cupronickel section had a lower potential than the nickel sections as the copper additions increased the thermodynamic likelihood of corrosion. To predict the susceptibility of each pairing to galvanic corrosion, absolute values of potential difference were calculated, where a larger difference can indicate a higher likelihood of galvanic corrosion. The largest potential difference was measured between the sections of the 500L coin, followed by the E£1, then the UK £1 and £2 with values of 59.9, 47.5, 25.0 and 11.3 mV respectively.

The results showed potential differences of 15.4 mV, 83.8 mV, 31.2 mV and 45.9 mV for the UK £2, E£1, 500L and UK £1 respectively, shown in Table 3.2. The potential difference (PD) measured for the UK £2 sections was similar, whilst for the E£1 and UK £1, the PD doubled. The sections of the 500L showed half the PD compared to the separated measurements. All experiments show there is a potential difference developed between all sections of the coins investigated, and therefore there is a risk of galvanic corrosion occurring in each case.

Table 3.2. Open Circuit values for the bimetallic sections investigated in 3.5% NaCl

Coin	**Ring (mV vs. SCE)**	**Pill (mV vs. SCE)**	**Difference (|mV|)**
UK £2	-228	-216	12
Egypt £1	-188	-236	48
500L	-238	-178	60
UK £1	-239	-214	25

A galvanic series for the metals and alloys under these experimental conditions is shown in Table 3.3 which ranks the sections of each coins from highest to lowest potential. The sample at the top is the most noble whilst the one at the bottom is most thermodynamically likely to corrode. The sections with similar compositions are close on this table, but not necessarily identical, due to slight variations in composition or oxide formations. The further apart metals are in a galvanic series, the higher the likelihood of corrosion when coupled. The order of metals in this table is the same as previous experiments conducted in seawater [27], [125].

The most noble sections were those made from nickel-plated steel, followed by the cupro-nickel in the middle of the table, and finally the nickel-brass sections with the lowest potentials. This means nickel-brass is the most anodically susceptible – most likely as it contains zinc, which is known to have a low potential and corrode readily in chloride containing solutions.

Table 3.3. Galvanic series of the bimetallic sections investigated in 3.5% NaCl and artificial sweat solution

Coin and section	**Potential (mV vs. SCE) [± 5 mV]**	
	3.5% NaCl	Artificial sweat solution
Sierra Leone 500L (pill – nickel-plate)	-178	-118
Egypt £1 (ring – nickel-plate)	-188	-122
UK £1 (pill – nickel-plate)	-214	-148
UK £2 (pill – cupro-nickel)	-216	-167
UK £2 (ring – nickel-brass)	-228	-197
Egypt £1 (pill – brass plate)	-236	-207
Sierra Leone 500L (ring – nickel-brass)	-238	-204
UK £1 (ring – nickel-brass)	-239	-201

OCP measurements were also carried out in AFS solution, to see if there was a significant difference in the potentials measured. The results are shown in Table 3.4. Overall, the values obtained in AFS solution are higher, lowering the thermodynamic likelihood of corrosion in this solution. The potential differences between the sections is larger in AFS solution in all cases, especially for the 500L and UK £1 where the PD doubles. Overall, this suggests whilst coins are less likely to corrode in AFS solution, the risk of galvanic cell development increases. The pairing with the largest PD was the 500L, closely followed by the £E1, then the UK £1 and finally the UK £2. The order of magnitude of PD’s was the same in both the 3.5% NaCl and AFS solutions, suggesting similar corrosion mechanisms overall.

Table 3.4. Open Circuit values for the bimetallic sections measured in artificial sweat solution

Coin	Ring (mV vs. SCE)	Pill (mV vs. SCE)	Difference (|mV|)
UK £2	-197	-167	30
Egypt £1	-122	-207	85
500L	-204	-118	86
UK £1	-201	-148	53

3.3.1.2 Zero Resistance Ammetry (ZRA)

Following on from OCP, Zero Resistance Ammetry (ZRA) was carried out. The section with the lowest OCP from each pair was predicted to be the anode and used as the working electrode; the section with the higher OCP was predicted to be the cathode and connected as the reference electrode. Three different cathode areas were examined, whilst the anode area was kept constant. A potentiostatic experiment was carried out, maintaining a zero potential for the duration of the experiment. Each pairing was held for 1 hour in a 3.5% NaCl electrolyte. The results were plotted as current density versus time, where a high galvanic current indicated a higher corrosion rate.

The ZRA results are shown in Figure 3.1 - Figure 3.4 for the UK £2, £E1, 500L and UK £1 coins respectively. In all cases, the size of the anode (brass or nickel-brass section) was used to normalise the values for current density.

Figure 3.1 shows the ZRA results on the UK £2 sections. As an increasing cathode surface area was exposed, the measured current significantly increased. Averages of current density for the final 30 minutes were measured at 1.01 x10^{-6}, 2.17 x10^{-6} and 3.50 x10^{-6} amps·cm^{-2}, as the cathodic to anodic surface area increased from 1:2 to 1:1 to 3:2.

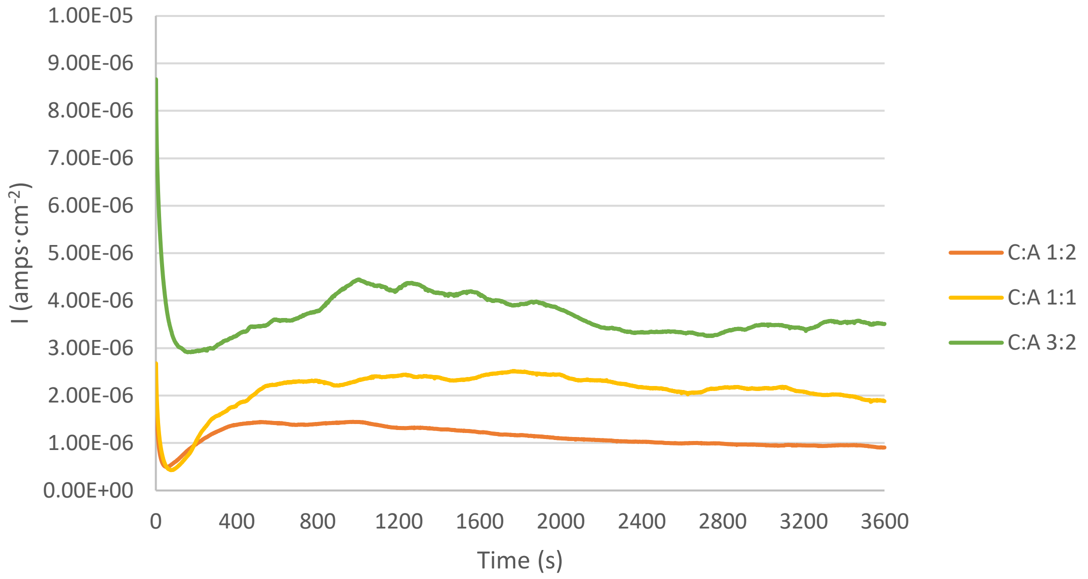

Figure 3.1. ZRA results - UK £2, 3.5% NaCl

Figure 3.2 shows the results from the ZRA investigations on the Egyptian £1-coin sections. As the cathodic surface area was increased, the average current density increased, although not to the extent of the UK £2. Averages of the measured current for the final 30 minutes were 3.39 x10^{-7}, 5.59 x10^{-7} and 8.64 x10^{-7} amps·cm^{-2} as the cathodic to anodic surface area was increased from 1:2 to 1:1 to 3:2.

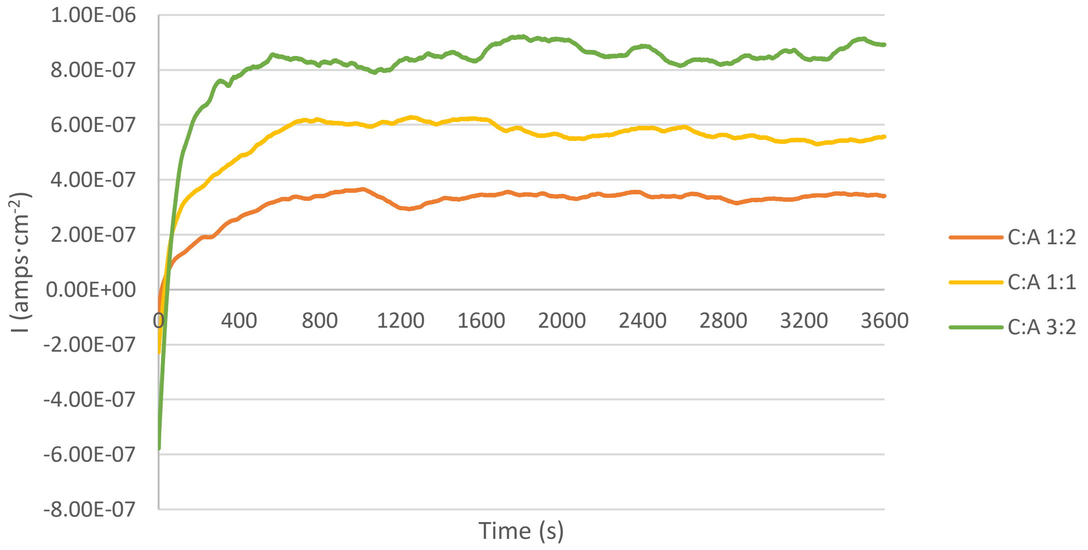

Figure 3.2. ZRA results – Egypt £1, 3.5% NaCl

Figure 3.3 shows the results from the Sierra Leone 500L coin sections. As the cathode surface area increased, an increase was measured in the average current density, to a greater extent than the £E1 sections, but significantly less than the UK £2 sections. Current density averages for the final 30 minutes were 2.75 x10^{-7}, 6.67 x10^{-7} and 9.52 x10^{-7} amps·cm^{-2} as the cathodic to anodic surface area was increased from 1:2 to 1:1 to 3:2.

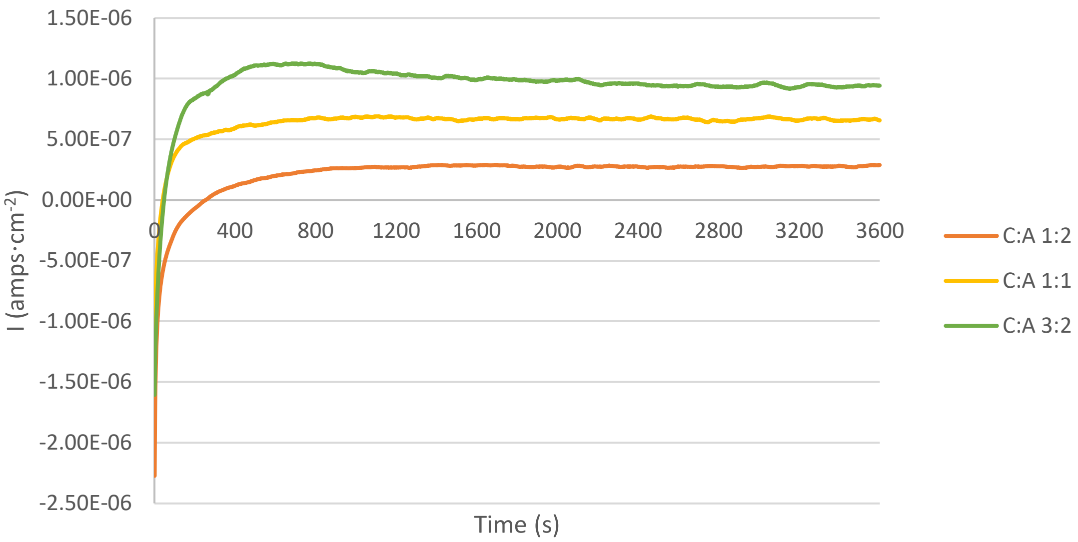

Figure 3.3. ZRA results – Sierra Leone 500L, 3.5% NaCl

Figure 3.4 shows the results of ZRA investigations on the UK £1-coin sections. As the cathode surface area increased, the resulting current density was increased to a greater extent than the E£1 and 500L sections, but not as much as the UK £2. Averages of the measured current for the final 30 minutes were 3.66 x10^{-7}, 7.31 x10^{-7} and 1.39 x10^{-6} amps·cm^{-2} as the cathodic to anodic surface area was increased from 1:2 to 1:1 to 3:2.

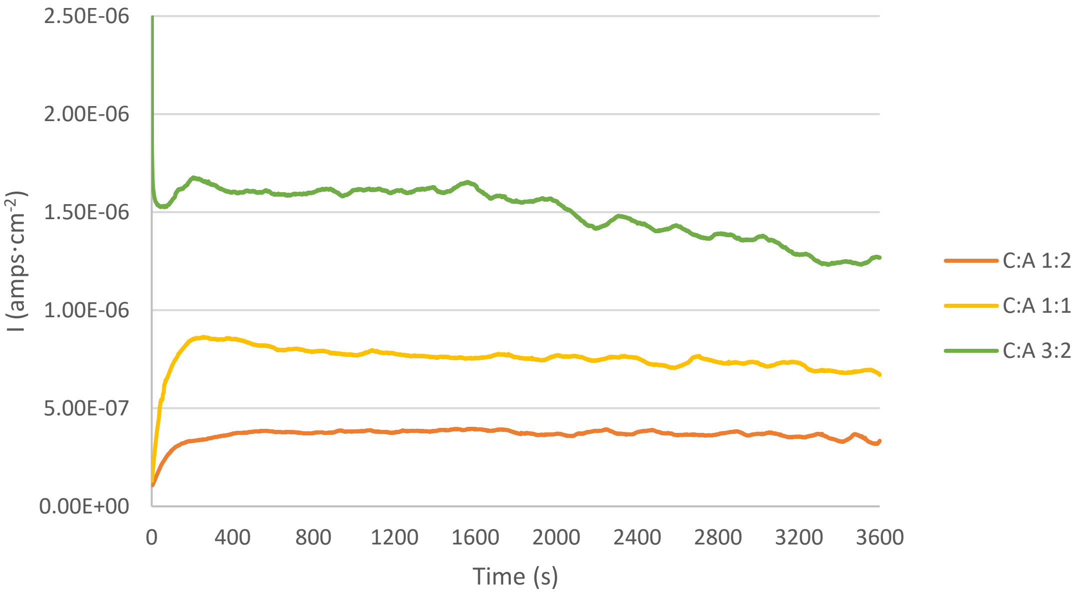

Figure 3.4. ZRA results - UK £1, 3.5% NaCl

Figure 3.5 shows a comparison of the ZRA results for each pairing assessed. This shows results obtained from the £E1, 500L and UK £1 were similar, whilst the current densities for the UK £2 were significantly higher. The lowest current density measured between the UK £2 sections with the smallest exposed anode was higher than most of the results for the other pairings, even with a large exposed cathode. The largest cathode area for the UK £2 resulted in a current density 2.5 times larger than any other current density measured.

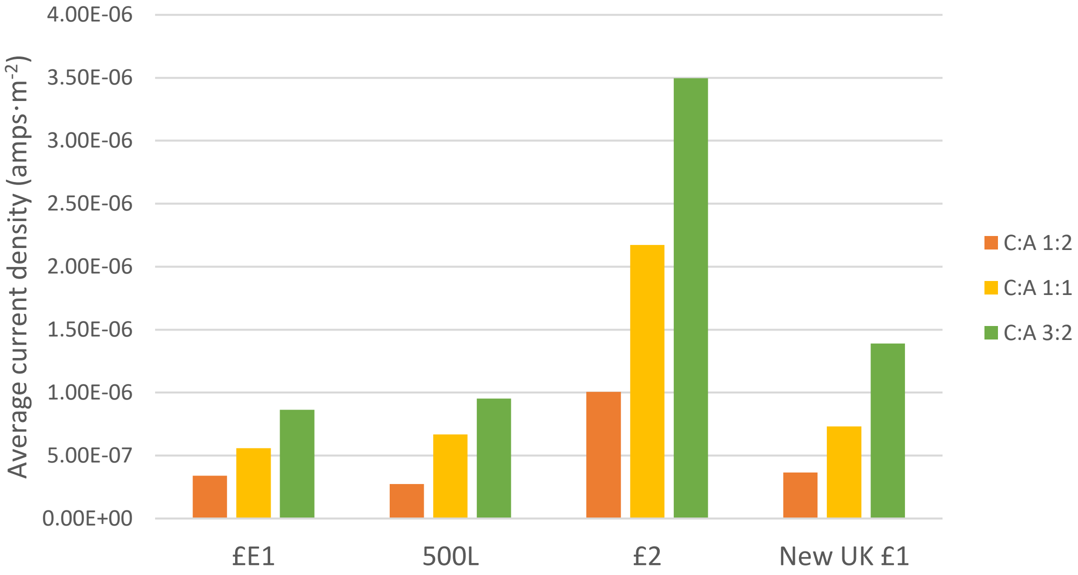

Figure 3.5. ZRA results - comparison

Overall the ZRA investigations showed current density intensified with increasing cathode surface area in all cases. The results for the £E1 and 500L were similar in the increases observed and the absolute values, the UK £1 showed slightly higher current densities whilst the UK £2 showed significantly higher current densities. This indicates the UK £2 is most susceptible to galvanic corrosion, even if the ratio of exposed cathode to anode is small.

3.3.2 Evaluation of localised bimetallic corrosion using SVET

Potentiostat based techniques only provide a bulk measurement and give an overview of events on the surface, so SVET was chosen as a localised technique to identify the locations of anodic and cathodic activity. Experiments were carried out in artificial sweat solution, prepared as described in section 2.3. This electrolyte was selected as it provided good conductivity and minimised significant background noise on the SVET scan.

SVET scans were performed on uncirculated minted coins. Experiments were completed on a small section of each coin where the two metals were in contact (coupled), and another on an area where only the more active metal was exposed (uncoupled).

Figure 3.6, Figure 3.9, Figure 3.12 and Figure 3.15 show coloured height profiles of the coins and scans taken at 0, 2, 4, 6, 8, 10, 12 and 24 hours, for the UK £2, £E1, 500L and UK £1 coins respectively. Colour scales are included in each figure; negative values representing cathodic activity are blue and positive values depicting anodic activity are red. Any areas in white indicate a zero reading.

Figure 3.7, Figure 3.10, Figure 3.14 and Figure 3.17 show how total anodic current density per scan varies between experiments completed under coupled and uncoupled conditions.

3.3.2.1 United Kingdom £2

SVET scans performed over a section of the two metals are shown in Figure 3.6. These scans show clear separation of anodic and cathodic activity between the sections. The majority of anodic activity was focused on the nickel-brass ring, whilst most of the cathodic activity took place on the cupro-nickel pill. This separation of electrochemical events persisted for the duration of the experiment.

At hour 0, there was a mix of anodic and cathodic activity on the nickel-brass section, with anodic activity mainly developing on the raised profile areas caused by minting; these can be matched to areas on the height scan. Nearly all cathodic activity was focussed on the cupronickel section. At hour 2, the nickel-brass was almost completely covered in anodic activity, whilst the cupronickel was the main location for cathodic activity. This separation of anodic and cathodic activity persisted for the duration of the 24-hour experiment. From the hour 2 scan onwards, anodic activity on the surface detail of the nickel-brass increases in intensity, also where the two metals are joined. It is possible the deformation caused in the minting process augmented the grain structure increasing its susceptibility to corrosion. The range of corrosion currents observed was -0.1 to 0.25 amps·m^{-2}.

Scans were also completed on the section found as the anode from OCP and SVET, in this case the nickel-brass ring and was scanned without electrical coupling to the cupro-nickel pill section, which are shown in

Figure 3.7. This provided a comparison of corrosion intensity between the metal in the coupled and uncoupled state, and helped develop a better understanding of how coupling affects this alloy pairing.

Figure 3.7 shows changes in the total anodic current density per hour for the coupled and uncoupled experiments. The green line shows the total anodic current per hour for the uncoupled nickel-brass section, and the blue line shows the same for the coupled alloy. This shows an increase in anodic activity of around 10 times on the coupled section compared to the uncoupled section. Pairing these two dissimilar metals results in a significantly increased corrosion rate on the nickel-brass section compared to investigations on the individual section.

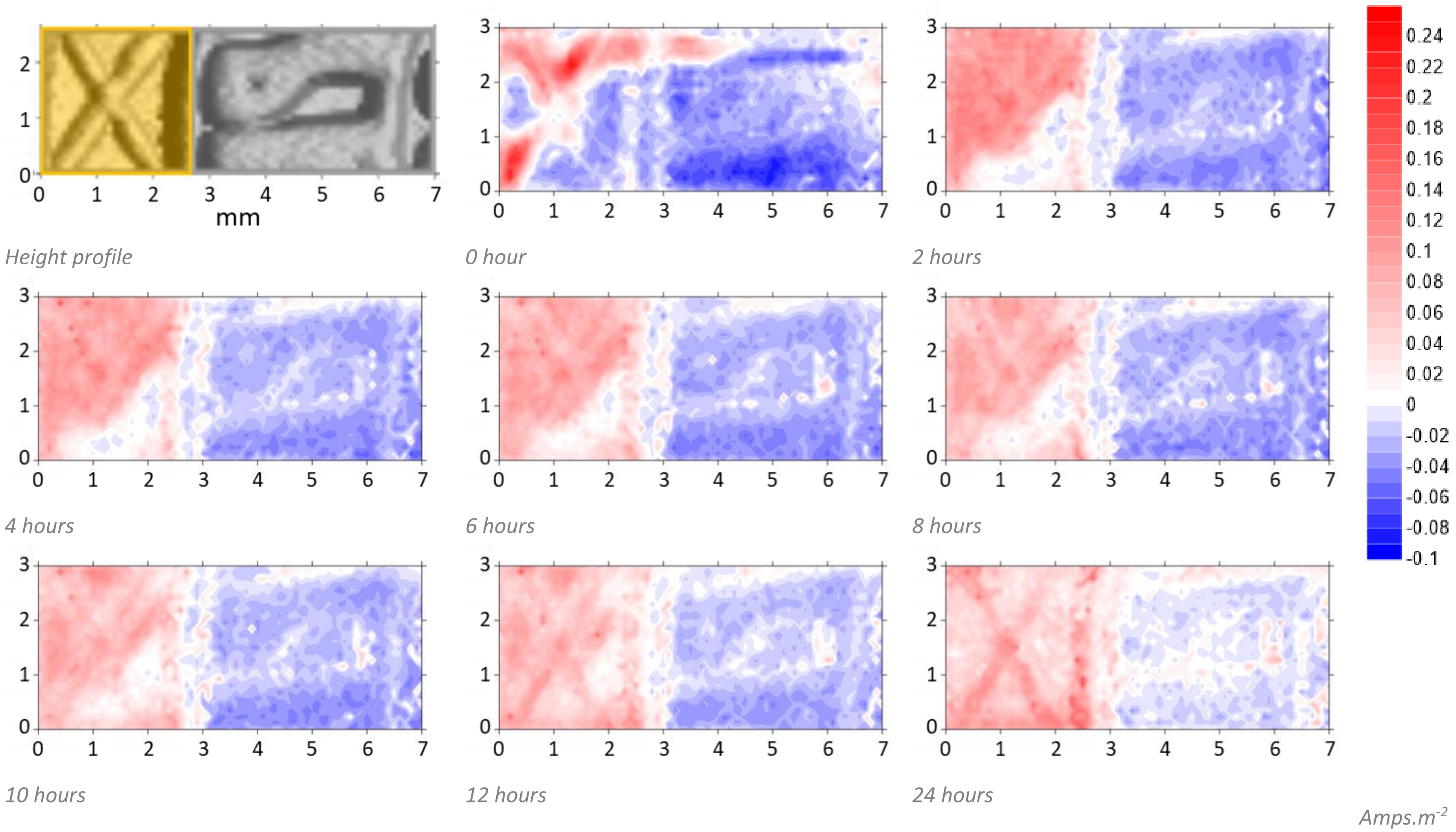

Height profile

0 hour

2 hours

4 hours

6 hours

8 hours

10 hours

12 hours

24 hours

Figure 3.6. SVET scans from hours 0, 2, 4, 6, 8, 10, 12 and 24 on the coupled UK £2 sections in artificial sweat solution

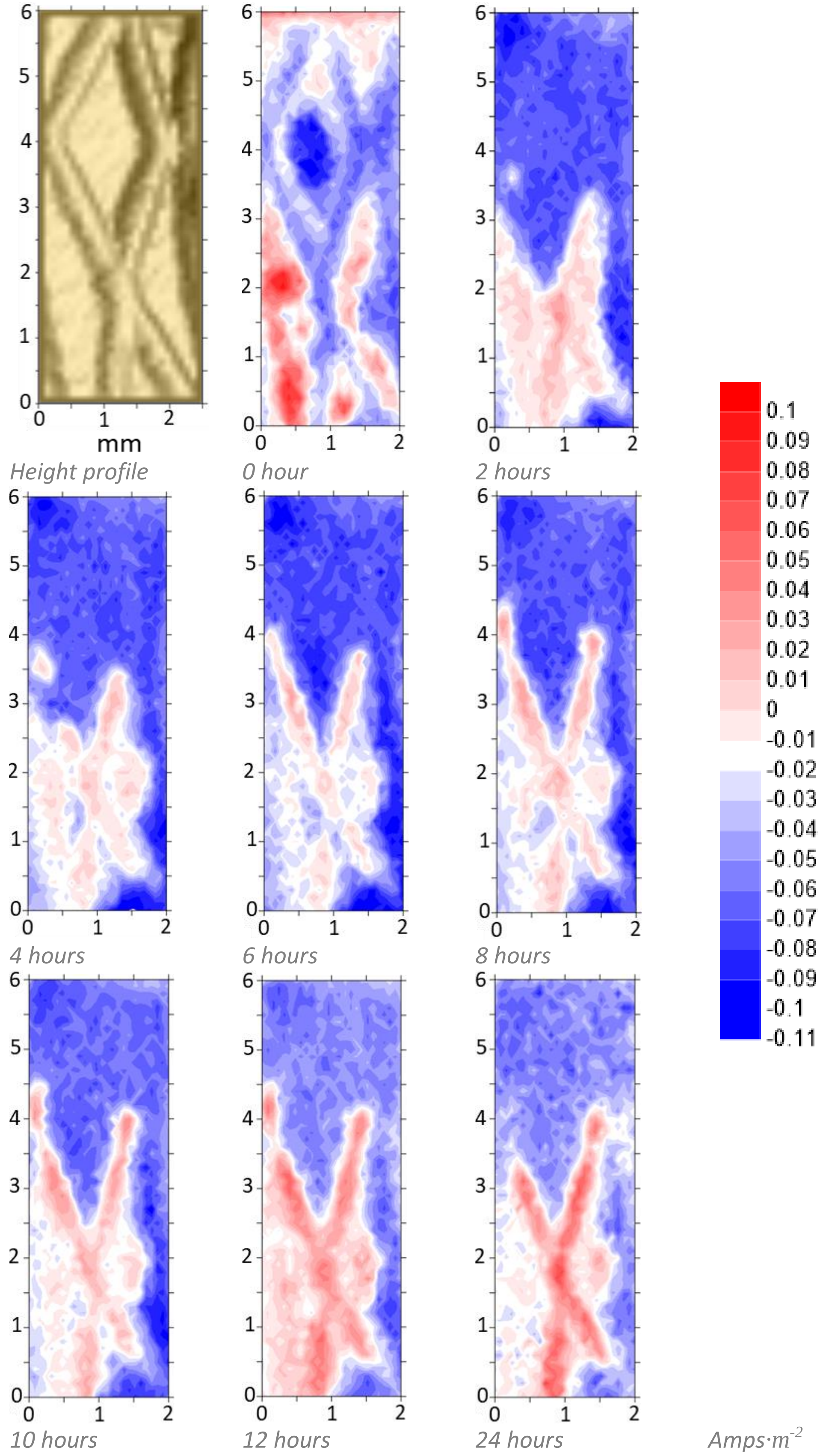

Height profile

0 hour

2 hours

4 hours

6 hours

8 hours

10 hours

12 hours

24 hours

Amps·m^{-2}

Figure 3.7. SVET scans from hours 0, 2, 4, 6, 8, 10, 12 and 24 on the uncoupled UK £2 Ni-brass ring in AFS solution

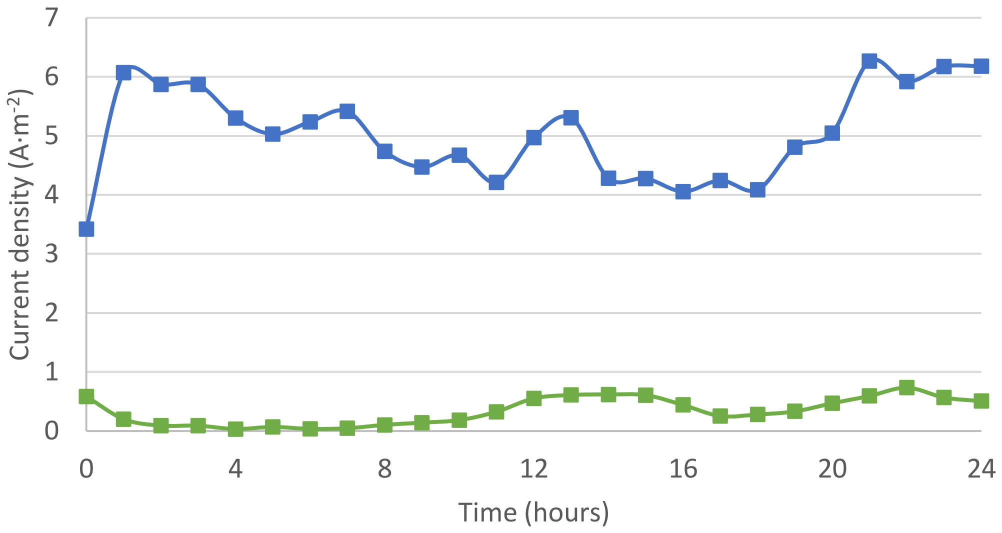

Figure 3.8. SVET total anodic current density results, coupled (blue) and uncoupled (green) UK £2

3.3.2.2 Egyptian £1

SVET maps from the scans on the joined sections are shown in Figure 3.9. The maps show a clear difference in corrosion activity on the two sections. The strongest anodic and cathodic activity was seen on the duplex brass plated pill whilst only small amounts of cathodic activity took place on the nickel-plated ring. This separation of activity persisted for the duration of the experiment.

At hour 0, the anodic and cathodic activity was very intense, both focussed on the brass plated pill. The area affected by each was similar, but the intensity of the anode was around 5 times that of the cathode. At this stage, low level cathodic activity covered much of the nickel-plated ring, although the intensity was significantly less than on the brass section. By hour 2, the area and intensity of anodic activity on the brass plated section decreased slightly, so there was a small increase in the cathode surface area. The area where cathodic activity was previously strongest weakened slightly, and stronger cathodic activity developed on a passivated anode. This is likely because anodic activity de-passivated the surface making cathodic reduction more favourable.

Maps at hours 4, 6, 8, 10 and 12 continue to show decreases in the anode and small increases in the size and intensity of the cathode on the brass section. There is very little change in activity on the nickel-plated section. Over these scans, a small anode develops at the junction between the two sections, which persists for the duration of the experiment. This is likely to be crevice corrosion, initiated due to the small gap where the sections are joined. The intensity of this did not increase significantly, so either the crevice was too narrow, or activity occurred at greater depth, where potential gradients in solution terminated below the plane of scan.

The final scan shows a reduction in the intensity of all activity. On the brass-plated pill, the anode area increased but intensity had decreased, and intensity of the cathode also decreased. Almost no activity happened on the nickel-plated section at this point. The anodic activity occurring between the sections was still active and had spread along the joint. The range of corrosion current mapped over the 24-hour experimental period was between -0.05 and 0.25 amps$\cdot$m^{-2}.

The distinction in activity between the two sections was very clear. The intense anodic and cathodic activity happened on the brass-plated pill, whilst on the nickel-plated ring only a very low level of cathodic activity persisted. It is possible the activity on the nickel-plated section showed low intensity because the SVET cannot monitor generalised corrosion, which may have been happening here. The SVET struggles with this because the lines of isopotential from the surface terminate below the scanning height of the tip (<100 µm), and therefore are effectively invisible to this technique, as explained in section 2.6.2. It is possible there was more activity on the nickel section than can be resolved by this technique.

As well as examining a section covering both metals of the E£1 coin, scans were also completed on the section where most anodic activity happens, which are shown in Figure 3.10. Figure 3.11 shows how the total anodic current density for the coupled (blue) and uncoupled (green) sections compare. When coupled, an initial high current density was observed, which decreased over the first 6 hours before levelling out. The uncoupled section also showed high initial current density, which decreased and levelled off after 10 hours. Overall, the current density values of the coupled sample were around double that of the uncoupled sample. This increase suggests the nickel-plated section may undergo more activity than seen from the SVET scans and acts to increase the corrosion rate of the brass plated alloy.

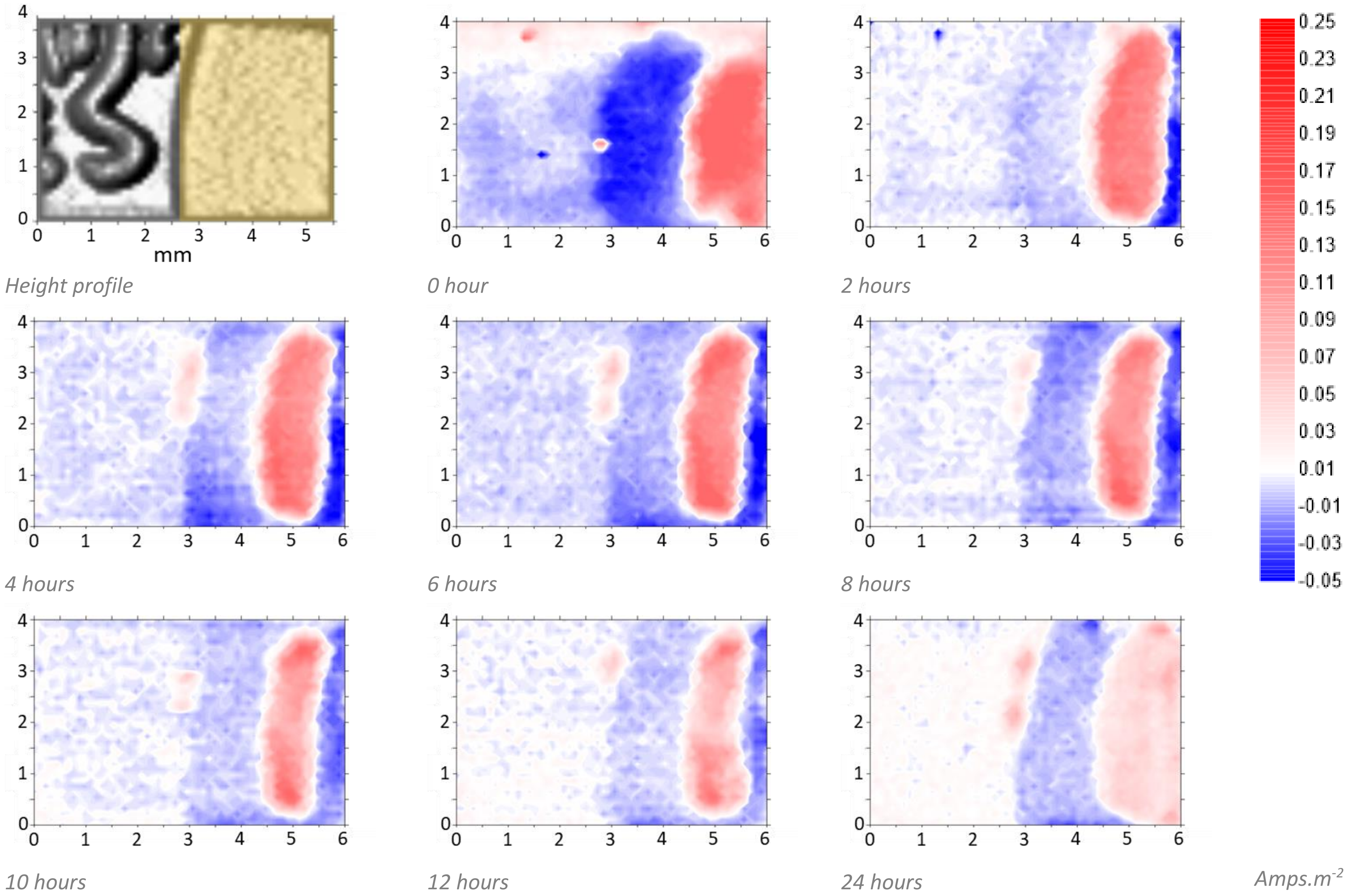

Height profile

0 hour

2 hours

4 hours

6 hours

8 hours

10 hours

12 hours

24 hours

Figure 3.9. SVET scans from hours 0, 2, 4, 6, 8, 10, 12 and 24 on Egypt £1 in artificial sweat solution

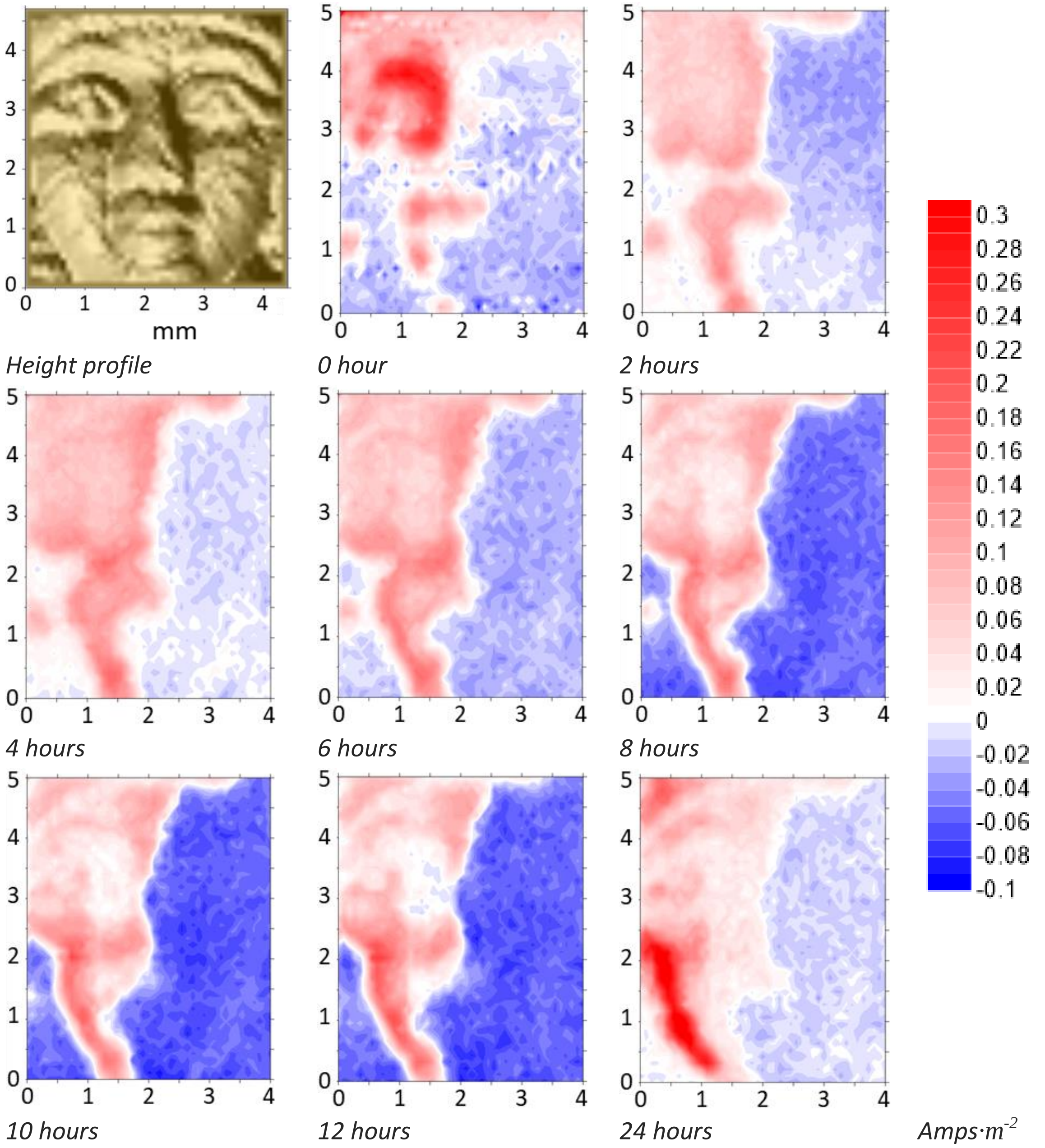

Figure 3.10. SVET scans from hours 0, 2, 4, 6, 8, 10, 12 and 24 on the uncoupled Egypt £1 brass plated pill in AFS solution

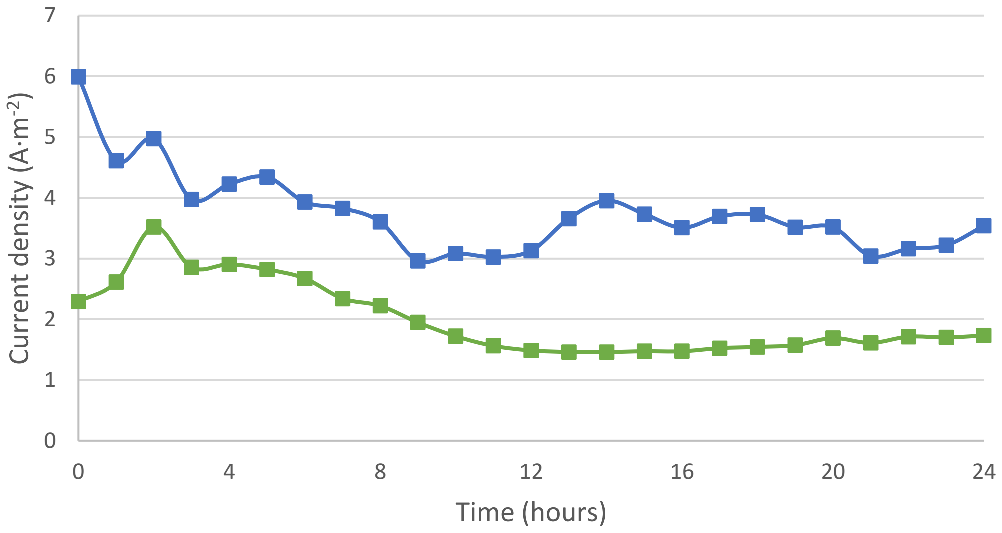

Figure 3.11. SVET total anodic current density results, coupled (blue) and uncoupled (green) Egypt £1

3.3.2.3 Sierra Leonian 500 Leones

SVET scans performed on the joined sections are shown in Figure 3.12. Scans on this coin showed a difference in the activity on the nickel-brass ring and the electroplated nickel pill. The majority of both the anodic and cathodic activity was focused on the nickel-brass ring section, whilst a low level of cathodic activity was measured on the nickel-plated pill section. This occurred for the duration of the experiment.

On the initial scan, all the anodic activity developed on the nickel-brass section, especially on the raised areas of the minting design. The majority of strong cathodic activity also occurred on this section. There was some cathodic activity on the nickel-plated section, but the colour was less intense suggesting a lower level of activity. By hour 2, the area covered by anodic activity increased, and remained solely on the nickel-brass section. Through scans at hours 4, 6, 8, 10 and 12 the amount of anodic activity on the ring section remained consistent and was very clearly focussed on the raised parts of the minted design – in this case, on the letters ‘O’ and ‘F’. Over this time, cathodic activity remained predominantly on the nickel-brass section, with very low-level activity spread over the nickel-plated pill. By hour 24, anodic activity had reduced, and cathodic activity increased slightly. The range of corrosion currents mapped was between -0.1 and 0.12 amps·m^{-2}.

Similar to the scans on the £E1, the distinction in activity between the sections is clear. The nickel-plated pill showed low level cathodic activity over the surface, whilst the nickel-brass ring showed high intensity anodic and cathodic activity. Much of the anodic activity was focused on the raised profile areas of the minted design, suggesting the deformation caused by minting led to reduced corrosion resistance. There may be more corrosion on the nickel-plated surface than seen here, due to the SVET's resolution limitations.

Further scans were completed on the section predicted to be the anode from OCP and SVET, which are shown in Figure 3.13. Figure 3.14 shows how the total anodic current density for the coupled (blue) and uncoupled (green) sections compare in terms of total anodic current density in $A \cdot m^{-2}$. The results from both investigations showed an overall decrease in current density per hour over the 24-hour experiment. Between hours 0 to 15, a much higher current density was recorded from the coupled sections, however, after hour 15 there was very little difference in this value relative to the uncoupled sections. This indicated that for this pairing, coupling influenced the initial corrosion rate, but did not lead to a long-term increase. This suggests the two sections reached equilibrium, where a stable, passive oxide layer formed on one or both sections.

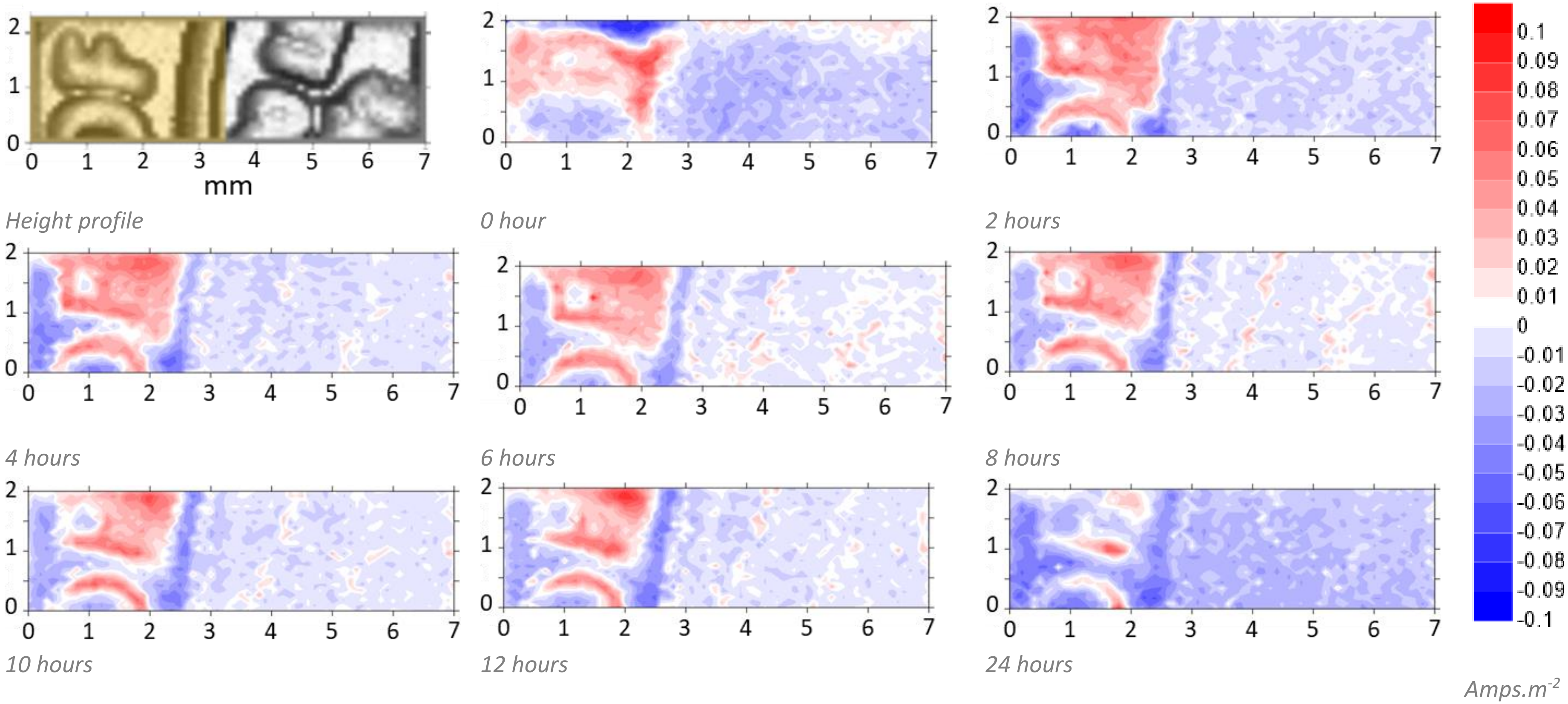

Figure 3.12. SVET scans from hours 0, 2, 4, 6, 8, 10, 12 and 24 on Sierra Leone 500L in artificial sweat solution

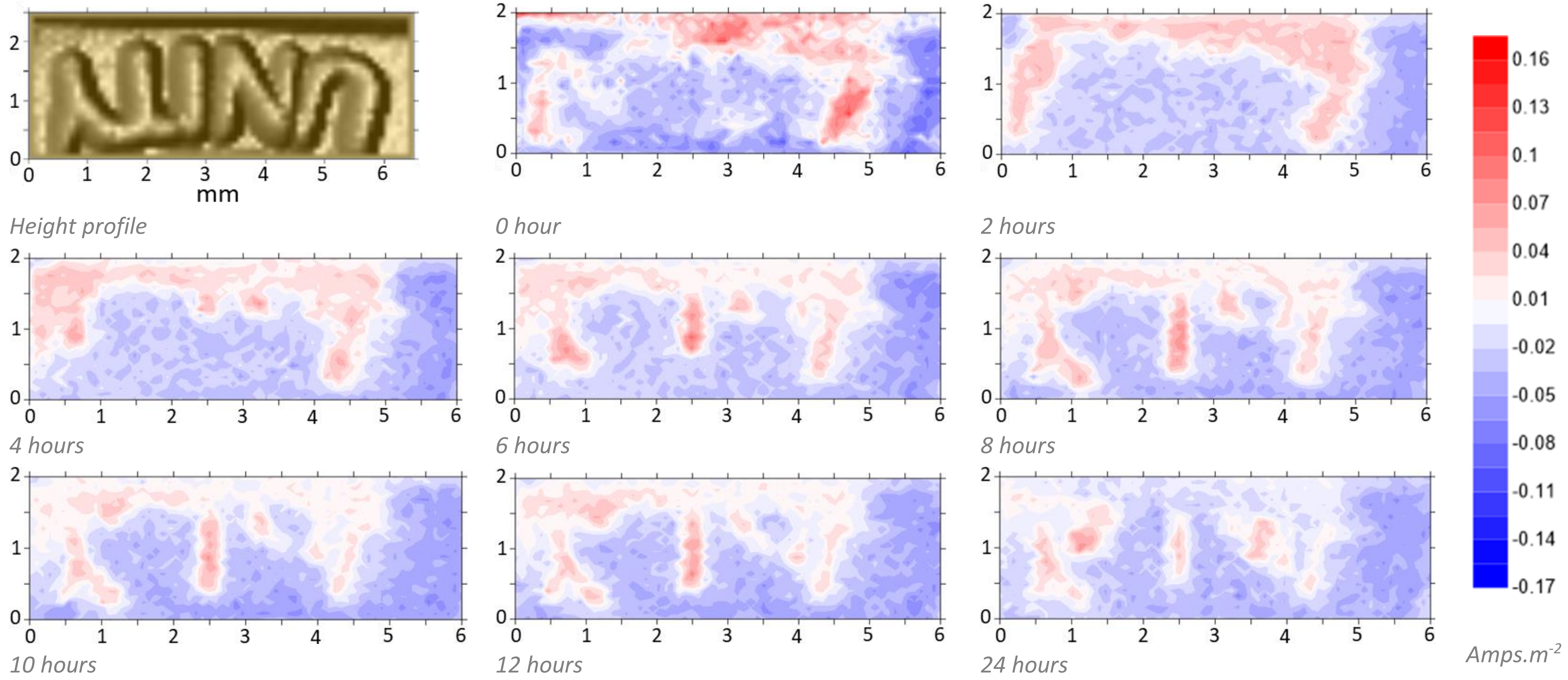
Height profile

0 hour

2 hours

4 hours

6 hours

8 hours

10 hours

12 hours

24 hours

Figure 3.13. SVET scans from hours 0, 2, 4, 6, 8, 10, 12 and 24 on the uncoupled Sierra Leone 500L Ni-brass ring in AFS solution

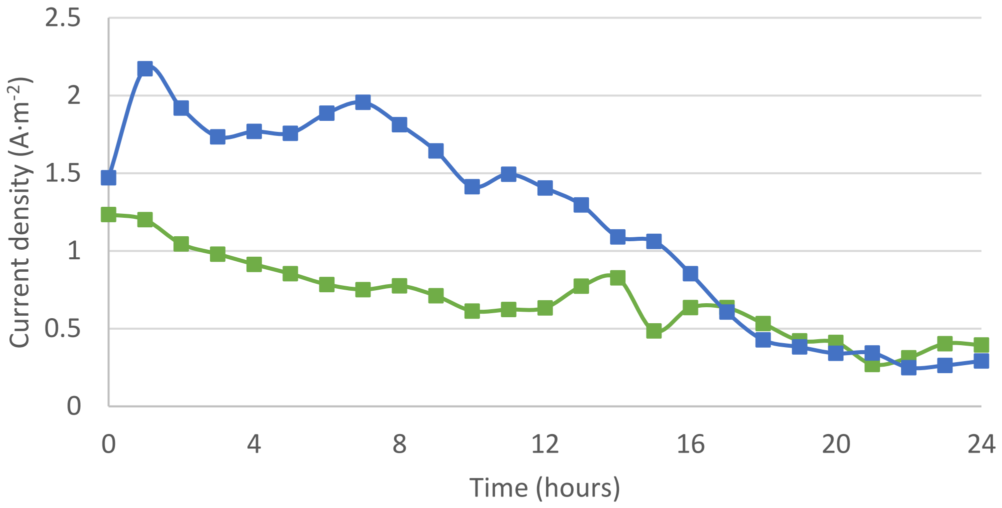

Figure 3.14. SVET total anodic current density results, coupled (blue) and uncoupled (green) Sierra Leone 500L

3.3.2.4 United Kingdom £1

SVET scans performed on the joined sections of the UK £1 are shown in Figure 3.15. The maps show a clear difference in activity and intensity between the sections. All anodic activity, and the most intense cathodic activity happened on the nickel-brass ring, whilst a very low level of cathodic activity was solely present on the nickel-plated pill section for the duration of the experiment.

At hour 0, there was a high intensity of both anodic and cathodic activity on the nickel-brass section, with most of the anodic activity on the raised areas of the minted design confirmed by comparison to the height profile. This was also seen on the UK £2 and 500L coin scans. On this initial scan, little activity was seen on the nickel-plated section, potentially due to the limitations of SVET for monitoring generalised corrosion. By hour 2, the intensity of the anodic and cathodic activity on the nickel-brass section decreased, and the intensity of the cathodic activity on the nickel-plated section increased very slightly. From hour 4 onwards, the size and intensity of the anodic and cathodic behaviour was consistent until hour 24, where there was an increase in intensity for one of the anodes on the nickel-brass ring. The range of corrosion current density was -0.06 to 0.2 amps·m^{-2}.

Further scans were completed on the section shown as the site for anodic activity from previous OCP trials and SVET scans, shown in Figure 3.16. Figure 3.17 shows the total anodic current density at each scan for the coupled (blue) and uncoupled (green) sections, in A·m^{-2}. The results showed the current density was very consistent for both sections over the duration of the experiment. There was minimal variation between the intensity of activity seen on the sections, indicating the coupling had little effect on the corrosion of this coin. This coin showed the most similar levels of activity between the coupled and uncoupled sections. Overall, the intensity of the activity seen was slightly more than for the 500L, but less than the E£1 and significantly less than the UK £2.

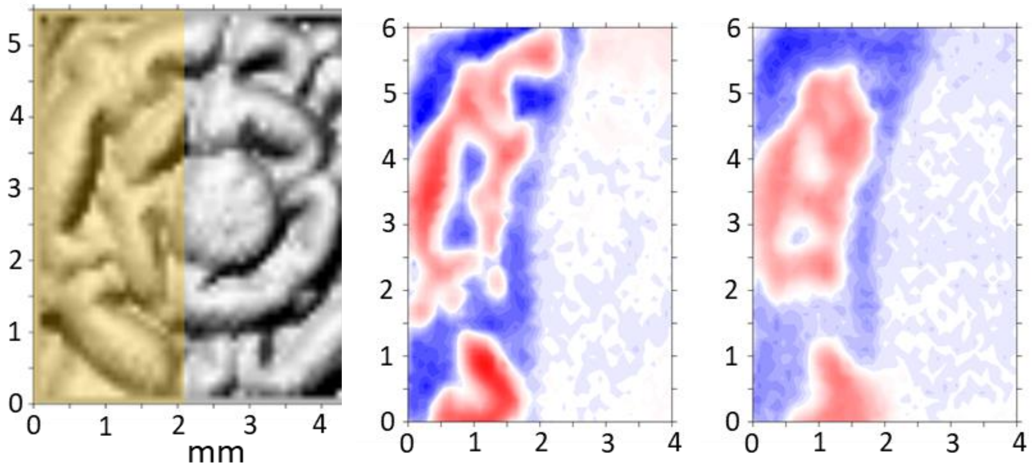

Height profile *0 hour* *2 hours*

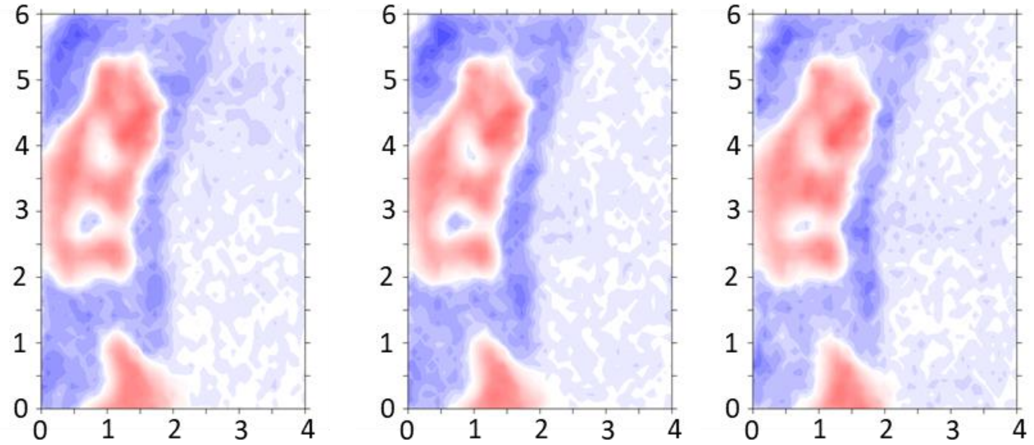

4 hours *6 hours* *8 hours*

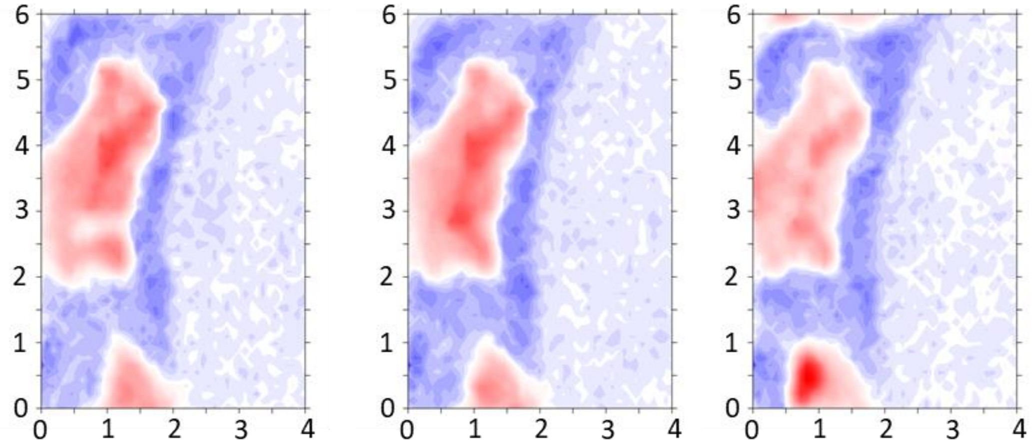

10 hours *12 hours* *24 hours*

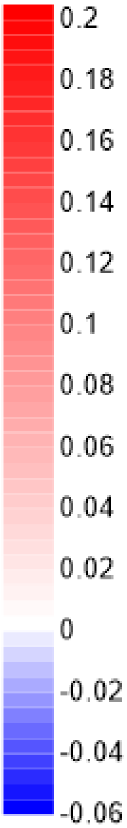

Amps.m^{-2}

Figure 3.15. SVET scans from hours 0, 2, 4, 6, 8, 10, 12 and 24 on UK £1 in artificial sweat solution

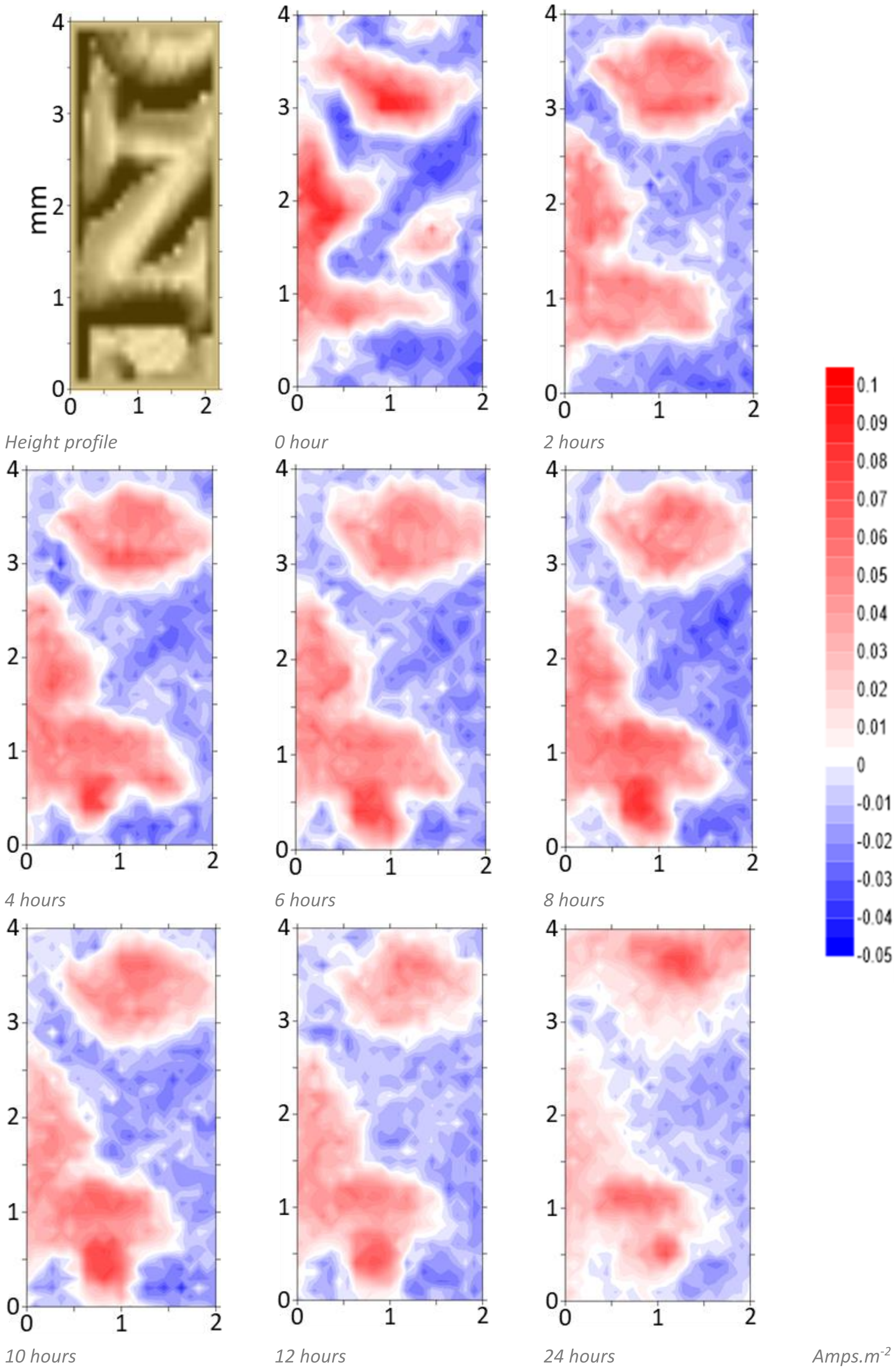

Height profile   0 hour   2 hours

4 hours   6 hours   8 hours

10 hours   12 hours   24 hours

Figure 3.16. SVET scans from hours 0, 2, 4, 6, 8, 10, 12 and 24 on the uncoupled UK £1 Ni-brass ring in AFS solution

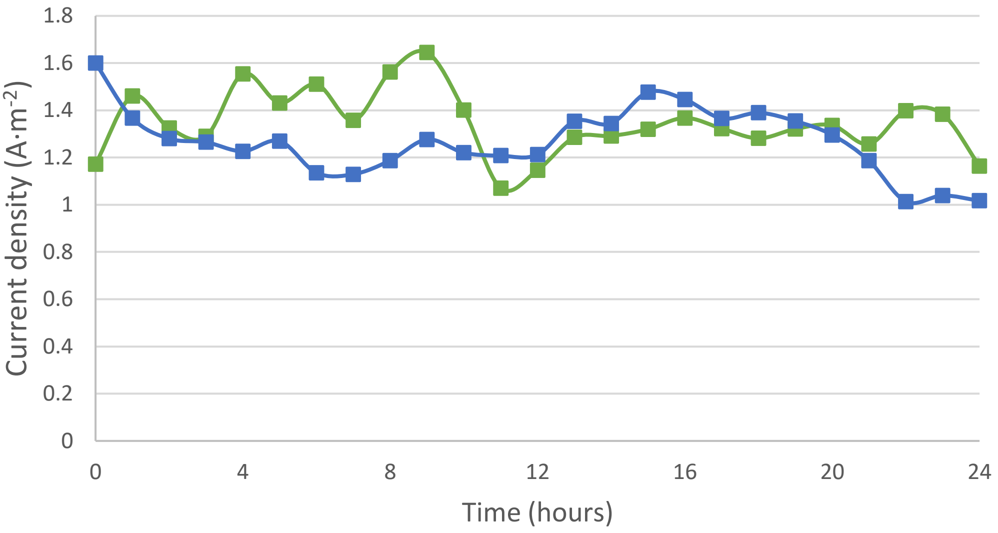

Figure 3.17. SVET total anodic current density results, coupled (blue) and uncoupled (green) UK £1

3.3.2.5 SVET conclusions

The SVET profiles have been used to spatially resolve and identify locations of anodic and cathodic activity initiation and progression. The four bimetallic pairings assessed demonstrated two different ways the sections of bimetallic coins interact with each other.

The UK £2 coin displayed typical behaviour for a galvanic couple – the nickel-brass ring formed the anode, whilst the cupro-nickel pill formed the cathode. There was clear separation of corrosion activity between these sections. The results showed that when the sections of this coin are joined, the total anodic current density significantly increased due to galvanic coupling.

The E£1 did not display the same bimetallic corrosion characteristics seen in the UK £2, where most of the anodic and cathodic activity happened on the brass plated pill. Little activity was seen on the nickel-plated section, aside from some low intensity cathodes. It is possible the level of general corrosion on this section has been underestimated, due to the limited resolution of the SVET. The Sierra Leone 500L displayed similar behaviour to the E£1, whereby all the strong anodic and cathodic activity was confined to the nickel-brass ring. This could be because the potential difference between the sections was not great enough to increase the current density, so the nickel-brass corroded as if it was isolated. Some cathodic activity took place on the nickel-plated section, however, was of lower intensity than on the nickel-brass section. As strong anodic and cathodic activity occurred on the nickel-brass section, it is likely the nickel-plated section had little effect on the corrosion. The 500L sample showed a small difference in total anodic current density when coupled and uncoupled, suggesting there is little interaction in this case. The UK £1 again showed similar behaviour to the E£1 and 500L. Nearly all the cathodic and anodic activity was seen on the nickel-brass section, with very minimal activity on the nickel-plated section. The coupled and uncoupled section scans showed the smallest difference in total anodic current density, again suggesting very little interaction happens between these sections.

Table 3.5. Current density range for SVET scans

Coin	Min. J (A·m^{-2})	Max. J (A·m^{-2})
UK £2	-0.10	0.25
E£1	-0.05	0.25
500L	-0.10	0.12
UK £1	-0.06	0.20

Table 3.5 above shows the minimum and maximum current density values for SVET maps. These values can be compared for the intensity of corrosion that took place. This shows the crevice corrosion experienced by the E£1 was much more intense than the corrosion on the other samples. However, the current density over the remainder of the surface was 0.1 to -0.1 A·m^{-2}, similar to the level experienced by the 500L. The UK £1 showed a higher level of anodic intensity than the 500L sample, but less than the maximum seen from the E£1 and UK £2. In terms of galvanic corrosion, the UK £2 experienced the highest intensity of positive and negative current densities over a large area of the sample surface, and overall suffered the highest total amount of corrosion activity.

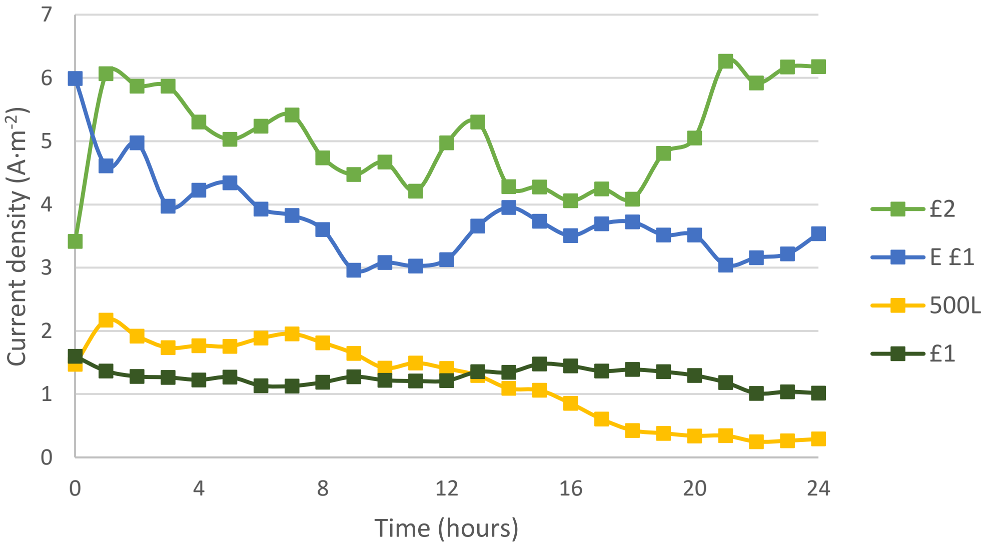

Figure 3.18. Current densities per hour for the coupled section scans on each coin

Figure 3.18 above compares the total anodic current densities measured at each hour of the SVET scan completed on each coin. This clearly demonstrates the fastest corrosion rate is seen on the sections of the UK £2, followed by the E£1. Overall, the corrosion rates appear similar for the 500L and UK £1. Total charge passed for each experiment has also been calculated and is shown in Figure

3.19. This shows the same trend and indicates that overall the 500L coin underwent slightly less corrosion than the UK £1, although this difference could easily exist within the range of experimental error.

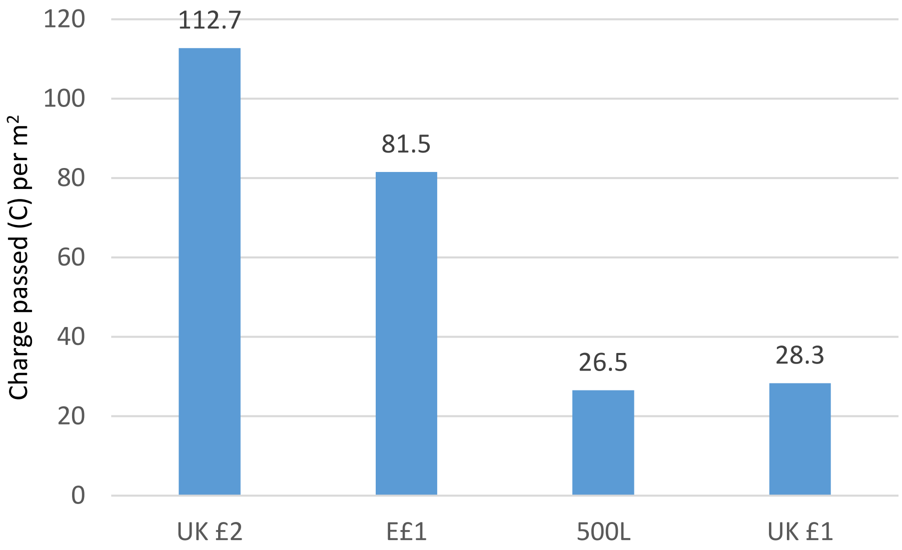

Figure 3.19. Total charge passed for the coupled section scans on each coin

3.3.3 Evaluation of bimetallic corrosion using SKP

Experimentation with both potentiostat techniques and SVET observed the corrosion of coins under immersion conditions, which they are unlikely to experience regularly in circulation. The SKP is a localised technique which maps corrosion events and can identify areas of different Volta potential difference under atmospheric conditions. The humidity in the environment chamber is set using salt solutions; 5% NaCl was used to obtain a 89% RH level measured using a humidity sensor. Under these conditions a thin layer of electrolyte only a few molecules thick forms on the samples surface, which is more representative of circulation conditions. The SKP was calibrated and the sample height scanned as described in sections 2.7.3 and 2.7.5 respectively. An area 5 mm x 5 mm was scanned over a section of each coin where both metals were exposed.

The samples used for SKP were uncirculated minted coins, mounted on M10 nuts for use with the stage available. Figure 3.20 shows images of the coins in column i, the height profiles mapped by the SKP in column ii with false colour for easy identification of the metals. Columns iii, iv and v show the spatially resolved scans completed at 0, 1 and 18 hours, for the UK £2, E£1, 500L and UK £1 coin respectively, with the corresponding colour scales in column vi showing the intensity of the maps.

Figure 3.21a-c to Figure 3.24a-c show line scans taken from each scan and the potential differences measured between the sections of the coins. These are shown as values in Figure 3.21d to Figure 3.24d.

The results from the UK £2, £E1, 500L and UK £1 are very similar, as the scans show the same progression and distribution of potentials across the two sections. The spatially resolved maps from these experiments have been plotted and are shown in Figure 3.20. The maps show there is a significant difference in Volta potential measured between the sections under atmospheric conditions. The SKP data shows lower potentials were observed on the nickel-based sections, whilst higher potentials were measured on the brass-based sections. This separation of activity was found to persist for the 18-hour duration of the experiments.

The first scans were completed immediately on closing the environment chamber, meaning the humidity was around 40%, the same as the laboratory. The initial scans for the UK £2, E£1, 500L and UK £1 all show a clear difference in the intensity of activity on the sections, indicating a large separation in Volta potential difference. The E£1 and 500L coins displayed a marked decrease in potential on the raised, minted areas compared to the rest of the surface. The second scans performed after 1 hour in 89% RH showed similar potential distribution to the initial scan, with a small increase in the potential across both sections. The final scan completed after 18 hours showed a significant increase in the potential on all the nickel-based sections, and a small increase on the brass-based sections. All scans indicated under atmospheric conditions the brass-based section was more noble, whilst the nickel-based section was more active. As the nickel-based sections showed the lowest potential, they are more likely to form the anode under these conditions. This disagrees with the results from the potentiostat techniques and SVET scans completed previously, which suggested the brass-based sections had the lower potentials and were more likely to form the anode.

A horizontal line from the middle of each scan was plotted separately, shown in Figure 3.21 to Figure 3.24 to quantify the potential differences measured between the sections. The potential differences found for the UK £2 were 58 mV, 67 mV and 59 mV, for the £E1 154 mV, 121 mV and 101 mV, for the 500L 128 mV, 100 mV and 55 mV and for the £1 108 mV, 99 mV and 75 mV for the initial scan, after 1 hour at 89% RH and after 18 hours at 89% RH respectively. The greatest potential differences were observed between the sections of the UK £1, followed by the 500L, E£1, and the smallest difference was between the sections of the UK £2. When coupled, the mass loss estimates for the UK £2 seem to be the highest by a large margin, although the small difference in Volta potential difference shown by SKP would predict otherwise.

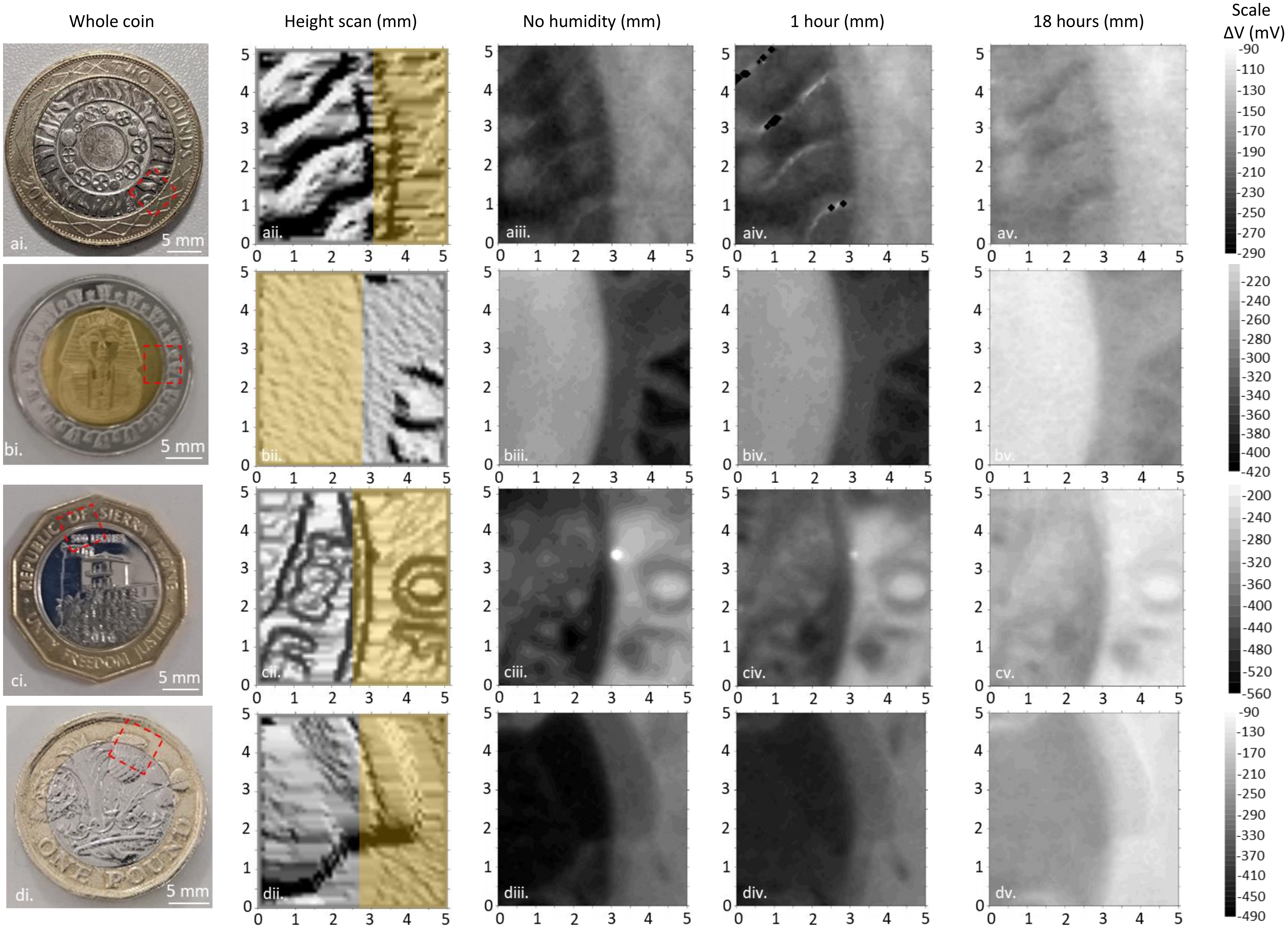

Figure 3.20. SKP scan of £2, E£1, 500L and £1 after 0 hours, 1 hour and 18 hours at 89% RH

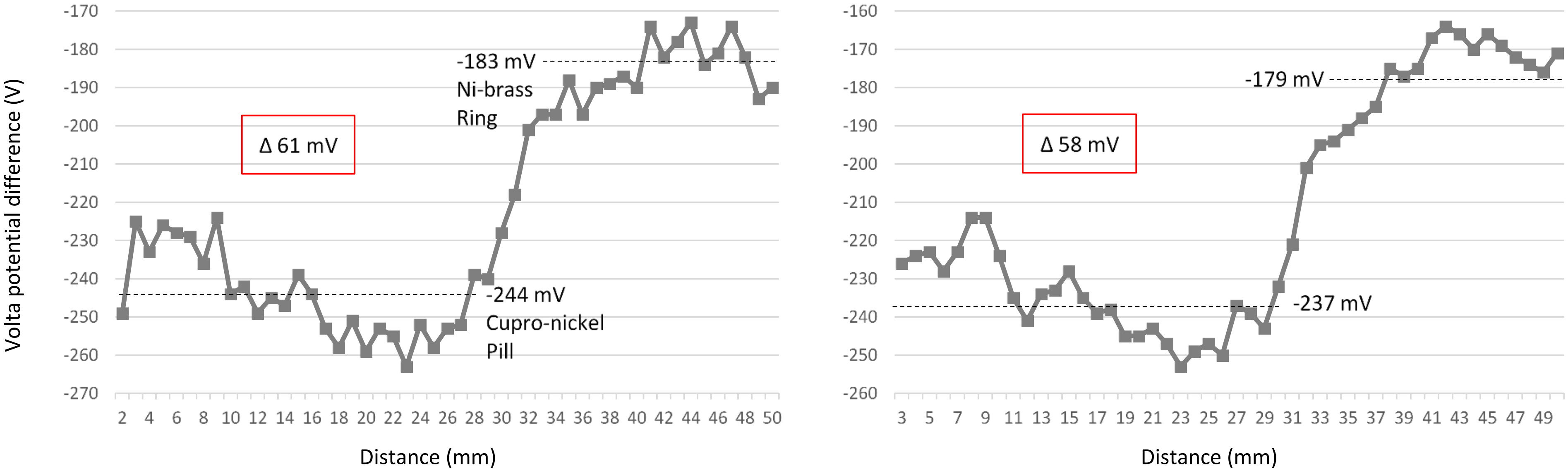

£2 room RH

£2 1hr 5% NaCl

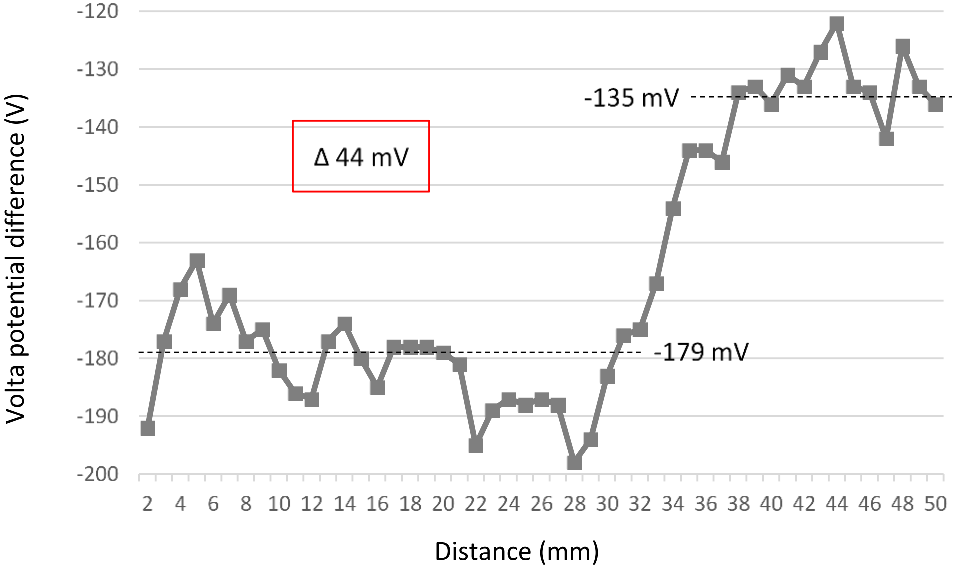

£2 18hr 5% NaCl

Humidity	Potential difference (mV)
Room humidity	61
1hr in 5% NaCl	58
18 hr in 5% NaCl	44

Figure 3.21. Line scans from SKP on £2. a. initial b. 1 hour at 89% RH c. 18 hours at 89% RH

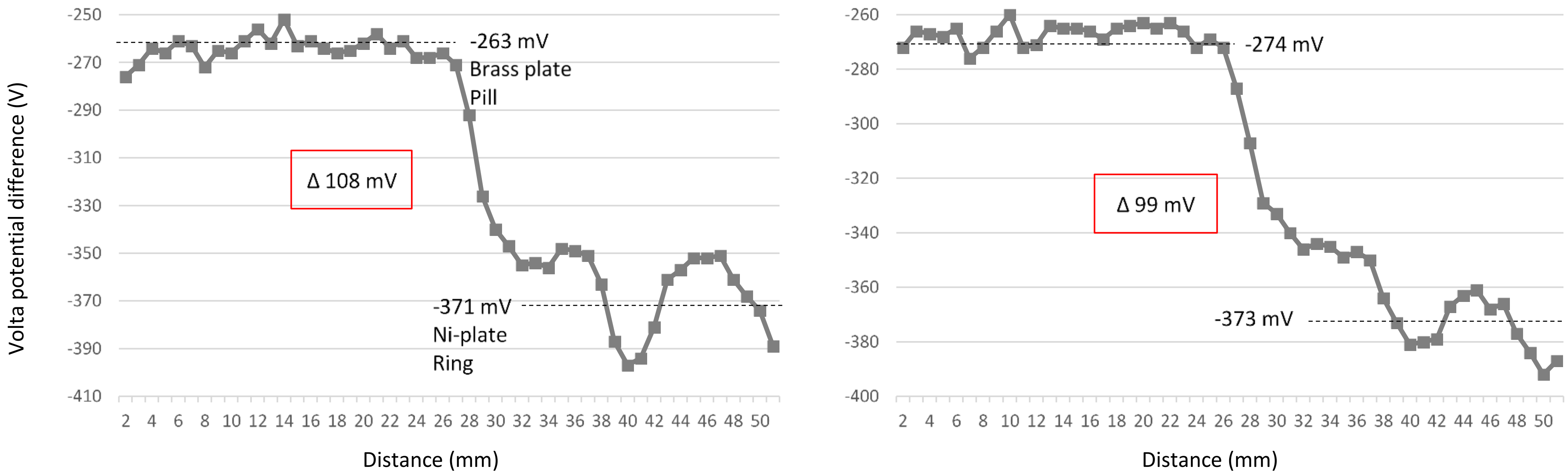

E£1 room RH

E£1 1hr 5% NaCl

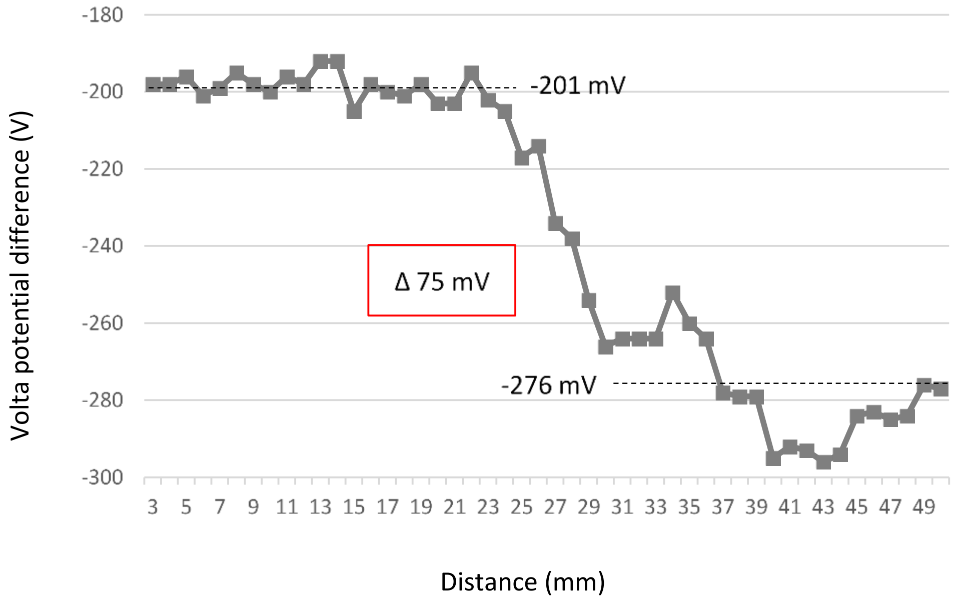

E£1 18hr 5% NaCl

Figure 3.22. Line scans from SKP on E£1. a. initial b. 1 hour at 89% RH c. 18 hours at 89% RH

Humidity	**Potential difference (mV)**
Room humidity	108
1hr in 5% NaCl	99
18 hr in 5% NaCl	75

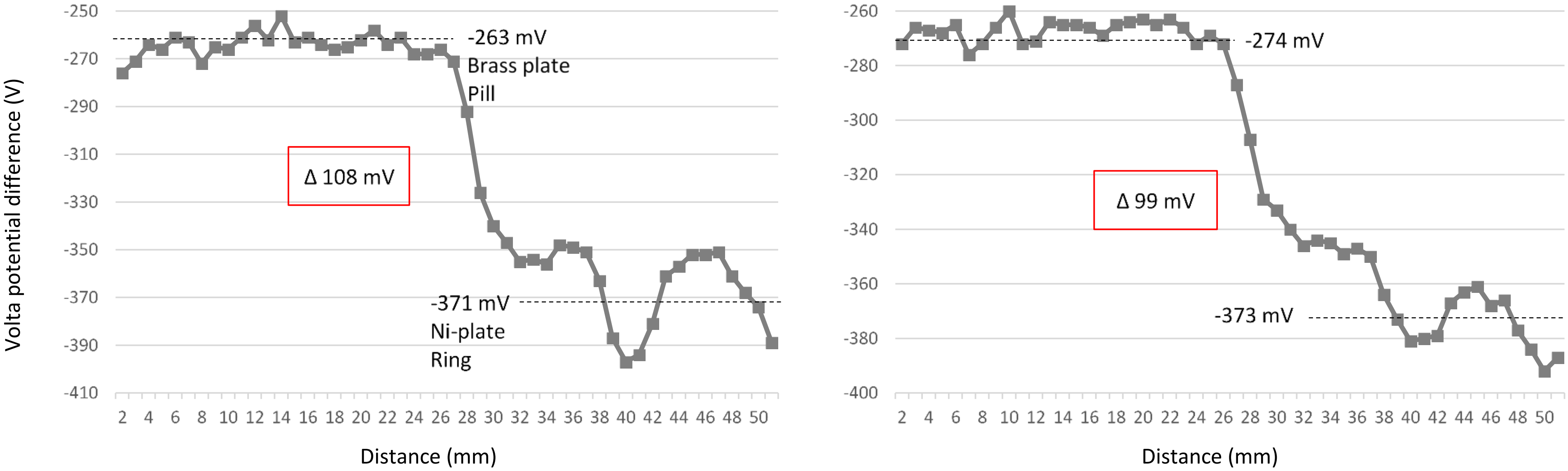

E£1 room RH

E£1 1hr 5% NaCl

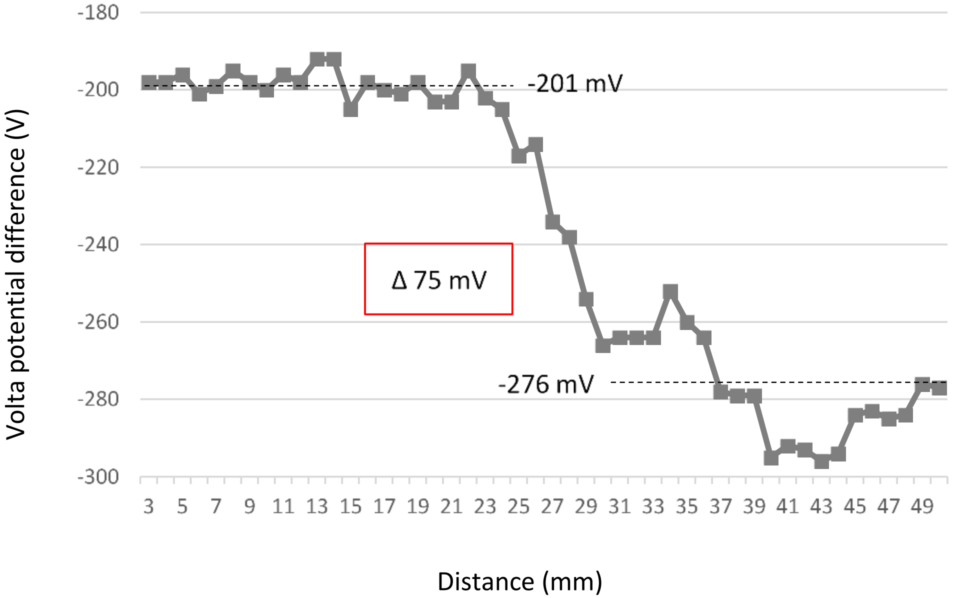

E£1 18hr 5% NaCl

Humidity	Potential difference (mV)
Room humidity	108
1hr in 5% NaCl	99
18 hr in 5% NaCl	75

Figure 3.23. Line scans from SKP on 500L. a. initial b. 1 hour at 89% RH c. 18 hours at 89% RH

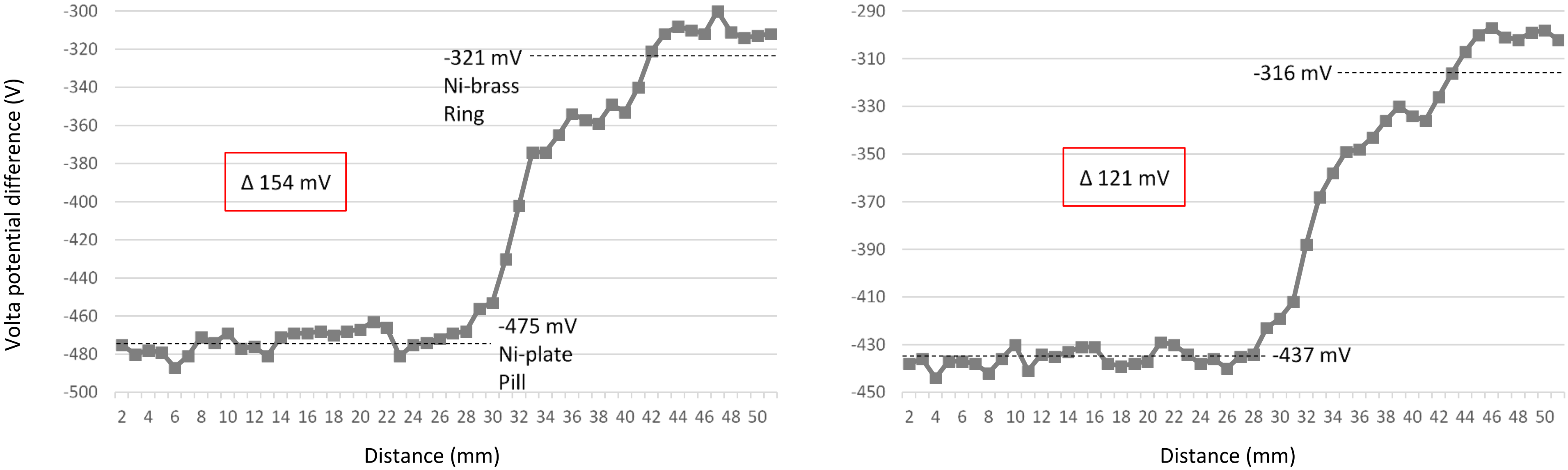

£1 room RH

£1 1hr 5% NaCl

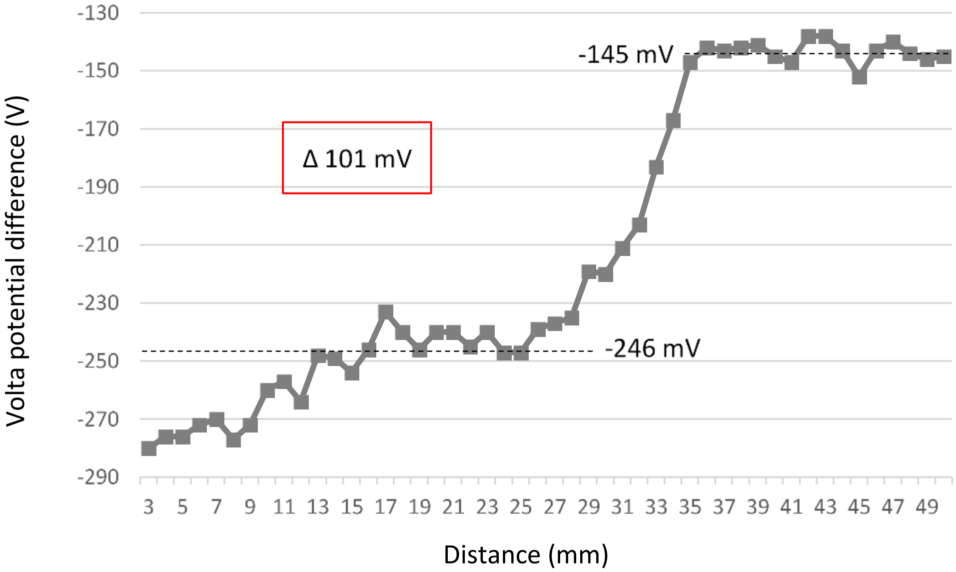

£1 18hr 5% NaCl

Humidity	Potential difference (mV)
Room humidity	154
1hr in 5% NaCl	121
18 hr in 5% NaCl	101

Figure 3.24. Line scans from SKP on £1. a. initial b. 1 hour at 89% RH c. 18 hours at 89% RH

3.3.4 Discussion on the galvanic activity of bimetallic coins

Investigations in this chapter focussed on the tendency for galvanic corrosion to occur between the sections of selected two metal coins in circulation around the world. Experimentation conducted by scanning and electrochemical techniques showed there is clear potential for a galvanic corrosion cell to develop.

The results from OCP potentiostat experiments demonstrated there is a potential difference between each of the pairings, meaning it is thermodynamically possible for a galvanic cell to form. Any potential difference between metals indicates a corrosion current can develop, however it cannot provide information on corrosion kinetics, or predict reaction rate [126]. In many cases increased potential difference results in a larger corrosion current and therefore more corrosion, but not in every instance [29]. It has been claimed that thresholds can be determined to predict if a two-metal pairing is safe or not. It is generally accepted that any difference in potential can lead to the formation of a galvanic couple, however the severity of corrosion depends on the metals as well as environmental factors such as conductivity, composition of the electrolyte, and temperature [27].

As shown in section 3.3.1.1, when investigated in 3.5% NaCl solution, the largest potential difference vs. SCE was 59.9 mV between the 500L sections, followed by the E£1 at 47.5 mV, then the UK £1 at 25.0 mV, and the lowest was 11.3 mV between the UK £2 sections. In the AFS solution, potential differences of 86.9 mV, 85.2 mV, 52.7 mV and 30.0 mV were measured for the 500L, E£1, UK £1 and UK £2 respectively. The size of the potential differences was the same in both solutions. The greatest potential difference and likelihood for galvanic corrosion was between the 500L sections, followed by the E£1, UK £1 and UK £2. In all cases, the brass-based sections had a lower potential than their nickel-based counterparts, meaning the brass-based sections were predicted to be the anodes and the nickel-based sections were predicted to be the cathodes. Similar behaviour has been found in previous experimentation both on coins and metal sections. Searle et al. [106] completed a similar investigation in artificial sweat solution and found potential differences of 15 to 80 mV. They examined the sections of a UK £2 coin and found a potential difference of 18 mV. Nestle et al. [5] completed OCP experiments in AFS solution on a 1-euro coin, with similar composition to the UK £2, and found a potential difference of 30 mV after 10 hours, and 40 mV after 24 hours. In this thesis, a potential difference of 11.3 mV was found in 3.5% NaCl and 30.0 mV in AFS solution between the UK £2 sections, which is comparable to the previous work.

Further potentiostat experimentation in the form of zero resistance ammetry (ZRA) was used, as shown in section 3.3.1.2. This technique was chosen to measure the galvanic corrosion current developed between the coin sections when different cathode areas were exposed. The area of exposed anode was maintained, whilst the cathode was varied to be one half, equal, and one and a half times the anode size. All coin sections demonstrated an increase in corrosion current when a larger cathode area was exposed. The E£1 and 500L both reached a maximum galvanic current at 1 x 10^{-6} A·cm^{-2}, the highest for the UK £1 was 1.5 x 10^{-6} A·cm^{-2}, and the UK £2 sections reached a maximum at 3.5 x 10^{-6} A·cm^{-2}. This indicates the highest level of corrosion will be seen on the UK £2, followed by the UK £1, 500L and E£1. However, it is unlikely coins in circulation will experience forced potentials or long-term immersion, so further investigation using more realistic environmental conditions was completed.

There are many studies discussing the effect of larger cathode areas on increases in corrosion rate at the anode [27]–[30], [127]–[129]. This chapter demonstrates that a larger exposed cathode increases galvanic current, resulting in a faster corrosion rate at the anode. As the variation in cathode area had a significant effect on the corrosion current, it can be concluded that the system is under cathodic control [28]. A British Standard Document notes the risk of bimetallic corrosion under immersion conditions increases when the area of the more noble metal is larger compared to the area of the more active metal [126]. A larger cathode area leads to an increase in the rate of oxygen reduction, increasing the galvanic current developed at the anode, leading to a larger amount of metal dissolution [27]. The findings from the ZRA experiments are in agreement with the OCP results; there is potential for a galvanic corrosion cell to form on bimetallic coins, and the brass-based section is most likely to form the anode.

The results from the zero resistance ammeter experiments completed in section 3.3.1.2 on the UK £2, E£1, 500L and UK £1 all demonstrate the effect explained above. In each case, when a larger cathode area was exposed, more oxygen reduction happened on this surface, resulting in an increased rate of current flow to the anode. The electrolyte formed a conductive path for metal ions to flow from the anode to the cathode. This process caused the anode to degrade and break down at an increased rate.

For example, for a couple of nickel and brass:

$$Zn \rightarrow Zn^{2+} + 2e^{-} \qquad \text{(anodic reaction)} \qquad 3.1$$

$$O_2 + 2H_2O + 4e^{-} \rightarrow 4OH^{-} \qquad \text{(cathodic reaction)} \qquad 3.2$$

Zinc is more active than copper, and therefore is normally released first from nickel-brass alloys [53]–[56], [130] and has been used to demonstrate the anodic reaction occurring. As the electrolyte was pH 7, oxygen reduction was the most likely cathodic reaction, shown in equation 3.2. If the solution had been acidic, the hydrogen evolution reaction shown in equation 3.3 would have been more favourable.

$$2H^+ + 2e^- \rightarrow H_2 \tag{3.3}$$

The potentiostat techniques provides data which is area averaged and can give a good indication of the overall reaction on a surface. However, the exact location and intensity of each anodic and cathodic event was impossible to determine. Therefore, SVET was chosen to map the during corrosion to identify the locations and intensity of the activity. The scans completed on each coin showed slightly different results. The UK £2 coin displayed true galvanic behaviour, with one metal supporting anodic activity, and the other, cathodic activity. Searle et al. [106] also completed SVET scans on a UK £2 coin, and obtained similar results with each type of activity confined to one section. The SVET has previously been used to measure galvanic activity at the cut edge of galvanised steels [103], [104], and is highly suitable for monitoring this type of corrosion.

The E£1, 500L and UK £1 showed the majority of both anodic and cathodic activity on the brass-based section of each coin, with some low-level cathodic activity across the nickel-plated section. In all three cases, there was little interaction between the sections in terms of galvanic corrosion, and limited overall activity on the nickel-plated section. Pure nickel is most likely to be passive under the conditions employed here, especially in the presence of more anodically susceptible brass-based alloys. If any generalised corrosion reaction was taking place, it is possible the SVET tip scanned above the height where isopotential lines emanated from the corroding surface, [131] an effect previously described in section 2.6.2. This limited its ability to monitor this form of corrosion. An alternative explanation is that nickel had a much higher OCP than brass in AFS and passivated to form a stable oxide layer. Any corrosion currents generated between the sections was not great enough to overcome any oxide layer. This passivation meant both parts of the corrosion reaction took place on the nickel-brass section.

3.3.5 Comparison of the activity on bimetallic coins

The values obtained from SVET and potentiostat techniques cannot be directly compared, partly due to the comparison of bulk and localised techniques as well as the use of different electrolytes. For potentiostat techniques, 3.5% NaCl was used as a high conductivity solution was required to obtain consistent results. However, when this electrolyte was used for SVET experiments, the signal-to-noise ratio was poor, and little significant data could be obtained. Therefore, a lower conductivity electrolyte, artificial sweat solution, was used instead. OCP values were obtained in both 3.5% NaCl and AFS, which showed slight variation in the absolute values, but the same order of corrosion potential. The overall performance of the pairings has been compared between these techniques.

The UK £2 showed the greatest tendency for corrosion current to be generated in the potentiostatic ZRA experiments, as well as the clearest, strongest galvanic activity from the SVET scans. Despite showing the smallest potential difference from OCP experimentation, these sections showed the greatest tendency for galvanic corrosion to occur. The magnitude of potential difference from OCP measurement is not necessarily an indicator for the strength of bimetallic corrosion, merely an indicator that some level of bimetallic corrosion is possible.

This has also been shown from the experiments completed on the Sierra Leone 500L samples. These sections revealed the largest potential difference from OCP, yet they showed the least corrosion from SVET experiments (see Figure 3.19), and second lowest values from ZRA measurements. This indicated that whilst some galvanic corrosion may occur here, it is significantly lower than for the UK £2, and slightly lower than seen for the UK £1 sections. The E£1 showed a higher rate of corrosion from SVET results than both the UK £1 and 500L, but a lower rate from ZRA measurements. Overall the UK £1, 500L and £E1 showed similar, lower corrosion rates from both SVET scans and ZRA experiments compared to the UK £2.

Whilst potentiostat techniques and SVET are well-suited for monitoring corrosion under immersion conditions, SKP provided information on the behaviour of bimetallic coins under more realistic atmospheric conditions. It is worth noting that SKP measurements can be used to predict which metal is more noble of the two; however, it does not provide any direct measures of corrosion rate. In this work, SKP showed more noble behaviour on the brass-based sections, whilst nickel-based sections displayed lower potentials and therefore more active behaviour. This contrasts the results obtained from potentiostat and SVET, which suggested the brass-based sections would corrode much more readily than the nickel-based metals.

There are several explanations for this switch in activity.

Under increasing humidity, a greater amount of water vapour was present in the environment chamber. As the humidity increased, the potential for a thin layer of water to adsorb onto the surface increased. Despite the humidity building due to the presence of sodium chloride solutions, only water was present in layers formed, as changes in vapour pressure only solubilised water. Such adsorbed layers are only a few molecules thick, and do not contain aggressive ions such as chloride, so do not have the same effect as immersion on a sample. Different results are often observed in atmospheric conditions compared to immersion conditions due to changes in corrosion mechanism.

Such layers are highly resistive, so any currents developed can only travel a few nano-meters, making it unlikely a galvanic couple will form under these conditions.

As brass is an alloy, small galvanic cells may develop between the copper-rich and zinc-rich areas of the surface. Previous work found zinc-rich areas on the surface of a Cu-20Zn alloy at 90% RH had a lower Volta potential than surrounding copper rich areas [130]. Chemical analysis previously showed oxide layers formed on brass in ambient conditions was contributed to by both the zinc and copper in an equal ratio to the bulk alloy [132]. On introduction to 90% RH, it was found an aqueous adlayer formed, thought to be sufficient to obtain bulk water properties; this led to dissolution of zinc and copper from the bulk material and the formation of ZnO and Cu_2O. In-situ Infrared Reflection Absorption Spectroscopy (IRAS) has been used to show ZnO production was favourable to Cu_2O [130], forming an amorphous passive layer and increasing the overall corrosion resistance of the alloy [133]. This mixed oxide layer may explain why the Volta potentials measured by the SKP under 89% RH conditions on the brass-based sections were higher than those measured on the nickel-based sections.

Under humid conditions, previous experimentation found nickel forms a thin passive layer containing nickel oxide (NiO) and nickel hydroxide ($Ni(OH)_2$) [46]. It has previously been found that nickel exhibits a high initial corrosion rate prior to passivation [7], [20], [21], [134], which may explain why the initial potential difference between the metals was so high, as passive layer formation on nickel appears to be more time dependant than on brass.

From the SKP scans, potential differences between the ring and pill sections could be measured. Despite the potentials being opposite to those seen from potentiostat and SVET, the order of magnitude was of interest. The smallest potential difference was seen between the sections of the UK £2, the same as from OCP experiments. The greatest potential difference was measured between the sections of the UK £1, closely followed by the £E1 and 500L. The differences observed were slightly larger than those from OCP measurements, which was also the case when Searle et al. [106] completed similar investigations on galvanic couples.

3.4 Conclusions

In this chapter, the potential for galvanic corrosion to occur between the sections of circulation bimetallic coins has been explored. Open circuit potential experiments showed the nickel-brass sections of bimetallic coins have a lower rest potential in both 3.5% NaCl and AFS solution than their nickel-based pairs. This means the nickel-brass section is more thermodynamically likely to corrode and therefore expected to form the anode when a coin is immersed. A galvanic series was created from the data obtained, and the greatest potential difference was seen between the sections of the 500L, predicting this coin would show the greatest corrosion rate. This was followed by the E£1, UK £1 and UK £2 from most likely to corrode to least, based on the OCP data.

A further potentiostat technique, ZRA, was used to measure the intensity of the galvanic couples, by varying the exposed surface area of the predicted cathode. The exposed area of the predicted anode was kept constant, whilst an area of cathode equal to one half, the same and one and a half times that of the anode was exposed. In all four cases, the measured current density increased with a larger exposed cathode, due to increased rate of oxygen reduction. Galvanic corrosion has been shown to be highly dependent on the ratio of exposed cathode to anode. If the cathode surface area is large compared to the anode, a large current density can be generated at the anode leading to a fast corrosion rate. If the cathode surface area is small and the anode large, the resulting current density will be small, as a large anode spreads the current density and weakens the corrosive effect.

The Scanning Vibrating Electrode Technique was used to collect information on location and intensity of anodic and cathodic areas on the surface. By observing maps from all the samples, the best pairing appeared to be nickel-brass coupled with nickel-plate. This construction has been used for the E£1, 500L and UK £1. In these cases, the majority of both the anodic and cathodic activity happened on the nickel-brass section, whilst some low-level cathodic activity happened on the nickel-plated section. This technique also showed anodes tend to develop on raised minted areas, indicating deformation caused by the minting process may affect the structure of the metal, decreasing its corrosion resistance.

The SVET showed clear galvanic activity developing between the sections of the UK £2. This sample was composed of a nickel-brass and cupro-nickel section. The scans illustrated most of the anodic activity happened on the nickel-brass section, whilst the majority of the cathodic activity happened on the cupro-nickel section, displaying characteristics of a true galvanic couple. SVET results indicated the UK £2 was most likely to form a galvanic couple from the samples assessed.

The Scanning Kelvin Probe was used to expose the coins to a humid environment, similar to what might be experienced in circulation. The potentials over the surface were measured using a Kelvin probe to assess the corrosion activity. The results showed in all cases that the brass-based sections developed higher, more noble potentials whilst the nickel-based sections showed lower, more active potentials. In all cases, the intensity of activity was different between the ring and pill, suggesting a galvanic cell could develop. However, due to the thin electrolyte layer and high resistance within this, it is more likely that small corrosion cells developed on each metal. This technique also showed some variance in surface potential at the raised minted areas, as seen on the SVET scans, indicating that the deformation caused by the minting process affects the microstructure and corrosion resistance.

Overall, the experiments completed on these bimetallic coins shows there is significant potential for a galvanic corrosion cell to develop. The conditions used for most of these experiments were significantly more aggressive than coins would normally experience in circulation. In terms of the OCP, ZRA and SVET, coins are not normally fully immersed for long periods in corrosive electrolyte, or have an applied potential, so the results are accelerated in comparison to circulation conditions. The SKP was used to imitate circulation conditions more accurately; this technique also indicated potential for a galvanic cell to develop, however in the opposite direction to other examination methods. This is likely due to the different passivation times and compositions seen under bulk and atmospheric conditions.

Chapter 4. Secondary cathodic spreading in atmospheric conditions

4.1 Introduction

One of the main issues with standard nickel electroplating and electroless plating methods is the potential for deposits to contain porosity. In coinage applications, steel is the most commonly used substrate for nickel plating. If there is porosity in the nickel plate, a corrosion cell can develop due to the difference in galvanic potential between nickel and steel. This effect is described in greater detail in section 1.3.4.

Nickel plated coins do not often experience substrate breakthrough in circulation, however previous experimentation has shown under immersion in artificial sweat solution that this is possible [7]. It is therefore important to understand the effects porosity could have on the corrosion resistance of coins. To mimic this effect, defects were made in the surface of standard nickel-plated samples, and droplets of different chloride types and concentrations were introduced onto the surface to instigate corrosion. Defect size was altered whilst droplet size maintained to see if this affected corrosion.

Previous experimentation using droplets of sodium chloride found a secondary spreading effect can occur, characterised as a thin layer of electrolyte forming outside the perimeter of the original droplet. It is not fully understood if this effect changes the cathodic processes or corrosion mechanism in and around the droplet area. Time lapse photography was used to monitor this spreading effect, with different salts, concentrations, and defect sizes. A Scanning Kelvin Probe was used to observe the distribution of potentials under the droplet and the surrounding metal surface. SEM analysis of post corrosion specimens was used to characterise the corrosion products formed in and around the droplet, and to assess the composition and location of corrosion products. Previous experimentation has shown the effect of secondary spreading on zinc [51], steel [52] and copper [135], [136].

4.2 Samples and sample preparation

The samples for examination were provided by The Royal Mint, Llantrisant. For this scheme of work, steel blanks electroplated with a 25 µm layer of nickel and homogeneous steel blanks were used as substrates and are shown in Figure 4.1. The electroplated nickel samples are commonly used for circulation coinage, and the steel provided used as the substrate for nickel plating.

Prior to experimentation, samples were cleaned using a 5 µm alumina paste to remove any surface oxides and manufacturing residues, followed by a rinse with distilled water and ethanol. Defects were initiated in the centre of the nickel-plated samples using a Dremel drill, equipped with bits of various diameter. Defect depth was kept constant using the gauge on the drill workstation.

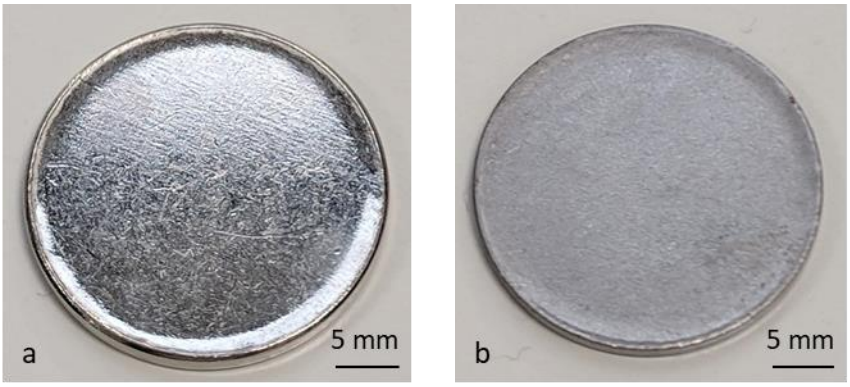

Figure 4.1. a) Electroplated nickel blank and b) Steel blank

4.3 Experimental methods

A range of different hole sizes were made in the surface of the nickel-plated samples. Holes of 0.5, 1, 1.6 and 2 mm diameter were made in the centre of these samples.

The majority of experimentation was carried out using sodium chloride droplets at 0.1, 0.5, 1, 2 and 5 M concentrations, to study environments with differing humidity's. Each sample was placed in a petri dish, above an electrolyte reservoir. A constant droplet size was maintained by sealing the environment using the lid of the petri dish, whilst the reservoir was of identical composition to the droplet on the sample. This minimised any droplet shrinkage due to evaporation, or changes in volume due to differences in concentration of the droplet and reservoir. The RH was measured during the experiments using a sensor, and the values measured at the different concentrations are given in Table 4.1. Further investigations were carried out using a 0.5 M magnesium chloride solution to compare the effect of different cation types.

Table 4.1. Measured RH at different chloride concentrations

NaCl concentration (M)	Measured relative humidity (%)
0.1	94
0.5	91
1.0	88
2.0	85
5.0	74

Initially, nickel plated samples with defects of 0.5 mm diameter and 1 µl electrolyte droplets were used. An example hole and its dimensions are shown in Figure 4.2. The electrolytes used were sodium chloride droplets with 0.1, 0.5, 1, 2 and 5 M concentration, and 0.5 M magnesium chloride. The same electrolyte compositions and concentrations were also used on steel blanks without defects to compare how secondary spreading affected the substrate material. In the second part of this work, defects with diameters of 0.5, 1, 1.6 and 2 mm were made in the nickel-plate using Dremel drill bits, and an electrolyte droplet volume of 5 µl. Sodium chloride droplets of 2 M concentration were used to observe the effects of defect size on secondary spreading. The experimental set-up is explained and shown schematically in section 2.12, including the image analysis using Photoshop CS6.

To compliment the time-lapse images, a Scanning Kelvin Probe was used to monitor potentials under and around the droplet area, on a nickel-plated sample with a 0.5 mm defect and a 1 µl droplet of 2 M NaCl. Prior to each Volta scan, a height profile was taken of the droplet, explained in section 2.7.3. Scans were performed 1, 2, 3, 4, 5, 6, 7 and 24 hours after droplet introduction to the defect. A beaker containing 2 M NaCl solution was placed in the environment chamber to maintain the droplet and the relative humidity at around 85%. Post experiment, maps were plotted in Surfer cartography software and spreading analysed using Photoshop CS6 software as described in section 2.12.

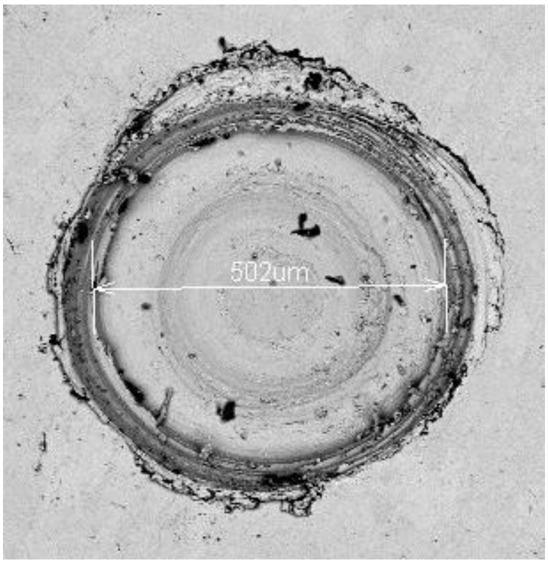

Figure 4.2. Example of 0.5 mm defect on a nickel-plated sample

4.4 Results

4.4.1 Atmospheric corrosion of nickel-plated samples with defects in chloride-based environments

Experiments were initially performed using five different sodium chloride concentrations and one magnesium chloride concentration on nickel-plated samples with 0.5 mm diameter circular defects. A typical progression of images from 2 M NaCl and 0.5 M $MgCl_2$ are shown at hours 0, 2, 6, 12, 24 and 48 in Figure 4.3 and Figure 4.4. Images after 48 hours are shown for all solutions in Figure 4.5. The radius of spreading over time for all experiments has been measured as described in section 2.12, plotted as spreading distance from the centre of the droplet versus time in Figure 4.6.

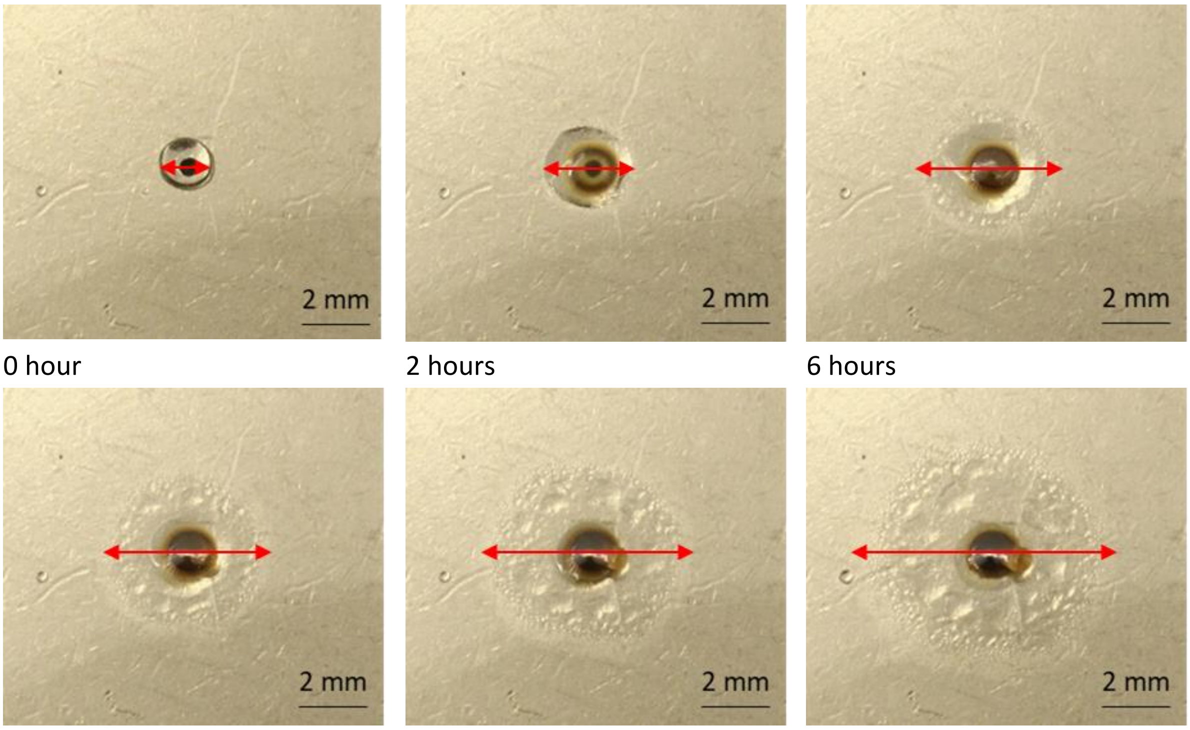

0 hour 2 hours 6 hours

12 hours 24 hours 48 hours

Figure 4.3. Images from nickel plate with 0.5 mm defect under 2 M NaCl droplet experiment (RH ~ 85%)

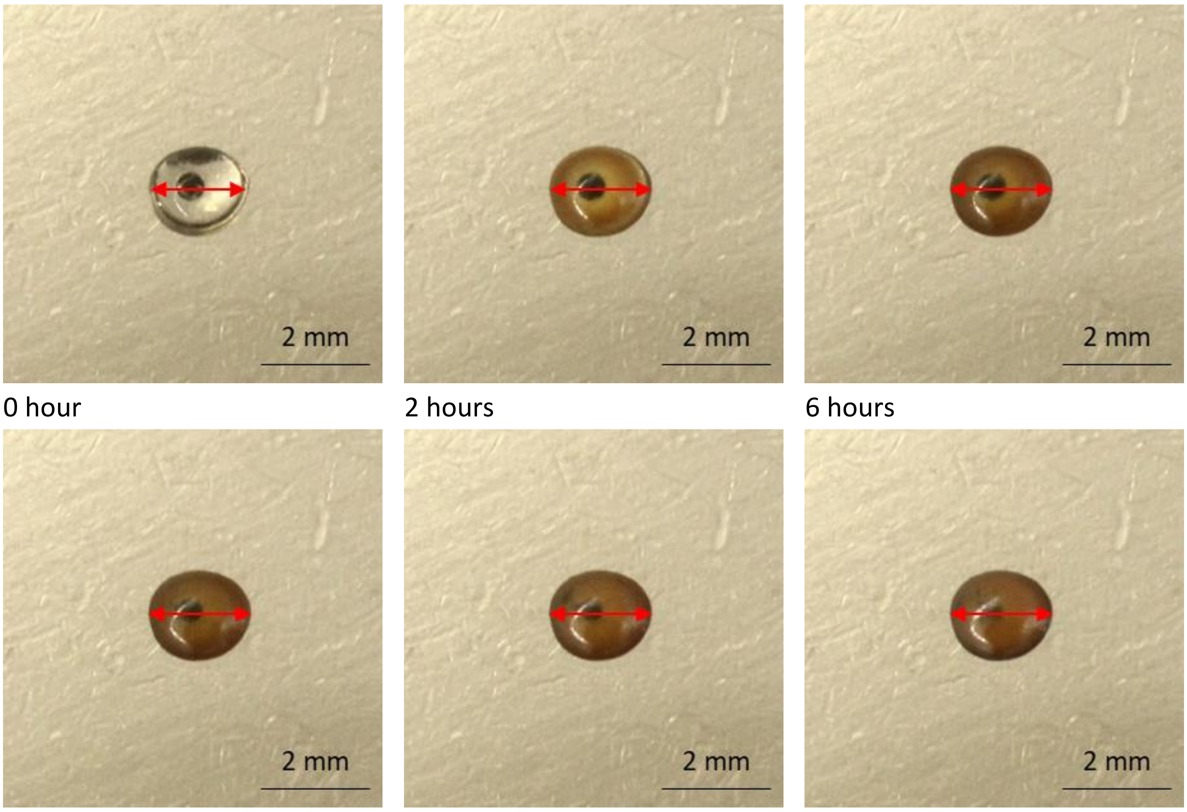

0 hour 2 hours 6 hours

12 hours 24 hours 48 hours

Figure 4.4. Images from nickel plate 0.5 mm 0.5 M $MgCl_2$ droplet experiment

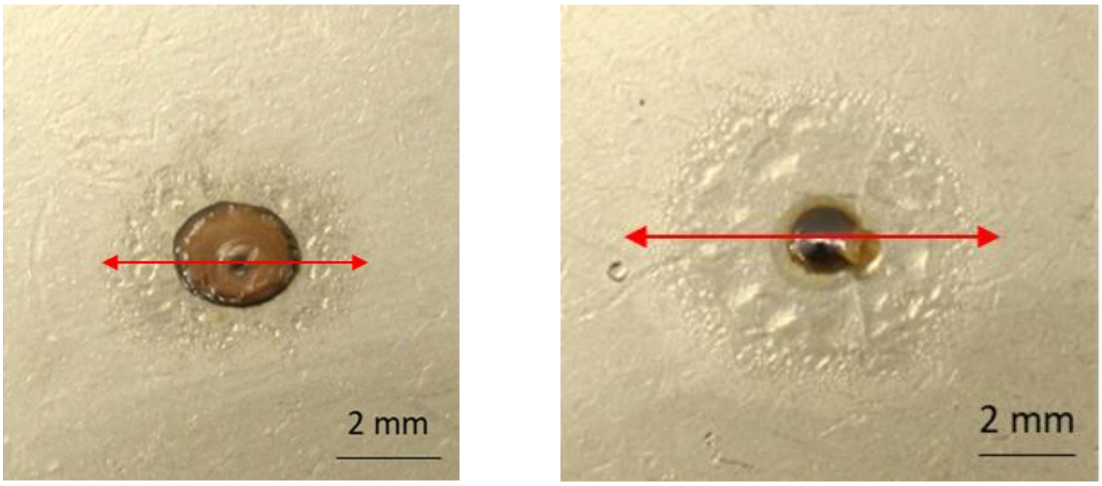

a) Nickel plate with 0.5 mm defect under 5 M NaCl droplet experiment (RH ~ 74%) after 48 hours

b) Nickel plate with 0.5 mm defect under 2 M NaCl droplet experiment (RH ~ 85%) after 48 hours

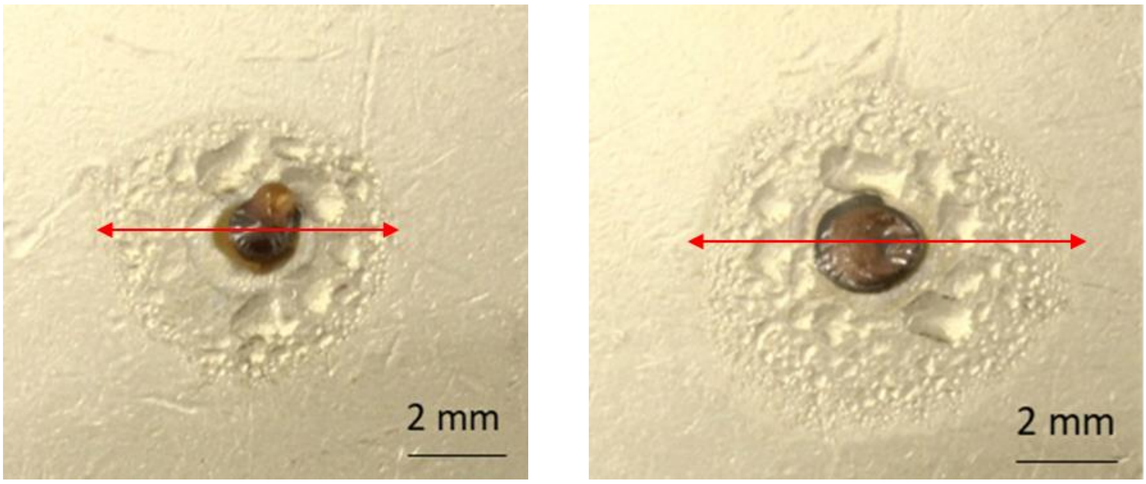

c) Nickel plate with 0.5 mm defect under 1 M NaCl droplet experiment (RH ~ 88%) after 48 hours

d) Nickel plate with 0.5 mm defect under 0.5 M NaCl droplet experiment (RH ~ 91%) after 48 hours

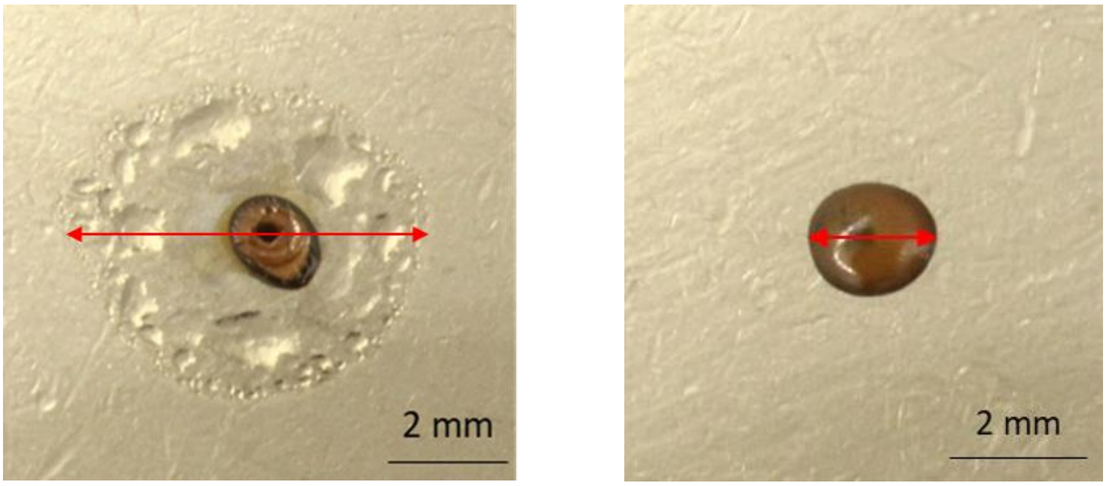

e) Nickel plate with 0.5 mm defect under 0.1 M NaCl droplet experiment (RH ~ 94%) after 48 hours

f) Nickel plate with 0.5 mm defect under 0.5 M $MgCl_2$ droplet experiment after 48 hours

Figure 4.5. a-f Images of nickel-plated samples with 0.5 mm defects after 48 hours in different environments

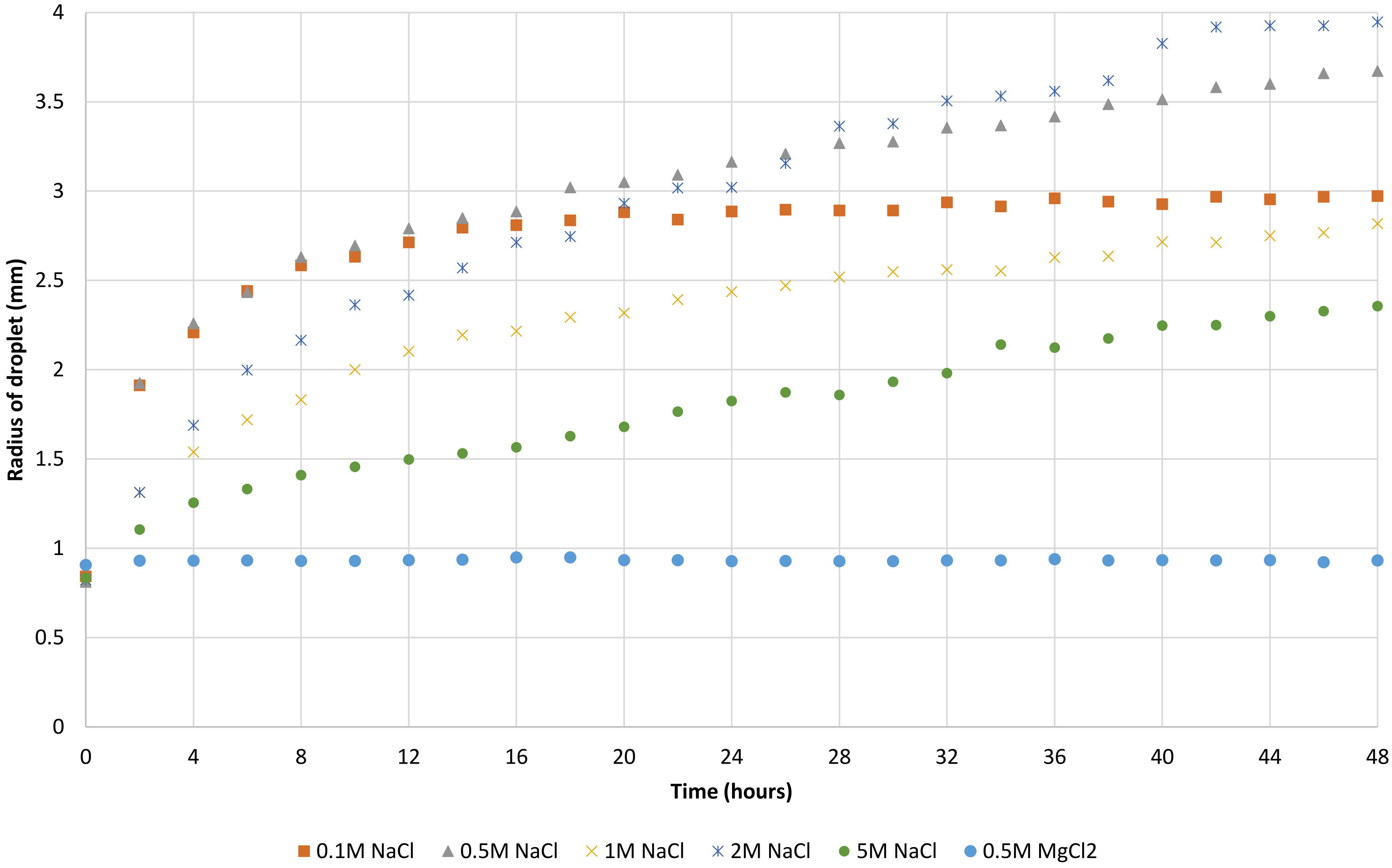

Figure 4.6. Spreading distance from droplet centre on nickel plated samples with 0.5 mm diameter defects

The results from these experiments showed that samples exposed to sodium chloride displayed clear secondary spreading effects, whereas the sample exposed to magnesium chloride showed very little spreading. The greatest spreading radius was seen from the 2 M NaCl droplet, followed by the 0.5 M NaCl, 0.1 M NaCl, 1 M NaCl, 5 M NaCl droplets, and the least spreading under the 0.5 M $MgCl_2$ droplet. The final spreading radii were 3.95 mm, 3.67 mm, 2.97 mm, 2.82 mm, 2.36 mm and 0.93 mm respectively. The average initial droplet size was 0.84 mm.

4.4.2 Atmospheric corrosion of steel substrates in chloride-based environments

For comparison, steel substrates with no defects were examined under the same electrolyte conditions. A typical progression of images from 2 M NaCl and 0.5 M $MgCl_2$ are shown at hours 0, 2, 6, 12, 24 and 48 in Figure 4.7 and Figure 4.8. Images after 12 hours are shown for all solutions in Figure 4.9. The graphs of the spreading radii over time for all these samples is shown in Figure 4.10.

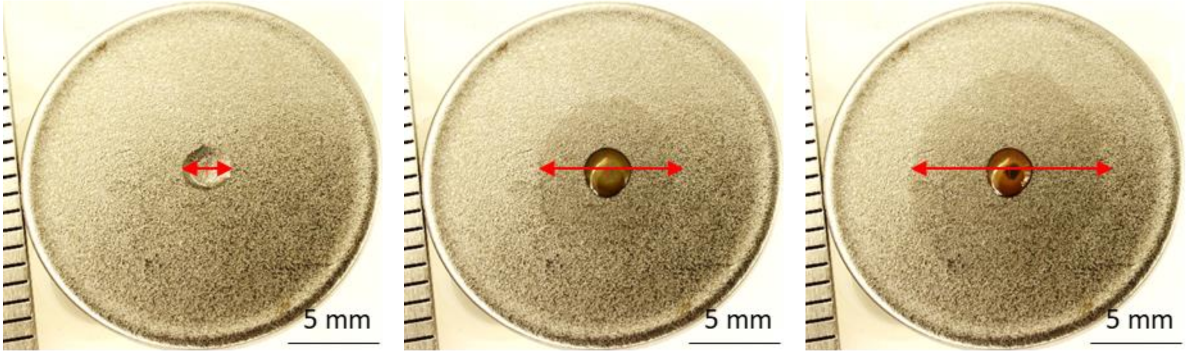

0 hour 2 hours 6 hours

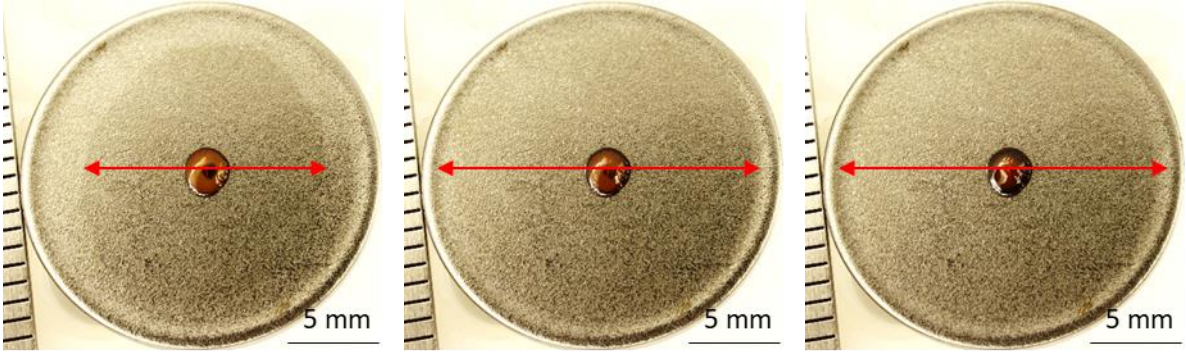

12 hours 24 hours 48 hours

Figure 4.7. Images from steel blank under 2 M NaCl droplet experiment (RH ~ 85%)

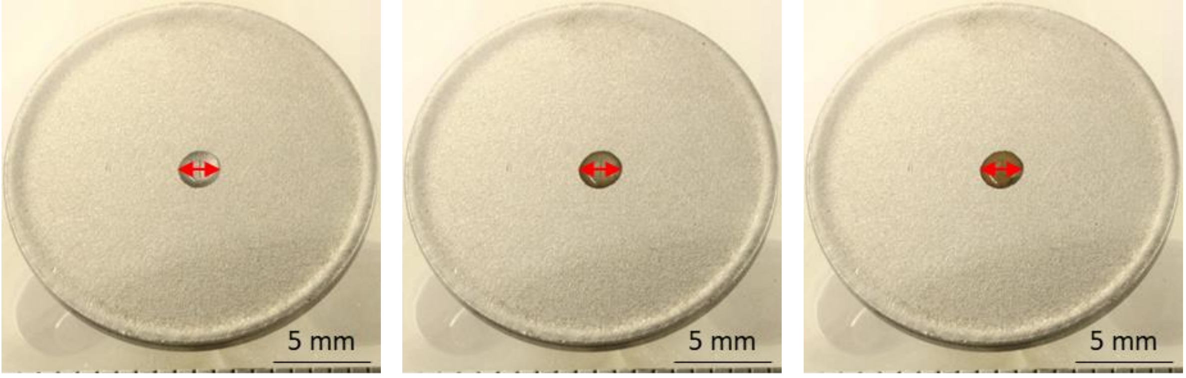

0 hour 2 hours 6 hours

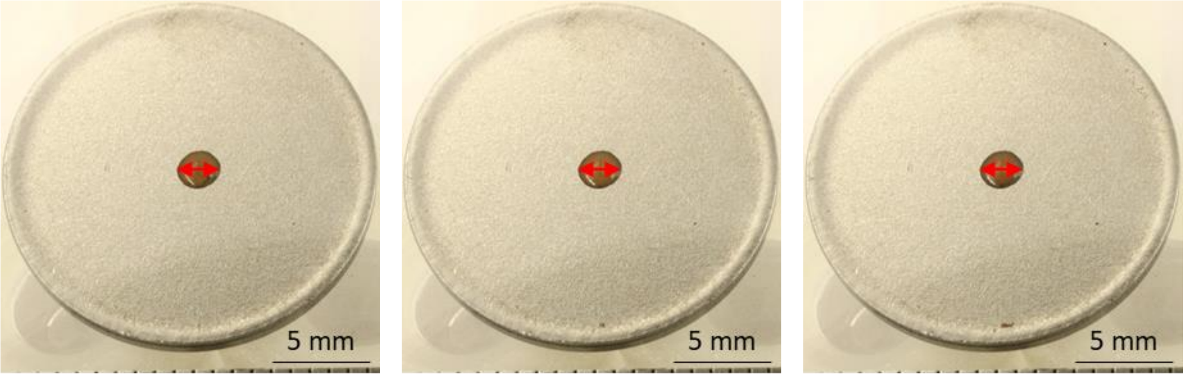

12 hours 24 hours 48 hours

Figure 4.8. Images from steel blank under 0.5 M $MgCl_2$ droplet experiment

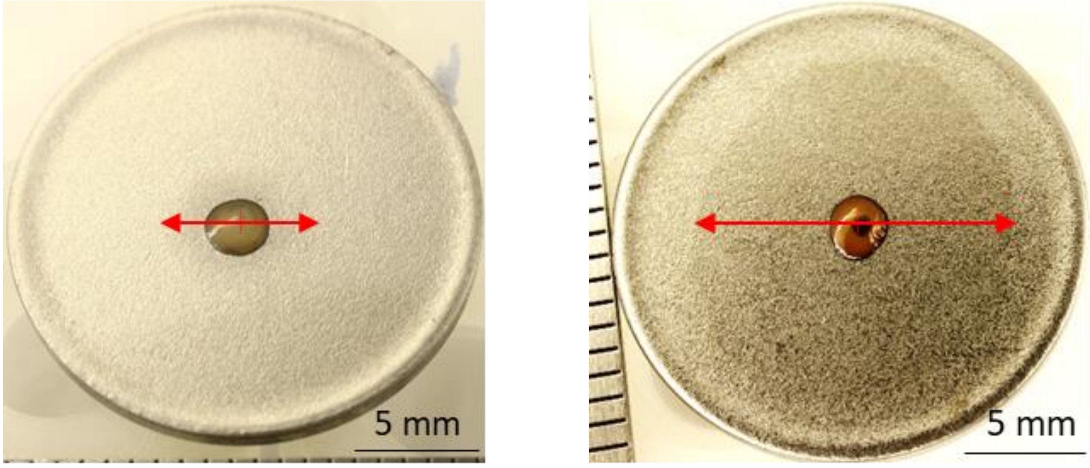

a) Steel blank under 5 M NaCl droplet experiment (RH ~ 74%) after 12 hours

b) Steel blank under 2 M NaCl droplet experiment (RH ~ 85%) after 12 hours

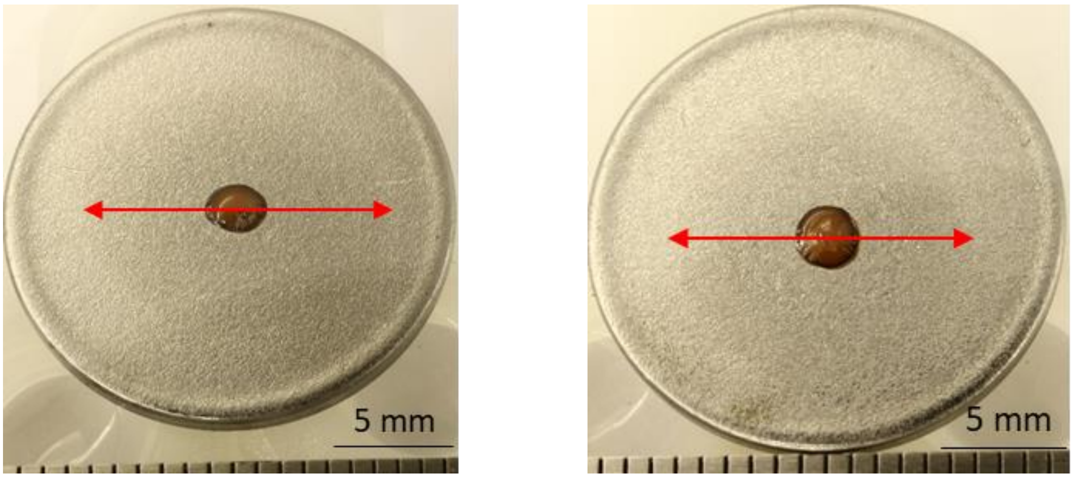

c) Steel blank under 1 M NaCl droplet experiment (RH ~ 88%) after 12 hours

d) Steel blank under 0.5 M NaCl droplet experiment (RH ~ 91%) after 12 hours

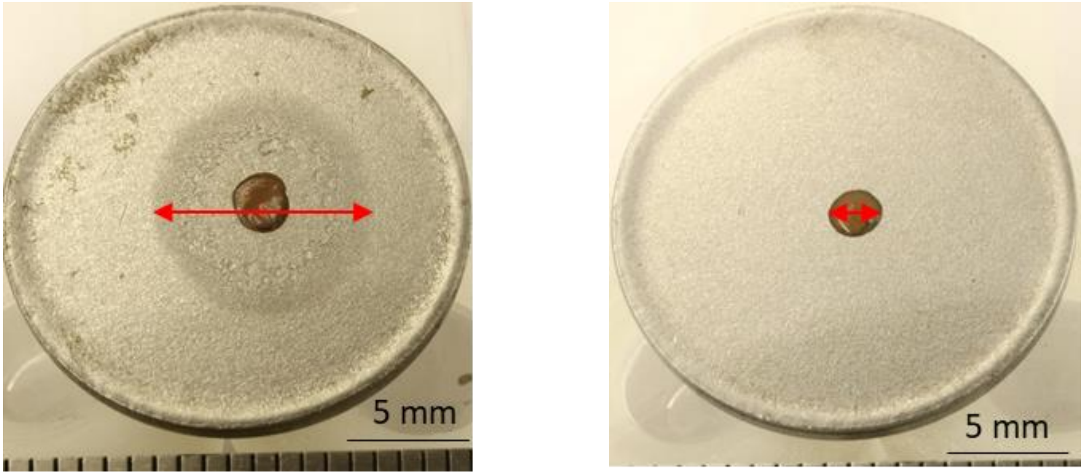

e) Steel blank under 0.1 M NaCl droplet experiment (RH ~ 94%) after 12 hours

f) Steel blank under 0.5 M $MgCl_2$ droplet experiment after 12 hours

Figure 4.9. a-f Images of Steel blank samples after 12 hours

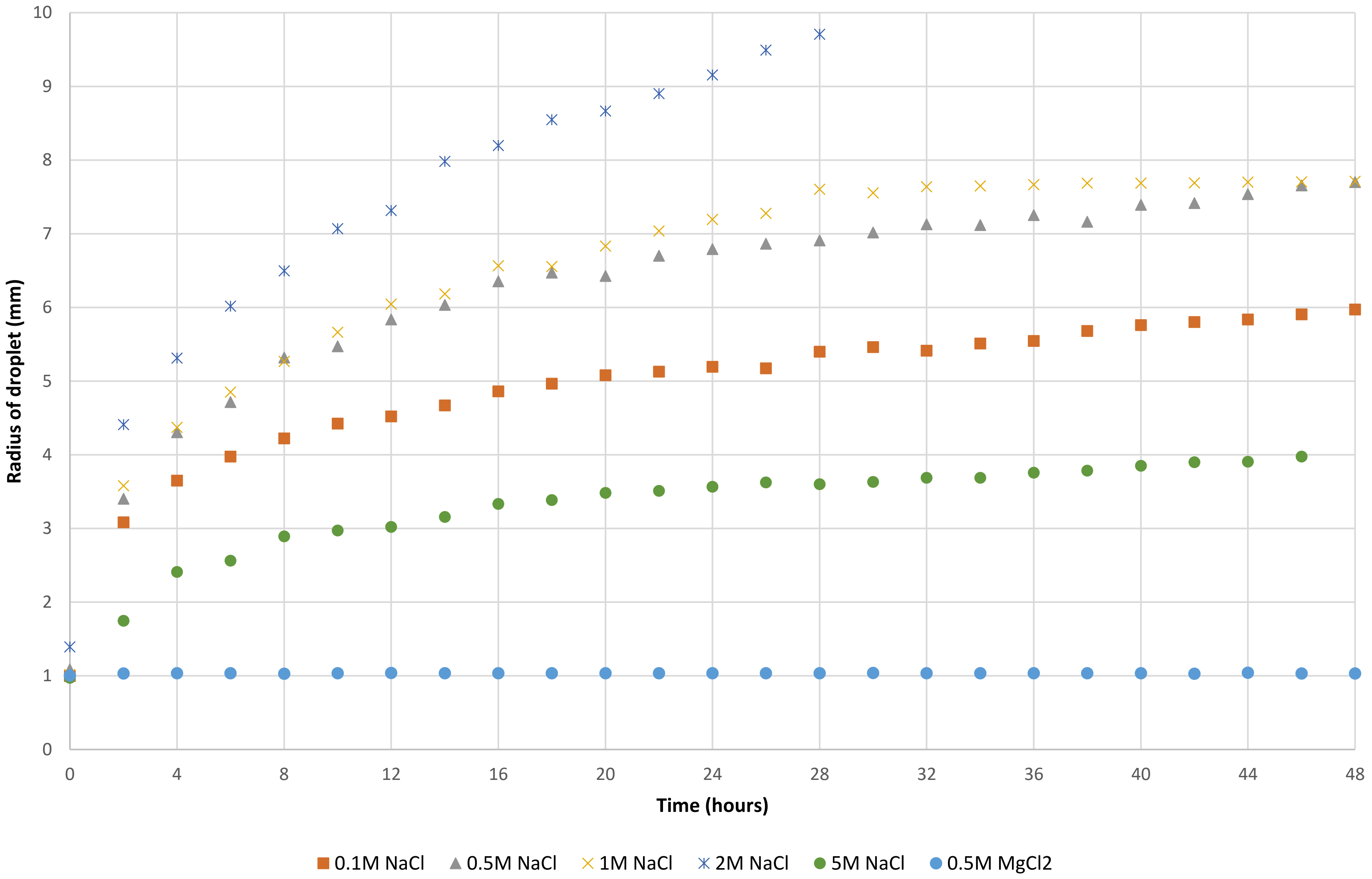

Figure 4.10. Droplet spreading on steel blank samples

The results from experiments on steel revealed that samples exposed to sodium chloride electrolytes displayed clear spreading effects, whereas on exposure to magnesium chloride only minimal spreading was seen. The greatest spreading distance was measured from the 2 M NaCl droplet, followed by the 1 M NaCl, 0.5 M NaCl, 0.1 M NaCl, 5 M NaCl droplets, and least spreading was observed from the 0.5 M $MgCl_2$ droplet. Final spreading distances were 9.77 mm (the secondary spreading reached edge of the sample before 48 hours), 7.71 mm, 7.70 mm, 5.97 mm, 3.97 mm and 1.03 mm respectively. The average initial droplet size was 1.08 mm.

4.4.3 Atmospheric corrosion of nickel-plated samples with different defect sizes

To monitor the effect of defect size on secondary spreading, holes of 0.5 mm, 1 mm, 1.6 mm and 2 mm diameter were drilled in the centre of each nickel-plated blank using a Dremel with a set depth gauge. A droplet of 5 µL was used to completely cover the larger defect sizes. This range of conditions will investigate whether the spreading phenomenon observed previously is controlled by the size of the local anodic site; which is assumed in this case to be proportional to the defect area. Images from hours 0, 2, 6, 12, 24 and 48 of these experiments are shown in Figure 4.11 to Figure 4.14. A graphical illustration of spreading radius over time is depicted in Figure 4.15.

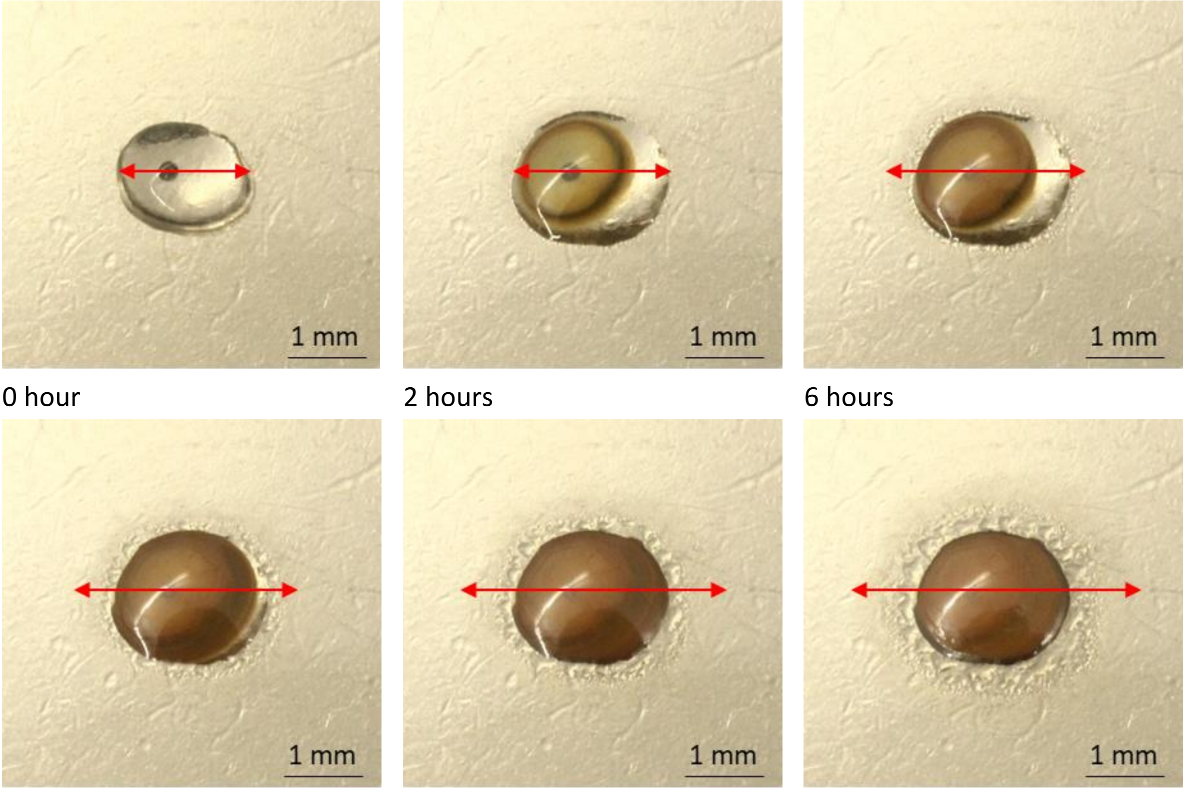

0 hour

2 hours

6 hours

12 hours

24 hours

48 hours

Figure 4.11. Droplet spreading on nickel samples with 0.5 mm defect in 2 M NaCl

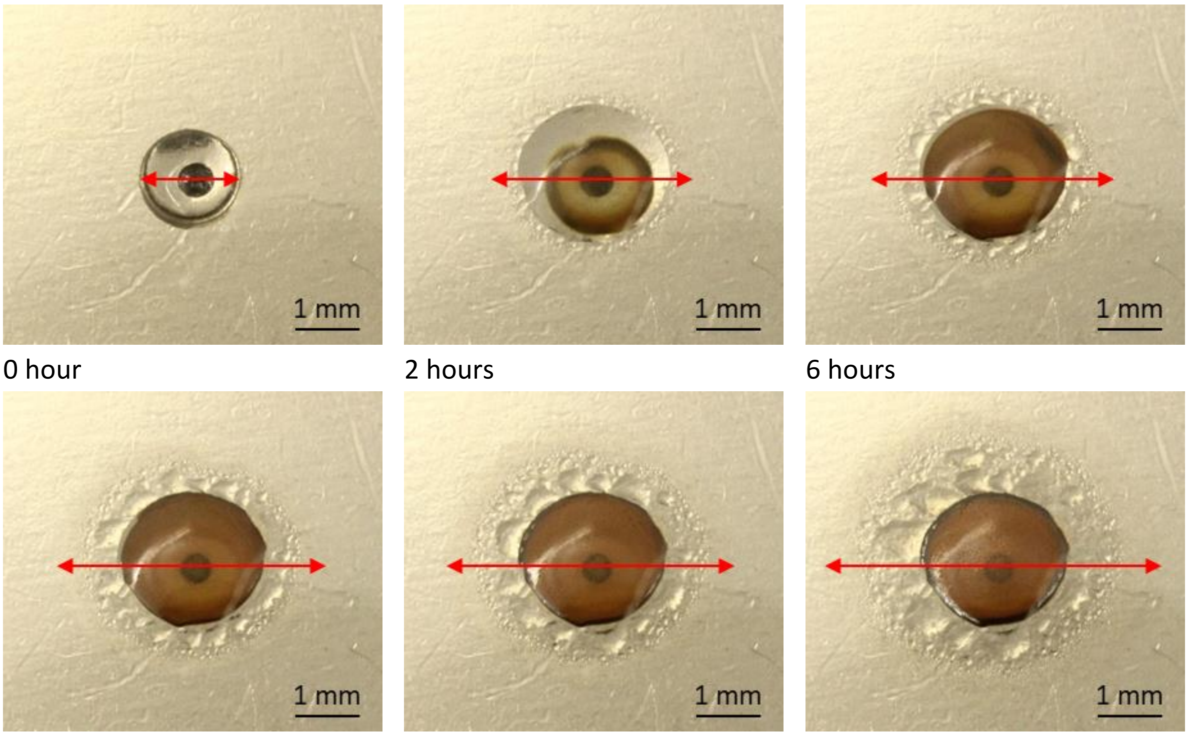

0 hour

2 hours

6 hours

12 hours

24 hours

48 hours

Figure 4.12. Droplet spreading on nickel samples with 1 mm defect in 2 M NaCl

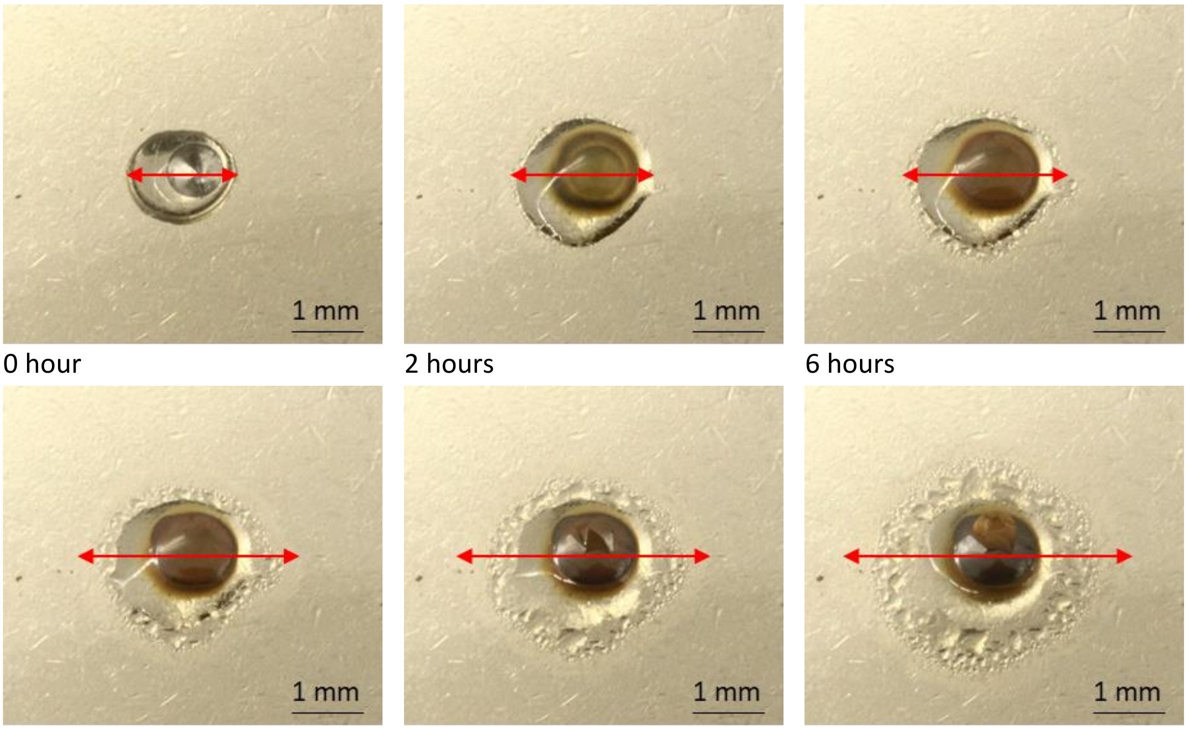

0 hour 2 hours 6 hours

12 hours 24 hours 48 hours

Figure 4.13. Droplet spreading on nickel samples with 1.6 mm defect in 2 M NaCl

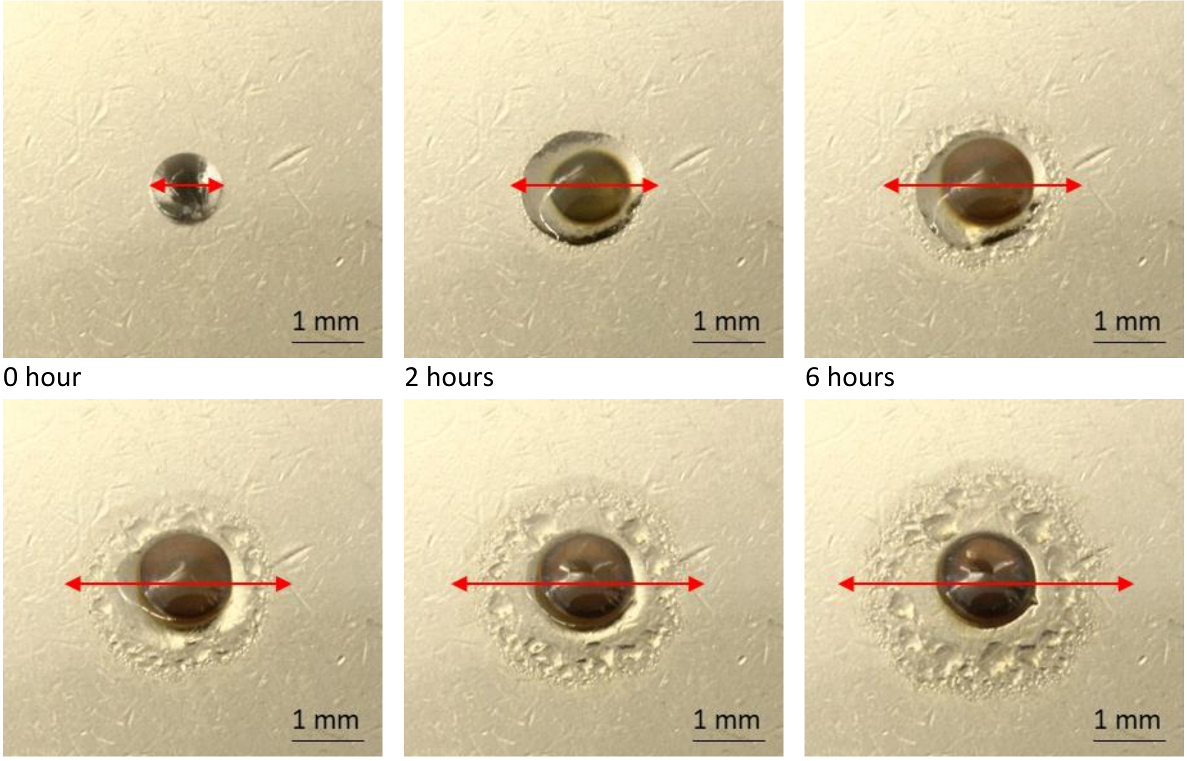

0 hour 2 hours 6 hours

12 hours 24 hours 48 hours

Figure 4.14. Droplet spreading on nickel samples with 2 mm defect in 2 M NaCl

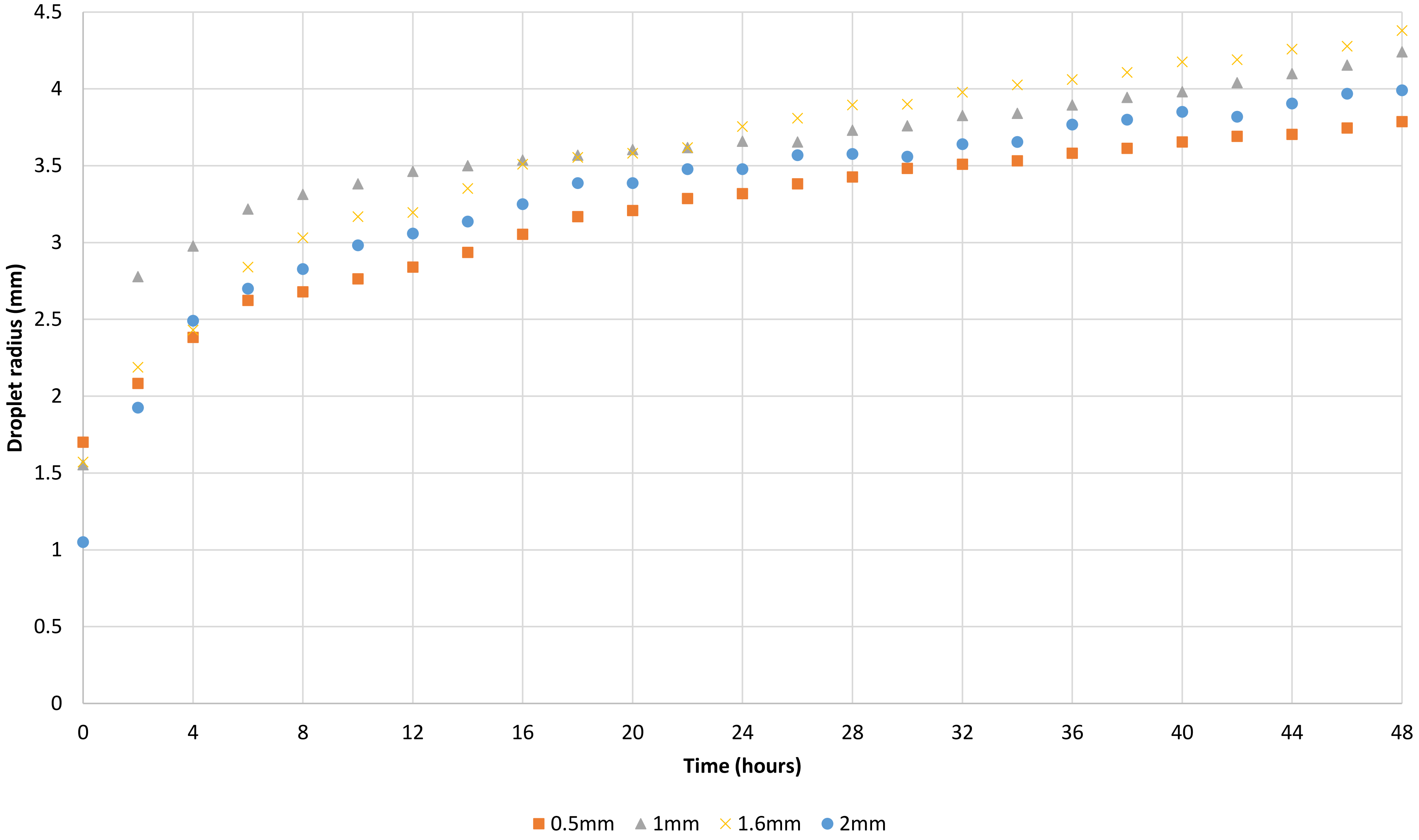

Figure 4.15. Droplet spreading on nickel plate with varying defect sizes under 2 M NaCl

Results from experiments on nickel-plated substrates with different size defects under a 5 µL 2 M NaCl droplet demonstrated that the size of the defect had minimal effects on spreading over a 48-hour period. The greatest spreading distance was seen on the sample with the 1.6 mm defect, followed by the 1 mm, 2 mm then 0.5 mm defects. Final spreading distances of 4.38 mm, 4.24 mm, 3.99 mm and 3.79 mm were measured respectively, from an initial average droplet of 1.47 mm.

4.4.4 SEM/EDS analysis of samples post corrosion

On completion of the 48-hour experiments, samples were removed from humidity and droplets were left to completely evaporate. The corroded samples were analysed using a desktop SEM with corresponding EDS system, described in section 2.10. False colour images were produced showing the location of different elements on the sample surface. Figure 4.16 a-f, Figure 4.17 a-f and Figure 4.18 a- e show the location of nickel, iron, oxygen, sodium and chlorine on the surface of three different samples.

Figure 4.16 shows the location of these elements on the nickel-plated sample with a 0.5 mm defect under a 2 M NaCl droplet. Image a) shows the overlay of all the elements and images b-f show the individual distribution. The results show outside the defect is nickel, except for corrosion product deposits composed of oxygen and sodium. Inside the defect, the substrate material of iron is present, as well as oxygen and chlorine. These EDS scans show the migration of sodium ions outward, away from the centre of the droplet, and chloride ions remaining inside the defect and original droplet area.

Figure 4.17 shows the locations of these different elements on the nickel-plated sample with a 0.5 mm defect under a 0.5 M $MgCl_2$ droplet. Image a) shows the overlay of all the elements and images b-f show maps of the individual distribution. Outside the defect, nickel is prevalent with some small deposits of chloride. Inside the defect is mainly iron with oxygen and chlorine evenly distributed. The magnesium present is inside the initial droplet area and concentrated around the circumference. Some small areas outside the original droplet area show the presence of iron, oxygen and chlorine, where it is likely small pits have formed.

Figure 4.18 shows the locations of these different elements on the steel blank sample under a 2 M NaCl droplet. Image a) shows the overlay of all the elements, with images b-e, the individual element distribution. These images show overall presence of iron, and in the centre under the droplet, a high concentration of oxygen and chlorine. The area outside the droplet had a higher concentration of sodium. The locations of these elements are similar to the EDS maps taken from the nickel-plated sample under a 2 M NaCl droplet.

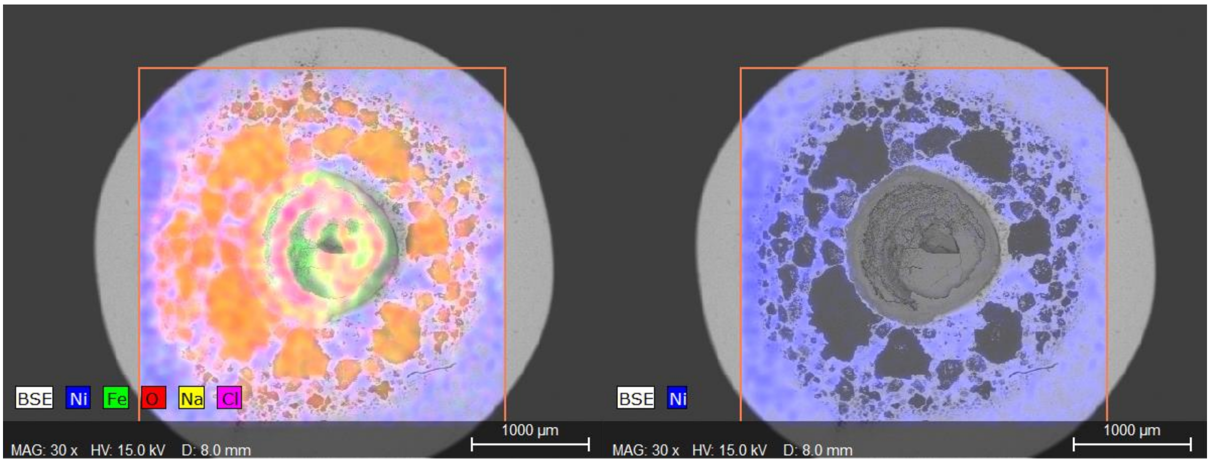

a. EDS map all *b. EDS map Ni*

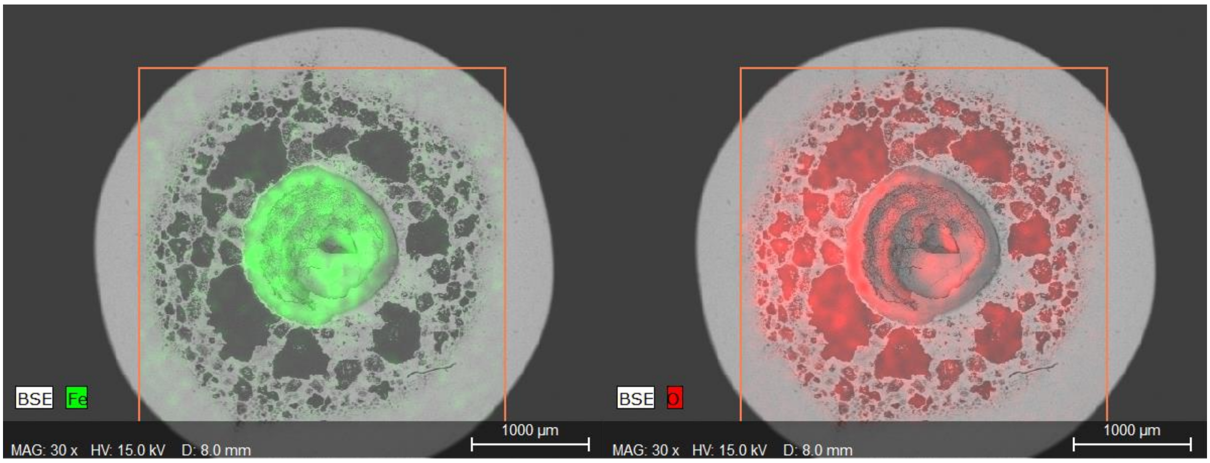

c. EDS map Fe *d. EDS map O*

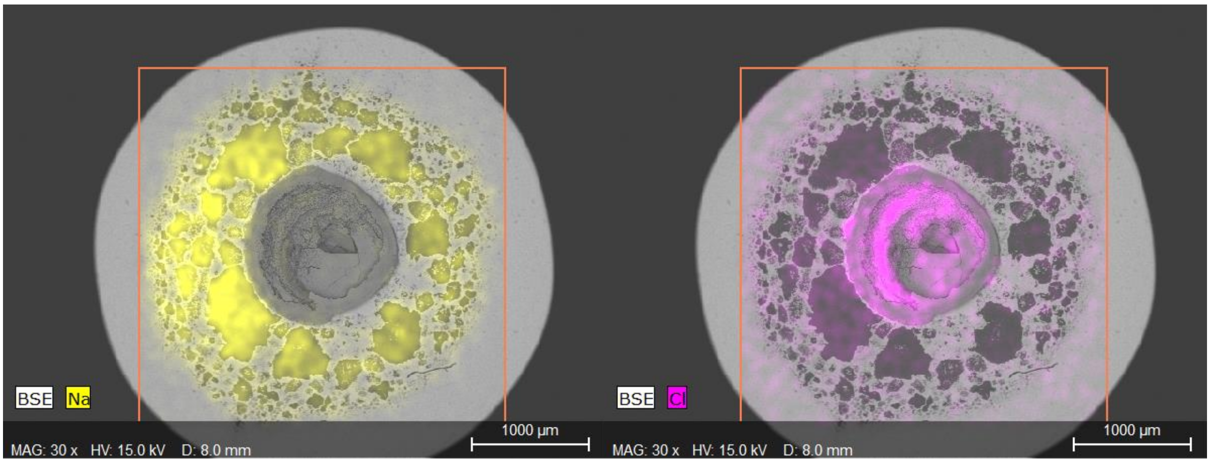

e. EDS maps Na *f. EDS maps Cl*

Figure 4.16. a-f. SEM EDS images for 2 M NaCl droplet on nickel-plated sample with 0.5 mm defect

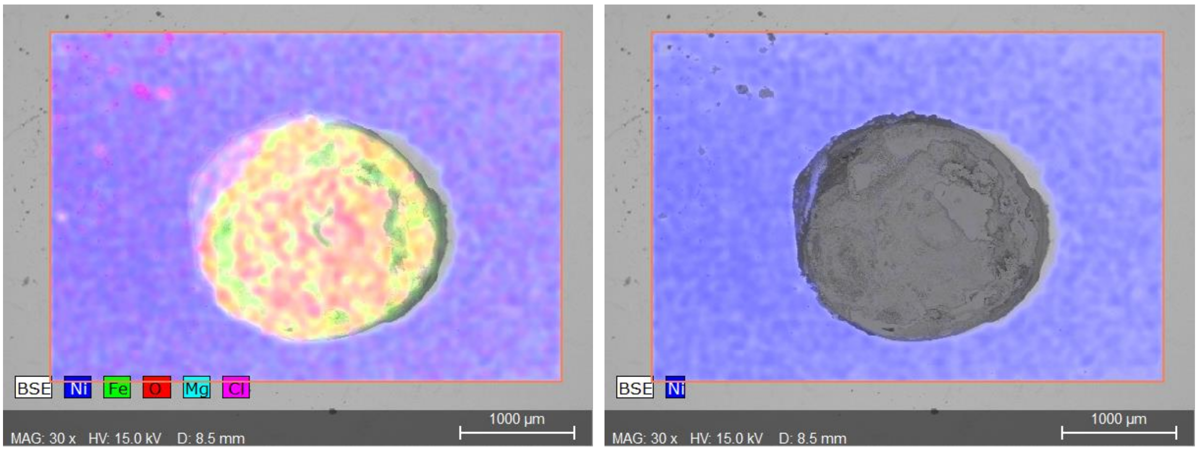

a. EDS map all *b. EDS map Ni*

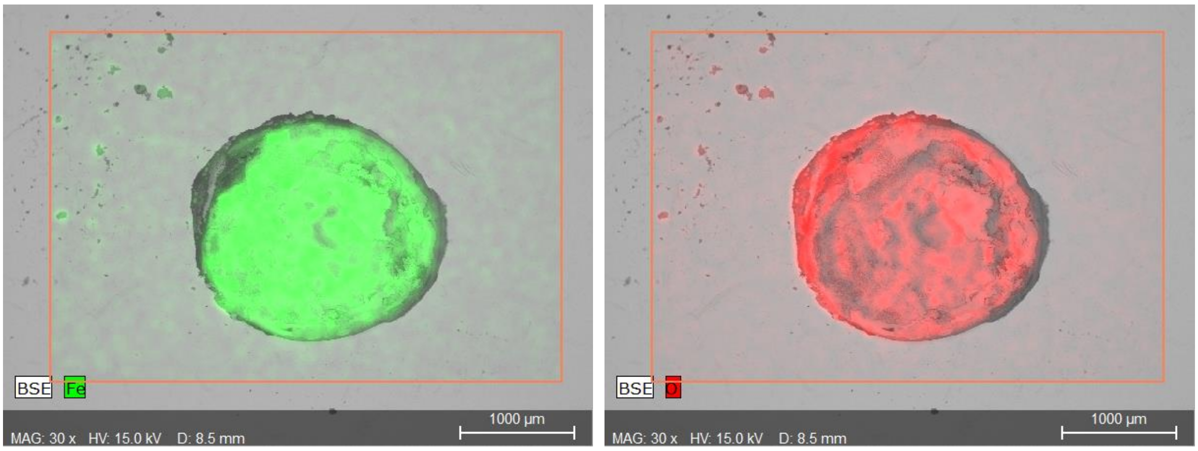

c. EDS map Fe *d. EDS map O*

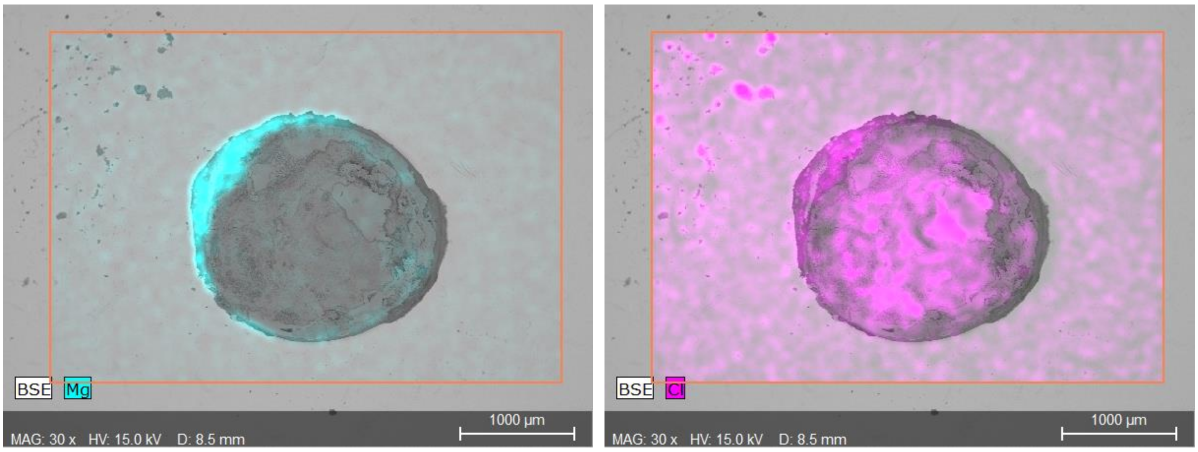

e. EDS maps Mg *f. EDS maps Cl*

Figure 4.17. a-f. SEM EDS images from 0.5 M $MgCl_2$ on nickel-plated sample with 0.5 mm defect

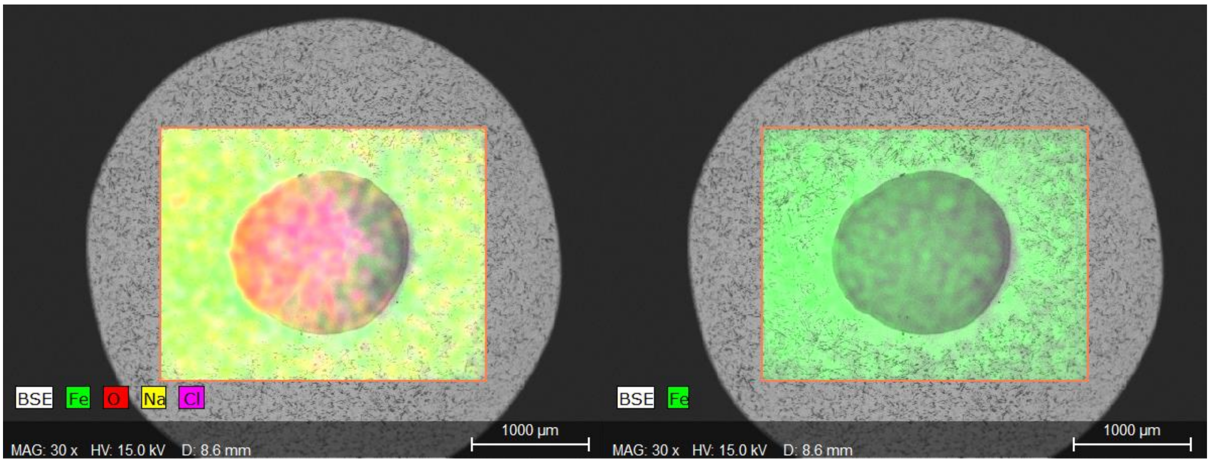

a. EDS map all *b. EDS map Fe*

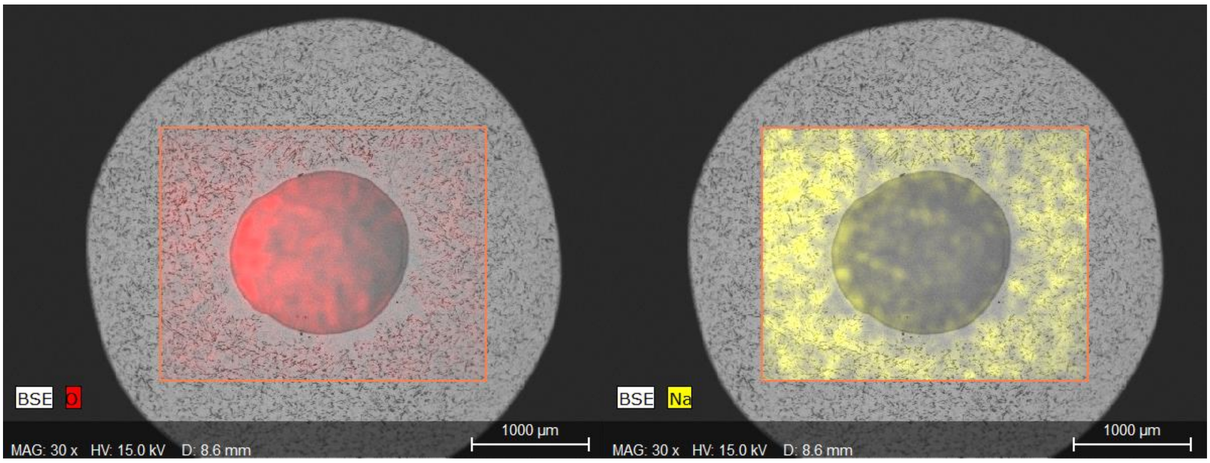

c. EDS map O *d. EDS map Na*

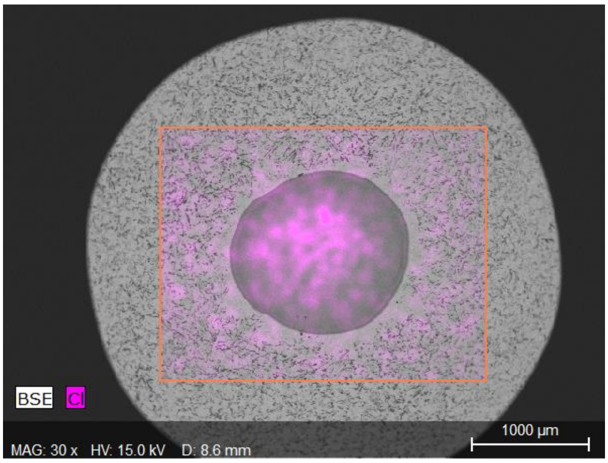

e. EDS maps Cl

Figure 4.18. a-e. SEM EDS images for 2 M NaCl droplet on steel substrate

Spreading extended beyond the area scanned by SEM/EDS for the steel-based samples. This area was chosen to capture the changes in elemental composition around the defect and immediate surrounding area.

4.4.5 Scanning Kelvin Probe analysis of droplet spreading

To understand if secondary spreading affected the corrosion intensity in the defect, SKP was used to observe Volta potential distribution changes in the immediate vicinity of the original droplet. For this experiment, a nickel-plated sample with 0.5 mm defect and 1 µL 2 M NaCl droplet was used, as these conditions provided the greatest amount of spreading during time-lapse experiments. Height scans were taken prior to each Volta scan to monitor any changes in droplet morphology. The droplet height was reasonably stable over the experiment duration, at an average maximum of 310 µm above the surface. Maps of the 5 x 5 mm scans at 1, 2, 4, 6 and 24 hours, and the initial height scan are shown in Figure 4.19. A comparison of spreading radius between time lapse photography and SKP potentials is shown in Figure 4.20. Line scans of Volta potential from the centre of the droplet at 1, 7 and 24 hours are shown in Figure 4.21.

Figure 4.19 shows the height profile of the initial droplet and Volta potential maps at hours 1, 2, 4, 6 and 24 after introduction of the 1 µL 2 M NaCl droplet on the defect in the nickel-plated sample. The scan after 1 hour shows the defect and droplet in the centre with significantly lower potential than the surrounding nickel-plated surface. At this stage, the area of low potential is similar in size to the initial droplet, shown in the height profile. After 2 hours there was a small increase in the area of low potential, characterised by the development of a slightly higher potential at the extremity of the original droplet area. After 4 hours, a clear ‘bullseye’ had formed at the centre of the scan; this comprised the original droplet area in the centre with the lowest potential, surrounded by a ring of slightly higher potential, believed to be the secondary spreading region. This region of secondary spreading increased in diameter for the remainder of the experiment. By hour 24, the potential at the original droplet location increased slightly, and the radius of secondary spreading increased significantly.

A comparison between the spreading measured from time lapse photography and SKP is shown in Figure 4.20. The data showed a similar trend for increased spreading radii, however, was slightly faster in the time lapse photography analysis than the potential changes measured from the SKP Volta scans. This is most likely because the environment for time lapse photography reached RH faster than the SKP chamber due to the smaller environment volume.

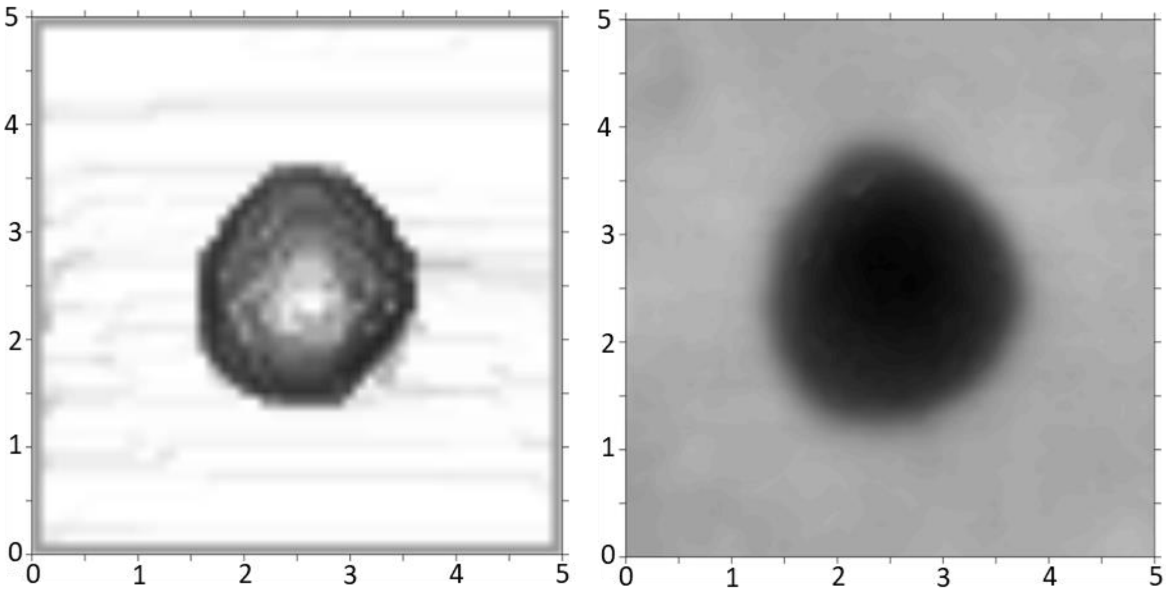

Height profile (all axis measurement in mm)

1 hour

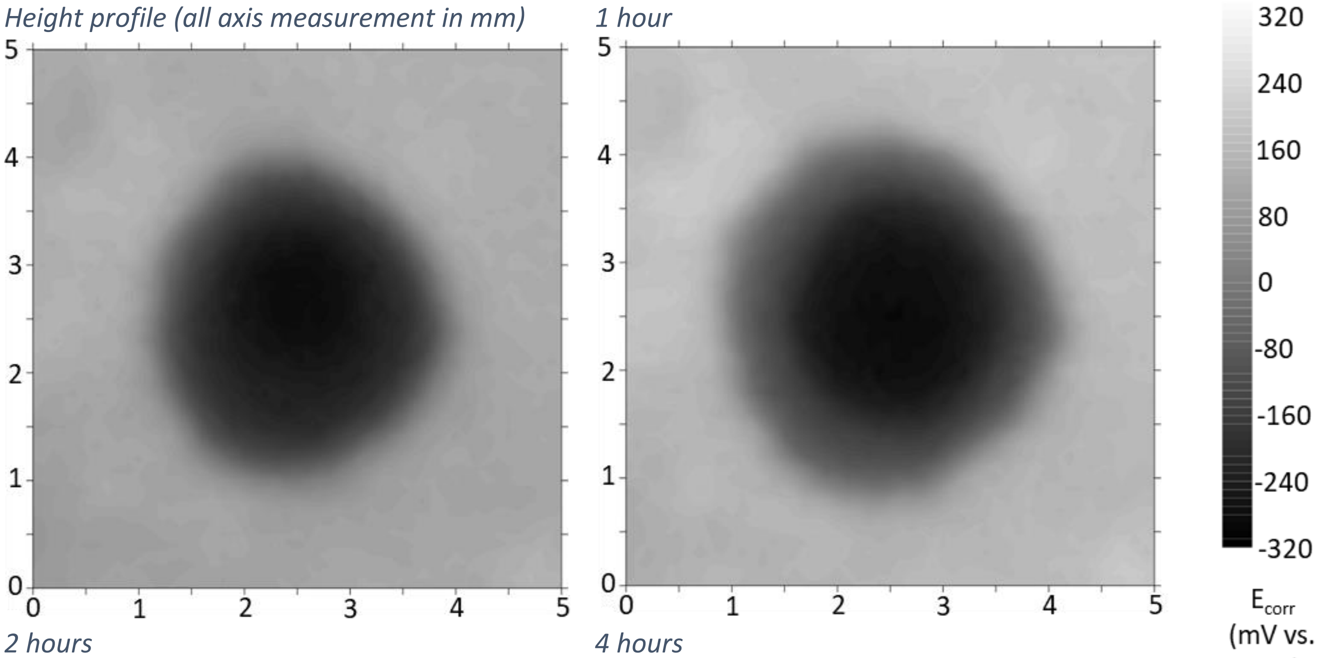

2 hours

4 hours

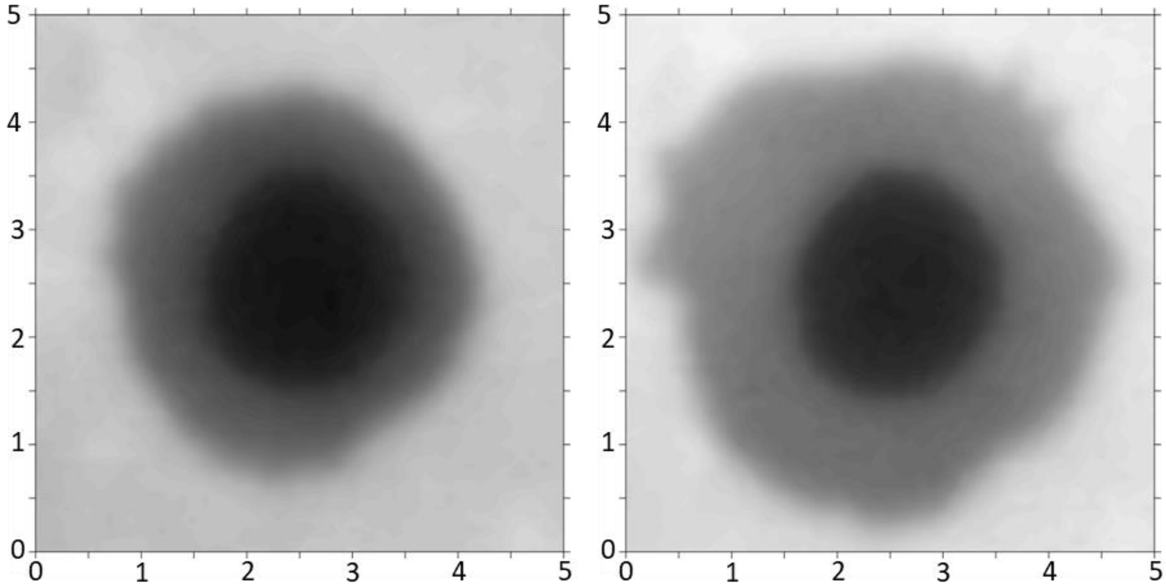

6 hours

24 hours

Figure 4.19. SKP Volta potential scans on nickel-plated sample with 0.5 mm defect and 1 µl 2 M NaCl droplet

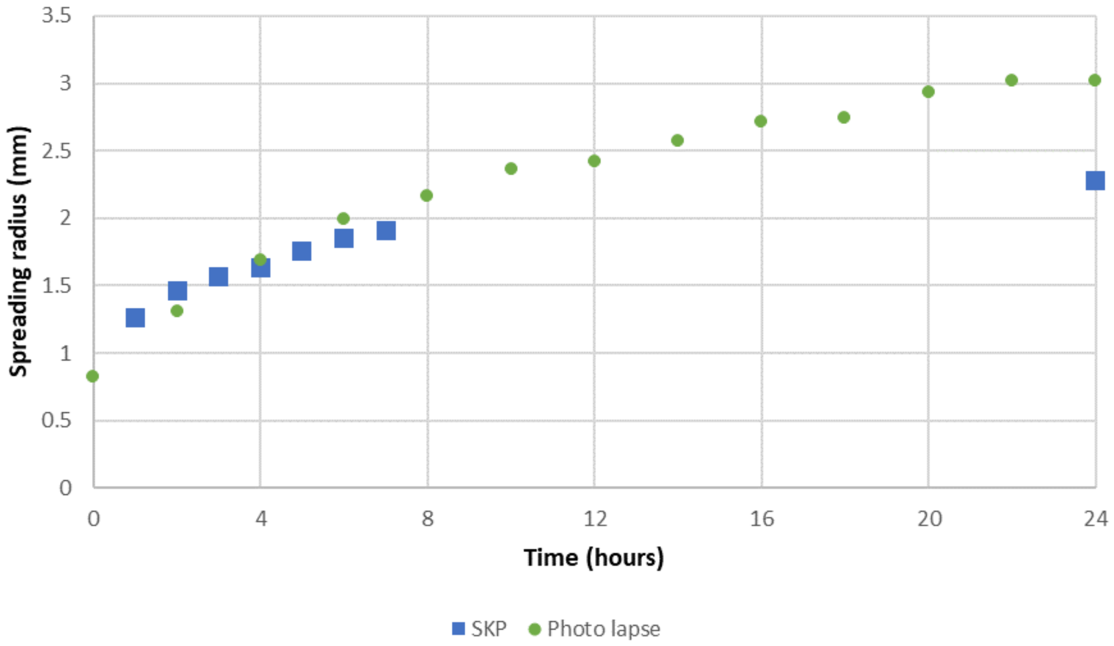

Figure 4.20. Comparison of spreading radii measured from SKP and time lapse photography

Line scans were plotted from the centre of the Volta scans performed at 1, 7 and 24 hours, shown in Figure 4.21. The first scan, shown in green demonstrates a smooth curve, with clear changes in potential at the edges of the droplet. The initial E_{corr} value at the centre of the defect is a -300 mV vs. SHE, slightly higher than the expected -400 mV vs SHE for steel under NaCl. Moving away from the centre of the droplet, the potential rapidly increases to -150 mV vs. SHE at the interface between the droplet and the intact nickel surface. This potential persists across the rest of the surface.

The second scan, in blue, shows a similar peak and significant broadening of lower potential areas away from the droplet. The E_{corr} value at the centre increased slightly to -250 mV vs. SHE and moving away from the defect in the centre rapidly increases to -125 mV vs. SHE. The increase in potential moving outwards slows until -50 mV vs. SHE where the edge of the droplet spreading is reached. After this region, the potential increases rapidly over the region of secondary spreading to 225 mV vs. SHE, where the spreading ceases and the intact nickel surface is reached. The potential at the nickel-plated layer increased from the initial scan, likely due to passivation of the surface in the high humidity environment.

The 24-hour scan, in yellow, shows an initial E_{corr} value of -230 mV vs. SHE, which rapidly increases to -50 mV vs. SHE further away from the defect. The potential then slowly increases to 50 mV vs. SHE over the region of droplet spreading. Moving outwards, from here, the region of secondary spreading shows a rapid increase in potential to more than 250 mV at the edge of the scan area.

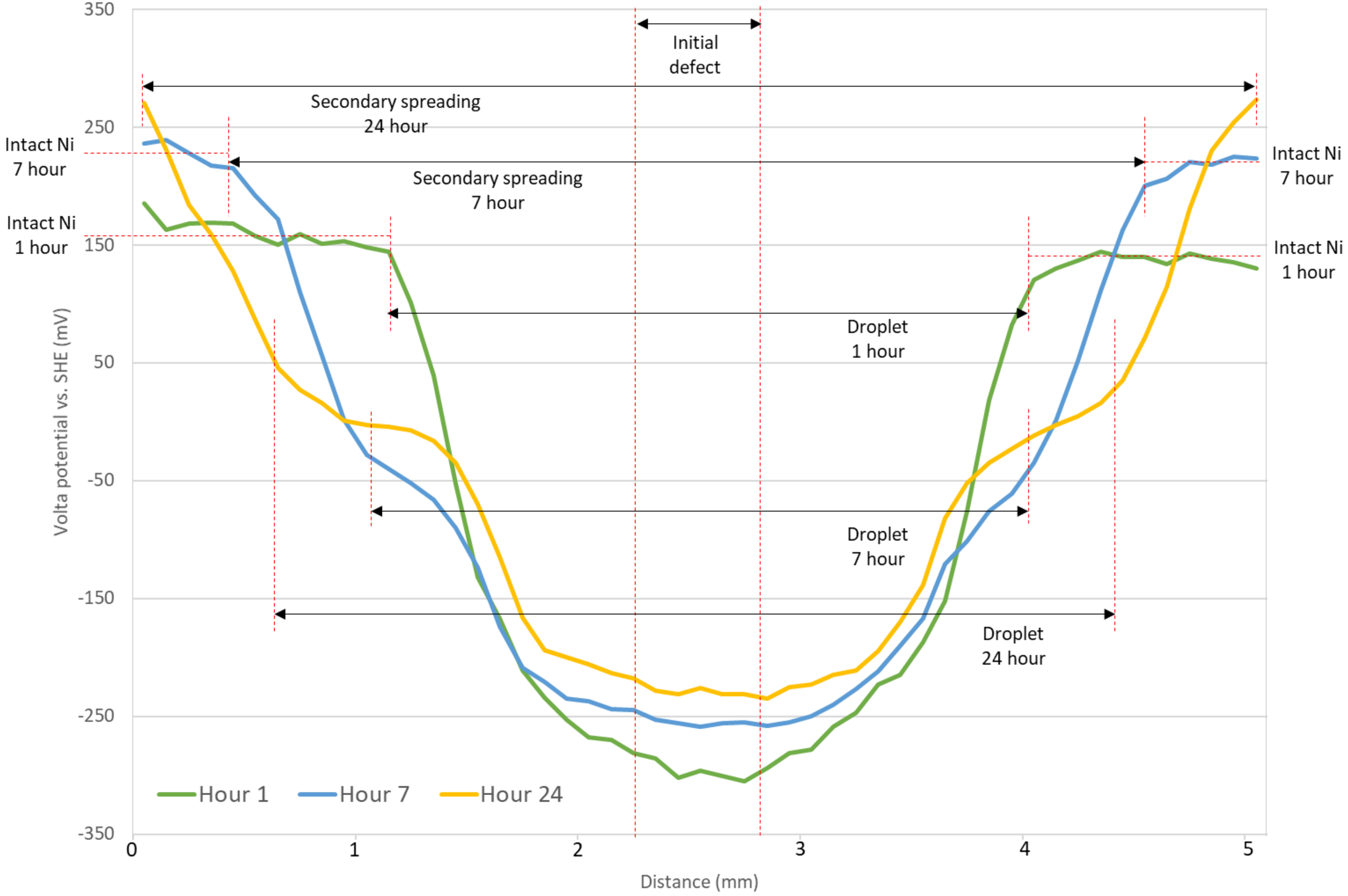

Figure 4.21. Line scans from SKP Volta potential data at hours 1, 7 and 24 for nickel-plated sample with 0.5 mm defect under 2 M NaCl droplet

4.5 Discussion

4.5.1 Atmospheric corrosion of nickel-plated and steel blank samples with defects in chloride-based environments

Results from time-lapse experiments showed secondary spreading phenomena can affect nickel-plated samples with induced defects, and the surfaces of steel blank samples. The occurrence and magnitude of this was dependent on the composition and concentration of the corrosive electrolyte. Secondary spreading can be characterised by the progression of a thin film, a few microns thick and gradually proceeding away from the original droplet; this has previously been observed on zinc, where an increase of 2-3 times the original droplet radius was observed over 90 minutes [51]. There are several proposed mechanisms for this process to happen for NaCl droplets, or not happen for $MgCl_2$ droplets, which will be discussed here.

Whether a region of secondary spreading forms depends on the salt present in electrolyte. Evans [137], in his extensive work on droplet corrosion reported the centre of a droplet forms the anode, and the perimeter the cathode. In the case of sodium chloride, sodium ions migrate towards the edges of the droplet, likely caused by an increase in negatively charged molecules in this region. The extremity of the droplet has the shortest distance for oxygen diffusion, resulting in most of the cathodic oxygen reduction reaction, shown in equation 4.1, to happen at this location.

$$O_2 + 2H_2O + 4e^- \rightarrow 4OH^- \qquad 4.1$$

As the reaction persists, a concentration of OH^- ions builds up at the edge of the droplet, and Na^+ ions migrate here to maintain electroneutrality. The increase in OH^- ions at the circumference of the droplet increases the pH of this area, estimated to be around pH 13 [51]. The opposite happens with chloride ions; as metal dissolution happens, producing positive metal ions at the centre of the droplet, Cl^- ions are attracted here to maintain a net zero charge. This separation of activity is often referred to as a differential aeration cell. A schematic representation of this is shown in Figure 4.22.

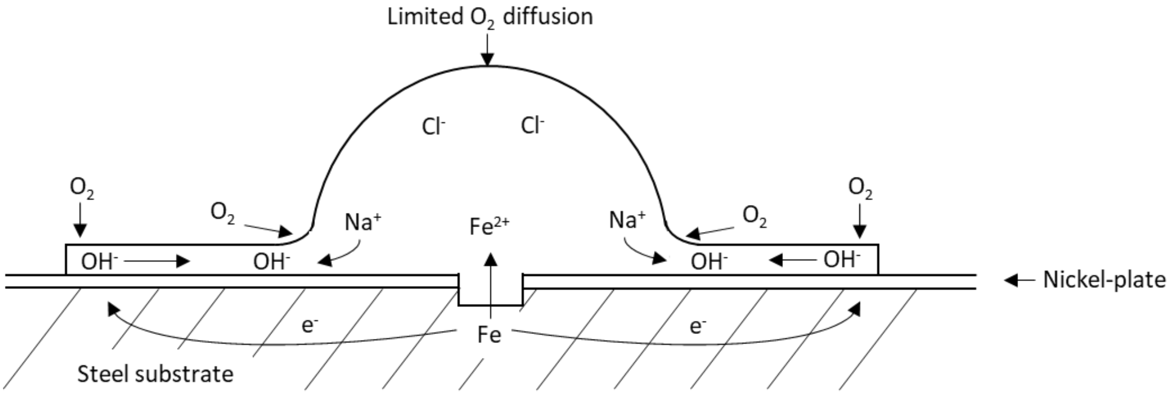

Figure 4.22. Schematic diagram to show spreading phenomena under a NaCl droplet

The SEM/EDS maps obtained in Figure 4.16 to Figure 4.18, show that corrosion products from sodium chloride droplets on nickel-plated and steel samples lead to the formation of sodium species at the periphery of the original droplet and region of secondary spreading, whereas aggressive chloride species remain in the centre. In the case of magnesium chloride most of the products formed remain within the defect and original droplet area. The final images from each experiment show that no corrosion product formed outside the original droplet area when investigated under a magnesium chloride droplet, whilst significant corrosion product formation and spreading formed when using sodium chloride droplets. Similar distributions of elements post-exposure have previously been observed [51], [138].

There are a couple of explanations as to why spreading is initiated under sodium chloride containing droplets. Neufeld et al. [51] suggested this expansion is observed due to changes in surface tension, as the ionic composition of the droplet is altered by the chemical processes happening beneath it. This change in composition leads to the propagation of a thin film, spreading away from the original droplet. Sodium and hydroxide ions are thought to be carried in this film as it spreads. Due to the high pH of this film, CO_2 solubility is high and can be absorbed more easily into the droplet. It is thought to be adsorbed and converted into carbonate species, through the process shown in equation 4.2. The spreading phenomenon is thought to cease on the formation of insoluble carbonate salts, the process shown in equation 4.3.

$$CO_2 + OH^- \leftrightarrow HCO_3^- \tag{4.2}$$

$$HCO_3^- + OH^- \leftrightarrow CO_3^{2-} + H_2O \tag{4.3}$$

Li and Hihara [138] suggested expansion of the secondary spreading area is forced by the high pH of the solution at the circumference of the droplet. They suggested expansion of the wet area is caused by absorption of water to dilute the solution and reduce the pH. This effect was seen on droplets containing NaCl, where the anode was contained in the original droplet area, but the cathode area expanded with time. For droplets containing magnesium chloride, the cathode was limited to the edge of the original droplet and not beyond. A schematic representation of this is shown in Figure 4.23.

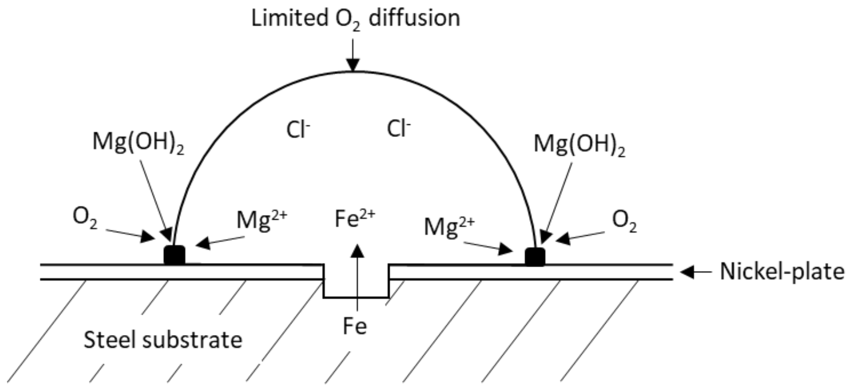

Figure 4.23. Schematic diagram to show lack of spreading phenomena under a $MgCl_2$ droplet

Overall, secondary cathodic spreading is initiated and develops as follows. As discussed, development of corrosion activity under the droplet is caused by the setup of a differential aeration cell. Results from this work have shown cations (Na^+) migrate to the edges of the droplet due to the electroosmotic effect to balance charges. These cations pull water molecules to the edge of the droplet, to dilute the concentration of OH^- ions. As these reactions proceed, the surface tension at the edge of the droplet changes, causing a thin layer of electrolyte to spread outwards. The data obtained from SKP shows the secondary spreading region has a different potential to the defect area and intact nickel surface.

4.5.1.1 Measuring potential over the droplet and spreading area using SKP

The SKP was used observe changes in potential over the droplet and surrounding area of secondary spreading formation. The potential of the initial droplet area remained stable, whilst the region of secondary spreading widened, increasing the area of low potential compared to the intact surface. Similar effects were observed by Neufeld et al. [139] on zinc substrates. The stabilisation of potentials in the secondary spreading region is likely to be due to the formation of stable oxide layers under the alkaline film.

Secondary spreading has been shown to cause separation of anodic and cathodic activity under the droplet, where anodic activity was confined to the centre, whilst cathodic activity spread with increasing secondary spreading zone [51]. This is clearly demonstrated in the SKP maps, by the 250 mV difference in activity seen between the centre of the droplet and the region of secondary spreading in the 24-hour scan. The spreading forms a large cathodic area which acts to increase the rate of oxygen reduction and increase anodic activity at the centre of the droplet. As seen in Chapter 3, increasing cathode size can significantly increase corrosion current at the anode.

The comparison of SKP and time-lapse photography showed a slightly faster and larger secondary spreading region from the photographs. This may be because secondary spreading was visible on the surface prior to any changes in potential on the surface. It is possible the variation in experimental procedure effected the results. The SKP environment chamber had a larger volume to maintain at humidity, so more evaporation of the droplet may have occurred.

4.5.1.2 Variation in results under sodium and magnesium chloride conditions

The reason for the different results observed for experiments in sodium and magnesium chlorides are due to their positions in the periodic table. Sodium, a group 1 metal nearly always forms soluble products. This means it can form soluble compounds with hydroxides and carbonates, both of which are likely to be present in the droplets. Magnesium is a group 2 element and generally forms insoluble precipitates under the conditions experienced at the periphery of the droplet, meaning it is unable to form soluble compounds with either hydroxide or carbonate species. This explains why, although most of the magnesium was seen at the circumference of the droplet, none was seen to spread beyond this as no soluble products could be formed. Solubility calculations for the 0.5 M $MgCl_2$ solution used in this work are shown below and indicate no soluble magnesium hydroxide products can form above pH 8.53; the pH is likely to be significantly greater than this at the edge of the droplet.

K_{sp} magnesium hydroxide = 5.61 x 10^{-12} $mol^3 \cdot dm^{-3}$ [140]

$$K_{sp} = [Mg^{2+}][OH^-]^2 \qquad 4.4$$

$$[OH^-] = \sqrt{\frac{5.61 \times 10^{-12}}{0.5}} = 3.35 \times 10^{-6}$$

$$pH = 14 - pOH \qquad 4.5$$

$$pH = 14 - [-\log(3.35 \times 10^{-6})]$$

$$pH = 8.53$$

Previous experimentation using magnesium chloride droplets has shown no secondary spreading effect, due to its inability to form soluble products [52], [141] under such conditions. On the other hand, sodium hydroxide is highly soluble in water; the pH of solution has little to no effect on its solubility even in the highly alkaline conditions at the edge of the droplet.

4.5.1.3 Effect of increasing chloride concentration

The concentration of sodium chloride had a significant effect on spreading observed on nickel-plated and steel blank samples. In both cases, samples examined under 5 M droplets experienced the least spreading, whilst those examined under 2 M droplets showed the greatest spreading. The differences observed were not only due to the concentration of NaCl, but also the RH these developed inside the environment chamber. To keep the composition of the droplet as similar as possible throughout the experiment, samples were placed in an environment containing a solution of the same concentration, with the aim of maintaining and constant RH and droplet size.

It is well known increasing NaCl concentration leads to increased corrosion, due to increased conductivity of the solution, leading to faster oxidation. However the ability of water to hold dissolved gases, such as oxygen, decreases with the addition of salts [142]. When a solution approaches saturation, oxygen diffusion becomes difficult. As an example, when sodium chloride is added to water, the water molecules separate the sodium and chlorine atoms to form hydrates, due to attraction caused by the hygroscopic nature of salts. Water is a polar molecule as the oxygen atom has a partial negative charge, whilst the hydrogen atoms have a partial positive charge. This means negative chloride ions are attracted to oxygen atoms, whilst positive sodium ions are attracted to hydrogen atoms. The bonds formed are significantly stronger than those formed between water molecules and oxygen atoms, meaning oxygen is forced out of solution when salts such as sodium chloride are added. When oxygen is limited in corrosive electrolyte, cathodic oxygen reduction cannot be completed efficiently due to unavailability of reactants, so becomes the rate limiting step. Previous experimentation using the manganous hydroxide method showed the solubility of oxygen in 1 M NaCl is 27% less and in 4 M NaCl 72% less than in deionised water at 25°C [142]. Values for solubility of oxygen in solutions containing NaCl and $MgCl_2$ are shown in Table 4.2 below. Temperature has been shown to effect oxygen solubility in water [143], however experiments in this chapter happened at a consistent temperature of 22°C so no related effects should be observed.

Data obtained from nickel-plated and steel samples under various chloride conditions showed droplets from 0.1 M to 2 M NaCl contain enough dissolved oxygen for corrosion to proceed without oxygen reduction becoming the rate limiting step. However, at 5 M NaCl oxygen reduction became the rate limiting step as most water molecules were involved in the hydration of sodium and chlorine atoms, reducing the availability of oxygen. This reduced the corrosion rate and therefore quantity of secondary spreading.

Table 4.2. Oxygen solubility and hydration of NaCl and $MgCl_2$ at 25°C in distilled water [142]

NaCl (M)	**Density at 25°C**	**Solubility of O_2 ($cc \cdot l^{-1}$)**	**Hydration**
0.5	1.017	4.92	15.2
1	10.38	4.20	14.0
2	1.075	3.05	11.7
4	1.149	1.62	8.5
$MgCl_2$ (M)			
0.5	1.044	4.37	26.2
1	1.085	3.18	24.0
2	1.160	2.22	15.6
4	1.343	0.54	6.8

Relative humidity also affected the quantity of spreading seen under different NaCl concentrations. The lowest NaCl concentration created the environment with the greatest RH (94%), whilst the highest NaCl concentration led to the environment with the lowest RH (74%). At lower RH spreading was reduced by less availability of moisture in the environment chamber. Due to increased water activity at higher RH, more moisture was available to condense on the surface. It was previously shown at higher RH, a greater number of adsorbed monolayers could form on a metal surface [35]. With aggressive chloride ions present on the surface from the initial droplet, corrosion reactions can progress quickly. Under the 5 M NaCl droplet and 74% RH, less water vapour was present so additional chloride could not increase the corrosion rate and lack of adsorbed water limited the quantity of secondary spreading.

Different metals have different sensitivities to changes in RH. Iron and steel are very sensitive, whilst little effects are seen on nickel [35]. As seen from experiments in this chapter, greater spreading radii were observed on steel compared to nickel-plate. This confirms steel's greater affinity to adsorb water vapour, explaining the increased rate of secondary spreading seen on its surface.

Rate data for nickel-plated samples with 0.5 mm defects, steel blanks and nickel-plated samples with various defect sizes are shown in Figure 4.24 to Figure 4.26 respectively for the first 900 minutes (30 hours). The progression rate of secondary spreading was determined by plotting droplet radius versus square root of time and taking the gradient. These values are shown in Table 4.3. and Figure 4.27.

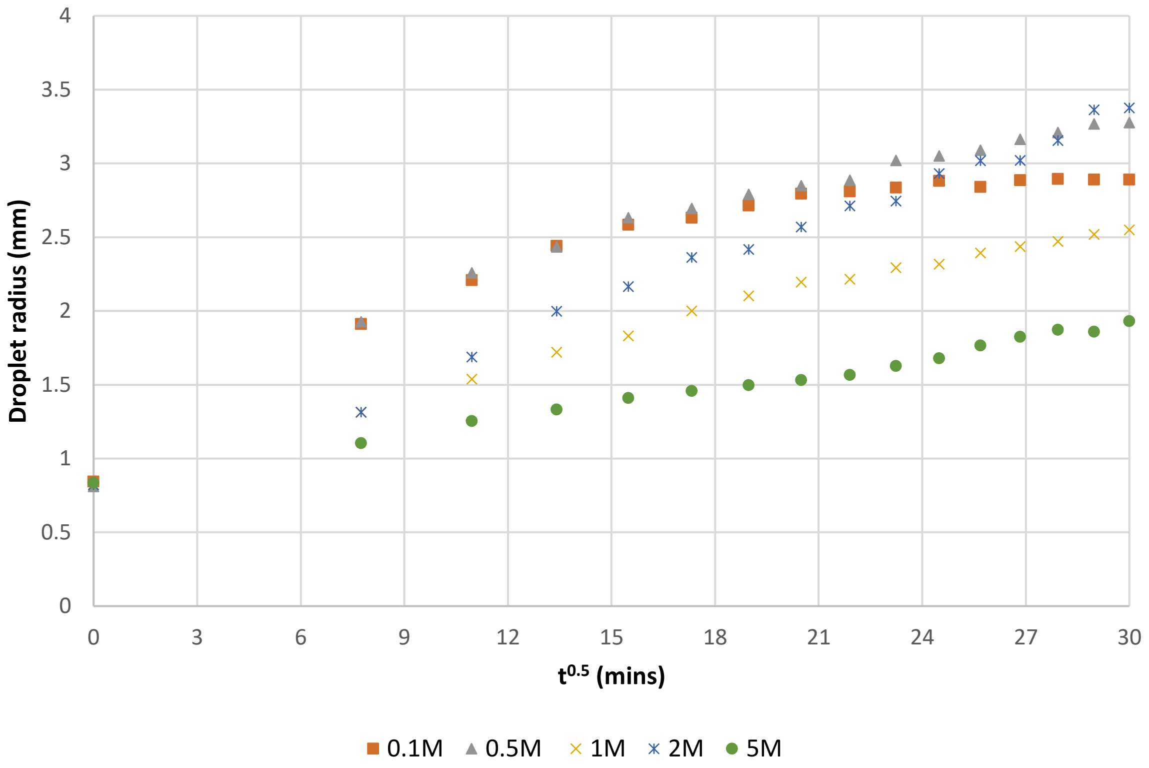

Figure 4.24. Rate data for photo-lapse experiments on nickel-plated steel with 0.5 mm defect

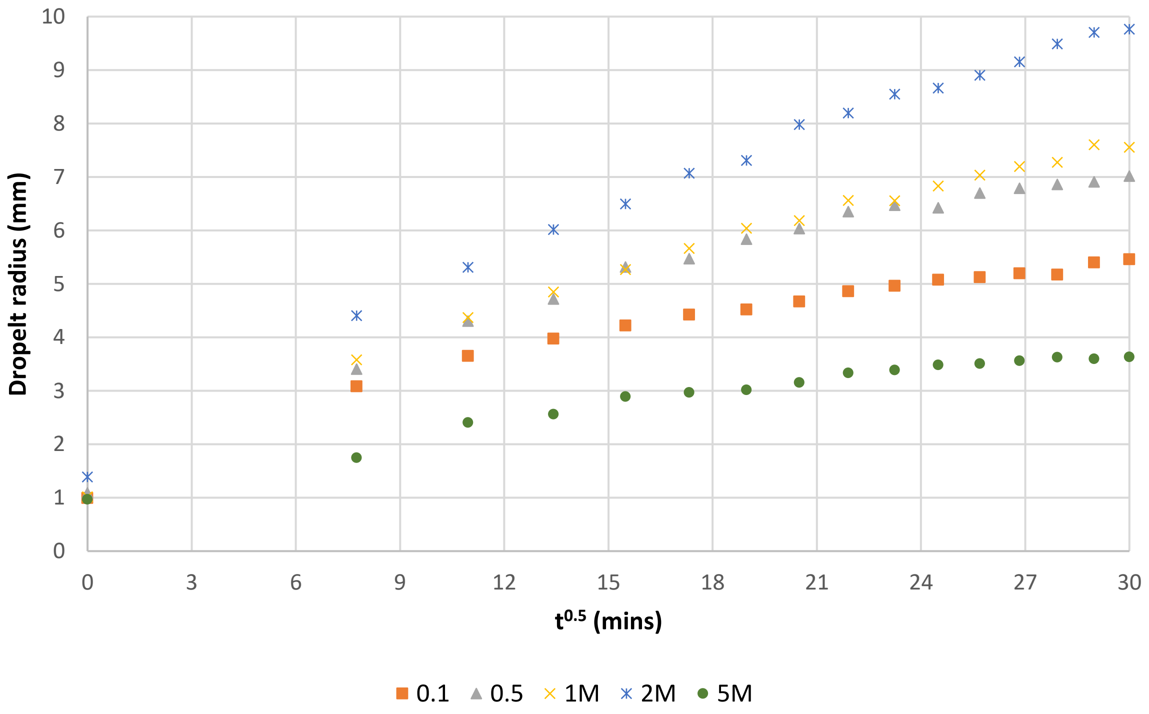

Figure 4.25. Rate data for photo-lapse experiments on steel blanks

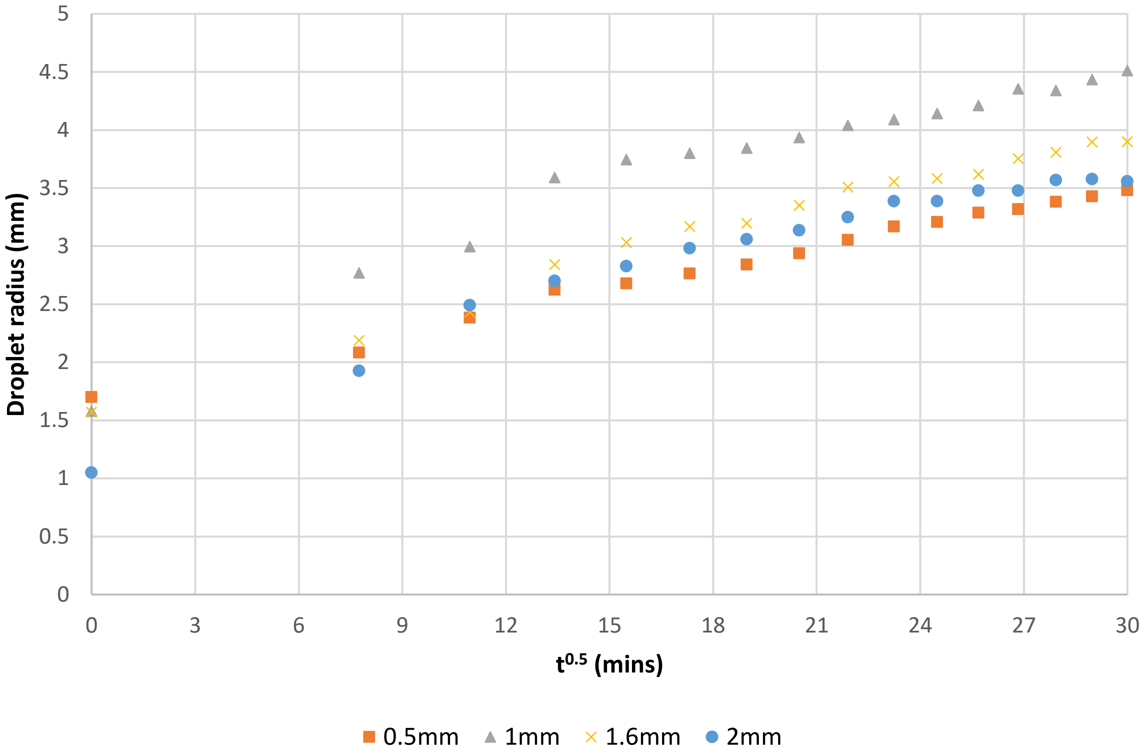

Figure 4.26. Rate data for photo-lapse experiments on nickel plate with different defect sizes

Table 4.3. Secondary spreading rates for samples under atmospheric corrosion conditions

Nickel-plated samples with 0.5 mm defects and various chloride concentrations	
NaCl concentration (M)	**Rate of spreading (mm·min$^{-0.5}$)**
0.1	0.073
0.5	0.062
1	0.049
2	0.086
5	0.041
Steel plated samples under various chloride concentrations	
NaCl concentration (M)	**Rate of spreading (mm·min$^{-0.5}$)**
0.1	0.105
0.5	0.147
1	0.209
2	0.272
5	0.071
Nickel plates samples with various defects under 2 M NaCl	
Hole diameter (mm)	**Rate of spreading (mm·min$^{-0.5}$)**
0.5	0.055
1.0	0.079
1.6	0.070
2.0	0.066

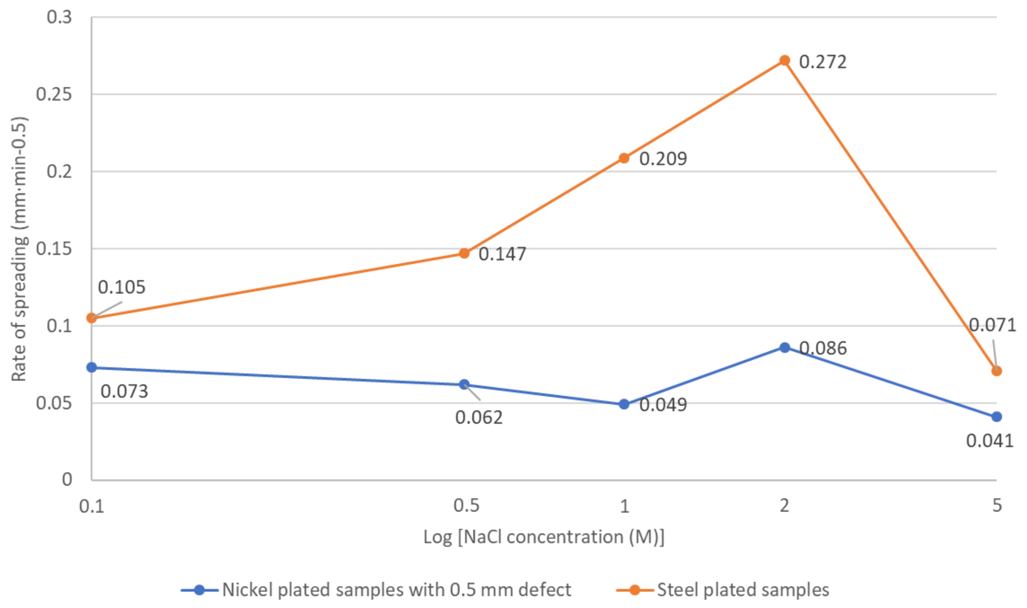

Figure 4.27. Secondary spreading rates for samples under atmospheric corrosion conditions in the presence of NaCl

For nearly every experiment, a close to linear gradient was observed, meaning the reaction on most samples was under mass transport control (cation, Na^+). The one exception was the nickel-plated sample with 0.5 mm defect in 0.1 M NaCl. The gradient was linear for the first 6 hours, however after this spreading rate dropped significantly and eventually plateaued. It is likely in this solution at higher RH and lower NaCl concentration spreading reduces because oxygen reduction becomes the rate limiting factor [119].

4.5.2 Atmospheric corrosion of nickel-plated samples with different defect sizes

Nickel-plated samples with different defect sizes showed similar amounts of spreading in each experiment. A trend of slightly larger defects leading to slightly larger spreading areas was observed for samples with 0.5, 1.0 and 1.6 mm defects, but the sample with a 2 mm defect showed slightly less spreading than expected. Figure 4.15 shows the initial droplet radius was smaller than the other samples, so less spreading may have happened as the larger hole held more of the droplet resulting in less spreading. The cathode area was decreased slightly by this smaller initial radius, possibly leading to slow initiation of the galvanic corrosion cell. The volume of the droplet was consistent, so the same number of reactants were present in each case. This meant the droplet could not spread significantly further, even though the anode size was increased.

This demonstrates the reaction happening in this case was not under anodic control, as only very small increases in spreading distance were observed with increased defect size. Otherwise, as the anode size was increased a more significant effect on spreading distance would have been expected.

4.6 Conclusions

Work in this chapter has shown secondary spreading can be initiated on nickel-plated samples with defects using sodium chloride droplets with a range of concentrations. The greatest amount of spreading was observed under a 2 M NaCl droplet, whilst the least was seen under a 5 M NaCl droplet. A reduction in spreading was seen at the highest NaCl concentration due to the lack of dissolved oxygen. This meant oxygen reduction became the rate limiting step for the development of a secondary spreading region, despite the very thin layer of electrolyte meaning oxygen access to the surface was favourable. Similar effects were observed on the plain steel substrate, with an increase in spreading area due to the reactivity of the metal. The spreading effect was thought to propagate due to changes in surface tension of the droplet as the pH at the edge increased. As the anodic reaction happened at the centre of the droplet, negative chloride ions migrated here to balance the charge of the positive metal ions produced, whilst positive sodium ions were drawn to the edge of the droplet to balance the charge of negative hydroxide ions formed during cathodic oxygen reduction. SEM/EDS showed the presence of chloride ions in the original droplet area, whilst most of the sodium ions had migrated to the region of secondary spreading. This region propagates until insoluble precipitates are formed, commonly with carbonate species present due to dissolved carbon dioxide in high pH areas.

SKP mapped potentials under the droplet and surrounding secondary spreading region, showing the potentials in these regions were very different. At the centre of the droplet, the potential was -250 mV vs. SHE whilst in the area of secondary spreading the potential was 0 mV vs. SHE. This compared to the substrate potential of 250 mV vs. SHE. From this it was assumed anodic activity happened under the original droplet area, whilst cathodic activity happened in the secondary spreading region. As a result, a larger distance of secondary spreading is likely to result in an increased corrosion rate.

Changing the size of the defect in the nickel-plated samples had little effect on the spreading of a 2 M NaCl droplet. There was a small increase in spreading area with increased defect size for most samples, although no significant trend was found.

Droplets containing magnesium chloride did not display any spreading effects, due to the formation of insoluble magnesium hydroxide, preventing the migration of ions beyond the confines of the original droplet. SEM/EDS observations saw chloride ions still migrated to the centre of the droplet and magnesium to the edges, but none was observed passed the boundary of the original droplet.

In conclusion, this work has shown if porosity is present in nickel plate, a corrosion cell could develop due to the galvanic action of nickel and steel. However, under most circumstances the amount of chloride ions present would probably be insufficient to drive corrosion to the extent observed in this work. It is essential the quality of nickel deposits is high, and porosity minimised during production, so coins manufactured in this way will not undergo this form of corrosion in circulation.

Chapter 5. Suitability of electroless nickel plating for coinage applications

5.1 Introduction

Every year, The Royal Mint produces billions of coins for circulation in over 60 countries. There are many different sizes, shapes and compositions used to ensure each denomination is clearly recognisable from another. The cost of producing coins from solid metal sections is constantly increasing, especially those made predominantly from copper or nickel. In recent years coin manufacture has moved away from solid, homogeneous sections and instead utilises plating technologies to cover cheaper metals, like steel, in a thin layer of another. In the UK until 1992 one and two pence coins were made from a 97% copper bronze alloy. With the rising price of copper, there was a risk the intrinsic value of the metal in the coin may surpass its designated value. From September 1992, both of these coins were manufactured by copper-plating a steel blank to reduce raw material costs [144], [145]. Likewise, more recently UK five and ten pence coins are no longer a homogeneous cupro-nickel alloy (75% copper, 25% nickel). Since January 2012, these coins have been produced by electroplating nickel onto steel blanks [146], [147].

Nickel is widely used as the outer layer of coins for several reasons. This is mainly because steel is not very corrosion resistant and nickel provides good protection from most environments coins encounter in circulation. Red rust forms in atmospheric conditions very quickly on untreated steel, whereas nickel is significantly more inert under the same conditions. Nickel is used as a barrier coating, meaning it needs to completely cover the substrate to provide protection. Steel is more reactive than nickel, so any exposed substrate will cause the steel to corrode in preference to the nickel coating. Nickel plating is prone to surface porosity, so a sufficient layer must be deposited to ensure the entire substrate is covered, normally around 25 µm. Due to the application of electrical current during plating, the plated layer will not be even as current concentrates at corners, so substrates must be plated for an adequate time to allow all areas to obtain a minimum plating thickness. This leads to some areas being coated in a thicker layer of nickel than necessary, increasing production costs.

Whilst changes in composition meant the face value of coins has remained below their intrinsic value, and reduced raw metal costs for The Royal Mint, electroplating is an expensive process. As well as initial investments to buy new equipment, consumables such as dissolvable anodes are required. An applied current is needed to reduce the dissolved metal cations in solution, which proceed to form a thin metal layer on a substrate. This process is very energy intensive, which leads to high energy consumption and large electricity bills. As a result, The Royal Mint are interested in finding an alternative, less energy intensive technology to reduce plant operation costs, and reduce the environmental impact of their manufacturing processes. This has led to investigations into the possibility of using electroless nickel plating as a less energy intensive manufacturing method.

Electroless nickel plating has been suggested as an alternative technology to standard nickel electroplating. There are many uses for this process, for example in the oil and gas industry, for automotive and aerospace components and in the chemical processing plants [85]. Electroless nickel coatings are co-deposited with an alloying element, depending on the reducing agent used in the plating bath. The reducing agent used here was sodium hypophosphite, so the deposit was nickel-phosphorous. The phosphorous content effects the properties of the deposit, overall electroless nickel deposits have lower density, lower melting point, more uniform deposit, higher hardness, better wear resistance, lower ductility and higher corrosion resistance compared to standard nickel electroplated layers [62], [72], [85], [86], [88].

This chapter will investigate three proprietary solutions provided by McDermid Enthone plated via electroless deposition onto steel substrates. These have been compared to a solution made in-house, plated via electroless deposition onto iron substrates at three different temperatures and solution pH's. The properties of these deposits have been examined using Scanning Electron Microscopy (SEM) to analyse the surface composition, observe surface features and measure cut edge plating thickness; potentiostat based corrosion monitoring techniques and Vickers hardness testing. The results from these experiments were compared to those obtained from a standard nickel electroplated layer. The main aim of this work is to establish if electroless nickel plating could be a viable alternative to more traditional electroplating methods, by evaluating deposit composition, corrosion properties and evenness of deposition.

5.2 Samples

The electroless nickel-phosphorous samples were plated from commercially available solutions, and from a solution made in-house. The procedures for plating from both bath types are listed in sections 2.4.1 and 2.4.2. Standard nickel electroplated samples were manufactured as described in section 2.5.

5.2.1 Sample preparation

Prior to any experimentation, samples were polished with a 5 µm alumina paste to remove any oxide layers. Samples for potentiostat experimentation were held in a sample holder, exposing an area of 0.95 mm^2 to the electrolyte.

5.3 Experimental methods

The Scanning Electron Microscope (SEM) used was a Hitachi TM3000 equipped with a Bruker Quantax70 EDS system, operated at an accelerating voltage of 15 V. Images were taken at either 1000 or 1200 times zoom, and EDS scans were carried out for 100 seconds each.

Electrochemical experiments including open circuit potential (OCP), linear polarisation resistance (LPR) and potentiodynamic polarisations (PDP) were carried out using a Solartron SI 1280 potentiostat, controlled by a PC and Scribner Associates CorrWare software. The electrolyte was 3.5% NaCl neutralised to pH 7 using 1 M and 0.1 M NaOH solutions. All experiments were carried out using a saturated calomel electrode (SCE) as the reference. Where a counter electrode was necessary, a platinum gauze was used. All samples were first held for 1-hour at OCP, to allow a stable surface oxide to develop. Linear polarisation resistance sweeps were carried out ±10 mV either side the OCP, at a rate of 0.25 $mV{\cdot}sec^{-1}$. Potentiodynamic polarisations were swept from -0.7 V to 0.2 V vs. SCE at a scan rate of 1 $mV{\cdot}sec^{-1}$. A detailed description of these techniques is given in section 2.8.

Hardness testing measures a material's resistance to permanent mechanical deformation. This is a very important property to consider for coinage alloys, as blanks must be minted to become legal tender. If an alloy is too hard, the image can lack definition, or crack on deformation, leading to delamination of the plated layer. If an alloy is too soft, the metal may not hold the image in circulation. Investigations was carried out using an Innovatest machine to perform Vickers hardness testing.

5.4 Results

5.4.1 Properties of samples plated from commercially available electroless nickel plating baths

Scanning Electron Microscopy (SEM) was employed to examine deposit microstructure and measure phosphorous incorporation using EDS. This was compared to the phosphorous content predictions provided by MacDermid Enthone. Three areas were scanned on each sample using an accelerating voltage of 15 kV. The average phosphorous contents measured by EDS for each sample are shown in Table 5.1 and Figure 5.1, below.

Table 5.1. Average EDS estimated phosphorous content for each plating time – commercial bath

Solution/plate time	30 mins (wt.% P)	60 mins (wt.% P)	120 mins (wt.% P)
Niklad ELV 835	10.17	9.32	9.66
Niklad ELV 849	9.98	9.98	10.28
Vand-Aloy 4100N	10.20	10.57	10.59

As these solutions are proprietary, the exact composition is unknown. However, each bath will contain certain components to allow plating to occur. A source of nickel ions will be present, along with a reducing agent, at least one complexing agent and most likely additional stabilising compounds.

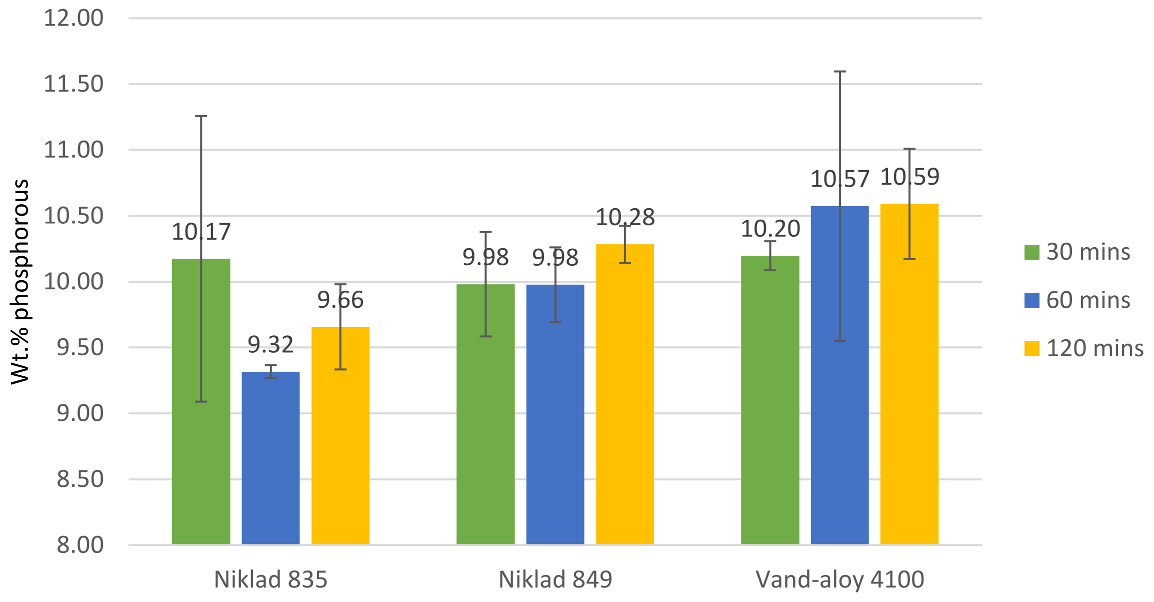

Figure 5.1. Average EDS estimated phosphorous content for each plating time – commercial bath

The results for all three solutions are similar, with a small range of 9.3 to 10.6 wt.% phosphorous across all three baths. The average from the Niklad ELV 835 solution was 9.72 wt.% P from a predicted range of 4-7 wt.% P, the average from the Niklad ELV 849 solution was 10.08 wt.% P from a predicted range of 7-9 wt.% P and the average from the Vand-Aloy 4100N solution was 10.45 wt.% P from a predicted range of 10-12 wt.% P. There was little distinction in phosphorous contents between the samples, making it difficult to relate properties obtained in this work to their composition. Some variation from predicted phosphorous contents could be due to low process control – pH was not monitored, and temperature was checked by eye using a mercury-in-glass thermometer. If plating solution composition is not kept under close control or if there are fluctuations in temperature or pH, significant variation in the composition and properties of the deposit can be observed [68], [148].

Images of the surface at 1000 times magnification are shown in Figure 5.2. Initial observations suggest clear differences in the surface features of the deposits. Samples plated from the Niklad ELV 835 solution have uniform size and distribution of nodules, with some agglomerations sitting above the surface. Images taken of samples plated in the Niklad ELV 849 solution show very smooth overall coverage, with few individual nodules visible. A few nodules can be seen sat above this continuous layer. Finally, samples plated from the Vand-Aloy 4100N solution have a much finer structure with much smaller nodules forming the surface. At lower plating times, small channels are visible in the top layer, leaving an uneven surface finish. Some larger nodules are present on the surface of all the Vand-Aloy samples, appearing to sit above the finer structure.

Plate time/solution	**Niklad ELV 835**	**Niklad ELV 849**	**Vand-Aloy 4100N**
30 minutes	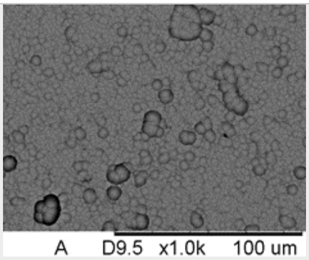	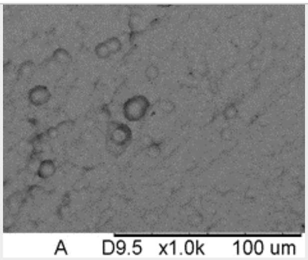	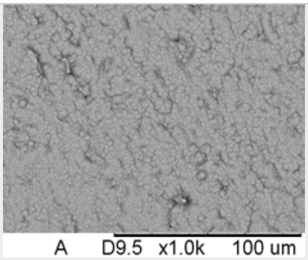
60 minutes	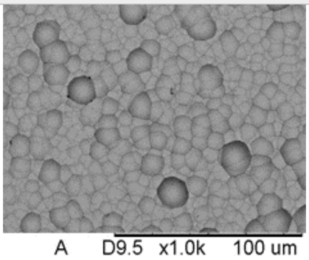	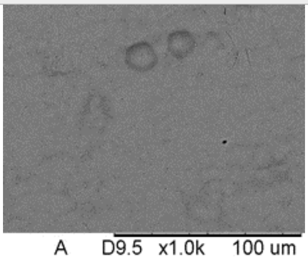	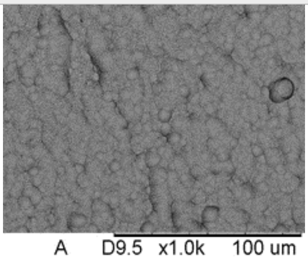
120 minutes	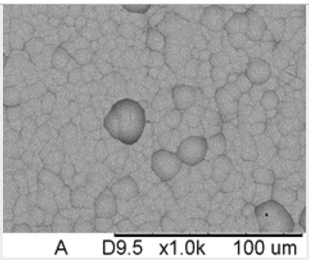	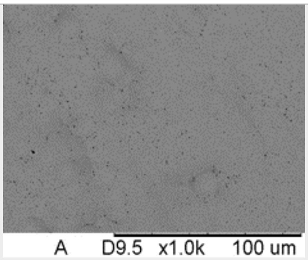	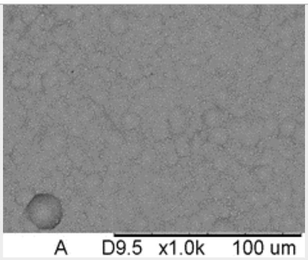

Figure 5.2. SEM images at 1000x magnification - commercial baths

Samples were sectioned and mounted for cut edge analysis. An average value for plating thickness and consistency were of interest. Samples for such investigation would normally be mounted in conductive, thermosetting Bakelite under high pressure. However, for this type of deposit hot mounting can promote the formation of cracks in the plated layer. This can be avoided by using a cold mount system, with no applied pressure [149]. Therefore, an acrylic conductive cold mount system, supplied by Spectrographic (Tong Park Industrial Estate, Bradford, BD17 7QD) was chosen. The main advantage of this system is that carbon is the conductive filler, compared to those that include either nickel or copper, which could affect the results seen by SEM/EDS. The average measurements taken are shown in Table 5.2 below. A typical micrograph taken during this investigation is shown in Figure 5.3.

Table 5.2. Plating thicknesses of samples deposited from commercial baths

Plating solution ↓		Plating thickness (µm)	
Plating time →	**30**	**60**	**120**
Niklad ELV 835	6.5 (± 1)	10.5 (± 0.1)	22.0 (± 0.3)
Niklad ELV 849	6.5 (± 0.4)	13.5 (± 0.3)	23.5 (± 0.2)
Vand-Aloy 4100N	3.5 (± 0.1)	8.0 (± 1)	18.5 (± 0.4)

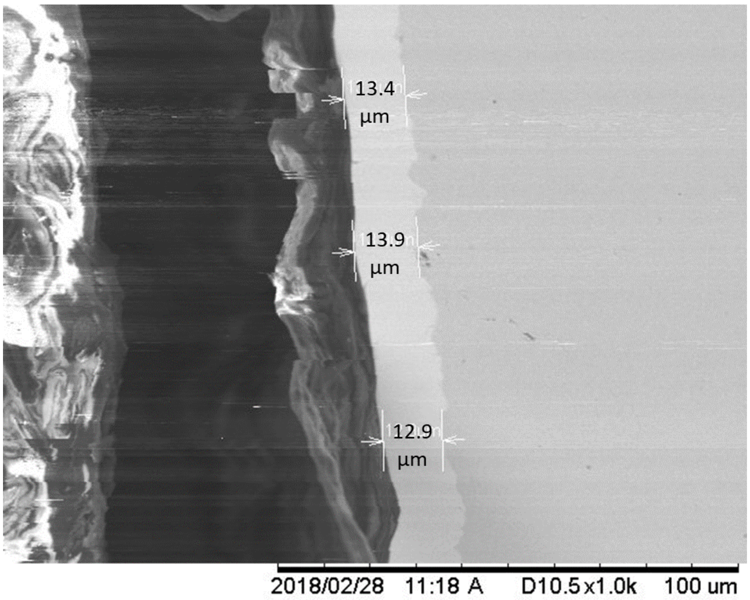

Figure 5.3. Typical cross section micrograph (Niklad ELV 849, 1-hour plating duration)

The documentation provided with each commercial solution estimated the plating rate achievable. For Niklad ELV 835, the estimated plating rate was 20-25 $\mu m \cdot hr^{-1}$, and the average achieved was 11.5 $\mu m \cdot hr^{-1}$. For Niklad ELV 849, documentation suggested a rate of 15-22 $\mu m \cdot hr^{-1}$, and the average measured rate was 12.8 $\mu m \cdot hr^{-1}$. Finally, the predicted plating rate for Vand-Aloy 4100N was 8-15 $\mu m \cdot hr^{-1}$, whilst the average measured plating thickness was 8.1 $\mu m \cdot hr^{-1}$. The plating rates for Niklad ELV 835 and 849 solutions were considerably less than predicted by MacDermid Enthone.

The results acquired from SEM suggests samples plated from proprietary solutions have slightly different phosphorous contents. As an average across the plating times, phosphorous content increased slightly from 9.72 wt.% P, to 10.08 wt.% P and 10.45 wt.% P from Niklad ELV 835, Niklad ELV 849 and Vand-Aloy 4100N respectively. Predicted compositions from the documentation provided suggested phosphorous contents of 4-7 wt.% P, 7-9 wt.% P and 10-12 wt.% P could be achieved from solutions Niklad ELV 835, Niklad ELV 849 and Vand-Aloy 4100N respectively. The deposits showed a variety of nodule sizes and agglomerations on the surface. It is difficult to establish if this is due to the slightly different phosphorous contents or related to the differing plating bath compositions.

For open circuit experiments, samples were exposed to 3.5% NaCl at pH 7 for 1 hour; long enough for surface oxides to stabilise and reach equilibrium conditions. Bai et al. [89] found similar alloys reached a steady state after 15-20 minutes in 3% NaCl, so this allowed plenty of time for an accurate rest potential to be reached.

The results shown in Figure 5.4 are averages of the final 30 minutes experimental data. For all plating solutions, there was a small decrease in OCP with increased plating time. This indicates a thicker layer of the nickel phosphorous alloy may result in a slightly more thermodynamically active layer. The results also showed a small decrease in OCP with increased phosphorous content.

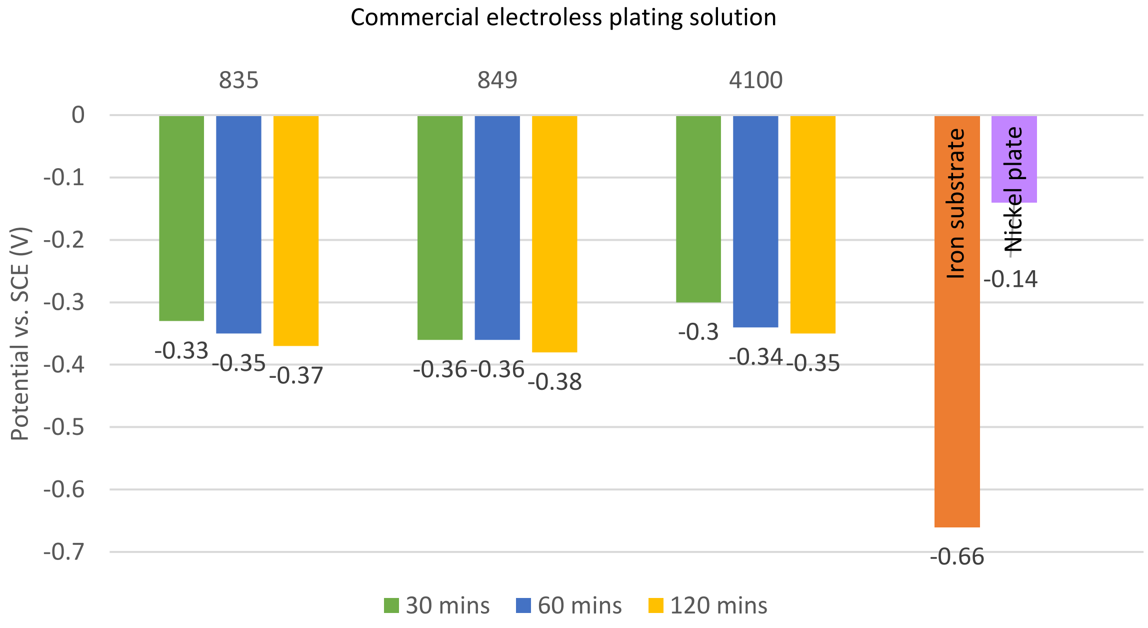

Figure 5.4. OCP in 3.5% NaCl pH 7 samples from commercial electroless plating baths

Potentiodynamic Polarisation (PDP) is an electrochemical technique which applies a potential bias to a sample accelerating the corrosion reaction and allowing an estimate for mass loss to be calculated. Here, the potential was swept from -0.7 V vs. SCE, in the positive direction at a rate of 1 $mV \cdot s^{-1}$. This starting value was chosen to be 300 mV lower than OCP. The experiment was terminated when current density was greater than 0.001 $amps \cdot cm^{-2}$. Tafel extrapolation was used to obtain a value for I_{corr}, the corrosion current. I_{corr} was used to estimate nickel mass loss, as described in sections 2.8.2 and 2.8.3. Examples of the curves obtained for the samples plated in the Niklad ELV 849 baths are shown in Figure 5.5, and the full results in Figure 5.6. The curves shown in Figure 5.5 indicate little difference in the corrosion behaviour of these samples around the OCP, but show some variation in breakdown potential at higher potentials.

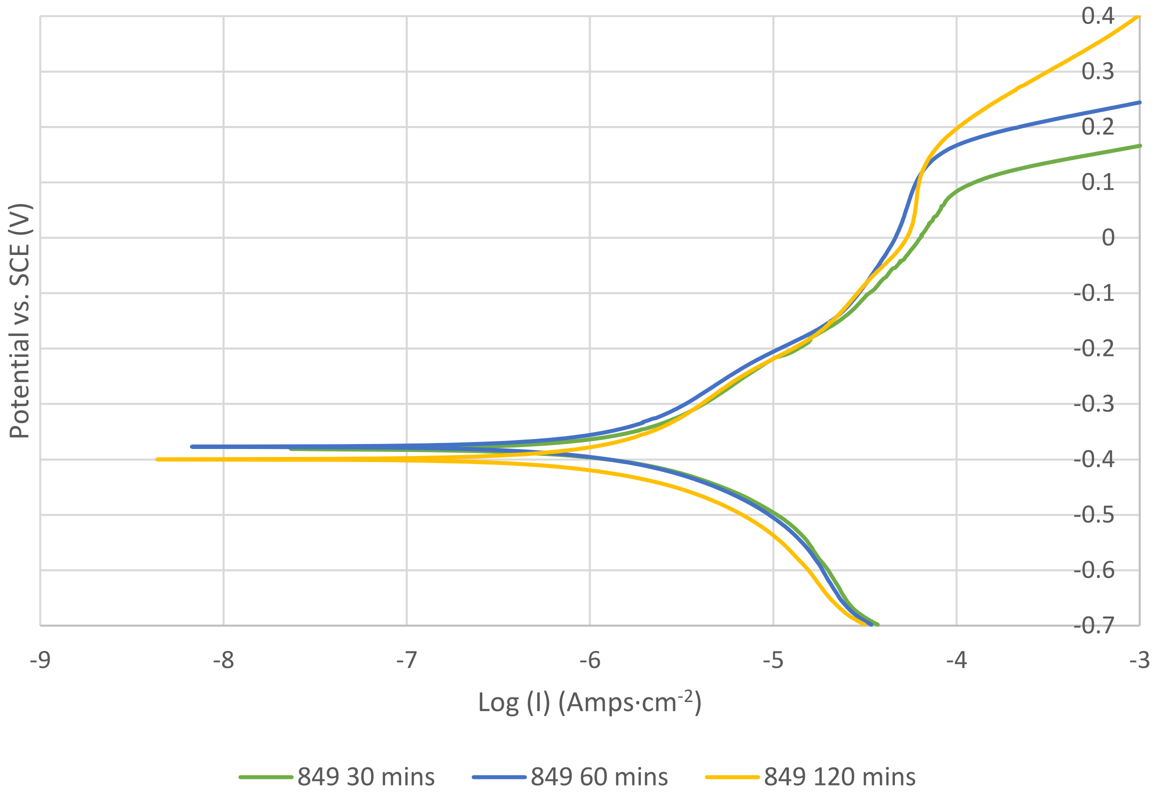

Figure 5.5. PDP curves for MacDermid Enthone Niklad ELV 849 samples at varies plating times

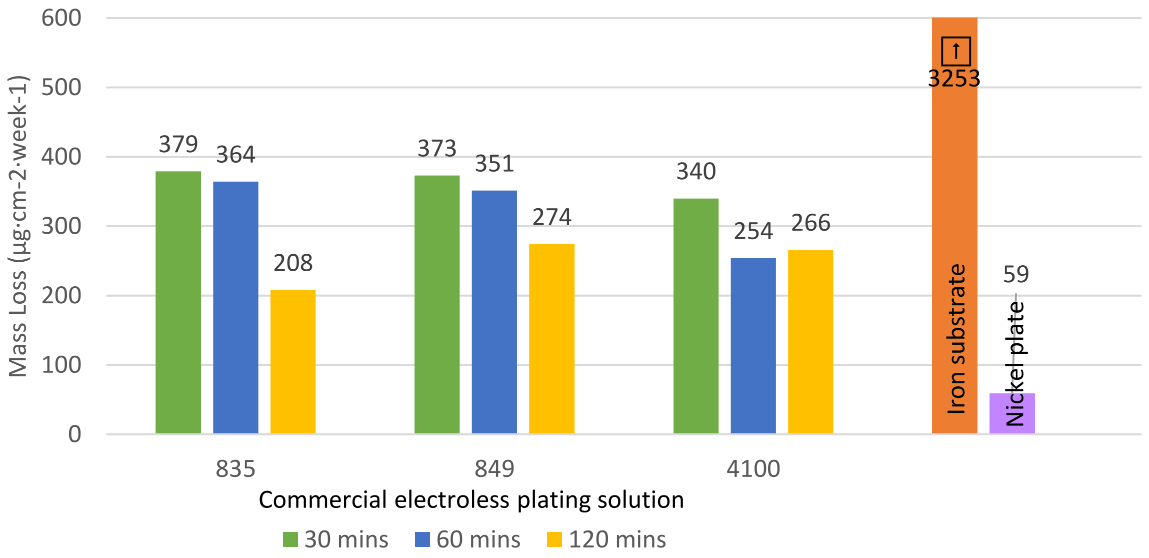

Figure 5.6. Estimated mass loss from PDP experiments for commercial baths

The results showed longer plating times resulted in lower estimated mass loss, most likely due to the formation of better barrier protection for the substrate. Samples plated for shorter times are more likely to contain pores, providing easy initiation points for localised corrosion, leading to increased corrosion rates. The general trend suggests increasing phosphorous content decreases the corrosion rate, although this requires repeats and samples with a wider range of phosphorous contents to confirm.

Vickers hardness testing was carried out with a load of 1 kg held for 10 seconds. Three indents were made in each sample, an average of these results is shown in Figure 5.7 below.

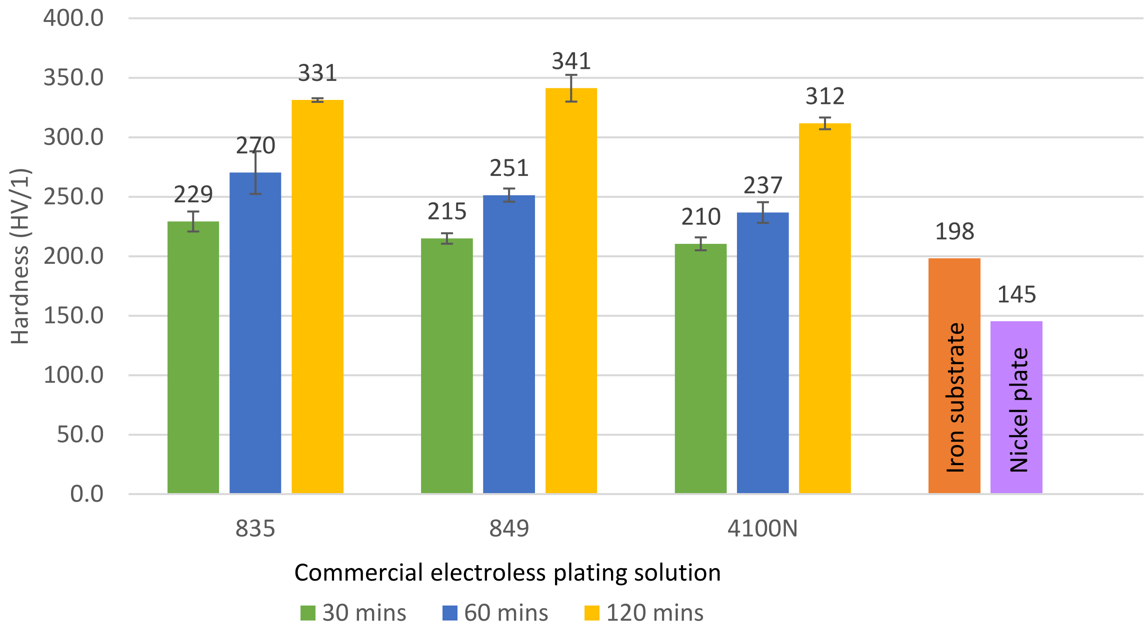

Figure 5.7. Results from Vickers's hardness testing from commercial baths

The results show a small decrease in hardness with increasing phosphorous content, however due to the low variation in phosphorous content no significant conclusions can be made. There is an obvious increase in hardness with increasing plating time. This could be due to lower interaction with the softer substrate below, increasing the measured hardness.

5.4.2 Properties of samples plated in-house at a range of pH's and temperatures

As the compositions of the commercially available plating solutions used above are unknown, a more systematic approach was required. This was achieved by developing an electroless nickel plating bath in the laboratory where the composition was known and kept constant, whilst variables such as temperature, which was varied from 70ºC to 80ºC and pH, which was varied from 4 to 6 and the effects on deposit properties were investigated. This solution contained 10 g·L^{-1} sodium acetate, 20 g·L^{-1} sodium hypophosphite and 30 g·L^{-1} nickel sulfate. A full description of the solution preparation can be found in Section 2.4.2.

SEM was used initially to examine the composition and structure of the deposits. These properties were then related to the pH and temperature of the plating bath. Three areas on each sample were scanned using a Hitachi Table-top Microscope (TM3000) equipped with a Bruker Quantax70 EDS system. The average phosphorous contents measured by EDS are shown in Table 5.3 and Figure 5.8.

Table 5.3. Average EDS estimated phosphorous content for different plating pH and temperature – in-house bath

pH/ Bath T (°C)	**70 (wt.% P)**	**75 (wt.% P)**	**80 (wt.% P)**
4	12.09	15.64	14.29
5	10.39	11.24	12.85
6	7.92	8.18	8.69

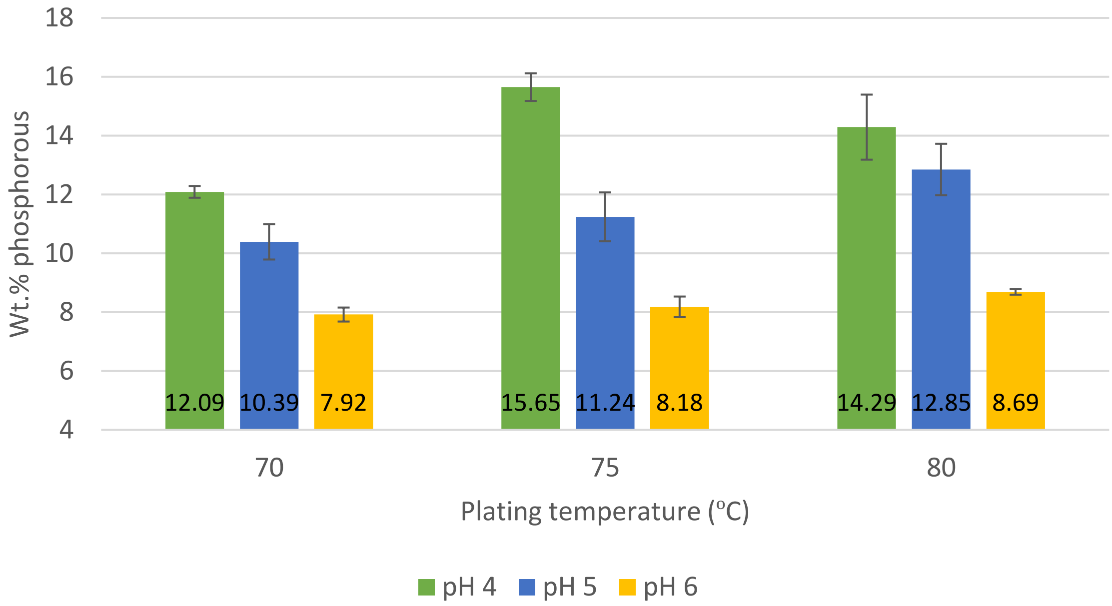

Figure 5.8. Average EDS estimated phosphorous content for different plating pH and temperature – in-house bath

Results showed changes in bath pH and temperature affected the amount of phosphorus co-deposited with nickel. Overall, there was a small increase in phosphorous content with increasing bath temperature, and a significant increase in phosphorous content with decreasing bath pH. The deposit containing the lowest phosphorous content was from the 70°C pH 6 bath, and the highest phosphorous content deposit was from the 75°C pH 4 bath. A range of phosphorous content from 7.92 to 15.65 wt.% P was obtained. The properties and behaviour of these samples can be related to their differing phosphorous contents.

Images of the surfaces were taken at 1200 times magnification and are shown in Figure 5.9. All the samples showed a similar structure; a generally smooth structure with nodules and agglomerations at the surface. The surface features varied depending on plating pH and temperature. Samples plated at higher pH showed an increased number and size of nodules and agglomerations on the surface. Increases in temperature caused a decrease in the frequency of these surface features.

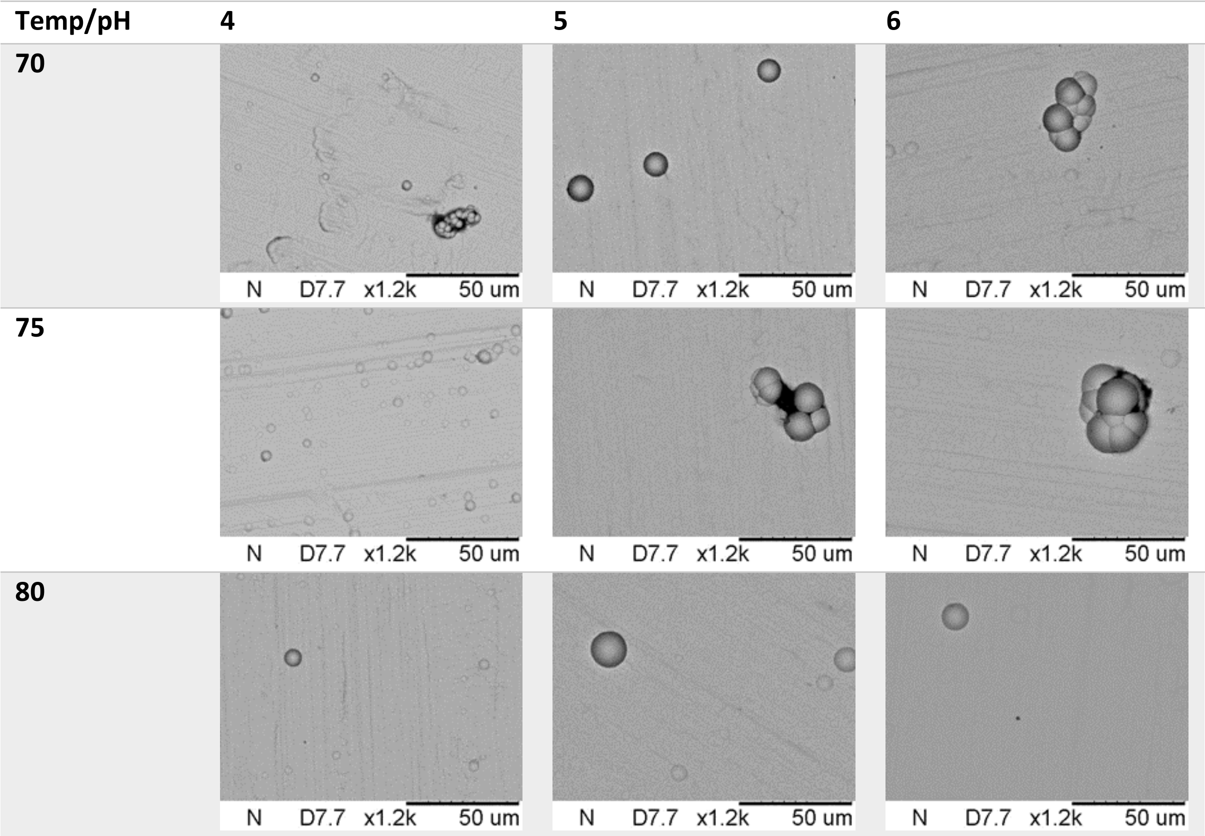

Figure 5.9. SEM images at 1200x magnification - in-house bath at different plating temperatures and pH's

Samples were sectioned and mounted to perform cross sectional analysis. Measurements of plating thickness were taken and are shown below in Table 5.4. As the pH and temperature of the bath increased, the plating thickness also increased. The pH had a great effect on plating thickness, which on average increased from 2.9 µm to 8.7 µm to 12.0 µm at pH's 4, 5 and 6 respectively, whereas temperature increases led to average plating thicknesses of 6.4µm, 8.0µm and 9.1µm at temperatures of 70°C, 75°C and 80°C respectively.

Table 5.4. Deposit thicknesses of samples plated from in-house baths after plating for 1 hour

Bath pH ↓	**Plating thickness (µm)**		
Bath T (°C) →	**70**	**75**	**80**
4	1.6 (± 0.1)	2.9 (± 0.1)	4.3 (± 0.1)
5	8.0 (± 0.1)	9.0 (± 0.1)	9.0 (± 0.1)
6	9.5 (± 0.1)	12.5 (± 0.2)	14.0 (± 0.1)

SEM results show by varying pH and temperature of the plating bath, composition of the deposit can be varied significantly. Samples from these baths had a range of phosphorous contents, from 7.92 to 15.65 wt.% P. The images of the surfaces showed little texture, with a few small nodules and agglomerations present. A lower bath pH and higher temperature resulted in the lowest number of surface features, and smoothest overall surface. Increasing plating temperature and pH led to an increase in the deposition rate. As shown in Table 5.4, the pH 4 bath resulted in low plating thicknesses which may not provide good protection to the substrate, whereas the deposits from the pH 5 and 6 baths are of sufficient thickness to protect the underlying iron substrate completely.

Open circuit potential measurements were carried out for 1 hour, so samples could reach equilibrium in the electrolyte. The results shown below in Figure 5.10 are averages of the final 30 minutes of experimental data. The open circuit values were all close together. The lower the OCP values indicate less thermodynamic stability and a highly likelihood of corrosion. On average the samples plated at pH 6 have the highest value, followed by pH 4, then pH 5. Results show phosphorous content had limited effect on the OCP values observed – those with the lowest phosphorous content showed the highest potentials, whilst the lowest potentials were seen on the samples with mid-range phosphorous content.

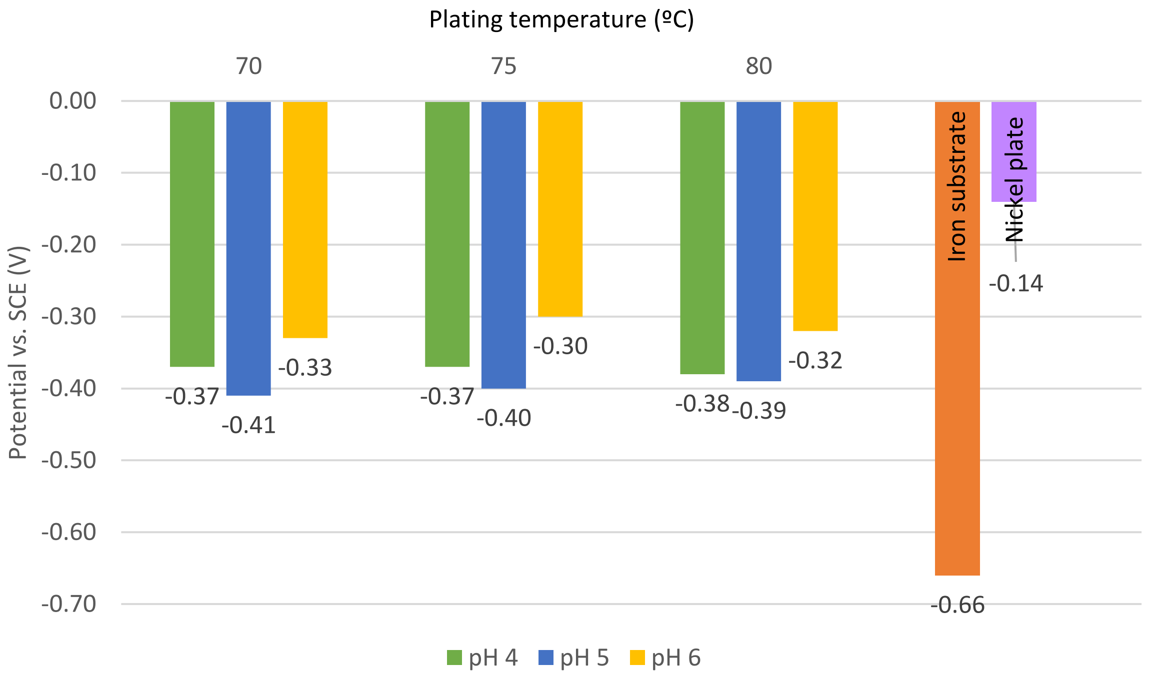

Figure 5.10. OCP values of samples plated from in-house baths

Potentiodynamic polarisations were carried out on these samples. The potential was swept from -0.7 V vs. SCE, in the positive direction at a rate of 1 mV.s^{-1}. The experiment was terminated when the current density was greater than 0.001 amps·cm^{-2}. Tafel lines were extrapolated to obtain co-efficient values for the Stern-Geary equation, used to calculate mass loss from linear polarisation resistance experiments, as described in section 2.8.2.

Linear polarisation resistance was used to approximate corrosion rate in open circuit conditions to calculate mass loss values. This process is explained in section 2.8.3. The calculated mass loss values are shown in Figure 5.11 below.

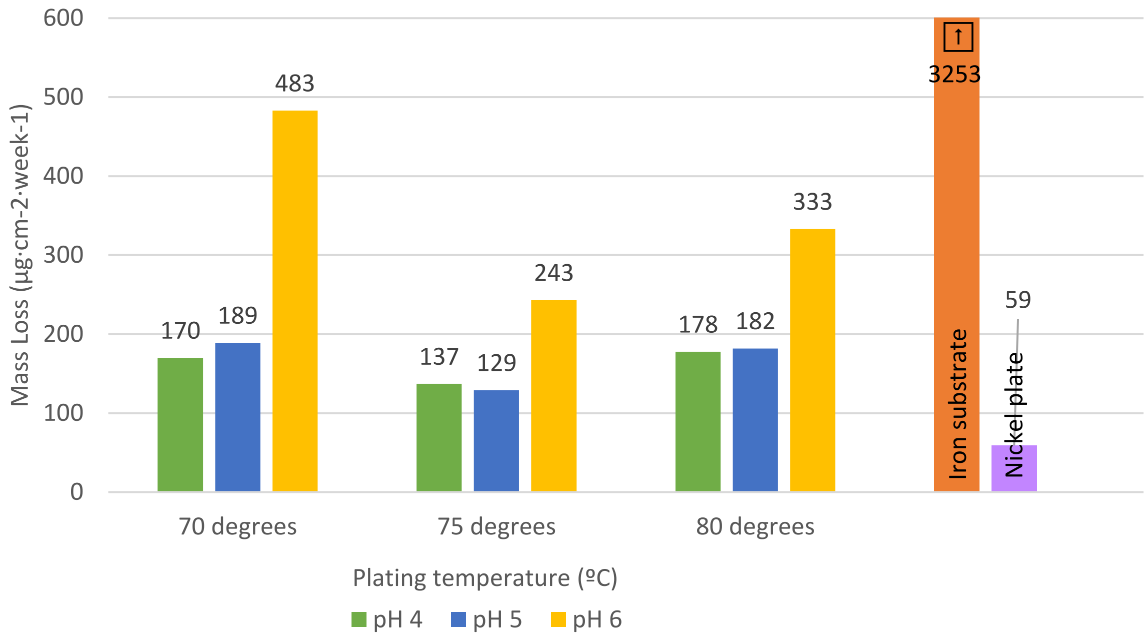

Figure 5.11. Mass loss values (LPR derived) for samples plated from in-house baths

Operating pH and temperature change the corrosion properties of the deposits. First, the effect of pH was examined. From the results obtained, higher bath pH leads to lower phosphorous contents, which in turn reduces the corrosion resistance of the sample. There was little difference in corrosion performance between samples plated in pH 4 and 5 baths. On average samples plated from the pH 4 bath have marginally better corrosion resistance, due to their higher phosphorous content. Operating temperature also effects corrosion performance of the deposit. Samples plated at each temperature had average mass loss values of 281, 170 and 231 µg·cm^{-2}·week^{-1} for 70, 75 and 80°C respectively. The samples plated at 75°C showed lower mass loss values than samples plated at the same pH at lower and higher temperatures.

Overall, results showed a lower bath pH results in deposits with better corrosion resistance, due to the increase in phosphorous co-deposited with nickel. Altering bath temperature also affected corrosion resistance. The median temperature, 75°C, produced the most corrosion resistant samples. This data showed higher phosphorous contents provide better corrosion resistance. It also demonstrated identifying optimum operating conditions for baths is essential for producing the best deposit; neither extremes of temperature provided deposits with the best corrosion resistance.

Vickers hardness testing was carried out on all samples plated from this bath. A load of 1 kg was applied for 10 seconds. Three indents were made in each sample, and an average of the calculated hardness is shown below in Figure 5.12.

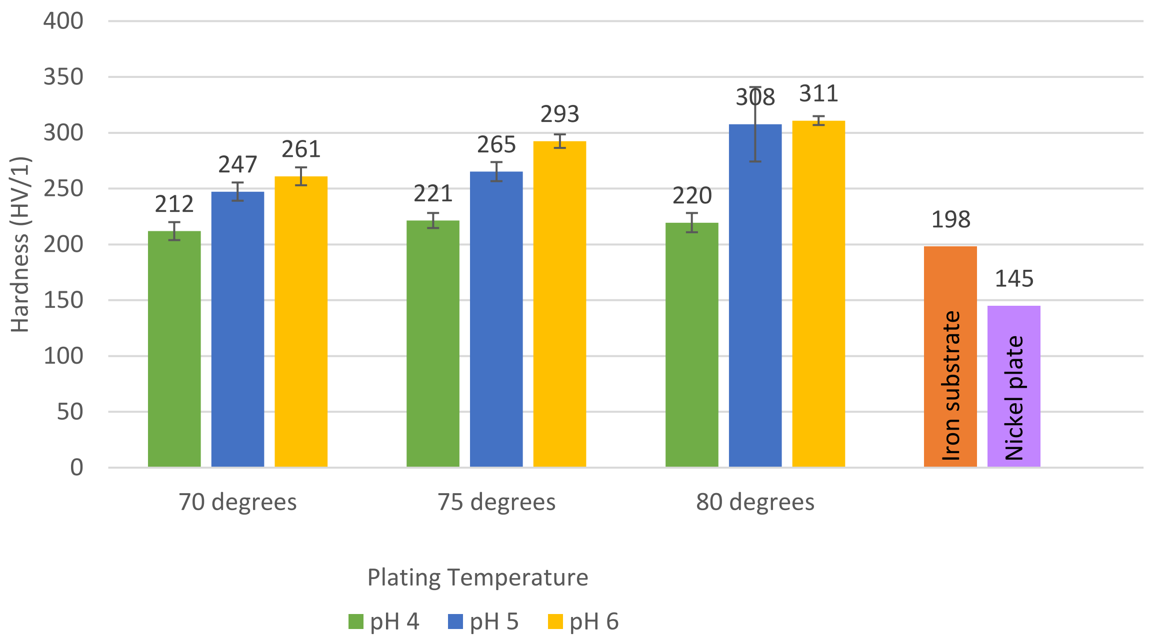

Figure 5.12. Hardness values for samples plated from in-house baths

Results showed that increasing plating pH caused the deposits to become harder. The average hardness at each pH was 218, 273 and 288 HV/1 for pH's 4, 5 and 6 respectively. Additionally, plating temperature caused differences in hardness. Values of 240, 260 and 279 HV/1 were recorded for plating temperatures of 70, 75 and 80°C respectively. The highest hardness was obtained from samples containing the least phosphorous, and the lowest recorded for those containing the most phosphorous. The sample with the highest hardness was plated at the highest pH and temperature, whilst the sample with the lowest hardness was plated at the lowest pH and temperature.

XRD was performed on one sample from each plating condition and compared to observe whether any noticeable differences were developed in crystal structures with varying pH and temperature. All scans were completed as described in section 2.11. A spectra of the substrate material is shown in Figure 5.13. The results from the electroless nickel deposits are shown in Figure 5.14.

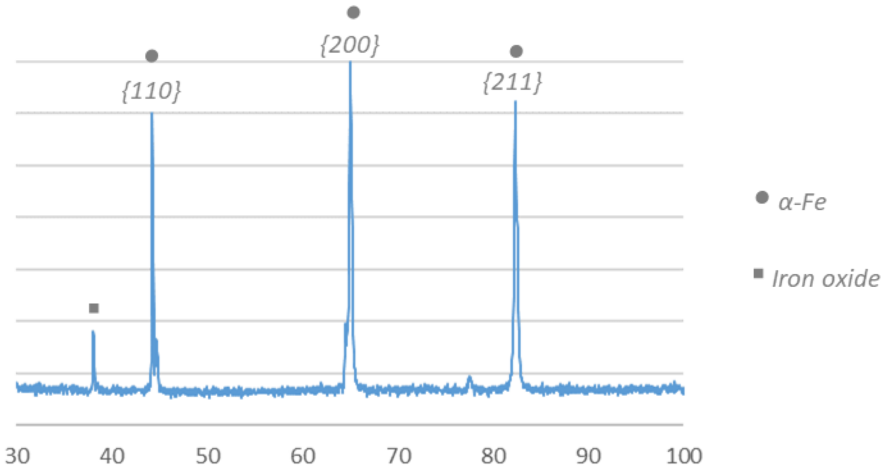

Figure 5.13. XRD diffraction pattern for the blank iron substrate

Figure 5.13 shows the diffraction pattern of the substrate material. The peaks at 44°, 65° and 82° are characteristic of α-iron with Miller indices of {110}, {200} and {211} respectively. The peak at 38° likely shows presence of iron oxide. This scan has been included to easily identify and ignore substrate peaks in the diffraction patterns from the plated samples.

Spectra were recorded on one sample plated from each bath. The results in Figure 5.14 show how the diffraction patterns were affected by changing bath pH and temperature. All scans showed a broad peak from ≈ 40° to 50°, characteristic of an amorphous phase. Unfortunately, the nickel {111} plane has a similar peak location to the iron {110} plane at 45°, so in some cases it was difficult to distinguish which was present. With increasing plating pH, an increase in intensity and sharpness of the peak at 40° to 50° was observed at all temperatures. This is indicative of an increase in crystallinity. Additionally, a reduction in intensity of substrate peaks was seen with increasing plating pH. As the temperature of the plating solution was increased, a greater presence of nickel {220} was seen. There was also a small increase in the height of the nickel {111} peak.

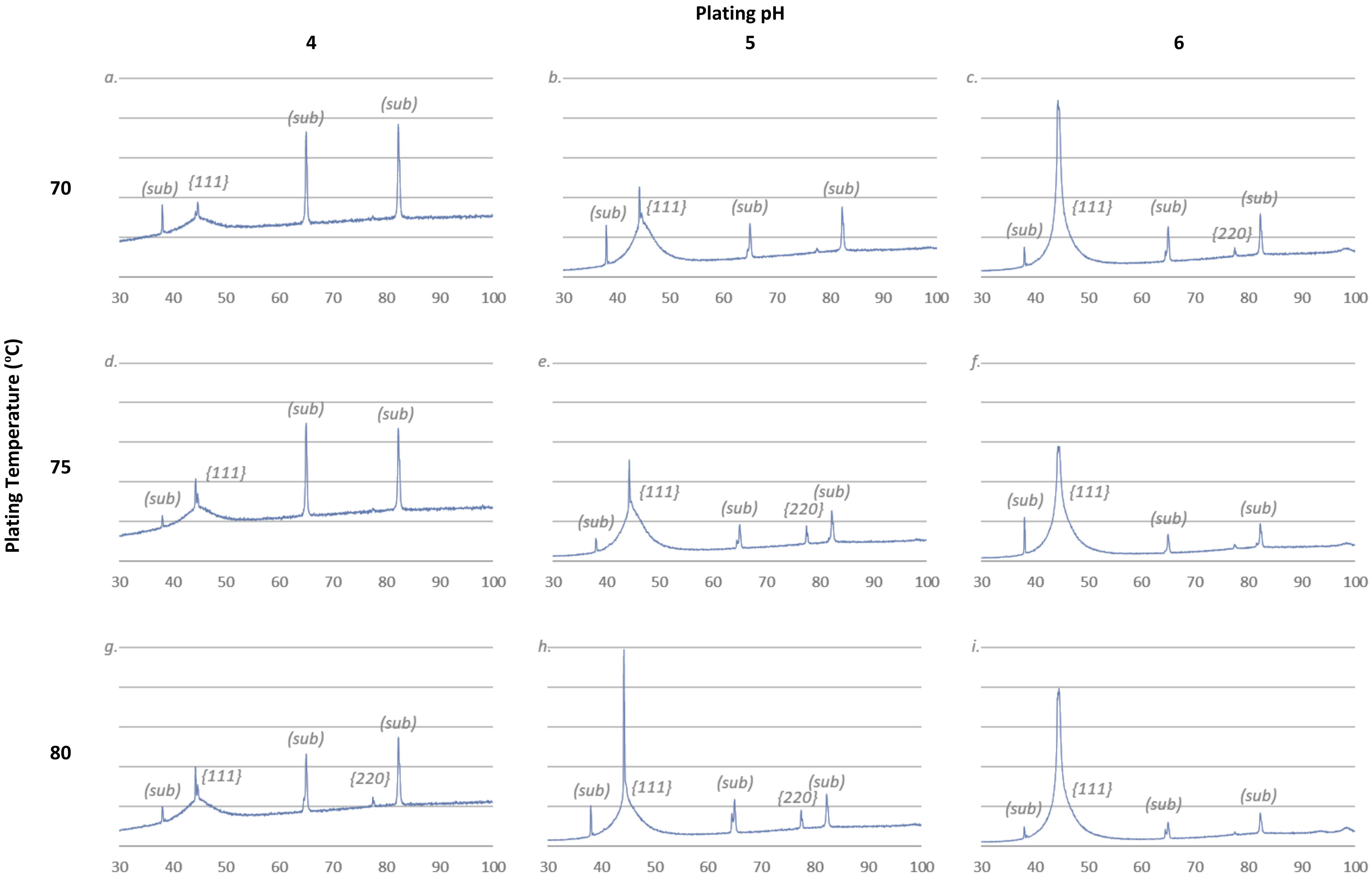

Figure 5.14. XRD diffraction patterns for plating baths at a. pH 4, 70°C b. pH 5, 70°C c. pH 6, 70°C d. pH 4, 75°C e. pH 5, 75°C f. pH 6, 75°C g. pH 4, 80°C h. pH 5, 80°C i. pH 6, 80°C

5.5 Discussion

5.5.1 Assessment of electroless nickel deposits using SEM

SEM was initially used to assess the composition of the deposits. Whilst no conclusions could be drawn on how phosphorous content was affected by solution composition from proprietary solutions supplied by MacDermid Enthone, it was possible to link the compositions of the in-house deposits to bath conditions. The phosphorous content of the in-house samples increased from 7.92 to 12.09 wt.% at 70°C, from 8.18 to 15.64 wt.% at 75°C and from 8.69 to 14.29 wt.% at 80°C with decreasing solution pH from 6 to 4 in each case.

Plating pH is known to be an important factor in determining the composition of deposits. Previous experimentation found increasing bath pH results in a decreased phosphorous content of the deposit, but will lead to an increase in plating speed [70], [79], [150].

The anodic oxidation of sodium hypophosphite was found to be the leading factor in the rate of electroless deposition. The deprotonation of this reducing agent can be expressed as:

$$H_2PO_2{}^- \rightarrow (HPO_2)^-{}_{surf} + H_{ads} \qquad 5.1$$

$$(HPO_2)^-{}_{surf} + OH^- \rightarrow (HPO_2OH)^-{}_{solution} + e^- \qquad 5.2$$

As the pH of the plating bath increases, the reaction rate of equation 5.1 increases, speeding up the anodic reaction [151]. As a result of faster electron production from equation 5.2, the rate of nickel reduction speeds up leading to an increase in the quantity of nickel deposited at higher bath pH's.

Additionally, as the pH of the plating bath increases, the rate of phosphorous reduction decreases. The proposed mechanism for the formation of elemental phosphorous is thought to be a secondary reaction between hypophosphite and atomic hydrogen, shown in the following equation [61], [69], [152]:

$$H_2PO_2{}^- + H \rightarrow P + OH^- + H_2O \qquad 5.3$$

This reaction happens more readily at lower pH values, due to the increased availability of hydrogen ions in solution. The solubility of hypophosphite species increases at lower pH values [79], so more reactants were available for the reaction in equation 5.3 to happen. This leads to increased phosphorous reduction, and therefore more deposited at lower bath pH.

At higher pH's, this reaction was less likely to happen due to the increased presence of hydroxide ions. Therefore, at increasing bath pH, the amount of phosphorous in the coating is decreased [148], as less phosphorous is reduced, so less is available to be co-deposited. As the nickel reduction reaction increases at higher pH levels, the plating rate can be significantly increased under these conditions.

The optimum plating pH range for acid electroless nickel baths is thought to be between 4 - 6.5 [74], although they can operate outside this range depending on bath composition. Below pH 4, the deposition rate is severely affected, resulting in little or no deposition [153]. Baths can be operated in alkaline conditions; however, these normally have different compositions to acid baths.

Results showed the phosphorous content of the in-house samples increased from 12.09 to 14.29 wt.% at pH 4, from 10.39 to 12.85 wt.% at pH 5 and from 7.92 to 8.69 wt.% at pH 6, with increasing plating temperature from 70°C to 80°C in each case.

Increases in phosphorous content with increasing temperature are less significant than those produced when altering solution pH. This is probably due to increased temperature increasing overall reaction rate, and more phosphorous availability for incorporation in the final deposit. Increases in phosphorous content with increasing plating temperature have previously been observed for electrolytic plating of nickel-phosphorous alloys [96]; there are few observations of effects of plating temperature from EN baths on their composition.

Whilst no link can be made between solution composition, plating conditions and surface properties for the MacDermid Enthone proprietary solutions, samples were plated for various times, so comparisons between plating time and surface properties can be made. Overall solutions showed small increases in average phosphorous content from 9.72 wt.%, to 10.08 wt.% and 10.45 wt.% for solutions Niklad ELV 835, Niklad ELV 849 and Vand-Aloy 4100N respectively. When plating time was increased from 30 to 120 minutes, an increase in the phosphorous content of the deposit was observed. The pH of the bath was not monitored during plating, so the most likely reason for this composition change is a drop in pH over the plating time. As part of the chemical deposition of nickel during the oxidation of hypophosphite, hydrogen ions are generated. Whilst some of these will form hydrogen gas and evolve during plating [149], some will dissolve in solution. Increasing the concentration of H^+ ions in the solution will lead to a decrease in the pH of the plating bath [66]. As discussed previously, lower bath pH results in increased phosphorous incorporation [148]. It is likely increased plating time has led to a decrease in bath pH [149], increasing the solubility of phosphite species [79], depositing more phosphorous.

The cross-sectional analysis carried out for the in-house samples showed increased plating temperature resulted in a faster plating rate, due to increased energy speeding up the reactions. A significant amount of energy is required for plating, so optimising plating temperature for fast plating rates and good properties is essential. If plating temperature is too low, little energy is available, so the reactions cannot occur with the result that plating is either very slow or does not proceed at all [148]. For an acid bath a minimum of 65°C is suggested for deposition to occur [154]. If plating temperature is too high, bath decomposition or plate out is likely, which would result in total bath failure [148]. For an acid bath, a maximum operating temperature of 90°C is suggested [66]. The operating temperature employed is dependent on bath composition. For example in the case of alkaline baths, significantly lower temperatures are used, commonly 50-80°C, but can be as low as 30°C [81]. This means they can be used to plate on to a wider variety of substrates, such as polymer surfaces.

A higher solution pH led to an increase in plating rate, due to the speed and prevalence of anodic oxidation of sodium hypophosphite [151] as described above. As the pH of the plating bath increased, the rate of reducing agent oxidation was increased due to the increased availability of OH^- ions. This increased the nickel reduction rate due to greater electron availability, thereby increasing the observed plating rate. It has previously been shown increasing bath pH and temperature will increase plating rate [61], [65], [74], [144], [150].

The cross-sectional analysis results for samples plated in commercial solutions showed increasing plating time led to a near linear increase in deposit thickness. Once deposition started, the process was auto catalytic, providing plating temperature, pH and bath composition remain within a stable range, plating rate was constant. The documentation provided with the commercial solutions estimated plating rates each solution could achieve. The Vand-Aloy 4100N solution plated at an average rate of 8.1$\mu m \cdot hr^{-1}$ within the predicted range of 8-15 $\mu m \cdot hr^{-1}$, whilst the Niklad ELV 835 and 849 solutions plated at average rates of 11.5 $\mu m \cdot hr^{-1}$ and 12.8 $\mu m \cdot hr^{-1}$ compared to predicted ranges of 20-25 $\mu m \cdot hr^{-1}$ and 15-22 $\mu m \cdot hr^{-1}$ respectively, which were significantly slower than expected. This is likely because plating conditions were not optimised. The suggested operating temperature of 88°C was used for all baths, and carefully maintained to ± 1°C during deposition, however pH was not checked prior to plating or throughout the experiment, so could have deviated outside the suggested range. The solutions were pre-mixed by MacDermid Enthone, and were provided ready to plate, with the correct composition and pH.

5.5.2 Assessment of electroless nickel deposits using potentiostat based techniques

Potentiostat techniques were used for accelerated corrosion investigations. The corrosion properties of deposits from the commercial MacDermid Enthone baths could not be linked to bath composition or conditions; however this is possible for samples plated in-house. The corrosion performance was estimated by calculating mass loss from I_{corr}, shown in Figure 5.6, determined by the Tafel extrapolation method. Mass loss increased with raising pH from 4 to 6, whilst temperature increases from 70°C to 80°C decreased the mass loss. Samples plated at 75°C showed lower mass loss than their pH equivalents at lower and higher temperatures. Overall samples with higher phosphorous content had the lowest calculated mass loss.

As previously shown, increasing pH and temperature of the solution increased the phosphorous content of deposits, so in this section the effect of phosphorous content on corrosion properties will be discussed, and linked back to plating pH and temperature. Overall it was found as the phosphorous content of deposits increased, corrosion resistance also increased, suggesting the addition of phosphorous affects corrosion properties.

As the phosphorous content of nickel-phosphorous alloys increases, changes in microstructure have previously been observed. At phosphorous contents below 4 wt.% a fully crystalline structure has been seen. As phosphorous content increases from 4-11 wt.%, an amorphous phase is developed, and increases in volume fraction, containing a dispersion of nano-crystalline nickel particles within it. Above 14 wt.% phosphorous, the structure of these deposits is fully amorphous [92]. Phase diagrams have been constructed to estimate which phases are present. Equilibrium phase diagrams have been suggested for this system [156], although they do not account for non-equilibrium phases formed between 0-15 wt.% phosphorous content. Several non-equilibrium phase diagrams have been suggested and Figure 5.15 shows an example of one proposed equilibrium and one non-equilibrium phase diagram.

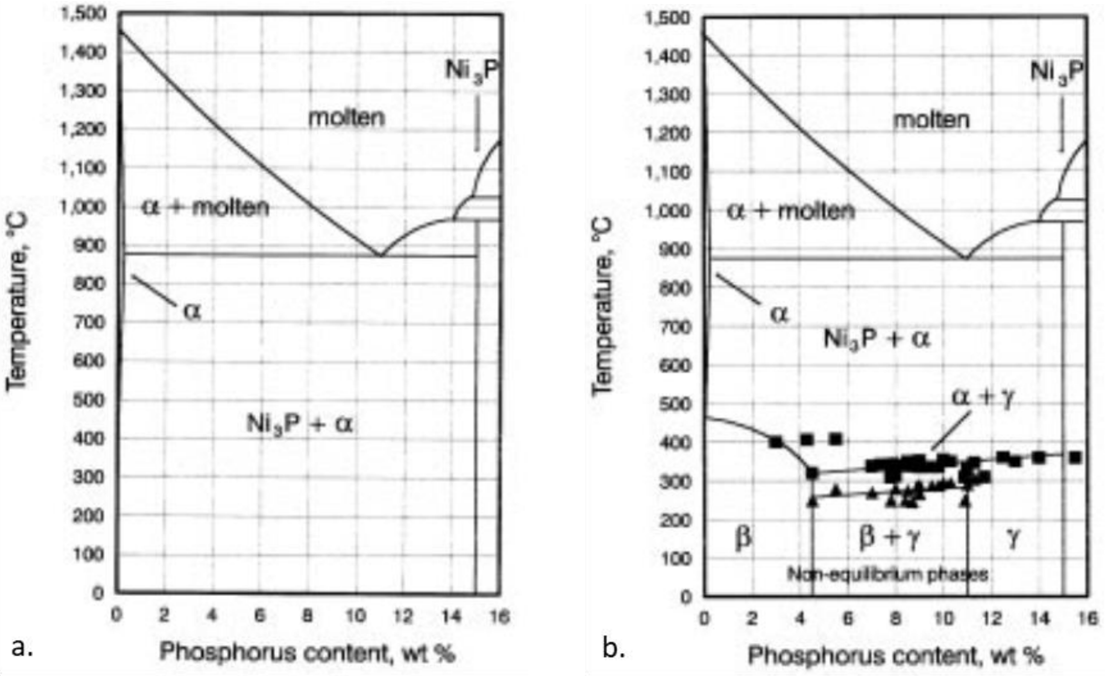

Figure 5.15. Examples of a. an equilibrium and b. a non-equilibrium phase diagram for the nickel-phosphorous alloy system [157]

For Ni_3P crystals to grow, there would have to be significant movement of large numbers of atoms by surface diffusion. However, during electroless plating, there is insufficient time for this to occur before further deposition occurs. This means atoms of phosphorous become trapped between atoms of nickel, leading to supersaturation. The FCC structure of nickel cannot be maintained over large areas due to the presence of trapped phosphorous, leading to small grain sizes. When an alloy contains more than 11 wt.% phosphorous, no order can be maintained in the structure which is what causes the microstructure to change from crystalline to amorphous with increased phosphorous content [158]. Amorphous alloys are generally more corrosion resistant than their crystalline counterparts, due to the lack of defects in amorphous structures. Crystalline structures have a greater number of defects where corrosion can be initiated, such as grain boundaries and dislocations [154], [159]–[161].

The corrosion of nickel-phosphorous alloys in acidic environments happens due to the simultaneous occurrence of oxidation and reduction reactions. The anodic reaction is thought to be a two-step process; first the oxidation of phosphorous to a hypophosphite anion ($H_2PO_2^-$), followed by the oxidation of phosphorous ($P^{(I)}$) in hypophosphite to phosphate ($P^{(V)}$) and second the oxidation of nickel to either Ni^{2+} or Ni^{3+}. The cathodic reaction is the reduction of H^+ to hydrogen gas (H_2) [162].

The corrosion resistance of any metal depends on the formation of protective oxide films. The presence of phosphate species in a system can initially accelerate corrosion, if there is not enough available for a protective film to fully establish. If soluble PO_4^{3-} is present in solution with Ni^{2+} ions this anodic inhibitor can act to block anodic sites, by forming insoluble deposits such as $Ni_3(PO_4)_2$ [163]. These compounds can be deposited on the surface of the metal and cover anodically active sites, reducing the rate of corrosion. This has previously been shown with sodium phosphate in solution with zinc, where zinc ions released interact with phosphate in solution to form zinc phosphates, which precipitate onto the metal surface, specifically anodic sites, to inhibit corrosion [164], [165].

Figure 5.16 below shows examples of potentiodynamic polarisation curves for samples with 3 different phosphorous contents. The curves for samples containing 14.3 wt.% P and 12.9 wt.% P are very similar; both have above 11 wt.% P so are fully amorphous explaining why their corrosion properties are similar. The LPR mass loss calculations yielded values of 178 and 182 $\mu g \cdot cm^{-2} \cdot week^{-1}$ respectively. The sample containing 8.69 wt.% P is predicted to have a different crystal structure, an amorphous matrix containing nano-crystalline nickel, so the potentiodynamic polarisations showed different corrosion properties. The anodic section of the curve for this sample displayed similar behaviour and values to the other samples with higher phosphorous contents; however, the cathodic branch was significantly shifted in the anodic direction, suggesting some cathodic activation may have taken place. LPR calculations for this sample estimated mass loss of 333 µg·cm^{-2}·week^{-1}. This sample showed a small increase in E_{corr}, suggesting it may be less thermodynamically likely to corrode, however the curves also showed an increase in I_{corr}, meaning a faster corrosion rate. This corresponds to the theory phosphate species in solution may initially increase corrosion rate, however the formation of stable intermediate nickel-phosphate compounds reduces overall corrosion [159]. These results indicated that crystal structure may have a significant effect on corrosion properties.

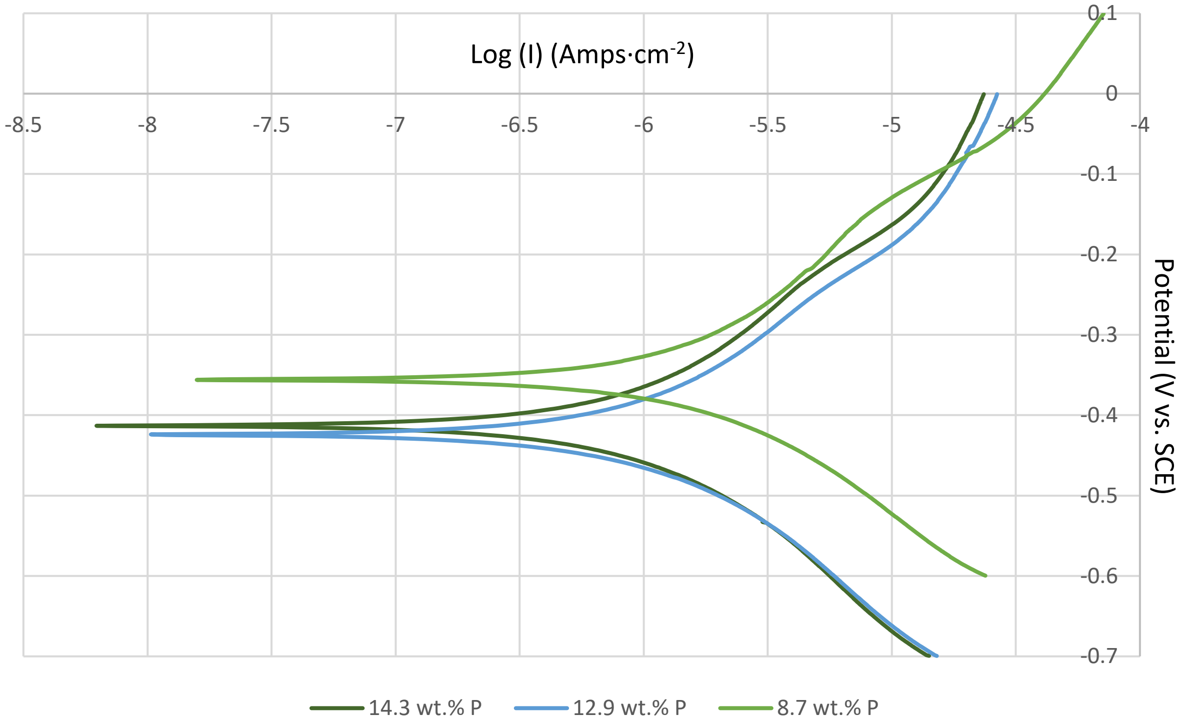

Figure 5.16. Potentiodynamic polarisation curves: in-house samples plated at 80°C and pH 4, 5 and 6

Corrosion resistance of electroless plated nickel-phosphorous alloys has been found to increase with greater phosphorous content and therefore amorphous microstructure [153], [166] in 3.5 wt.% sodium chloride solution [153], and 3 wt.% sodium chloride [89]. However, this can depend on the conditions encountered, for example high phosphorous alloys fare worse in nitric acid solutions [157].

Aside from a plating temperature of 75°C at pH 4, an increase in plating temperature led to a small increase in phosphorous content. From the discussion above, it can be assumed this increase led to an increase in corrosion resistance. The mass loss values from LPR showed the bath operated at 75°C produced deposits with the greatest corrosion resistance, followed by the bath at 80°C, and the worst performing samples were plated at 70°C, with average mass loss values of 170, 231 and 281 μg·cm^{-2}·week^{-1} for these temperatures respectively. Electroless nickel plating baths have optimum operating conditions, depending on composition and required deposit characteristics. It is likely that for corrosion performance in 3.5% NaCl at pH 7, the alloy formed at the median plating temperature had the best characteristics to resist corrosion.

Although the corrosion properties of samples plated from commercial MacDermid Enthone solutions cannot be linked to bath composition or conditions as they are unknown, these samples showed a small increase in corrosion resistance with increasing phosphorous content. These samples were plated for 30, 60 and 120 minutes, so variations in plating thickness can be related to corrosion resistance. From the Niklad ELV 835 and 849 solutions, increased plating time led to a significant decrease in mass loss, from 379 to 208 μg·cm^{-2}·week^{-1} for the 835 solution and 373 to 274 μg·cm^{-2}·week^{-1} for the 849 solution at plating times of 30 and 120 minutes respectively. A decrease from 340 to 254 μg·cm^{-2}·week^{-1} was observed for the 4100N solution when plating time was increased from 30 to 60 minutes, however at 120 minutes the mass loss increased slightly to 266 μg·cm^{-2}·week^{-1}. Overall, increasing deposit thickness improved the corrosion resistance, irrespective of deposit composition.

There are several potential reasons why deposit thickness would affect corrosion resistance. In many cases, plated deposits suffer from high occurrence of porosity [8]. Whilst some studies report electroless nickel phosphorous layers have lower porosity than equivalent electroplated nickel layers [66], [167], porosity can still cause issues. As deposit thickness increases, corrosion performance improves as pores are less likely to reach the underlying substrate. Where pores do extend from exterior of the nickel-plated deposit to the substrate, corrosion is very likely to occur, as nickel is often used to protect metals with lower nobility.

Pitting corrosion is the predominant corrosion mechanism for electroless nickel-phosphorous deposits in chloride based solutions [166], [168]. In alternative environments, other mechanisms such as intergranular attack have been recorded for example in 1N H_2SO_4 [169]. In the present case chloride containing environments are the greatest concern, so the effect of pitting corrosion on these will be discussed. Nickel-phosphorous coatings need to completely cover a substrate, especially where the coating is on a more electrochemically active metal, such as steel. If any pores reach from outside the coating to the substrate, it is likely pitting corrosion will be initiated by the galvanic couple formed between the coating and substrate. As steel is more reactive, it would become the anode, whilst cathodic activity would be sustained on the nickel-phosphorous plated layer. Due to the large surface area of the cathode compared to the anode, current density in the pit would be high and lead to rapid corrosion [66]. Zaimi et al. [170] showed increasing coating thickness of nickel phosphorous based alloys improves corrosion resistance in chloride solutions, and once coatings reach a critical thickness, corrosion behaviour remains stable irrespective of additions made to the base alloy.

For comparison, the same corrosion investigations were carried out on nickel plated steel samples currently used in the production of UK coinage. These deposits were pure nickel, electroplated from a Watts type bath. The blanks were plated using a nickel chloride [$NiCl_2 \cdot 6H_2O$] bath at 800 $A \cdot m^2$, for 7026-amp hours, and had an average deposit thickness of 25 µm. The average mass loss at room temperature was 57 $\mu g \cdot cm^{-2} \cdot week^{-1}$ compared to the lowest mass loss of 129 $\mu g \cdot cm^{-2} \cdot week^{-1}$ obtained from the electroless nickel plating baths.

In general, previous experimentation showed electroless nickel deposits have greater corrosion resistance than standard nickel electroplate [62], [72], [85], [86], [88]. However, this has not been observed here, and there are several possible reasons to explain this. As plating performed here was in a bath of simple composition, it is possible the deposit was not continuous, and contained regions of porosity which reduced the corrosion resistance [8]. Other work showed coatings with a minimum thickness of 12 µm show a significant reduction in porosity [168] which improves corrosion resistance; only two samples plated here had deposit thickness greater than 12 µm, which may explain why the corrosion resistance was lower than the electroplated samples. It is possible closer control of plating temperature, pH and composition is necessary to ensure uniform deposits are obtained. These parameters are very important to the integrity of deposits [64]. Many baths, especially those available commercially contain a great number of ingredients to change deposit properties. The lowest mass loss value obtained from proprietary solutions was 208 $\mu g \cdot cm^{-2} \cdot week^{-1}$, significantly greater than samples plated in-house at pH 4 and 5.

5.5.3 Assessment of electroless nickel deposits using Vickers hardness testing

The results from samples plated in-house showed that deposit hardness increases with higher temperature and pH. This means that hardness increases with greater deposit thickness and decreasing phosphorous content. The results from samples plated in commercial MacDermid Enthone solutions showed deposit hardness increased with plating time. Thicker deposits are likely to be harder, as there is less interaction with the softer, steel substrate. The overall trend suggests increasing phosphorous content decreases hardness, shown previously [157], [159], [171] (although disagreed in [172]), due to changes in crystal structure with various phosphorous contents.

The equilibrium phase diagram for nickel-phosphorus shown previously in Figure 5.15 indicates at temperatures below 875°C, and composition between 0.17 and 15 wt.% phosphorus, two phases can form – Ni_3P + α. However, it is well documented the crystal structure changes from crystalline to amorphous in this region with increasing phosphorous content [76], [81], [84], [148], [150], [173]–[176] indicating changes in phase. The structure can be returned to crystalline using a post plating heat treatment if required [88], [92], [149]. To account for phases not present in the equilibrium phase diagram, a non-equilibrium version for nickel and phosphorous has been proposed [177], with two additional phases. This suggests a β phase is the only phase at phosphorus contents between 0 and 4.4 wt.%, comprising of a crystalline solution of phosphorous in nickel. The second additional phase γ, is completely amorphous, and the only phase at phosphorous contents between 11 and 15 wt.% P. Between 4.4 and 11 wt.% phosphorous contents, phases β and γ exist together in decreasing and increasing amounts respectively. These phases have different properties, which can affect hardness. The β phase is harder, meaning peak hardness can be obtained at around 4 wt.% phosphorous, where the microstructure comprises this single phase. As phosphorous content increases between 4.4 – 11 wt.%, the γ phase increase, and the β phase decreases. The γ phase is softer than the β phase, so hardness decreases at greater phosphorous contents [153], [157].

Overall, plating time and phosphorous content play a significant role in deposit properties. Increasing plating time results in a harder deposit [68], and increasing phosphorous content decreases hardness due to changes in the microstructure and phase content.

5.5.4 Assessment of electroless nickel deposits using x-ray diffraction

From diffraction patterns obtained by XRD, all samples showed a broad peak from ≈ 40^o to 50^o, indicating an amorphous phase characteristic of higher phosphorous electroless nickel alloys. A wide peak at this location is commonly seen on XRD diffraction patterns for Ni-P samples [12], [71], [75], [178], [179]. These results showed increasing temperature increased the size and sharpness of the nickel {111} peak, indicating increased crystallinity of the sample, consistent with the reduction in phosphorous content seen from EDX at higher plating temperatures. Lower phosphorous contents have been found to increase crystallinity due to less distortion of the lattice structure [81], [84], [158]. Increasing bath temperature led to the formation of nickel in the {220} direction, potentially due to increased deposition rate. The intensity of substrate peaks decreased with increasing bath pH due to increased thickness of the deposit. As deposit thickness increased, more radiation was absorbed before x-rays reached the substrate resulting in the lower intensity measured [178].

These results confirm changes in properties observed in other previous experiments. Broad peaks at high phosphorous content demonstrate the amorphous nature of the deposit, whilst samples with lower phosphorous content showed sharper peaks, indicating a more crystalline structure. This confirms phase changes happen in the material at different compositions, and why some of the properties change so drastically.

5.6 Conclusions

From this work it can be concluded that whilst no direct comparisons can be drawn between samples plated in-house and those from a commercial proprietary solution, it is possible to obtain deposits with similar properties. Samples plated from MacDermid Enthone solutions had phosphorous contents between 9.66 to 10.59 wt.% P, plating rates from 7.0 to 13.5 $\mu m \cdot hr^{-1}$, mass loss values from 208 to 379 $\mu g \cdot cm^{-2} \cdot week^{-1}$ and Vickers hardness values ranging from 210 to 341 HV/1. Samples plated from in-house solutions had a range of phosphorous contents between 7.92 and 15.64 wt.% P, plating rates from 2.9 to 12.5 $\mu m \cdot hr^{-1}$, mass loss values from 129 to 483 $\mu g \cdot cm^{-2} \cdot week^{-1}$ and Vickers hardness values ranging from 212 to 311 HV/1.

From the proprietary MacDermid Enthone solutions, it was difficult to obtain deposits with the characteristics required. These solutions did not provide deposits with the properties suggested by the accompanying documentation. This could be due to limited bath monitoring, or due to the fact that solutions were not mixed optimally to produce plated layers of the stated composition. From these samples, it was also determined that plating time can affect deposits by increasing corrosion resistance and hardness.

By maintaining a constant bath composition and altering both plating temperature and pH, a range of samples were obtained from an in-house solution. It was found increasing plating temperature resulted in an increase in phosphorous content, plating rate, corrosion resistance (up to 75^{o}C, then a small decrease in performance up to 80^{o}C) and Vickers hardness. Increasing plating pH resulted in a decrease in phosphorous content of the deposit, but corresponding increased the plating rate, while decreasing the corrosion resistance and increasing the Vickers hardness.

These results showed electroless nickel deposition can provide samples at an increased plating rate with increased hardness. However the corrosion resistance of electroplated samples is currently much greater than those produced by electroless deposition. The following chapter examines how the corrosion resistance, plating rate and other important properties could be changed by using organic additives in the plating bath.

Chapter 6. The use of organic additives in electroless nickel plating baths

6.1 Introduction

Electroless nickel plating represents a viable replacement for standard electroplating in terms of plating rate and hardness. However, as shown in Chapter 5, the corrosion resistance of samples plated from the commercial and in-house solutions was significantly less than standard nickel electroplate. A reduction in corrosion resistance could cause serious issues if electroless plated coins were released into circulation, as lifetime could be significantly reduced. It is important coins maintain their integrity in circulation. Previous studies showed electroless nickel plated samples can have excellent corrosion resistance [62], [85], [88], however these are often plated from complex baths requiring many different chemical additions.

To address this, several additions were made to the basic in-house electroless nickel bath used in the previous chapter in order to improve the corrosion properties of deposits, without adversely affecting other properties. A wide range of chemical additions have previously been trialled, as discussed in the literature review, so finding new additions required considerable thought. Different amino acids have previously been added to electroless nickel plating baths. These include cysteine [77], [78], which changed the plating rate to varying extents under different plating conditions and methionine [78] which decreased the plating rate. Both were added in concentrations ranging from 10^{-9} to 10^{-5} $M\cdot L^{-1}$.

Amino acids thiamine hydrochloride and taurine were selected as promising organic additions due to their non-toxic nature, low cost and similarity in chemical structure to previous additives. These compounds also contain sulphur, which is frequently used in nickel plating technology to increase deposit brightness [37], [180]–[182]. The chemical structures of these are depicted in Figure 6.15 and Figure 6.16. The properties of these deposits were evaluated using Scanning Electron Microscopy to analyse surface composition and plating rate, potentiostat based techniques to assess corrosion properties, Vickers hardness testing and x-ray diffraction for phase analysis. The results were compared to values obtained in the absence of additives and with specimens produced via conventional electroplating.

6.2 Samples

Electroless nickel-phosphorous samples were deposited from the same basic in-house solution used in the previous chapter, with various additions of taurine (0.0001, 0.001 and 0.01 M) and thiamine hydrochloride (0.00001, 0.0001 and 0.0002 M) shown in Table 6.1 below. These concentrations were selected as initial experiment data showed greater additions of thiamine hydrochloride caused the plating reaction to cease. The bath pH was 5 and temperature 75°C for all samples produced in this chapter. Standard nickel electroplated samples were deposited as described in section 2.5.

Table 6.1. Plating bath composition with organic additives

	Bath 1 ($g\cdot L^{-1}$)	Bath 2 ($g\cdot L^{-1}$)
Sodium acetate	10	10
Sodium hypophosphite	20	20
Nickel sulphate	30	30
Taurine ($C_2H_7NO_3S$)	0.0125, 0.125 and 1.252	0
Thiamine hydrochloride ($C_{12}H_{17}ClN_4OS \cdot HCl$)	0	0.0034, 0.0336 and 0.0675

6.2.1 Sample preparation

Prior to examination, samples were polished with a 5µm alumina paste to remove any oxide layers from the surface. Samples for potentiostat investigation were held in a sample holder, where an area of 0.95 mm^2 was exposed to electrolyte.

6.3 Experimental methods

To analyse the properties of these samples, the same experimental techniques were used as described in chapter 5, section 5.3. SEM/EDS was used to analyse the phosphorous content and observe features on the surface, potentiostat techniques, OCP, LPR and PDP to assess corrosion properties and Vickers hardness testing to monitor the effect of additions on this property.

6.4 Results

6.4.1 Determination of composition and properties of deposits from taurine containing baths

The properties of deposits vary greatly depending on the quantity of nickel and phosphorous present. A scanning electron microscope equipped with an EDS detector was used to estimate the quantity of these elements in the deposit. These results were compared to those obtained for the sample plated at the same pH and temperature (pH 5 and 75°C) to observe the effects of different organic additions on the phosphorous content of the deposit. Three areas on each sample were scanned using SEM/EDS, set to an accelerating voltage of 15 kV. The average phosphorous contents measured by EDS for taurine additions are shown in Figure 6.1.

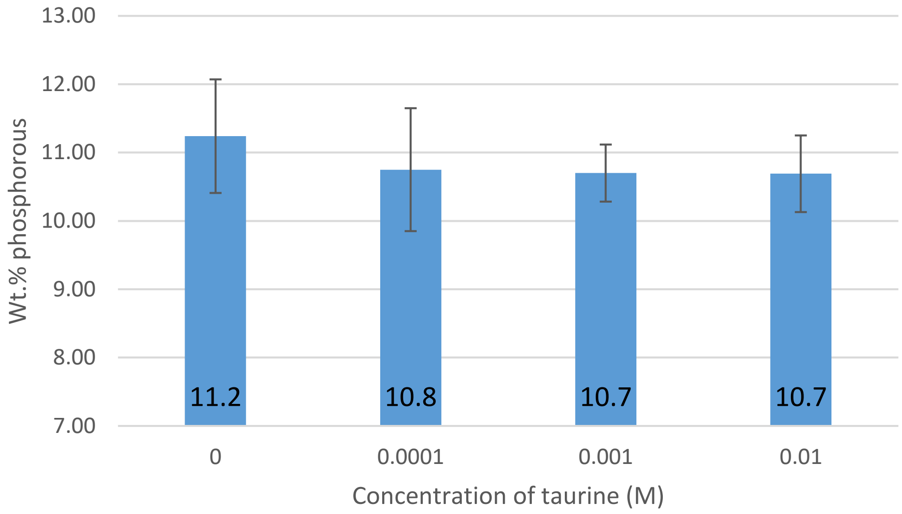

Figure 6.1. Average EDS estimated phosphorous content for EN baths with taurine additions

The results show additions of taurine to the bath makes minimal difference to the final phosphorous content. The sample plated with no additions contained 11.24 wt.% P, whilst baths containing 0.0001, 0.001 and 0.01 M taurine incorporated 10.75, 10.70 and 10.69 wt.% P respectively. A decrease in phosphorous content was observed compared to the sample with no additions.

Images of the surface were taken at 1000x magnification, shown in Figure 6.2. These images show some variation in structure with differing taurine additions. The surface of all samples was generally very smooth, with some nodules plated on top of this layer. The sample with the greatest taurine addition showed a larger number of agglomerations composed of small nodules on the surface. As taurine concentration decreased, the nodules increased in size, but formed agglomerations less often, reducing the number of surface features. The sample with the lowest taurine content had very few nodules. The deposit from the bath with no additions shown previously in Figure 5.9 was characterised by agglomerations of larger nodules in random locations across the surface. At the lowest concentration of additive (0.0001 M), a decrease in the total number of nodules was observed, meaning this bath produced the most consistent deposit.

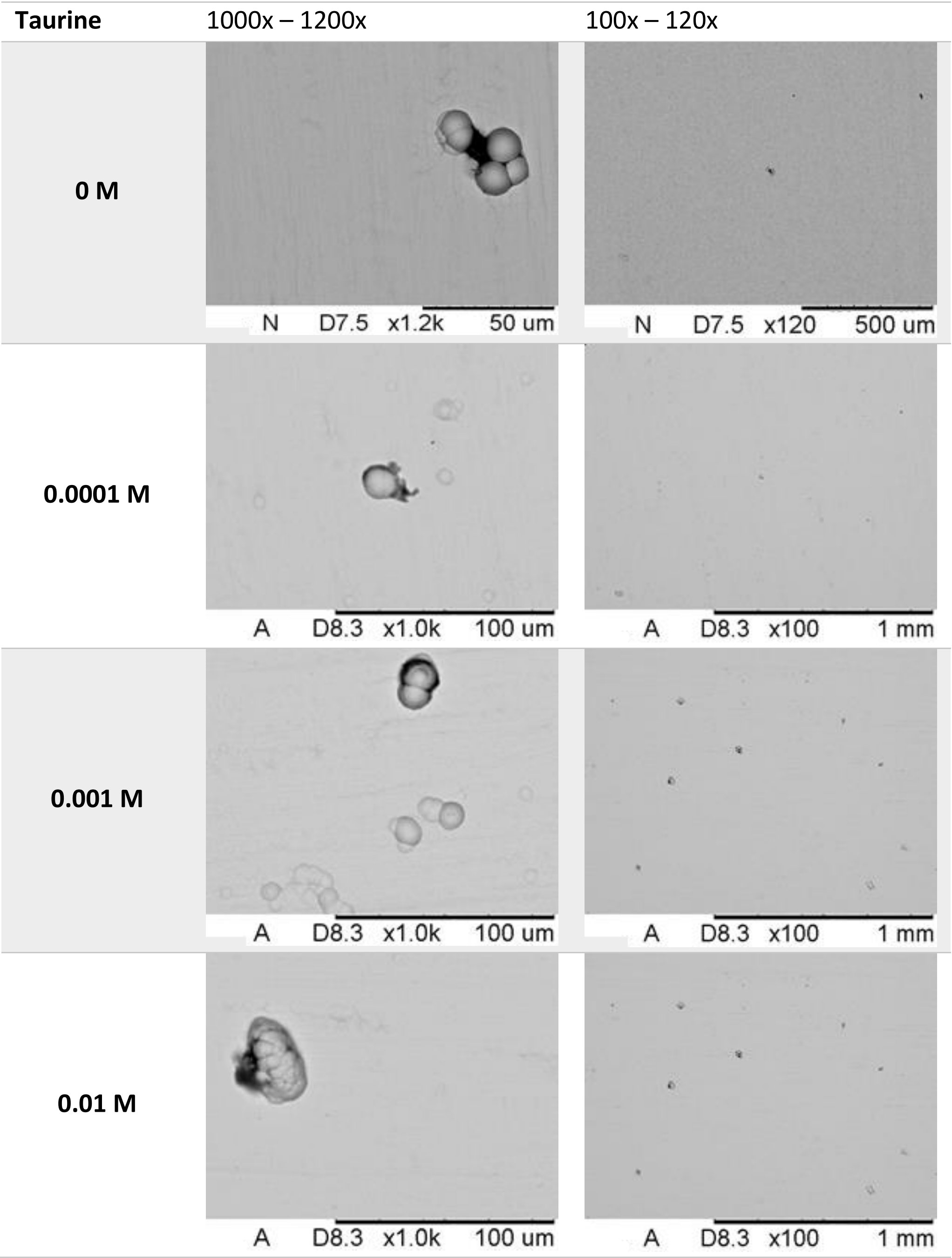

Figure 6.2. Images of the surface of samples plated in baths containing taurine

These samples were sectioned and mounted vertically to investigate deposit thickness. The samples were examined using SEM, and measurements of deposit thickness taken, shown in Table 6.2. Additions of taurine to the bath appeared to change the plating rate. At higher taurine additions, 0.01 and 0.001 M, deposit thickness was slightly reduced from 9.0 µm with no additions to 8.7 and 8.4 µm respectively. At the lowest concentration of taurine, 0.0001 M, deposit thickness was significantly reduced to 6.3 µm.

Table 6.2. Deposit thickness of samples plated with taurine additions

Concentration taurine (M)	Deposit thickness (µm)
0	9.0
0.0001	6.3
0.001	8.4
0.01	8.7

Overall, additions of taurine led to a reduction in the phosphorous content of the alloy compared to no additions and phosphorous content decreased slightly as more taurine was added. As the quantity of taurine in the bath increased, more nodules formed on the surface. Taurine appeared to slow down the plating rate in all cases, with the lowest reduction observed under the highest addition concentration.

Open circuit potential measurements were carried out for 1 hour in 3.5% NaCl at pH 7, to allow the samples to equilibrate and form a stable oxide layer. The results are shown in Figure 6.3 plotted as averages of the final 30 minutes of the experiment. OCP values for samples plated in baths containing taurine were more positive than the sample plated in the bath with no addition. The sample with the highest concentration addition of taurine (0.01 M) showed the greatest increase in OCP, followed by the sample with the smallest addition (0.0001 M). The OCP values were -0.353, -0.321 and -0.332 V vs. SCE for baths with additions of 0.0001 M, 0.001 M and 0.01 M respectively, whilst the bath with no addition had an OCP of -0.396 V vs. SCE.

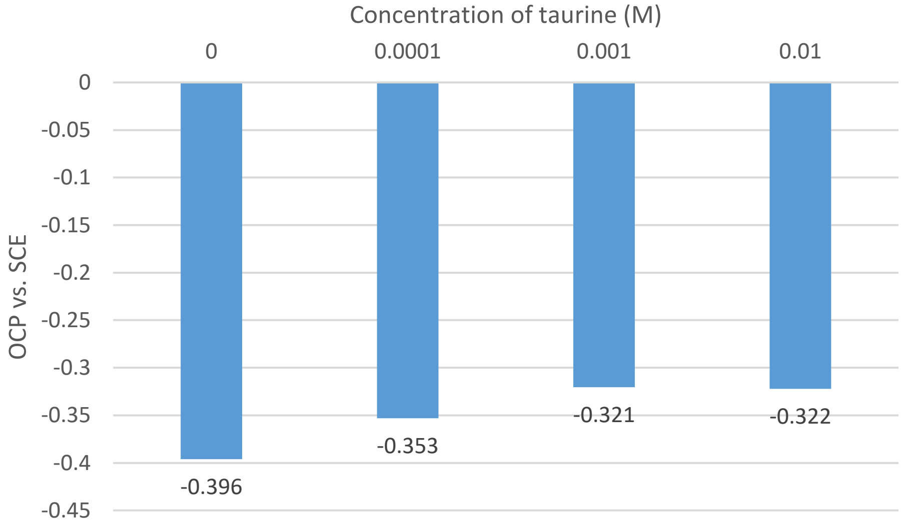

Figure 6.3. OCP values for samples plated in baths with taurine additions

Potentiodynamic polarisations were performed on these samples, the potential swept from -0.7 V to 0.1 V vs. SCE in the positive direction at 1 mV·s^{-1}. Tafel slopes were determined in order to obtain Stern-Geary co-efficient to calculate mass loss from LPR experiments, as described in section 2.8.2.

Linear polarisation resistance was used to approximate corrosion rate in open circuit conditions to calculate mass loss values. The samples are only polarised ±10 mV around the OCP at a rate of 0.25 mV·s^{-1}. An explanation of how this can be used to calculate mass loss can be found in section 2.8.3. Some examples of the PDP curves obtained are shown in Figure 6.4, and the calculated values for mass loss for all samples are shown in Figure 6.5 below.

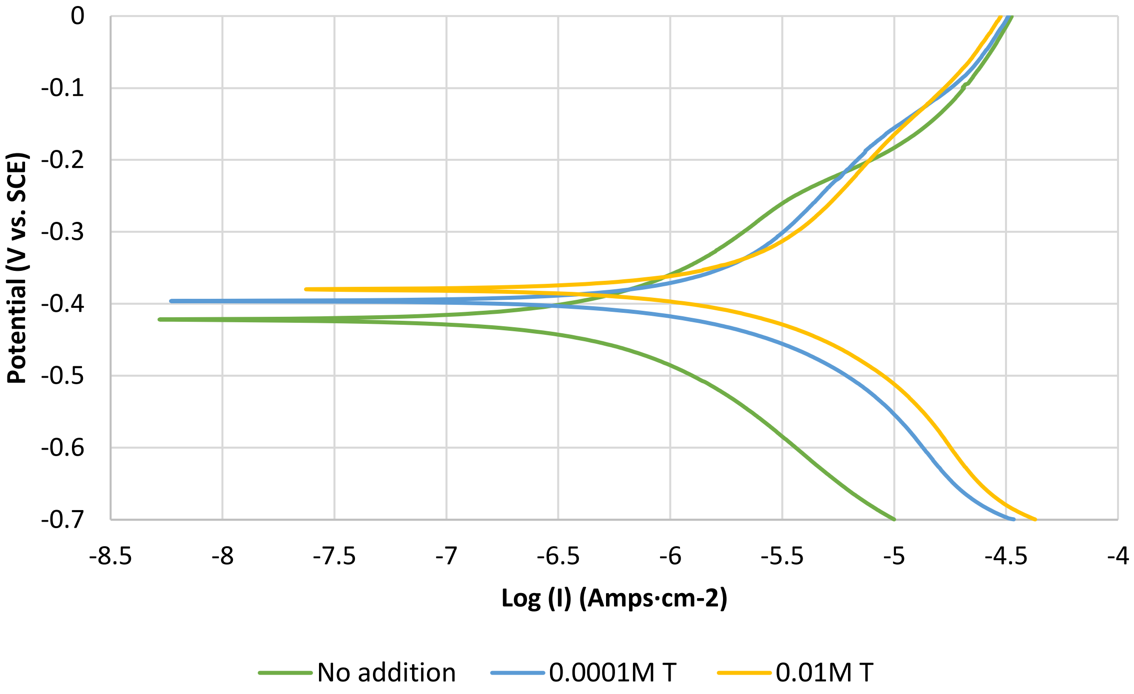

Figure 6.4. Example PDP curves for samples in a bath containing taurine additions

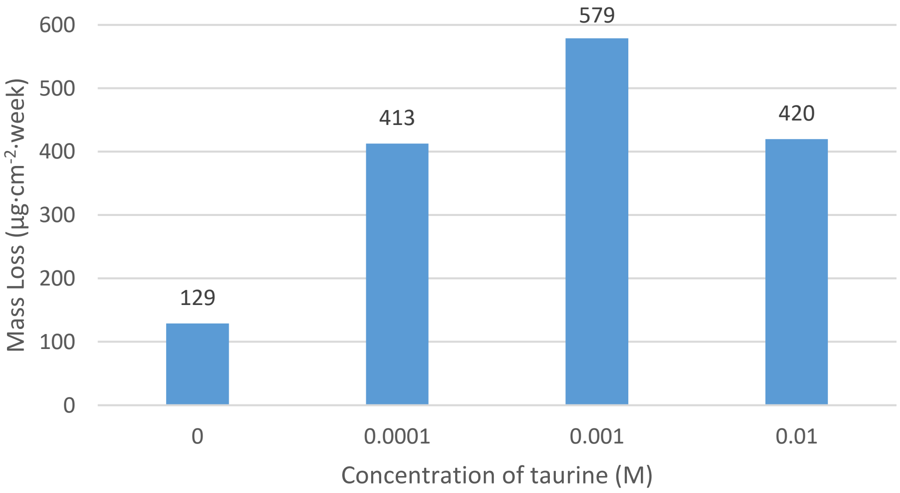

Figure 6.5. Mass loss values (LPR derived) from samples plated in a bath containing taurine

The results show additions of taurine to the electroless nickel plating bath increased the mass loss in all cases. Samples plated in the bath with no additives had a calculated mass loss of 129 µg·cm^{-2}·week, whilst the samples plated with taurine additions had mass loss values of 413, 579 and 420 µg·cm^{-2}·week with 0.0001, 0.001 and 0.01 M additions respectively.

Vickers hardness testing was carried out on samples plated from the baths containing taurine, where a load of 1 kg was applied for 10 seconds. Three indents were made in each sample, and an average of hardness for each deposit is shown in Figure 6.6.

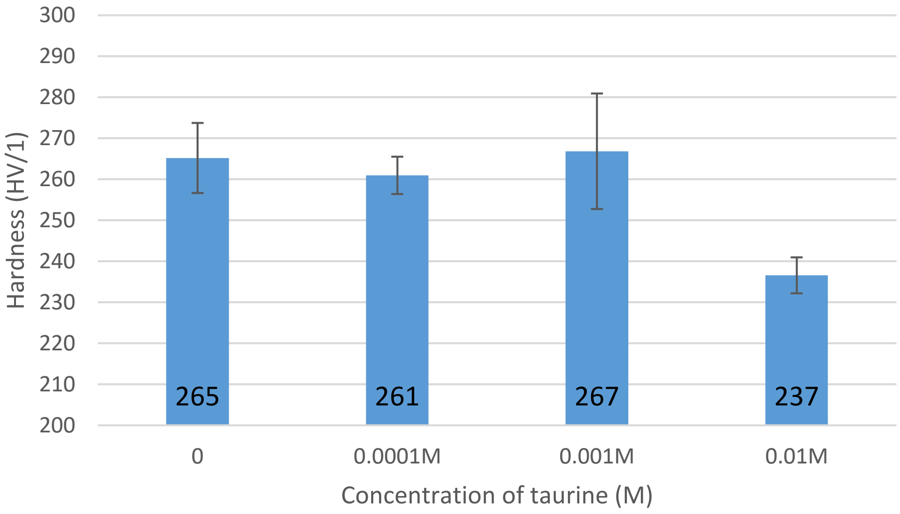

Figure 6.6. Average Vickers hardness values for baths containing taurine

The results show additions of taurine at lower concentrations led to similar hardness values to bath with no addition, whilst the highest addition caused a slight decrease in hardness. The values ranged from 265 HV/1 with no addition to 261, 267 and 237 HV/1 with additions of 0.0001 M, 0.001 M and 0.01M of taurine respectively.

XRD was performed on samples with the highest and lowest additions of taurine, and diffraction patterns for these were compared to the sample from the basic bath. All scans were run as described in section 2.11. The results are shown in Figure 6.7 below.

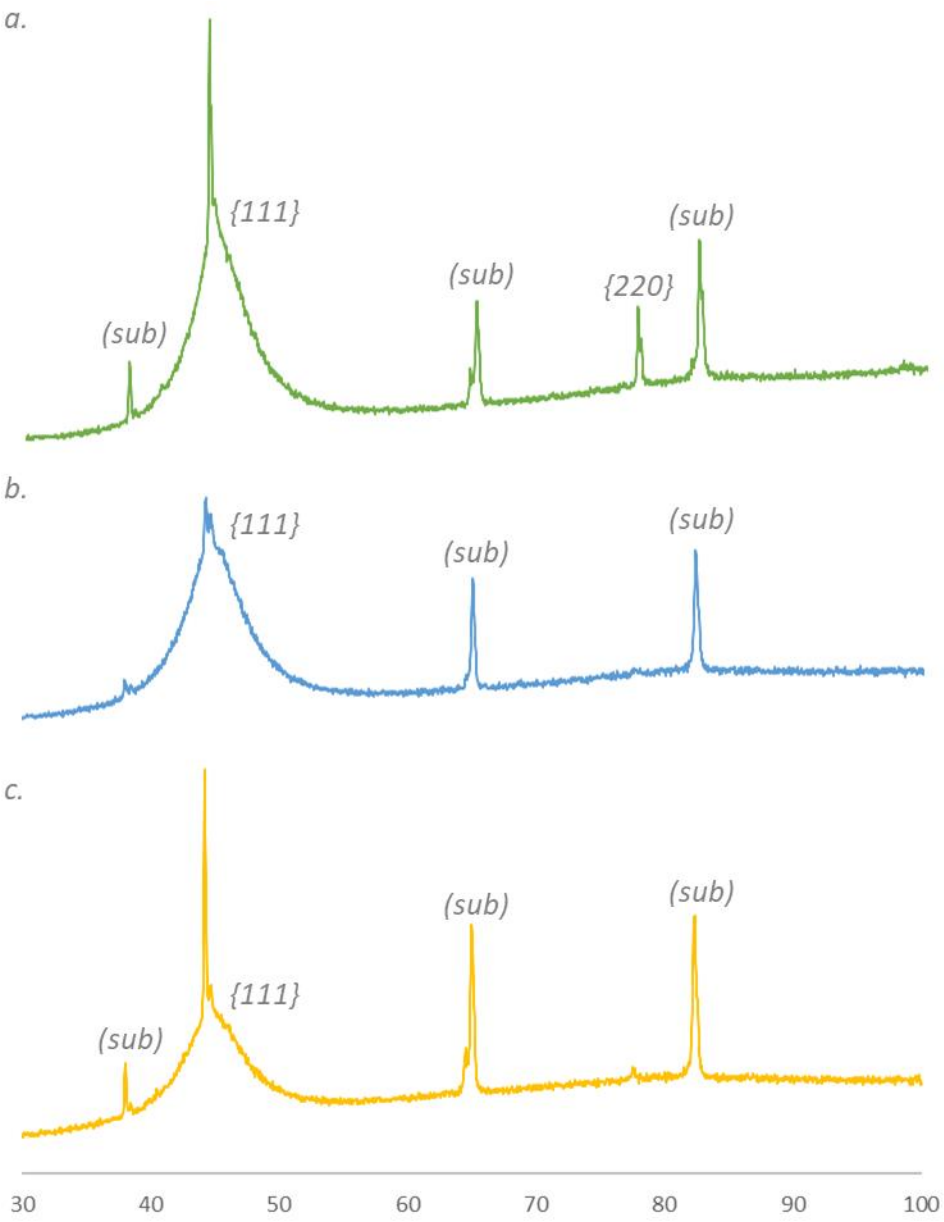

Figure 6.7. XRD diffraction patterns for plating baths with a. no additions, b. 0.0001 M taurine and c. 0.01 M taurine

The results from XRD show compared to the sample plated with no bath additions, samples from baths containing taurine showed nickel only in the {111} direction. The broad peak for nickel {111} plane displays the amorphous or nanocrystalline nature of the deposit. With the 0.0001 M addition of taurine, a small decrease in the height and width of this peak was seen, whilst a significant decrease was seen with the 0.01 M addition of taurine.

6.4.2 Determination of composition and properties of deposits from thiamine hydrochloride containing baths

SEM equipped with EDS was used to analyse the samples plated in baths containing thiamine hydrochloride. The phosphorous content was analysed for each bath addition and compared to samples produced with no additives. Three areas on each sample were scanned using the SEM/EDS system. An accelerating voltage of 15 kV was used. The average phosphorous contents measured by EDS are shown in Figure 6.8.

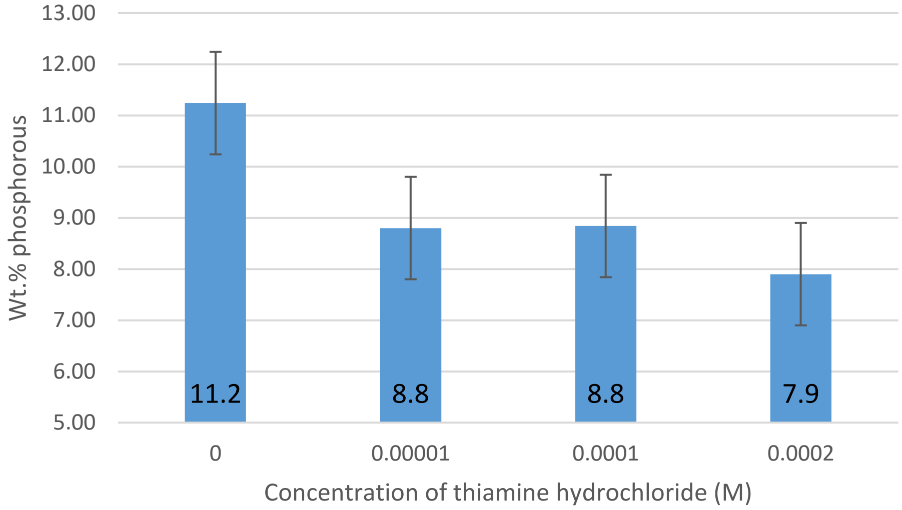

Figure 6.8. Average EDS estimated phosphorous content for in-house EN baths with thiamine hydrochloride additions

These results show additions of thiamine hydrochloride to EN plating baths makes a noticeable difference to the phosphorous content of deposits. The sample deposited with no additions contained 11.24 wt.% P, whilst baths containing 0.00001, 0.0001 and 0.0002 M thiamine hydrochloride incorporated 8.80, 8.84 and 7.90 wt.% P respectively. Higher additions of thiamine hydrochloride led to less phosphorous in the deposit. Overall, all additions of thiamine hydrochloride led to a decrease in phosphorous content.

Images of the surface were taken at 1000x magnification, shown in Figure 6.9. The smoothest surface was observed with the greatest addition of thiamine hydrochloride at 0.0002 M, there were few nodules above the smooth surface. At 0.0001 M additions, larger agglomerations of nodules were formed on the smooth deposit surface. At the lowest 1 x 10^{-5} M addition, a much greater number of surface features were observed, in the form of agglomerations as well as striations of small nodules across the entire surface.

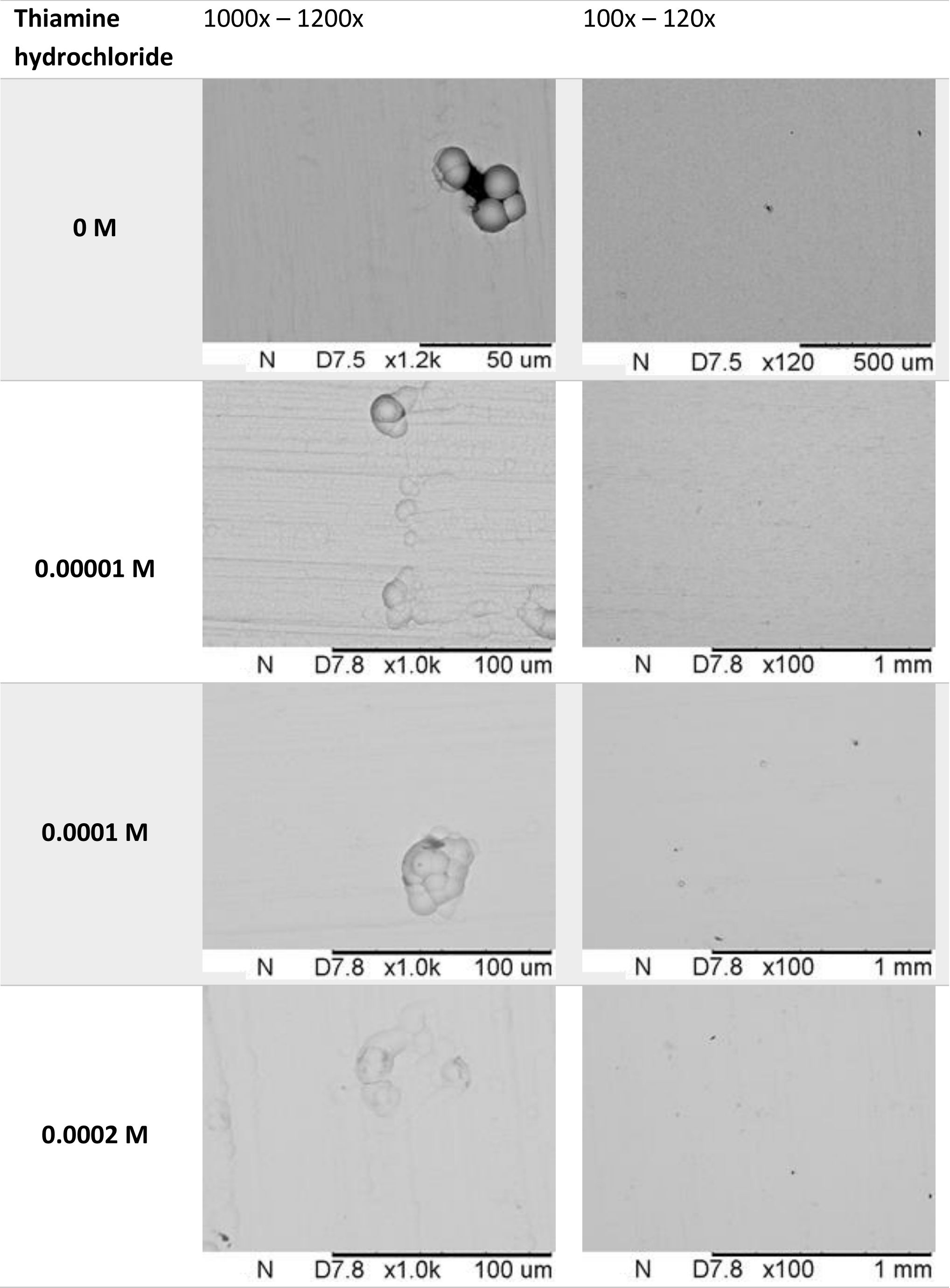

Figure 6.9. Images of the surface of samples plated in baths containing thiamine hydrochloride

Samples were sectioned and mounted to analyse the plating thickness using SEM, the results are shown in Table 6.3 below. The additions of thiamine hydrochloride increased the plating rate in all cases. Whilst the bath with no additive plated 9 µm·hr^{-1}, the baths with 0.00001, 0.0001 and 0.0002 M thiamine hydrochloride additions plated 11.5, 11.0 and 12.1 µm·hr^{-1} respectively. Overall, the addition of thiamine hydrochloride to the bath increased the plating rate, leading to a higher deposit thickness.

Table 6.3. Deposit thickness of samples plated in a bath with thiamine hydrochloride additions

Concentration thiamine hydrochloride (M)	Deposit thickness (µm)
0	9.0
0.00001	11.5
0.0001	11.0
0.0002	12.1

In terms of corrosion investigations, open circuit potential measurements were carried out in 3.5% NaCl at pH 7 for 1 hour so the surface formed a stable oxide layer. The results are shown in Figure 6.10 below; values are plotted as averages of the final 30 minutes of the experiment. The lower concentrations of thiamine hydrochloride, 0.00001 and 0.0001 M had higher OCP values at -0.334 and -0.369 V vs. SCE than the sample without bath additions, which had a measured OCP of -0.396 V vs. SCE. The bath with 0.0002 M thiamine hydrochloride addition had lower OCP -0.496 V vs. SCE. It is worth noting that the deposits plated in baths containing greater than 0.0002 M thiamine hydrochloride suffered from significant steel exposure on the surface, and therefore the lower OCP values observed are in part due to this.

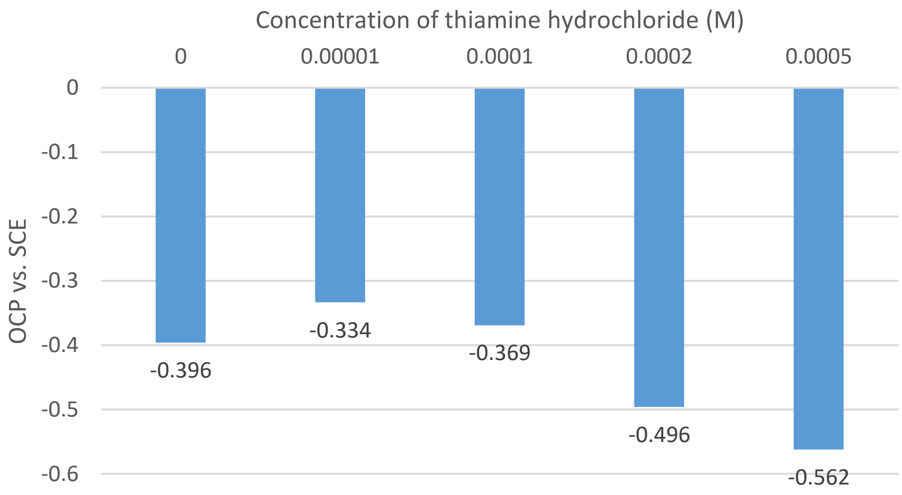

Figure 6.10. OCP values for samples plated from in-house baths with thiamine hydrochloride additions

Potentiodynamic polarisations were carried out, where potential was swept from -0.7 to 0.2 V vs. SCE at 1 mV·s^{-1}. Tafel lines were extrapolated to calculate mass loss values from LPR experiments, described in sections 2.8.2 and 2.8.3. Examples of the polarisation curves obtained are shown in Figure 6.11.

Linear polarisation resistance was used to calculate mass loss values. Samples were polarised ±10 mV around OCP at 0.25 mV·s^{-1}. The mass loss values from these experiments are shown in Figure

6.12 below. Again, where the bath contained greater than 0.0002 M thiamine hydrochloride, significant amounts of the steel substrate were still exposed, leading to very poor corrosion resistance.

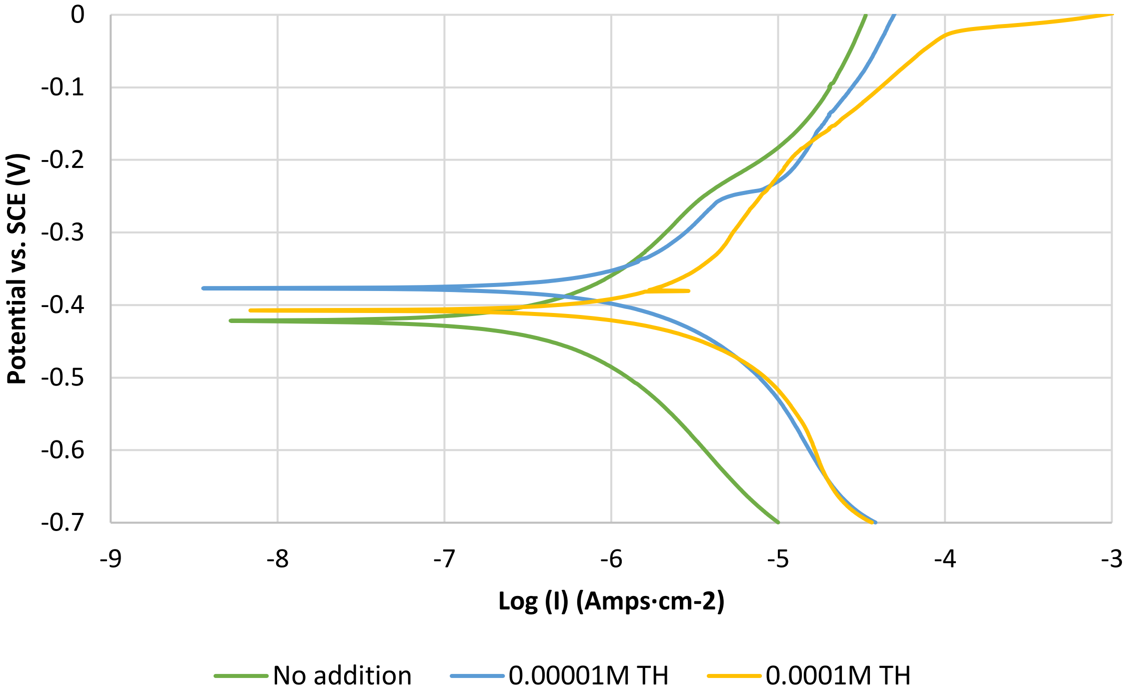

Figure 6.11. Example polarisation curves for samples plated in bath containing thiamine hydrochloride

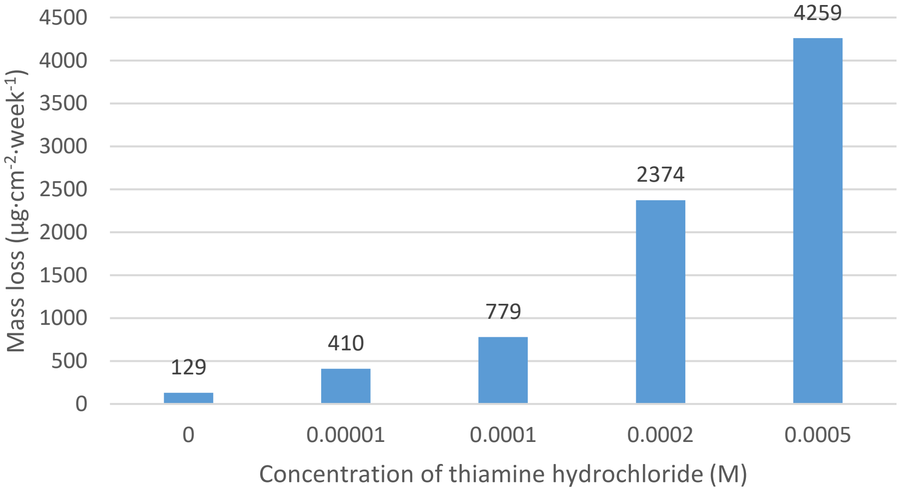

Figure 6.12. Mass loss values (LPR derived) for samples plated from baths containing thiamine hydrochloride

The results show all additions of thiamine hydrochloride significantly increased mass loss values. Samples plated in the bath with no additive had a mass loss of 129 µg·cm^{-2}·week, whilst samples plated from baths with thiamine hydrochloride additions had mass loss values of 410, 779 and 2374 µg·cm^{-2}·week with 0.00001, 0.0001 and 0.0002 M additions respectively. The smallest addition of thiamine hydrochloride gave the best corrosion resistance of samples plated in this way, however it remained significantly inferior to the sample plated in the absence of additions.

Vickers hardness testing was carried out on all samples plated from baths containing thiamine hydrochloride, where a load of 1 kg was applied for 10 seconds. Three indents were made in each sample and an average hardness was calculated, shown in Figure 6.13.

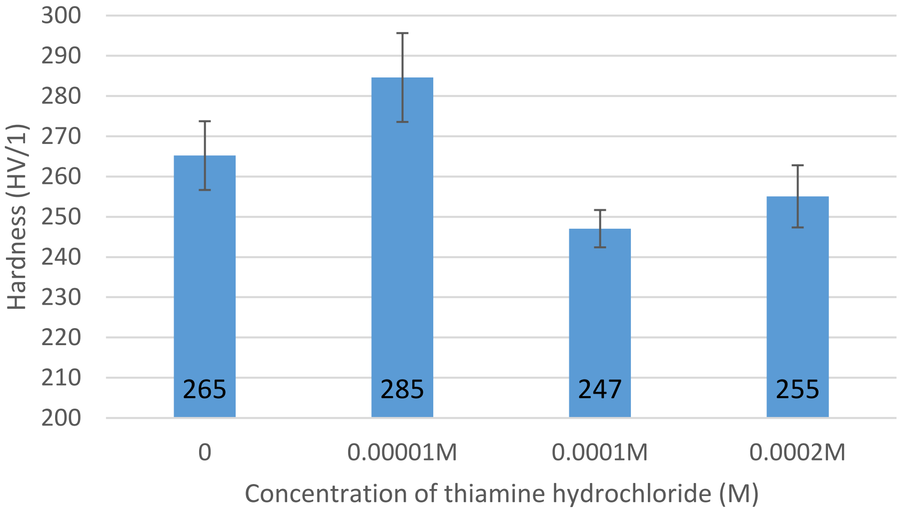

Figure 6.13. Average Vickers hardness values for in-house EN baths with thiamine hydrochloride additions

The results show additions of thiamine hydrochloride to baths led to an increase in the hardness of the deposit with the lowest addition of 0.00001 M, from 265 HV/1 to 285 HV/1 This decreased to 247.0 HV/1 with the 0.0001 M addition and then increased slightly to 255.1 HV/1 with the largest addition of 0.0002 M.

XRD was performed on samples with the highest and lowest additions of thiamine hydrochloride, and the spectra for these compared to the sample with no addition. All scans were performed as described in section 2.11, and the results are shown in Figure 6.14 below.

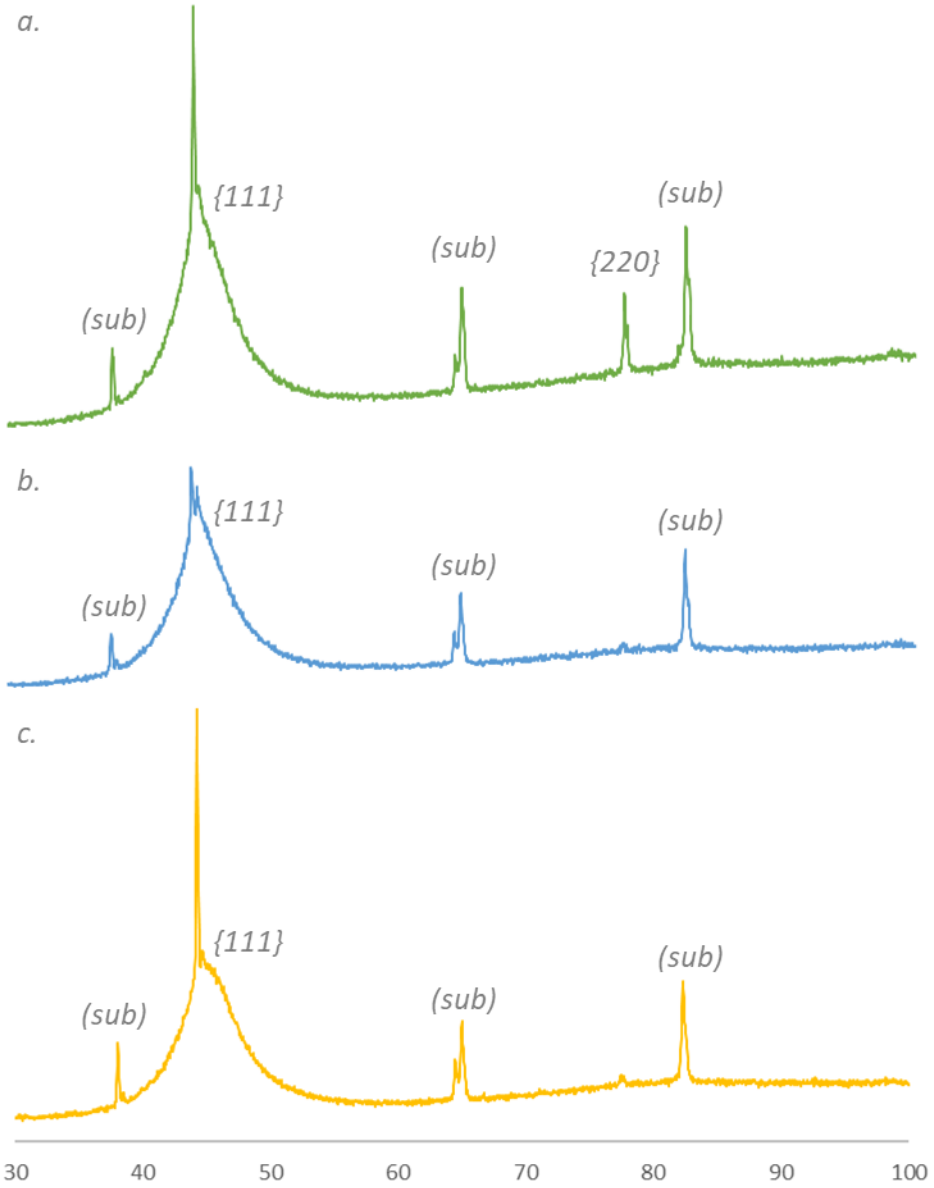

Figure 6.14. XRD diffraction patterns for plating baths with a. no additions, b. 0.00001 M thiamine hydrochloride and c. 0.0002 M thiamine hydrochloride

XRD diffraction patterns showed compared to samples with no additions, only nickel peaks in the {111} plane. The broad peak between 40° and 50° indicates an amorphous or nanocrystalline deposit structure. With both the 0.00001 M and 0.0002 M additions of thiamine hydrochloride, a small decrease in width and intensity of the broad peak was observed. A decrease in the intensity of the substrate peaks at 65° and 82° was also seen with these additions.

6.5 Discussion

6.5.1 Effect of sulphur containing organic compounds

Amino acids have previously been found to adsorb to metal surfaces, such as zinc and nickel [77], [109]. It was found unsaturated organic additives act to modify deposition of electroplated layers through adsorption, hydrogenation and/or desorption [183]. Macheras et al. [184] claimed for such unsaturated organic additives, the hydrogenolysis of C-S and S=O bonds leads to the production of sulphur anions, which are adsorbed onto the plating surface and cause changes in the mechanism and direction of crystal growth. These anions can be incorporated in the final structure as sulphides. Further work using sulphur-containing compounds indicated their presence caused significant changes in the nucleation and growth of deposits [185]. It is the unsaturated nature of such compounds that allows easy adsorption onto metal surfaces, effectively blocking active sites and potentially leading to stabilisation of the plating reaction.

In some cases where organic additives were used in plating baths, deposition rate increased, rather than decreased and stabilised. In both the cases of thiourea and cysteine, this was shown to happen by decreasing the activation energy required for electroless plating to occur. It was concluded both of these additives may form a reactive intermediate which increased the rate of hypophosphite oxidation, the rate determining step, and therefore increased the rate of the entire plating reaction [76], [77], [186].

6.5.2 Effect of taurine additions

Taurine is an organic compound and an amino sulfonic acid, derived from the amino acid cysteine. The structure of this molecule is shown in Figure 6.15. The effect of taurine additions to the basic plating bath produced deposits with an overall decreased phosphorous content, decreased plating rate, increased OCP, increased corrosion rate and had little effect on hardness.

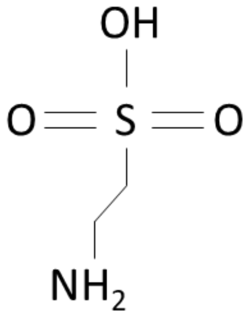

Figure 6.15. Structure of the taurine molecule

Sulfonic acids such as taurine have previously been added to electroless nickel plating baths as complexing and stabilising agents [187], [188], although no literature looking specifically at the effects of this compound was found. Some literature suggested taurine, amongst other sulfonic acids have been used as catalysts in bioorganic chemistry [189], [190]. At pH 5, the starting value for this bath, taurine is believed to exist in its zwitterion form with estimated pKa values of -1.50 and 9.06 [140], resulting in a net balanced charge on this compound, existing in the form $H_3N^+CH_2CH_2SO_3^-$.

Sodium hypophosphate has a pKa of 2.55 [191], meaning the reducing agent was fully deprotonated in the plating bath.

A small decrease in phosphorous content and deposit thickness was observed with all taurine additions. As previously mentioned, adsorption of unsaturated compounds to the substrate surface is highly possible. Adsorption is most likely to happen at active sites and therefore can reduced deposition rate. This effect has been described as the additive acting as a foreign body to interfere with processes on the surface [192]. This effect may have caused the reduction in plating rate leading to the lower phosphorous content of the deposit. It is most likely the additive led to localised areas of different chemical activity which inhibited the deposition of metal at localised points on the substrate [181]. It has been suggested amino acids and hypophosphite react at the same active sites on substrates [78], and therefore when amino acids are present they reduce the number of available active sites for the oxidation of hypophosphite.

In terms of corrosion properties, additions of taurine led to a small average increase in OCP but an overall reduction in corrosion resistance of the deposit compared to samples plated from the basic bath. Only a minimal drop in phosphorous content of the deposit was observed, so it is unlikely this change in composition affected the corrosion properties so drastically. Taurine is a sulphur containing compound, and it is likely that upon adsorption the C-S bond undergoes hydrogenolysis, releasing sulphur anions which can become incorporated within the deposit [77], [184], [186], [193]. No sulphur was seen on EDS analysis of these samples, this could be because it was only present in very small quantities and could not be resolved by the instrument used for analysis. Whilst sulphur containing compounds are often used in nickel electroplating baths to increase deposit brightness, it is well known such additions can have a detrimental effect on corrosion performance [182], [194], due to structural changes caused by adsorbed sulphide species.

Sulphur, in situations such as these has been found to sit preferentially at grain boundaries [195]. In terms of corrosion performance, this means the crystalline structure of the nickel alloy is compromised. Inclusions, such as sulphur provide perfect initiation points for corrosion; as the concentration of taurine was increased, the corrosion performance decreased, potentially due to sulphur enrichment at grain boundaries.

In terms of hardness, there was a small increase for one sample but overall the results were similar, with a small decrease in phosphorous content. It has previously been observed a decrease in phosphorous content results in an increase in hardness due to the microstructural changes which occur at varying alloy compositions [157], [159], [171]. However, in this case the reduction in phosphorous content was small, so it is possible alongside this, the presence of taurine may have caused some grain refinement. Other research has shown another organic sulphur containing compound, saccharin, causes a significant decrease in grain size of electrodeposited nickel coatings [196], whilst other sulfonic acid additions have also shown a significant reduction in grain size [197], [198]. It is therefore likely additions of taurine decreased the grain size of deposits.

XRD results showed samples deposited from taurine baths did not display a nickel {220} peak, possibly due to the additive causing grain refinement; the organic addition may have modified the surface meaning nickel preferentially deposits in the {111} direction. Small changes in crystal structure may also be shown by the decrease in width and height of the broad nickel {111} peak, likely due to the small reduction in phosphorous content resulting in a more crystalline structure. A sharp peak may not be observed if crystallites are smaller than 100 nm, or of there is significant lattice strain [178]. It is possible if grain size was decreased by this additive, the peaks representative of the {200} and {220} directions of nickel could be widened to the point where they are not visible in the diffraction pattern due to increased quantity of random scattering with the larger number of grain boundaries present [199]. As the quantity of taurine in the plating bath was increased, broadening of the nickel {111} peak decreased slightly due to the small drop in phosphorous content but remained broad as the deposit was still mainly amorphous and may have undergone a decrease in grain size.

6.5.3 Effect of thiamine hydrochloride additions

Thiamine hydrochloride, more commonly known as vitamin B_1 is an essential amine commonly used as a dietary supplement. The structure of this molecule is shown in Figure 6.16. The effect of thiamine chloride additions to the basic plating bath led to an overall decreased phosphorous content, increased plating rate, both increased and decreased OCP, an increased corrosion rate and little effect on the hardness of the deposit.

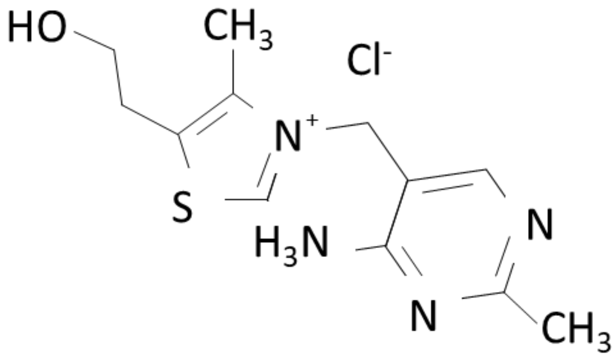

Figure 6.16. Structure of the thiamine hydrochloride molecule

Thiamine hydrochloride has previously been used as a brightener in zinc electroplating baths [200], [201], an eco-friendly additive in a copper acetate bath [185] and an additive in multi-layer Zn-Ni alloy bath [202]. In this work bath pH was 5, meaning thiamine hydrochloride existed in its fully protonated form with estimated pKa values of 5.54 and 15.5 [203]. This compound exhibited an overall positive charge in solution and was therefore likely to interact with sodium hypophosphite in solution, which has a pKa of 2.55 [191] meaning at pH 5 it was fully deprotonated. It has previously been suggested amines used as stabilisers should ideally be in their fully protonated form as they are less volatile which helps provide long term bath stability [187]. This compound is stable at acidic pH, but unstable in alkaline solutions so would not be suitable for plating baths operating at pH levels greater than 7.

In terms of deposit composition, additions of thiamine hydrochloride decreased the phosphorous content whilst increasing the plating rate. In section 5.5.1 it was discussed that the rate determining step for electroless nickel plating is oxidation of sodium hypophosphite. From these results, it appears additions of thiamine hydrochloride increased protonation rate of the reducing agent leading to an increased quantity of nickel deposited. Thiamine hydrochloride additions made to copper electrodeposition baths were found to increase the rate of deposition by increasing bath conductivity [185]. The same addition was also used in zinc acetate baths, where thiamine shifted the potential in the negative direction, as higher polarisation of the metal surface led to greater adsorption on active substrate sites [181], [200].

Regarding the corrosion properties, OCP values from samples with this additive showed little difference to those plated from the basic bath. However, in terms of corrosion rate, the smallest addition (0.00001 M) gave the smallest increase, and as the concentration of additive increased the corrosion rate significantly increased. As phosphorous content of these samples was lower than from the basic bath, it is likely this reduction led to a change in deposit crystal structure, making it less amorphous and therefore less corrosion resistant. When phosphorous content falls below 11 wt.%, a mix of crystalline and amorphous structures are thought to be present. With a greater likelihood of a crystalline microstructure, samples plated in baths with thiamine hydrochloride are likely to have lower corrosion resistance as there are more defects such as grain boundaries where corrosion can initiate [154], [159]–[161]. Additions of thiamine hydrochloride in copper and zinc electroplating baths showed deposits with reduced crystallite size [185], [200]. As crystallite size falls, the number of grain boundaries increases, meaning there are a greater number of locations where corrosion can initiate. Additionally, as thiamine hydrochloride is also a sulphur containing compound like taurine, it is possible some sulphur was adsorbed during hydrogenation of C-S bonds at the surface. This could lead to precipitation of impurities such as sulphur at grain boundaries, which may decrease corrosion resistance as described previously.

Changes in microstructure to more crystalline at lower phosphorous content and the potential for decreased crystallite size may account for the increased hardness at the lowest additive concentration. The Hall-Petch equation [204] explains that as grain size decreases, the hardness of a material should increase, due to the presence of additional grain boundaries which impede dislocation motion. However, studies of nanocrystalline materials have shown a limit to this relationship and once grain size drops below a certain point, hardness decreases, known as the inverse Hall-Petch relationship [92], [205]. The alloys deposited here contain both crystalline and amorphous phases, however this may not be the only explanation for increased hardness. Due to the mixed structure present at 8.5 wt.% P, the average phosphorous content of samples plated from baths containing thiamine hydrochloride, nano-crystallites may act as strengthening particles within the amorphous matrix. The hardness of these Ni-P alloys was higher than pure nickel as less slip systems were present [92], resulting in materials with greater resistance to permanent deformation.

XRD diffraction patterns for samples containing thiamine hydrochloride did not display a nickel {220} peak, as seen from the samples plated in baths containing taurine. It is possible this additive caused some grain refinement, leading to preferential plating in the nickel {111} direction. A small reduction in the width and height of the broad nickel {111} curve was seen for samples plated in thiamine hydrochloride, probably due to the reduction in phosphorous content. However, there is no clear increase in peak intensity which would be expected with a drop in phosphorous content. It is possible the additive caused a decrease in grain size, resulting in more diffraction and peak broadening [199]. It was previously found additives which accelerate nickel reduction, such as this one, led to a more crystalline deposit [12]. More noticeably, a decrease in intensity of substrate peaks at 65^{o} and 82^{o} can be attributed to an increased plating rate and a thicker deposit. Less intense peaks are seen from XRD due to less x-ray interaction with the substrate [178].

6.6 Conclusions

This chapter has shown it is possible to change EN deposit properties using small additions of taurine and thiamine hydrochloride. Results from SEM/EDS scans showed additions of taurine caused a small decrease of around 5% in phosphorous content and additions of thiamine hydrochloride led to a minimum 20% decrease in phosphorous content. Cross section analysis showed additions of taurine led to an average decrease in deposit thickness of 13%, whilst additions of thiamine chloride led to an average increase of just under 22%. In terms of corrosion analysis, OCP increased by an average of 16% with taurine additions, the lowest two additions of thiamine hydrochloride led to an increase of just over 10% whilst the 0.0002 M addition led to a 25% decrease. The results for corrosion rate from LPR showed taurine additions increased corrosion rate by an average of more than 250%, whilst thiamine hydrochloride additions led to a minimum increase of 220% and a maximum of 1740%. Vickers hardness testing was also completed on these samples, and it was found both additions of taurine and thiamine hydrochloride had little effect on deposit hardness.

While none of the additions resulted in increased corrosion resistance, it was possible to change other characteristics of the deposits. The additions of taurine most led to a decrease in P content and thickness of the deposit, and a reduction in corrosion resistance, thought to be due to adsorption of unsaturated compounds to the substrate surface. The additions of thiamine hydrochloride led to an increase in plating rate, but a significant decrease in the corrosion resistance with greater quantities. These effects are thought to be because thiamine hydrochloride changed the conductivity of the plating solution and decreased crystallite size.

As a potential alternative to electroplating for The Royal Mint, it is unlikely electroless nickel plating will be adopted in the near future. Many of the current processes used by TRM are carried out on carousel barrel plating lines, which in itself does not cause any issues for electroless plating. However, to maintain baths at optimum operating conditions requires constant monitoring of pH, temperature, nickel content and so on, with additions and corrections made to counteract any changes in these operating parameters. A system to monitor all these variables would be very expensive to commission and install, and any issues could lead to a significant loss of machine time. Electroless plating bath solution has a limited lifetime, due to the build-up of ions such as NH_4^+, Na^+, $SO_4^=$, Cl^- [206] as well as phosphite species [207] and so on over time, as ingredients can only be replenished to a finite extent before the bath must be discarded and replaced with fresh solution. It is clear from the work in this and the previous chapter, a significant amount of research and development would be necessary to evolve a bath chemistry suitable for such large-scale production and optimise the corrosion and mechanical properties of deposits.

A further issue which may discourage TRM from adopting this technology is the significant volume of hydrogen produced during plating, due to the oxidation of sodium hypophosphite [149]. Currently plating is carried out in a large open warehouse; in this space it is possible the level of hydrogen released from electroless plating could build up to an explosive level. This means TRM would have to purchase and install an expensive, sophisticated extraction system to make the project a viable option for future production.

Chapter 7. Conclusions and Further Work

7.1 Conclusions

This thesis has investigated the use of nickel-plated steel in circulation coinage, the likely effects on the surface when defects are present and the possibility of using an alternative plating technique in the future.

Chapter 3 investigated the potential for a galvanic corrosion cell to develop between the sections of bimetallic circulation coins from different countries. A series of electrochemical and scanning techniques were used under a variety of conditions and solutions to assess the likelihood for two different metals to couple and accelerate corrosion. The samples selected for examination were Sierra Leones 500L, Egypt £1, UK £2 and UK £1.

Initially OCP was used to find the rest potentials of different brass-based and nickel-based sections used in the creation of these coins Results showed brass-based sections had lower potentials than nickel-based sections, indicating in all cases, when coupled together the brass-based section would always act as the anode and undergo metal dissolution in preference to the more noble, nickel-based section. In both 3.5% NaCl and AFS solutions the smallest potential difference was between the sections of the UK £2. In 3.5% NaCl, the next smallest difference was seen between the sections of the 500L, then the £1 and finally the £E1. In AFS solution, the next smallest difference in potential was seen between the £1, then the E£1 and the 500L. A small potential difference indicates there is less likelihood of a galvanic corrosion cell forming.

ZRA was used to measure the corrosion current generated between sections of coins when the size of the brass-based (anodic) section was kept constant and the surface area of the nickel-based (cathode) section was varied, to monitor the effect on the metal dissolution reaction. In all cases, increases in surface area of the nickel-based section led to an increase in measured corrosion current density. The E£1 and 500L showed very similar behaviour and the lowest current densities, a small increase was observed for the UK £1, whilst a significant increase was seen for the sections of the UK £2. These results contradict the OCP results, suggesting the UK £2 is most likely to be affected by interactions between different metal sections.

Scanning techniques were used to identify and monitor the intensity and location of corrosion events on the surface. The SVET was used to scan a small area covering both sections of each coin. Using an electrolyte of AFS, it was found in the cases of £E1, 500L and £1 the majority of anodic and cathodic activity was observed on the brass-based sections, whilst a small amount of low intensity cathodic behaviour was seen on the nickel-based sections. This could be due to a stable oxide layer on the nickel surface preventing corrosion from occurring, or to the limited resolution of SVET not showing generalised corrosion on the nickel-based surface. The highest intensity of anodic activity was seen on the brass-based section of the UK £2.

As all previous experimentation was carried out under immersion conditions, SKP was chosen to monitor surface activity under atmospheric conditions. A relative humidity of 89% was generated using a 5% NaCl solution. SKP scans showed opposite behaviour to previous experiments; nickel-based sections all displayed lower potentials compared to brass-based sections, indicating nickel-based sections were more active and likely to undergo metal dissolution. This is because under atmospheric conditions only a very thin layer of water can form, with high resistance meaning currents cannot flow between the sections, so it is unlikely galvanic corrosion activity happened between them. It is more likely different oxide layers formed under atmospheric conditions than in immersion, and under such conditions nickel may take some time to generate a protective film leading to very high initial corrosion rates, which may explain the results seen here.

It is obvious from these results there is a risk of a galvanic corrosion cell developing between the sections of bimetallic coins. However, all investigations performed here were either under immersion conditions or very high humidity, which is unrepresentative of environments normally experienced by coins.

Chapter 4 investigated the effects of defects in nickel-plated layers to the steel substrate under atmospheric conditions. Porosity is a known issue for electroplated nickel, and it has previously been shown breakthrough to the substrate can occur. Defects of a range of sizes from 0.5 to 2 mm were made using a Dremel drill, and droplets with concentrations of 0.1 to 5 M NaCl and 0.5 M $MgCl_2$ were used.

Time lapse photography was used to monitor droplet progression on nickel-plated samples over a 48-hour period. In the first set of experiments the defect was maintained at a constant 0.5 mm diameter whilst a range of different chloride solutions and concentrations were introduced. Results showed NaCl concentrations from 0.1 to 2 M NaCl increased the amount of spreading, whilst a decrease in spreading was observed under 5 M NaCl conditions. This was partially due to lack of oxygen in the droplet at higher concentrations, as well as changes in relative humidity with different chloride concentrations. The 0.1 M NaCl electrolyte generated the highest RH at 94%, whilst the 5 M NaCl electrolyte only provided a 74% RH. This meant at higher NaCl concentrations, less water vapour was present to form adsorbed layers on the samples leading to less spreading.

Secondary spreading was seen under NaCl droplets because surface tension changed at the edges as ionic composition was altered by chemical processes. Soluble carbonate species formed in this region, which spread with the droplet until insoluble carbonate precipitates formed, which stopped spreading progression. No spreading was observed under the 0.5 M $MgCl_2$ droplet, due to the formation of insoluble magnesium hydroxide products deposited at the perimeter. Due to the prevalence of the oxygen reduction reaction at the extremities of the droplet, the pH was high in this region, causing insoluble precipitates of this salt to form.

SEM/EDS maps showed sodium migration to the spreading region, whilst chloride species mainly remained within the original droplet confines. This was due to ion migration to maintain electroneutrality in the droplet. Sodium migration is due to the formation of soluble hydroxide species, which spread away from the original droplet. Similar results were seen on steel blank samples, although spreading distances were greater due to the lower nobility of steel compared to nickel.

The SKP monitored changes in potential across the surface during spreading with a 0.5 mm defect under 2 M NaCl conditions. Results found the potential of the initial droplet was lower than the surrounding area but maintained a constant potential over the 18-hour experiment. Over this time, the area of the original droplet appeared to expand with an area of slightly higher potential, illustrating growth of the secondary spreading zone. This clear difference in potential indicated separation of anodic and cathodic events on the surface, suggesting progression of the secondary spreading area may increase cathode size, which could increase the intensity of corrosion in the defect. Further work is needed to confirm this.

Varying defect size from 0.5 to 2 mm whilst maintaining a constant droplet size was investigated. Very little variation in spreading distance was seen despite changes in defect size. As the amount of spreading did not significantly increase as anode size increased, it suggests the reaction is under anodic control.

Chapter 5 investigated the possibility of using electroless nickel plating as an alternative to standard electrolytic plating. Initially, deposits from three commercially available solutions were examined for their physical, corrosion and mechanical properties. These were different from the expected deposits, and this could not be investigated as they were from proprietary solutions. Therefore, a basic in-house bath was created, and run at various temperatures and pH's. These deposits had phosphorous contents ranging from 7.92 to 15.64 wt.% and were examined for their corrosion and mechanical properties.

Plating temperatures from 70^{o}C to 80^{o}C were used. Increasing temperature led to greater phosphorus content, plating rate, corrosion resistance and Vickers hardness. Bath pH’s from 4 to 6 were used. Increases in the pH increased plating rate and Vickers hardness, and decreased phosphorous content and corrosion resistance. As temperature increased, a small increase in phosphorous content was observed due to faster reaction rates at higher temperatures. This also accounts for the increase in plating rate. As bath pH increased, the oxidation rate of hypophosphite increased, depositing more nickel and increasing thickness. The phosphorous content decreased at higher pH’s due to the requirement of hydrogen ions, which are more prevalent at lower pH’s.

Where increases in phosphorous content and plating rate were seen, this likely accounts for increases in corrosion resistance. At higher phosphorous contents, the microstructure becomes more amorphous, meaning there are less sites where corrosion can be initiated. Increases in hardness were due to the formation of the non-equilibrium intermediate phase β at phosphorus contents between 4.4 – 11 wt.%.

However, the corrosion resistance of the best performing electroless nickel sample was lower than for standard electroplated nickel. This was thought to be because coating thickness was not great enough to account for any porosity, leading to the increased rate of corrosion.

In Chapter 6, small additions of organic additives were made to the basic in-house electroless nickel-plating bath. Maintaining a bath pH of 5 and plating temperature of 75^{o}, additions were made the effects deposit properties was measured. Taurine and thiamine hydrochloride were selected as potential modifiers as they had similar structures to previously used additives. In both cases, the smallest additions led to samples with better properties. The higher additions generally led to a significant decrease in corrosion performance.

Additions of taurine decreased phosphorous content, plating rate and corrosion resistance. This was thought to be because the additive caused a decrease in crystallite size and there was potential for incorporation of sulphur. The additions of thiamine hydrochloride increased the plating rate but significantly decreased corrosion resistance, especially at higher additions and decreased phosphorous content. These effects are thought to be due to the additive changing solution conductivity which increased deposition rate and potentially decreased crystallite size.

7.2 Further Work

To progress this work further, there are several options which could be considered:

To complete the work on bimetallic coin corrosion, further investigation is required into the microstructure of minted coins at various locations of the surface, to try and understand if the minting process causes variation in grain size and composition over the surface. In the future, investigations could be completed on a wider range of coins with two-metal construction. From this, samples with a greater range of compositions could be examined to identify a more compatible couple. Another solution to the formation of a galvanic couple would be to electrically isolate the sections, and so some investigation into how this could be achieved may be worthwhile.

The next steps to tie together the atmospheric corrosion work would be to assess secondary spreading on a nickel-plated sample with no defect and on a solid nickel sample with a defect. This work could be further investigated by reducing the size of the defect to be more representative of pitting corrosion. Furthermore, work could be carried out to assess the secondary spreading effects of a wider range of salts, such as lithium, potassium and caesium. It is likely different levels of spreading would be observed under each, due to their varying solubility and mobility in solution, and may provide useful mechanistic information.

Further techniques, such as Time-of-Flight Secondary Ion Mass Spectrometry (ToF SIMS) could be used to analyse corrosion products in the secondary spreading region and confirm the identity of any soluble and insoluble precipitates which move away from the original droplet location.

There are many steps which could be taken to develop the electroless nickel plating bath. First, more temperature and pH combinations could be trialled from the basic bath to optimise deposits. Changes in the amounts of the three basic ingredients could also be trialled. A full system of monitoring for the quantity of nickel present in the bath, as well as real time monitoring of pH and temperature would help produce more consistent deposits and extend bath lifetime.

In terms of the organic additions, there are many more experiments which could be carried out to determine what effects the additions had on deposits. Monitoring changes in conductivity of the bath with and without additions could confirm some of the mechanisms predicted by this work. Using a wider range of the additives could also help determine what quantities are required to give deposits with the best properties.

References

[1] I. Rezić, M. Zeiner, and I. Steffan, “Determination of allergy-causing metals from coins,” *Monatshefte für Chemie - Chem. Mon.*, vol. 140, no. 2, pp. 147–151, Feb. 2009, doi: 10.1007/s00706-008-0071-9.

[2] C. R. Hamann, D. Hamann, C. Hamann, J. P. Thyssen, and C. Lidén, “The cost of nickel allergy: a global investigation of coin composition and nickel and cobalt release,” *Contact Dermatitis*, vol. 68, no. 1, pp. 15–22, Jan. 2013, doi: 10.1111/cod.12008.

[3] J. J. Hostynek and H. I. Maibach, Eds., *Nickel and the Skin: Absorption, Immunology, Epidemiology, and Metallurgy*. CRC Press LLC, 2002.

[4] J. P. Thyssen, D. J. Gawkrodger, I. R. White, A. Julander, T. Menné, and C. Lidén, “Coin exposure may cause allergic nickel dermatitis: a review,” *Contact Dermatitis*, vol. 68, no. 1, pp. 3–14, Jan. 2013, doi: 10.1111/j.1600-0536.2012.02127.x.

[5] F. O. Nestle, H. Speidel, and M. O. Speidel, “High nickel release from 1- and 2-euro coins,” *Nature*, vol. 419, no. 6903, pp. 132–132, Sep. 2002, doi: 10.1038/419132a.

[6] D. W. Ernst and F. Ogburn, “The Nature, Cause and Effect of Porosity in Electrodeposits: A Microscopic Examination of Nickel-Chromium Coatings after Atmospheric Corrosion,” *NASF Surf. Technol. White Pap.*, vol. 81, no. 6, pp. 3–14, 2017.

[7] R. Waldram, “Investigating Nickel Ion Release from Nickel Plate Using Various Test Methods - MRes thesis,” Swansea University, 2014.

[8] D. Baudrand and B. Durkin, “Automotive Applications of Electroless Nickel,” *Met. Finish.*, vol. 96, no. May, pp. 20–23, 1998, doi: 10.1016/S0026-0576(98)80080-9.

[9] M. S. Jagatheeshwaran, A. Elayaperumal, and S. Arulvel, “Wear characteristics of electroless NiP/bio-composite coatings on En8 steel,” *J. Manuf. Process.*, vol. 20, pp. 206–214, Oct. 2015, doi: 10.1016/j.jmapro.2015.08.002.

[10] M. Sribalaji, P. Arunkumar, K. Suresh Babu, and A. K. Keshri, “Crystallization mechanism and corrosion property of electroless nickel phosphorus coating during intermediate temperature oxidation,” *Appl. Surf. Sci.*, vol. 355, pp. 112–120, Nov. 2015, doi: 10.1016/j.apsusc.2015.07.061.

[11] B. Oraon, G. Majumdar, and B. Ghosh, “Application of response surface method for predicting electroless nickel plating,” *Mater. Des.*, vol. 27, no. 10, pp. 1035–1045, Jan. 2006, doi: 10.1016/j.matdes.2005.01.025.

[12] I. Baskaran, T. S. N. Sankara Narayanan, and A. Stephen, “Effect of accelerators and stabilizers on the formation and characteristics of electroless Ni–P deposits,” *Mater. Chem. Phys.*, vol. 99, no. 1, pp. 117–126, Sep. 2006, doi: 10.1016/j.matchemphys.2005.10.001.

[13] R. Spiewak, J. Pietowska, and K. Curzytek, “Nickel: a unique allergen – from molecular structure to European legislation,” *Expert Rev. Clin. Immunol.*, vol. 3, no. 6, pp. 851–859, Nov. 2007, doi: 10.1586/1744666X.3.6.851.

[14] U.S. Department of Health and Human Services, “Report on Carcinogens Twelfth Edition,” 2011.

[15] K. K. Das, S. N. Das, and S. A. Dhundasi, “Nickel, its adverse health effects & oxidative stress,” *Indian J. Med. Res.*, vol. 128, no. 4, pp. 412–25, Oct. 2008, [Online]. Available: http://www.ncbi.nlm.nih.gov/pubmed/19106437.

[16] L. K. Lu, E. M. Warshaw, and C. A. Dunnick, “Prevention of Nickel Allergy: The Case for Regulation?,” *Dermatol. Clin.*, vol. 27, no. 2, pp. 155–161, Apr. 2009, doi: 10.1016/j.det.2008.11.003.

[17] P.-G. Fournier and T. R. Govers, “Contamination by nickel, copper and zinc during the handling of euro coins,” *Contact Dermatitis*, vol. 48, no. 4, pp. 181–8, Apr. 2003, [Online]. Available: http://www.ncbi.nlm.nih.gov/pubmed/12786720.

[18] S. Colin, G. Krier, H. Jolibois, A. Hachimi, J. F. Muller, and A. Chambaudet, “Characterization of the corrosion layer of copper-nickel alloys in a synthetic sweat medium by FTMS and LAMMA laser microprobes,” *Appl. Surf. Sci.*, vol. 125, no. 1, pp. 29–45, Jan. 1998, doi: 10.1016/S0169-

4332(97)00400-5.

[19] I. Milošev and T. Kosec, “Metal ion release and surface composition of the Cu–18Ni–20Zn nickel–silver during 30 days immersion in artificial sweat,” *Appl. Surf. Sci.*, vol. 254, no. 2, pp. 644–652, Nov. 2007, doi: 10.1016/j.apsusc.2007.06.049.

[20] C. Lidén, L. Skare, and M. Vahter, “Release of nickel from coins and deposition onto skin from coin handling – comparing euro coins and SEK,” *Contact Dermatitis*, vol. 59, no. 1, pp. 31–37, Jul. 2008, doi: 10.1111/j.1600-0536.2008.01363.x.

[21] C. Lidén, “Nickel allergy and coins,” *MintWorld Compend.*, vol. 1, no. 1, pp. 12–13, 2012.

[22] C. Foti, S. Seidenari, A. Antelmi, D. Bonamonte, A. Conserva, and G. Angelini, “Provocative use test of 1 euro coin in nickel-sensitized subjects,” *Contact Dermatitis*, vol. 52, no. 3, pp. 167–168, Mar. 2005, doi: 10.1111/j.0105-1873.2005.0548i.x.

[23] O. Christensen and H. Moller, “External and Internal Exposure to the Antigens in the Hand Eczema of Nickel Allergy,” *Contact Dermatitis*, vol. 1, no. 3, pp. 136–141, 1975.

[24] British Standards Institution, “BS EN 1811:2011 - Reference test method for release of nickel from all post assemblies which are inserted into pierced parts of the human body and articles intended to come into direct and prolonged contact with the skin.” European Committe for Standardization (CEN), 2011, [Online]. Available: www.iso.org.

[25] G. Koch, J. Varney, N. Thompson, O. Moghissi, M. Gould, and J. Payer, “International Measures of Prevention , Application , and Economics of Corrosion Technologies Study,” *NACE Int.*, pp. 1–216, 2016, [Online]. Available: http://impact.nace.org/documents/Nace-International-Report.pdf.

[26] K. R. Trethewey and J. Chamberlain, *Corrosion for science and engineering*, Second. NACE International, Houston, TX (United States), 1995.

[27] National Physical Laboratory, “Guides to Good Practice in Corrosion Control - Bimetallic Corrosion,” in *NPL*, 2000, pp. 1–20.

[28] X. G. Zhang, “Galvanic Corrosion,” in *Uhlig’s Corrosion Handbook*, Hoboken, NJ, USA: John Wiley & Sons, Inc., 2011, pp. 123–143.

[29] ASTM, “ASTM G82-98 - Standard Guide for Development and Use of a Galvanic Series for Predicting Galvanic Corrosion Performance,” *Annual Book of ASTM Standards*. pp. 1–7, 2009, doi: 10.1520/G0082-98R09.2.

[30] A. Roy, “Galvanic Corrosion Testing Using Electrochemical and Immersion Techniques,” Lawrence Livermore National Laboratory, California, 1996.

[31] Atlas Steels, “Galvanic Corrosion,” no. 7. pp. 1–4, 2010.

[32] R. Baboian, *Corrosion Books: Corrosion Tests and Standards: Application and Interpretation*, Second. ASTM International, 2005.

[33] J. G. . Thomas and G. Hinds, *The Electrochemistry of Corrosion*, no. 1. .

[34] I. Odnevall and C. Leygraf, “The Atmospheric Corrosion of Nickel in a Rural Atmosphere,” *J. Electrochem. Soc.*, vol. 144, no. 10, p. 3518, 1997, doi: 10.1149/1.1838043.

[35] C. Leygraf, I. O. Wallinder, J. Tidblad, and T. Graedel, *Atmospheric Corrosion*, Second. Wiley, 2016.

[36] E. E. Abd El Aal, W. Zakria, A. Diab, and S. M. Abd El Haleem, “Anodic Dissolution of Nickel in Acidic Chloride Solutions,” *J. Mater. Eng. Perform.*, vol. 12, no. 2, pp. 172–178, 2003.

[37] L. Shreir, “Nickel and Nickel Alloys,” in *Shreir’s Corrosion*, T. Richardson, Ed. pp. 4:116-4:156.

[38] L.-F. Huang, M. J. Hutchison, R. J. Santucci, J. R. Scully, and J. M. Rondinelli, “Improved Electrochemical Phase Diagrams from Theory and Experiment: The Ni–Water System and Its Complex Compounds,” *J. Phys. Chem. C*, vol. 121, no. 18, pp. 9782–9789, May 2017, doi: 10.1021/acs.jpcc.7b02771.

[39] N. Sato and G. Okamoto, “Kinetics of the Anodic Dissolution of Nickel in Sulfuric Acid Solutions,” *J. Electrochem. Soc.*, vol. 111, no. 8, pp. 897–903, 1964.

[40] G. T. Burstein and G. A. Wright, “The anodic dissolution of nickel - 1Perchlorate and fluoride electrolytes,” *Electrochim. Acta*, vol. 20, no. 1, pp. 95–99, 1975.

[41] E. Kunze and K. Schwabe, “Beitrag zur passivität des nickels (Contribution to the passivity of nickels),” *Corros. Sci.*, vol. 4, no. 1–4, pp. 109–136, 1964.

[42] P. N. Clark, E. Jackson, and M. Robinson, “Effect of thiourea and some of its derivatives on the corrosion behaviour of nickel in 50% v/v (5.6M) hydrochloric acid,” *Br. Corros. J.*, vol. 14, no. 33, 1979.

[43] I. Milošev and M. Metikoš-Hunković, “Effect of chloride concentration range on the corrosion resistance of Cu-xNi alloys,” *J. Appl. Electrochem.*, vol. 29, pp. 393–402, 1999.

[44] J. Hahm and S. . Sibener, “Stress-modified electrochemical reactivity of metallic surfaces: atomic force microscopy imaging studies of nickel and alloyed aluminum,” *Appl. Surf. Sci.*, vol. 161, no. 3–4, pp. 375–384, Jul. 2000, doi: 10.1016/S0169-4332(00)00280-4.

[45] T. Tokuda and M. B. Ives, “Pitting corrosion of Ni,” *Corros. Sci.*, vol. 11, no. 5, pp. 297–306, May 1971, doi: 10.1016/S0010-938X(71)80063-X.

[46] S. Jouen, M. Jean, and B. Hannoyer, “Atmospheric corrosion of nickel in various outdoor environments,” *Corros. Sci.*, vol. 46, no. 2, pp. 499–514, Feb. 2004, doi: 10.1016/S0010-938X(03)00143-4.

[47] D. W. Rice, P. B. P. Phipps, and R. Tremouroux, “Atmospheric Corrosion of Nickel,” *J. Electrochem. Soc.*, vol. 127, no. 3, p. 563, 1980, doi: 10.1149/1.2129712.

[48] J.-P. Randin, “Corrosion resistance of nickel in artificial sweat and synthetic seawater,” *Mater. Corros. und Korrosion*, vol. 38, no. 5, pp. 233–236, May 1987, doi: 10.1002/maco.19870380505.

[49] U. R. Evans, *The Corrosion of Metals*. London: E. Arnold & co., 1926.

[50] R. J. Jiang and Y. F. Cheng, “Mechanism of electrochemical corrosion of steel under water drop,” *Electrochem. commun.*, vol. 35, pp. 8–11, Oct. 2013, doi: 10.1016/j.elecom.2013.07.019.

[51] A. K. Neufeld, I. S. Cole, A. M. Bond, and S. A. Furman, “The initiation mechanism of corrosion of zinc by sodium chloride particle deposition,” *Corros. Sci.*, vol. 44, no. 3, pp. 555–572, Mar. 2002, doi: 10.1016/S0010-938X(01)00056-7.

[52] T. Tsuru, K.-I. Tamiya, and A. Nishikata, “Formation and growth of micro-droplets during the initial stage of atmospheric corrosion,” *Electrochim. Acta*, vol. 49, no. 17–18, pp. 2709–2715, Jul. 2004, doi: 10.1016/j.electacta.2004.01.032.

[53] M. Kabasakaloğlu, T. Kıyak, O. Şendil, and A. Asan, “Electrochemical behavior of brass in 0.1 M NaCl,” *Appl. Surf. Sci.*, vol. 193, no. 1–4, pp. 167–174, Jun. 2002, doi: 10.1016/S0169-4332(02)00258-1.

[54] R. H. Heidersbach and E. D. Verink, “The Dezincification of Alpha and Beta Brasses,” *CORROSION*, vol. 28, no. 11, pp. 397–418, Nov. 1972, doi: 10.5006/0010-9312-28.11.397.

[55] R. K. Dinnappa and S. M. Mayanna, “The dezincification of brass and its inhibition in acidic chloride and sulphate solutions,” *Corros. Sci.*, vol. 27, no. 4, pp. 349–361, Jan. 1987, doi: 10.1016/0010-938X(87)90077-1.

[56] L. Burzyńska, A. Maraszewska, and Z. Zembura, “The corrosion of Cu-47.3 at% Zn Brass in aerated 1.0 M HCl,” *Corros. Sci.*, vol. 38, no. 2, pp. 337–347, Feb. 1996, doi: 10.1016/0010-938X(96)00132-1.

[57] S. Sohn and T. Kang, “The effects of tin and nickel on the corrosion behavior of 60Cu-40Zn alloys,” *J. Alloys Compd.*, vol. 335, no. 1–2, pp. 281–289, 2002, doi: 10.1016/S0925-8388(01)01839-4.

[58] C.-A. Wurtz, “Recherches sur la Constitution des Acides du Phosphore,” *C. R. Hebd. Seances Acad. Sci.*, vol. 21, pp. 149–155, 1845.

[59] M. P. Breteau, “Unknown,” *Bull. Soc. Chim. Fr.*, no. 32, pp. 9:515-518, 1911.

[60] F. A. Roux, “Process of producing metallic deposits,” 1207218, 1916.

[61] G. O’Mallory, “The Fundamental Aspects Of Electroless Nickel Plating,” in *Electroless Plating - Fundamentals and Applications*, William Andrew Publishing/Noyes, 1990, pp. 1–56.

[62] Metal Finishing Suppliers’ Associ, “Quality Metal Finishing Guide - Electroless Nickel Plating.”

[63] A. S. M. . Haseeb, P. Chakraborty, I. Ahmed, F. Caccavale, and R. Bertoncello, “XRD, XPS and SIMS investigations on electrodeposited nickel-phosphorous alloy coatings,” *Thin Solid Films*, vol. 283, no. 1–2, pp. 140–144, Sep. 1996, doi: 10.1016/0040-6090(95)08217-4.

[64] K. N. Srinivasan and S. John, “Electroless nickel deposition from methane sulfonate bath,” *J. Alloys Compd.*, vol. 486, no. 1–2, pp. 447–450, Nov. 2009, doi: 10.1016/j.jallcom.2009.06.178.

[65] L. Shreir, “Nickel Coatings,” in *Shreir’s Corrosion*, T. Richardson, Ed. pp. 13:78-13:98.

[66] M. Schlesinger, “Electroless deposition of nickel,” in *Modern Electroplating*, Fifth., M. Schlesinger and M. Paunovic, Eds. Wiley, 2010, pp. 447–458.

[67] A. Brenner, C. Chase, and G. E. Riddell, “Nickel Plating By Chemical Reduction,” 2532283, 1950.

[68] H. Ashassi-Sorkhabi and S. H. Rafizadeh, “Effect of coating time and heat treatment on structures and corrosion characteristics of electroless Ni–P alloy deposits,” *Surf. Coatings Technol.*, vol. 176, no. 3, pp. 318–326, Jan. 2004, doi: 10.1016/S0257-8972(03)00746-1.

[69] A. M. Fundo and L. M. Abrantes, “The electrocatalytic behaviour of electroless Ni–P alloys,” *J. Electroanal. Chem.*, vol. 600, no. 1, pp. 63–79, Feb. 2007, doi: 10.1016/j.jelechem.2006.03.023.

[70] A. Małecki and A. Micek-Ilnicka, “Electroless nickel plating from acid bath,” *Surf. Coatings Technol.*, vol. 123, no. 1, pp. 72–77, Jan. 2000, doi: 10.1016/S0257-8972(99)00423-5.

[71] H. R. Molla, H. Modarress, and M. Abdouss, “Electroless nickel–phosphorus deposition on carbon steel CK-75 and study of the effects of some parameters on properties of the deposits,” *J. Coatings Technol. Res.*, vol. 9, no. 2, pp. 183–188, Mar. 2012, doi: 10.1007/s11998-009-9231-z.

[72] Bal Seal, “Electroless Nickel Plating - A General Description of Electroless Nickel Plating and its Effect on BAL(tm) Seal Performance in Reciprocating and Rotary Service.”

[73] H. Keping and J. L. Fang, “Stabilization effect of electroless nickel plating by thiourea,” *Met. Finish.*, vol. 95, no. 2, pp. 73–75, Feb. 1997, doi: 10.1016/S0026-0576(97)81818-1.

[74] A. Brenner and G. Riddell, “Deposition of nickel and cobalt by chemical reduction,” *J. Res. Natl. Bur. Stand. (1934).*, vol. 39, pp. 385–395, 1947.

[75] H. Liu, N. Li, S. Bi, D. Li, and Z. Zou, “Effect of organic additives on the corrosion resistance properties of electroless nickel deposits,” *Thin Solid Films*, vol. 516, no. 8, pp. 1883–1889, Feb. 2008, doi: 10.1016/j.tsf.2007.10.008.

[76] W. J. Cheong, B. L. Luan, and D. W. Shoesmith, “The effects of stabilizers on the bath stability of electroless Ni deposition and the deposit,” *Appl. Surf. Sci.*, vol. 229, no. 1–4, pp. 282–300, May 2004, doi: 10.1016/j.apsusc.2004.02.003.

[77] K. P. Han and J. L. Fang, “Effect of cysteine on the kinetics of electroless nickel deposition,” *J. Appl. Electrochem.*, vol. 26, no. 12, pp. 1273–1277, Dec. 1996, doi: 10.1007/BF00249930.

[78] K. Wang, L. Hong, and Z.-L. Liu, “Investigation into the roles of sulfur-containing amino acids in electroless nickel plating bath,” *Ind. Eng. Chem. Res.*, vol. 47, no. 17, pp. 6517–6524, 2008, doi: 10.1021/ie800456b.

[79] G. O. Mallory, “The Electroless Nickel Plating Bath: Effect of Variables on the Process,” in *Electroless Plating: Fundamentals and Applications*, 1990, pp. 57–101.

[80] G. Gutzeit, “Catalytic Nickel Deposition from Aqueous Solution. I-IV,” *Plat. Surf. Finish.*, vol. 46, pp. 1158–1164, 1275–1275, 1377–1378, 1959.

[81] R. C. Agarwala and V. Agarwala, “Electroless alloy/composite coatings: A review,” *Sadhana*, vol. 28, no. 3–4, pp. 475–493, Jun. 2003, doi: 10.1007/BF02706445.

[82] T. Ookubo, S. Nishihama, and K. Yoshizuka, “Separation and Recovery of Nickel from Waste Electroless Nickel-Phosphorous Plating Solution,” *Solvent Extr. Res. Dev. Japan*, vol. 20, pp. 149–157, 2013, doi: 10.15261/serdj.20.149.

[83] N. M. Martyak and K. Drake, “Peak-profile analysis of electroless nickel coatings,” *J. Alloys Compd.*, vol. 312, no. 1–2, pp. 30–40, Nov. 2000, doi: 10.1016/S0925-8388(00)01099-9.

[84] P. Sampath Kumar and P. Kesavan Nair, “Studies on crystallization of electroless Ni-P

deposits," *J. Mater. Process. Technol.*, vol. 56, no. 1–4, pp. 511–520, Jan. 1996, doi: 10.1016/0924-0136(96)85110-7.
[85] R. Parkinson, "Properties and applications of electroless nickel."
[86] Anon., "The Engineering Properties of Electroless Nickel Coatings," 1983. [Online]. Available: https://docuri.com/download/engineering-properties-of-en-coatings_59c1cdebf581710b2863124a_pdf.
[87] R. Joseph Rathish *et al.*, "Corrosion Behaviour of Metals in Artificial Sweat," *Open Corros. J.*, vol. 3, no. 1, pp. 38–44, May 2010, doi: 10.2174/1876503301003010038.
[88] S. Kundu, S. K. Das, and P. Sahoo, "Properties of Electroless Nickel at Elevated Temperature-a review," *Procedia Eng.*, vol. 97, pp. 1698–1706, 2014, doi: 10.1016/j.proeng.2014.12.321.
[89] A. Bai, P.-Y. Chuang, and C.-C. Hu, "The corrosion behavior of Ni–P deposits with high phosphorous contents in brine media," *Mater. Chem. Phys.*, vol. 82, no. 1, pp. 93–100, Sep. 2003, doi: 10.1016/S0254-0584(03)00193-7.
[90] J. L. Dawson, G. John, and K. Oliver, "Management of corrosion in the oil and gas industry," *Shreir's Corros.*, pp. 3230–3269, 2010, doi: 10.1016/B978-044452787-5.00168-2.
[91] A. Brenner and G. E. Riddell, "Nickel Plating on Steel by Chemical Reduction," *J. Res. Natl. Bur. Stand. (1934).*, vol. 37, no. July, pp. 31–34, 1946.
[92] H.-C. Huang, S.-T. Chung, S.-J. Pan, W.-T. Tsai, and C.-S. Lin, "Microstructure evolution and hardening mechanisms of Ni–P electrodeposits," *Surf. Coatings Technol.*, vol. 205, no. 7, pp. 2097–2103, Dec. 2010, doi: 10.1016/j.surfcoat.2010.08.115.
[93] H. van Oosterhout, "Evaluation of Electroplated Nickel Phosphorous With High Phosphorous Content," *AMP J. Technol.*, vol. 2, pp. 63–69, 1992.
[94] R. L. Zeller and U. Landau, "Electrodeposition of Ni-P Amorphous Alloys," *J. Electrochem. Soc.*, vol. 139, no. 12, pp. 3464–3469, 1992, doi: 10.1149/1.2069100.
[95] C.-C. Hu and A. Bai, "Influences of the phosphorus content on physicochemical properties of nickel–phosphorus deposits," *Mater. Chem. Phys.*, vol. 77, no. 1, pp. 215–225, Jan. 2003, doi: 10.1016/S0254-0584(01)00592-2.
[96] C.-C. Hu and A. Bai, "Composition control of electroplated nickel–phosphorus deposits," *Surf. Coatings Technol.*, vol. 137, no. 2–3, pp. 181–187, Mar. 2001, doi: 10.1016/S0257-8972(00)01117-8.
[97] A. M. Pillai, A. Rajendra, and A. K. Sharma, "Electrodeposited nickel–phosphorous (Ni–P) alloy coating: an in-depth study of its preparation, properties, and structural transitions," *J. Coatings Technol. Res.*, vol. 9, no. 6, pp. 785–797, Nov. 2012, doi: 10.1007/s11998-012-9411-0.
[98] J. Chitty, A. Pertuz, H. Hintermann, M. H. Staia, and E. S. Puchi, "Influence of electroless Ni-P deposits on the corrosion-fatigue properties of an AISI 1045 steel," *Thin Solid Films*, vol. 308–309, pp. 430–435, Oct. 1997, doi: 10.1016/S0040-6090(97)00599-3.
[99] MacDermid Enthone, "NiKlad^{TM} ELV 835 Technical Data Sheet." pp. 1–14.
[100] MacDermid Enthone, "NiKlad^{TM} ELV 849 Technical Data Sheet." pp. 1–11.
[101] MacDermid Enthone, "Vand-Aloy 4100N Technical Data Sheet." pp. 1–7.
[102] J. Elvins, J. A. Spittle, and D. A. Worsley, "Microstructural changes in zinc aluminium alloy galvanising as a function of processing parameters and their influence on corrosion," *Corros. Sci.*, vol. 47, no. 11, pp. 2740–2759, Nov. 2005, doi: 10.1016/j.corsci.2004.11.011.
[103] J. Elvins, J. A. Spittle, J. H. Sullivan, and D. A. Worsley, "The effect of magnesium additions on the microstructure and cut edge corrosion resistance of zinc aluminium alloy galvanised steel," *Corros. Sci.*, vol. 50, no. 6, pp. 1650–1658, Jun. 2008, doi: 10.1016/j.corsci.2008.02.005.
[104] D. . Worsley, D. Williams, and J. S. . Ling, "Mechanistic changes in cut-edge corrosion induced by variation of organic coating porosity," *Corros. Sci.*, vol. 43, no. 12, pp. 2335–2348, Dec. 2001, doi: 10.1016/S0010-938X(01)00026-9.
[105] D. J. Penney, J. H. Sullivan, and D. A. Worsley, "Investigation into the effects of metallic

coating thickness on the corrosion properties of Zn–Al alloy galvanising coatings," *Corros. Sci.*, vol. 49, no. 3, pp. 1321–1339, Mar. 2007, doi: 10.1016/j.corsci.2006.07.006.

[106] J. R. Searle, C. F. Glover, K. Kahn, B. P. Wilson, G. Williams, and D. A. Worsley, "Electrochemical Scanning Techniques for the Examination of Bi-Metallic Coins," *ECS Trans.*, vol. 64, no. 28, pp. 47–59, 2015, doi: 10.1149/06428.0047ecst.

[107] R. Akid and D. J. Mills, "A comparison between conventional macroscopic and novel microscopic scanning electrochemical methods to evaluate galvanic corrosion," *Corros. Sci.*, vol. 43, no. 7, pp. 1203–1216, Jul. 2001, doi: 10.1016/S0010-938X(00)00091-3.

[108] J. Sullivan, N. Cooze, C. Gallagher, T. Lewis, T. Prosek, and D. Thierry, "In situ monitoring of corrosion mechanisms and phosphate inhibitor surface deposition during corrosion of zinc–magnesium–aluminium (ZMA) alloys using novel time-lapse microscopy," *Faraday Discuss.*, vol. 180, pp. 361–379, 2015, doi: 10.1039/C4FD00251B.

[109] N. Wint, J. H. Sullivan, and D. J. Penney, "The Role of pH on the Inhibition of Aqueous Zinc Corrosion by L-tryptophan," *J. Electrochem. Soc.*, vol. 164, no. 7, pp. C356–C366, May 2017, doi: 10.1149/2.0981707jes.

[110] L. Yang *et al.*, "Corrosion Behavior of Pure Magnesium with Low Iron Content in 3.5 wt% NaCl Solution," *J. Electrochem. Soc.*, vol. 162, no. 7, pp. C362–C368, Apr. 2015, doi: 10.1149/2.1041507jes.

[111] N. McMurray and D. A. Worsley, "Research in Chemical Kinetics Volume IV," in *Research in Chemical Kinetics Volume IV*, First., R. G. Compton and G. Hancock, Eds. Blackwell Science, 1997, p. 149.

[112] M. Stratmann and H. Streckel, "On the atmospheric corrosion of metals which are covered with thin electrolyte layers—I. Verification of the experimental technique," *Corros. Sci.*, vol. 30, no. 6–7, pp. 681–696, 1990, doi: 10.1016/0010-938X(90)90032-Z.

[113] M. Stratmann and H. Streckel, "On the atmospheric corrosion of metals which are covered with thin electrolyte layers—II. Experimental results," *Corros. Sci.*, vol. 30, no. 6–7, pp. 697–714, 1990, doi: 10.1016/0010-938X(90)90033-2.

[114] A. Leng and M. Stratmann, "The inhibition of the atmospheric corrosion of iron by vapour-phase-inhibitors," *Corros. Sci.*, vol. 34, no. 10, pp. 1657–1683, Oct. 1993, doi: 10.1016/0010-938X(93)90039-J.

[115] G. Williams, H. N. McMurray, and A. Bennett, "Inhibition of corrosion-driven organic coating delamination from a zinc surface using polyaniline pigments," *Mater. Corros.*, vol. 65, no. 4, pp. 401–409, Apr. 2014, doi: 10.1002/maco.201307571.

[116] M. Stratmann, H. Streckel, and R. Feser, "A new technique able to measure directly the delamination of organic polymer films," *Corros. Sci.*, vol. 32, no. 4, pp. 467–470, Jan. 1991, doi: 10.1016/0010-938X(91)90126-A.

[117] M. Stratmann, R. Feser, and A. Leng, "Corrosion protection by organic films," *Electrochim. Acta*, vol. 39, no. 8–9, pp. 1207–1214, Jun. 1994, doi: 10.1016/0013-4686(94)E0038-2.

[118] A. Leng, H. Streckel, and M. Stratmann, "The delamination of polymeric coatings from steel. Part 1: Calibration of the Kelvinprobe and basic delamination mechanism," *Corros. Sci.*, vol. 41, no. 3, pp. 547–578, Mar. 1998, doi: 10.1016/S0010-938X(98)00166-8.

[119] A. Leng, H. Streckel, and M. Stratmann, "The delamination of polymeric coatings from steel. Part 2: First stage of delamination, effect of type and concentration of cations on delamination, chemical analysis of the interface," *Corros. Sci.*, vol. 41, no. 3, pp. 579–597, Mar. 1998, doi: 10.1016/S0010-938X(98)00167-X.

[120] A. Leng, H. Streckel, K. Hofmann, and M. Stratmann, "The delamination of polymeric coatings from steel Part 3: Effect of the oxygen partial pressure on the delamination reaction and current distribution at the metal/polymer interface," *Corros. Sci.*, vol. 41, no. 3, pp. 599–620, Mar. 1998, doi: 10.1016/S0010-938X(98)00168-1.

[121] L.-E. Cheran, H.-D. Liess, and M. Thompson, "Scanning Kelvin microprobe in the tandem analysis of surface topography and chemistry," *Analyst*, vol. 124, no. 7, pp. 961–970, 1999,

doi: 10.1039/a809895f.

[122] G. Williams and H. N. McMurray, "Chromate Inhibition of Corrosion-Driven Organic Coating Delamination Studied Using a Scanning Kelvin Probe Technique," *J. Electrochem. Soc.*, vol. 148, no. 10, pp. 2–10, 2001, doi: 10.1149/1.1396336.

[123] B. C. Gee, P. R. Millard, and R. P. R. Dawber, "The new EURO releases nickel and elicits contact eczema," *Br. J. Dermatol.*, vol. 146, no. 1, pp. 155–156, Jan. 2002, doi: 10.1046/j.1365-2133.2002.46161.x.

[124] E. Nucera *et al.*, "Positive patch tests to Euro coins in nickel-sensitized patients," *Br. J. Dermatol.*, vol. 150, no. 3, pp. 500–503, Mar. 2004, doi: 10.1046/j.1365-2133.2004.05800.x.

[125] J. R. Davis, *Corrosion: Understanding the Basics*. ASM International, 2000.

[126] British Standards International, "PD 6484:1979 - Commentary on corrosion at bimetallic contacts and its allevation," 2011.

[127] ASTM, "G71-81 - Standard Guide for Conducting and Evaluating Galvanic Corrosion Tests in Electrolytes," *ASTM Standard*. pp. 1–5, 2003, doi: 10.1520/G0071-81R09.2.

[128] D. P. Schmidt, D. R. Skelton, and M. E. Malham, "Galvanic Corrosion Study on Stainless Steel Cartridge Design," 2008.

[129] F. Mansfeld, "Area Relationships in Galvanic Corrosion," *Corrosion*, vol. 27, no. 10, pp. 436–442, Oct. 1971, doi: 10.5006/0010-9312-27.10.436.

[130] P. Qiu and C. Leygraf, "Initial oxidation of brass induced by humidified air," *Appl. Surf. Sci.*, vol. 258, no. 3, pp. 1235–1241, Nov. 2011, doi: 10.1016/j.apsusc.2011.09.080.

[131] J. Sullivan, C. Weirman, J. Kennedy, and D. Penney, "Influence of steel gauge on the microstructure and corrosion performance of zinc alloy coated steels," *Corros. Sci.*, vol. 52, no. 5, pp. 1853–1862, May 2010, doi: 10.1016/j.corsci.2010.02.032.

[132] P. Qiu and C. Leygraf, "Multi-Analysis of Initial Atmospheric Corrosion of Brass Induced by Carboxylic Acids," *J. Electrochem. Soc.*, vol. 158, no. 6, p. C172, 2011, doi: 10.1149/1.3577600.

[133] M. Hourani and F. Wedian, "The effect of adatoms on the corrosion rate of copper," *Corros. Sci.*, vol. 42, no. 12, pp. 2131–2144, Dec. 2000, doi: 10.1016/S0010-938X(00)00039-1.

[134] A. Julander *et al.*, "New UK nickel-plated steel coins constitute an increased allergy and eczema risk," *Contact Dermatitis*, vol. 68, no. 6, pp. 323–330, Jun. 2013, doi: 10.1111/cod.12092.

[135] Z. Y. Chen, D. Persson, F. Samie, S. Zakipour, and C. Leygraf, "Effect of Carbon Dioxide on Sodium Chloride-Induced Atmospheric Corrosion of Copper," *J. Electrochem. Soc.*, vol. 152, no. 12, p. B502, 2005, doi: 10.1149/1.2098327.

[136] E. J. Schindelholz, H. Cong, C. F. Jove-Colon, S. Li, J. A. Ohlhausen, and H. K. Moffat, "Electrochemical aspects of copper atmospheric corrosion in the presence of sodium chloride," *Electrochim. Acta*, vol. 276, pp. 194–206, Jun. 2018, doi: 10.1016/j.electacta.2018.04.184.

[137] U. R. Evans, *The Corrosion and Oxidation of Metals*. Hodder Arnold, 1960.

[138] S. X. Li and L. H. Hihara, "Atmospheric corrosion initiation on steel from predeposited NaCl salt particles in high humidity atmospheres," *Corros. Eng. Sci. Technol.*, vol. 45, no. 1, pp. 49–56, Feb. 2010, doi: 10.1179/147842209X12476568584296.

[139] A. K. Neufeld, A. Bond, and I. S. Cole, "Characterisation of Corrosion Processes and Oxide Films Using a Kelvin Probe," in *Scanning Probe Techniques for Materials Characterisation at Nanometer Scale*, 2001, pp. 84–93.

[140] W. M. Haynes, Ed., *CRC Handbook of Chemistry and Physics*, 94th ed. CRC Press, 2015.

[141] A. du Plessis, "Studies of atmospheric corrosion processes in AA2024 - PhD Thesis," University of Birmingham, 2014.

[142] C. G. MacArthur, "Solubility of Oxygen in Salt Solutions and the Hydrates of These Salts," *J. Phys. Chem.*, vol. 20, no. 6, pp. 495–502, Jan. 1915, doi: 10.1021/j150168a003.

[143] H. Steen, "Determinations of the Solubility of Oxygen in Pure Water," *Limnol. Oceanogr.*, vol. 3, no. 4, pp. 423–426, Oct. 1958, doi: 10.4319/lo.1958.3.4.0423.

[144] "One Penny Coin," *The Royal Mint*. https://www.royalmint.com/discover/uk-coins/coin-design-and-specifications/one-penny-coin/ (accessed Mar. 16, 2018).

[145] "Two Pence Coin," *The Royal Mint*. https://www.royalmint.com/discover/uk-coins/coin-design-and-specifications/two-pence-coin/ (accessed Mar. 16, 2018).

[146] "Five Pence Coin," *The Royal Mint*. https://www.royalmint.com/discover/uk-coins/coin-design-and-specifications/five-pence-coin/ (accessed Mar. 16, 2018).

[147] "Ten Pence Coin," *The Royal Mint*. https://www.royalmint.com/discover/uk-coins/coin-design-and-specifications/ten-pence-coin/ (accessed Mar. 16, 2018).

[148] C. A. Loto, "Electroless Nickel Plating – A Review," *Silicon*, vol. 8, no. 2, pp. 177–186, Apr. 2016, doi: 10.1007/s12633-015-9367-7.

[149] A. W. Goldenstein, W. Rostoker, F. Schossberger, and G. Gutzeit, "Structure of Chemically Deposited Nickel," *J. Electrochem. Soc.*, vol. 104, no. 2, p. 104, 1957, doi: 10.1149/1.2428503.

[150] O. O. Ajibola, D. T. Oloruntoba, and B. O. Adewuyi, "Effect of Processing Parameters on the Protective Quality of Electroless Nickel-Phosphorus on Cast Aluminium Alloy," *J. Metall.*, vol. 2015, no. January 2016, pp. 1–12, 2015, doi: 10.1155/2015/386347.

[151] T. Anik *et al.*, "Influence of pH solution on electroless copper plating using sodium hypophosphite as reducing agent," *Int. J. Electrochem. Sci.*, vol. 7, no. 3, pp. 2009–2018, 2012.

[152] L. M. Abrantes and J. P. Correia, "On the Mechanism of Electroless Ni-P Plating," *J. Electrochem. Soc.*, vol. 141, no. 9, p. 2356, 1994, doi: 10.1149/1.2055125.

[153] R. Taheri, "Evaluation of Electroless Nickel-Phosphorus (EN) Coatings," Saskatchewan, 2003.

[154] W. Fields, R. Duncan, and J. Zickgraf, *ASM Metals Handbook Volume 5 - Surface Cleaning, Finishing and Coating*, 9th ed. ASM International.

[155] J. Sudagar, J. Lian, and W. Sha, "Electroless nickel, alloy, composite and nano coatings – A critical review," *J. Alloys Compd.*, vol. 571, pp. 183–204, Sep. 2013, doi: 10.1016/j.jallcom.2013.03.107.

[156] T. B. Massalski, *Binary Phase Diagrams*. American Society for Metals, 1986.

[157] R. N. Duncan, "The Metallurgical Structure of Electroless Nickel Deposits: Effect on Coating Properties," *Plat. Surf. Finish.*, pp. 65–69, 1996.

[158] D. B. Lewis and G. W. Marshall, "Investigation into the structure of electrodeposited nickel-phosphorus alloy deposits," *Surf. Coatings Technol.*, vol. 78, no. 1–3, pp. 150–156, Jan. 1996, doi: 10.1016/0257-8972(94)02402-2.

[159] A. A. Ashtiani, S. Faraji, S. A. Iranagh, and A. H. Faraji, "The study of electroless Ni–P alloys with different complexing agents on Ck45 steel substrate," *Arab. J. Chem.*, vol. 10, pp. S1541–S1545, May 2017, doi: 10.1016/j.arabjc.2013.05.015.

[160] R. Taheri, "Evaluation of Electroless Nickel-Phosphorous (EN) Coatings," Saskatchewan, 2003.

[161] J. L. Carbajal and R. E. White, "Electrochemical Production and Corrosion Testing of Amorphous Ni-P," *J. Electrochem. Soc.*, vol. 135, no. 12, p. 2952, 1988, doi: 10.1149/1.2095468.

[162] B.-H. Chen, L. Hong, Y. Ma, and T.-M. Ko, "Effects of Surfactants in an Electroless Nickel-Plating Bath on the Properties of Ni−P Alloy Deposits," *Ind. Eng. Chem. Res.*, vol. 41, no. 11, pp. 2668–2678, May 2002, doi: 10.1021/ie0105831.

[163] H. Z. Wang, Y. Song, Z. X. Zhang, S. W. Yao, and W. G. Zhang, "Corrosion behaviour of electrodeposited Ni–Sn–P alloys," *Surf. Eng.*, vol. 29, no. 1, pp. 6–10, Feb. 2013, doi: 10.1179/1743294412Y.0000000079.

[164] A. M. Simões, J. Torres, R. Picciochi, and J. C. S. Fernandes, "Corrosion inhibition at galvanized steel cut edges by phosphate pigments," *Electrochim. Acta*, vol. 54, no. 15, pp. 3857–3865, Jun. 2009, doi: 10.1016/j.electacta.2009.01.065.

[165] K. Aramaki, "The inhibition effects of organic inhibitors on corrosion of zinc in an aerated 0.5 M NaCl solution," *Corros. Sci.*, vol. 43, no. 10, pp. 1985–2000, Oct. 2001, doi: 10.1016/S0010-938X(00)00174-8.

[166] G. Cui, N. Li, D. Li, J. Zheng, and Q. Wu, "The physical and electrochemical properties of

electroless deposited nickel–phosphorus black coatings," *Surf. Coatings Technol.*, vol. 200, no. 24, pp. 6808–6814, Aug. 2006, doi: 10.1016/j.surfcoat.2005.10.015.

[167] R. Weil and K. Parker, "The properties of electroless nickel," in *Electroless plating*, 1990, pp. 111–137.

[168] C. Gu, J. Lian, G. Li, L. Niu, and Z. Jiang, "High corrosion-resistant Ni–P/Ni/Ni–P multilayer coatings on steel," *Surf. Coatings Technol.*, vol. 197, no. 1, pp. 61–67, Jul. 2005, doi: 10.1016/j.surfcoat.2004.11.004.

[169] T. Mimani and S. M. Mayanna, "The effect of microstructure on the corrosion behaviour of electroless Ni-P alloys in acidic media," *Surf. Coatings Technol.*, vol. 79, no. 1–3, pp. 246–251, Feb. 1996, doi: 10.1016/0257-8972(95)02446-8.

[170] M. Zaimi and K. Noda, "Effect of Coating Thickness on Corrosion Behavior of Electroless Quaternary Nickel Alloy Deposit in 3.5 wt% NaCl Solutions," *J. Adv. Manuf. Technol.*, vol. 8, no. 2, 2014.

[171] R. Taheri, I. N. A. Oguocha, and S. Yannacopoulos, "Effect of heat treatment on age hardening behaviour of electroless nickel–phosphorus coatings," *Mater. Sci. Technol.*, vol. 17, no. 3, pp. 278–284, Mar. 2001, doi: 10.1179/026708301773002950.

[172] W. Sha, X. Wu, and K. G. Keong, "Introduction to electroless copper and nickel-phosphorous (Ni-P) depositions," in *Electroless Copper and Nickel-Phosphorus Plating*, Woodhead Publishing Limited, 2011.

[173] K.-H. Hur, J.-H. Jeong, and D. N. Lee, "Microstructures and crystallization of electroless Ni-P deposits," *J. Mater. Sci.*, vol. 25, no. 5, pp. 2573–2584, May 1990, doi: 10.1007/BF00638061.

[174] R. M. Allen and J. B. VanderSande, "The Structure of Electroless Ni-P Films as a Function of Composition," *Scr. Metall.*, vol. 16, pp. 1161–1164, 1982.

[175] S. H. Park and D. N. Lee, "A study on the microstructure and phase transformation of electroless nickel deposits," *J. Mater. Sci.*, vol. 23, no. 5, pp. 1643–1654, May 1988, doi: 10.1007/BF01115703.

[176] K. Latt, "Results and Characterization of Electroless Nickel Phosphorus Alloy," 2003, pp. 68–76.

[177] J. Koeneman and A. G. Metcalfe, "The Solid Solubility of Phosphorus in Nickel," *Trans. Met. Soc. AIME*, vol. 212, 1958.

[178] W. Sha, X. Wu, and K. G. Keong, "Crystallisation of nickel–phosphorus (Ni–P) deposits with high phosphorus content," in *Electroless Copper and Nickel–Phosphorus Plating*, Woodhead Publishing Limited, 2011, pp. 141–162.

[179] H. Larhzil, M. Cissé, R. Touir, M. E. Touhami, and M. Cherkaoui, "Electrochemical and SEM investigations of the influence of gluconate on the electroless deposition of Ni–Cu–P alloys," *Electrochim. Acta*, vol. 53, no. 2, pp. 622–628, Dec. 2007, doi: 10.1016/j.electacta.2007.07.023.

[180] G. N. Flint, "A metallurgical approach to metal contact dermatitis," *Contact Dermatitis*, vol. 39, no. 5, pp. 213–221, Nov. 1998, doi: 10.1111/j.1600-0536.1998.tb05912.x.

[181] L. Oniciu and L. Mureşan, "Some fundamental aspects of levelling and brightening in metal electrodeposition," *J. Appl. Electrochem.*, vol. 21, no. 7, pp. 565–574, Jul. 1991, doi: 10.1007/BF01024843.

[182] D. Baudrand, "Nickel Sulfamate Plating, Its Mystique and Practicality," *Met. Finish.*, no. July, pp. 15–18, 1996.

[183] G. A. Di Bari, "Electrodeposition of Nickel," in *Modern Electroplating: Fifth Edition*, 5th ed., M. Schlesinger and M. Paunovic, Eds. John Wiley & Sons Inc., 2011, pp. 79–114.

[184] J. Macheras, D. Vouros, C. Kollia, and N. Spyrellis, "Nickel Electro- crystallization: Influence of Unsaturated Organic Additives on the Mechanism of Oriented Crystal Growth," *Trans. IMF*, vol. 74, no. 2, pp. 55–58, Jan. 1996, doi: 10.1080/00202967.1996.11871093.

[185] R. Seakr, "Microstructure and crystallographic characteristics of nanocrystalline copper prepared from acetate solutions by electrodeposition technique," *Trans. Nonferrous Met.*

Soc. China, vol. 27, no. 6, pp. 1423–1430, Jun. 2017, doi: 10.1016/S1003-6326(17)60164-X.

[186] H. Ke-Ping and F. Jing-Li, "Acceleration effect of electroless nickel deposition by thiourea," *Int. J. Chem. Kinet.*, vol. 28, no. 4, pp. 259–264, 1996, doi: 10.1002/(SICI)1097-4601(1996)28:4<259::AID-KIN3>3.3.CO;2-N.

[187] N. M. Martyak, F. Monzyk, and H. H. Chien, "Electroless Nickel Plating Baths," 5258061, 1993.

[188] G. Shahin, "Electroless Nickel Plating Solutions," US 2003/0232148 A1, 2003.

[189] N. Daneshvar, F. Shirini, M. S. N. Langarudi, and R. Karimi-Chayjani, "Taurine as a green bio-organic catalyst for the preparation of bio-active barbituric and thiobarbituric acid derivatives in water media," *Bioorg. Chem.*, vol. 77, pp. 68–73, Apr. 2018, doi: 10.1016/j.bioorg.2017.12.021.

[190] F. Shirini and N. Daneshvar, "Introduction of taurine (2-aminoethanesulfonic acid) as a green bio-organic catalyst for the promotion of organic reactions under green conditions," *RSC Adv.*, vol. 6, no. 111, pp. 110190–110205, 2016, doi: 10.1039/C6RA15432H.

[191] Chemicalize, "Sodium hypophisphite," 2019. https://chemicalize.com/#/calculation (accessed Jan. 24, 2018).

[192] T. C. Franklin, "Some mechanisms of action of additives in electrodeposition processes," *Surf. Coatings Technol.*, vol. 30, no. 4, pp. 415–428, May 1987, doi: 10.1016/0257-8972(87)90133-2.

[193] J. J. Hoekstra and D. Trivich, "The Uptake of Sulfur from Plating Brighteners by Copper and Nickel," *J. Electrochem. Soc.*, vol. 111, no. 2, p. 162, 1964, doi: 10.1149/1.2426076.

[194] D. R. Gabe and M. Clarke, "Plated Coatings," in *Shreir's Corrosion*, 2010, pp. 2577–2609.

[195] M. Yamaguchi, M. Shiga, and H. Kaburaki, "Grain Boundary Decohesion by Impurity Segregation in a Nickel-Sulfur System," *Science (80-.).*, vol. 307, pp. 393–397, Jan. 2005, doi: 10.1126/science.1104624.

[196] N. P. Wasekar, P. Haridoss, S. K. Seshadri, and G. Sundararajan, "Influence of mode of electrodeposition, current density and saccharin on the microstructure and hardness of electrodeposited nanocrystalline nickel coatings," *Surf. Coatings Technol.*, vol. 291, pp. 130–140, Apr. 2016, doi: 10.1016/j.surfcoat.2016.02.024.

[197] R. Sekar and S. Jayakrishnan, "Effect of sulphonic acids on electrodeposition of nickel and its structural and corrosion behaviour," *Trans. IMF*, vol. 90, no. 6, pp. 324–329, Nov. 2012, doi: 10.1179/0020296712Z.00000000032.

[198] R. Sekar, K. K. Jagadesh, and G. N. K. R. Bapu, "Microstructure and corrosion behavior of electrodeposited nanocrystalline nickel prepared from acetate bath," *Korean J. Chem. Eng.*, vol. 32, no. 6, pp. 1194–1200, Jun. 2015, doi: 10.1007/s11814-014-0289-7.

[199] S. Ahmadizadeh, S. M. Monirvaghefi, A. Saatchi, and A. Heidary Moghadam, "The effects of heat treatment on structure and corrosion behaviour of electroless Ni-P deposits on Al5083 alloy," in *Proceedings of Iran Internation Aluminium Conference (IIAC2009)*, 2009, no. April, pp. 182–186.

[200] R. Sekar and S. Jayakrishnan, "Electrodeposition of zinc from acetate based electrolytes," *Bull. Electrochem.*, vol. 15, no. 5–6, pp. 219–222, 1999.

[201] M. Chandran, "Effect of polyethylene glycol on electrodeposition of nano crystalline zinc," *J. Chem. Pharm. Res.*, vol. 5, no. 3, pp. 105–111, 2013.

[202] S. Yogesha and A. Chitharanjan Hegde, "Development of Composition Modulated Multilayer Alloy Coatings and their Corrosion Behavior," *J. Met. Mater. Miner.*, vol. 21, no. 1, pp. 83–92, 2011, [Online]. Available: http://www.material.chula.ac.th/Journal/v21-1/83-92 YOGESHA.pdf.

[203] Chemicalize, "Thiamine hydrochloride," 2019. https://chemicalize.com/#/calculation.

[204] W. Callister and D. Rethwisch, *Materials Science and Engineering*, Eighth Edi. John Wiley & Sons Inc., 2010.

[205] M. Sribalaji, O. S. Asiq Rahman, T. Laha, and A. K. Keshri, "Nanoindentation and nanoscratch behavior of electroless deposited nickel-phosphorous coating," *Mater. Chem. Phys.*, vol. 177,

pp. 220–228, Jul. 2016, doi: 10.1016/j.matchemphys.2016.04.022.
[206] M. J. Aleksinas, “Troubleshooting Electroless Nickel Plating Solutions,” in *Electroless Plating - Fundmentals and Applications*, 1990, pp. 101–109.
[207] F. Ogburn and C. E. Johnson, “Effects of electroless nickel process variables on quality requirements,” National Bureau of Standards, Annual Progress Report, Washington, 1973.